

VELOCITY STRUCTURE OF S.W. BRITISH COLUMBIA,
AND N.W. WASHINGTON, FROM 3-D NON-LINEAR
SEISMIC TOMOGRAPHY

by

Kumar Ramachandran

UNIVERSITY OF VICTORIA

Velocity Structure of S.W. British Columbia, and N.W. Washington, From 3-D Non-linear Seismic Tomography

by

Kumar Ramachandran

B.Sc., Madurai Kamaraj University, India, 1980
M.Sc.Tech., Indian School of Mines, Dhanbad, India, 1985
M.Tech., Indian School of Mines, Dhanbad, India, 1990

A Thesis Submitted in Partial Fulfillment of the
Requirements for the Degree of

DOCTOR OF PHILOSOPHY

in the

SCHOOL OF EARTH AND OCEAN SCIENCES

We accept this thesis as conforming
to the required standard

Dr. S. E. Dosso, Supervisor (School of Earth and Ocean Sciences)

Dr. G. D. Spence, Departmental Member (School of Earth and Ocean Sciences)

Dr. N. R. Chapman, Departmental Member (School of Earth and Ocean Sciences)

Dr. R. D. Hyndman, Outside Member (Pacific Geoscience Centre, Geological
Survey of Canada, Sidney, BC, Canada)

Dr. T.M. Brocher, External Examiner (U.S. Geological Survey, Menlo Park, CA,
USA)

© Kumar Ramachandran, November 24, 2001

UNIVERSITY OF VICTORIA

All rights reserved. This thesis may not be reproduced in whole or in part,
by photocopy or other means, without the permission of the author.

Supervisor: Dr. S. E. Dosso

Abstract

This thesis applies three-dimensional (3-D) non-linear seismic tomography to image crustal/upper mantle structure of S.W. British Columbia and N.W. Washington. Two tomographic inversions are carried out including high-resolution imaging of upper crustal structure using controlled source data, and deeper imaging by simultaneous inversion of controlled source and earthquake data.

Non-linear first arrival travel-time tomography is applied to controlled source data from the Seismic Hazards Investigation of Puget Sound (SHIPS) experiment conducted in 1998. Nearly 175,000 first arrival travel-times are inverted to obtain a minimum structure upper crustal velocity model to a depth of 12 km with a cubical cell size of 1 km. Results from checker-board tests for this velocity model indicate a lateral resolution of 20 km and above. The main geological and structural features in the study area are well defined by this velocity model. The structural outline of the sedimentary basins in the Straits of Georgia and Juan de Fuca are distinctly mapped. The Crescent Terrane is mapped beneath southern Vancouver Island with velocities up to 7 km/s that correlate well with the presence of gabbro in the subsurface. The northwest-southeast structural trend observed in the Strait of Georgia correlates with the observed seismicity. Shallow seismicity observed at the southern tip of Vancouver Island correlates with the location of the Leech River Fault.

An earthquake tomography algorithm was developed for joint estimation of hypocentral and velocity parameters, and tested on a synthetic data

set. Using this algorithm, tomographic inversion was performed simultaneously on earthquake and controlled source data from southwestern British Columbia and northwestern Washington. Approximately 15,000 first arrivals from 1,400 earthquakes and 40,000 first arrivals from the SHIPS experiment were simultaneously inverted for hypocentral parameters and velocity structure. Model resolution studies indicate a lateral resolution of 30 km and above.

Upper-crustal earthquakes close to southern Vancouver Island correlate with the velocity contrasts associated with the Leech River, Southern Whidbey Island, and Darrington-Devils Mountain faults. Three mafic to ultramafic high velocity units are identified at approximately 25 km depth beneath the Crescent Terrane and above the subducting Juan de Fuca crust. The continental crust and subducting Juan de Fuca crust and mantle are well mapped. The transition zone to continental mantle occurs at 35 km depth beneath the eastern Strait of Georgia. The slab seismicity beneath the Strait of Georgia at depths > 65 km lies below a low velocity zone mapped in the mantle wedge at depths of about 45–55 km. This low velocity zone may be indicative of the presence of fluids released during the phase change from basalt/gabbro to eclogite in the subducting slab.

Examiners:

Dr. S. E. Dosso, Supervisor (School of Earth and Ocean Sciences)

Dr. G. D. Spence, Departmental Member (School of Earth and Ocean Sciences)

Dr. N. R. Chapman, Departmental Member (School of Earth and Ocean Sciences)

Dr. R. D. Hyndman, Outside Member (Pacific Geoscience Centre, Geological
Survey of Canada, Sidney, BC, Canada)

Dr. T.M. Brocher, External Examiner (U.S. Geological Survey, Menlo Park, CA,
USA)

Table of Contents

1	Introduction	1
1.1	Motivation for the Study	1
1.2	Seismic Tomography	2
1.3	First Arrival 3-D Travel-time Tomography	3
1.4	Geology of Southern Vancouver Island and Adjoining Areas	5
1.5	Seismicity	12
1.6	Outline of Thesis	12
2	Controlled Source Tomography	15
2.1	Introduction	15
2.2	Theory: Controlled Source Tomography	15
2.2.1	Linearisation	15
2.2.2	Regularised Inversion	17
2.2.3	Resolution and Checkerboard Tests	23
2.3	Seismic Hazards Investigation of Puget Sound (SHIPS) . . .	25
2.4	Tomographic Inversion of SHIPS Data	27
2.5	Ray Coverage and Checkerboard Tests	44
2.6	Summary	45
3	Earthquake Tomography	54
3.1	Introduction	54
3.2	Theory: Earthquake Tomography	54
3.3	Synthetic Case Study	58
3.4	Tomographic Inversion of Earthquake Data	59
3.5	Ray Coverage and Checkerboard tests	81

3.6	Summary	82
4	Interpretation of Upper Crustal Structure	100
4.1	Introduction	100
4.2	Previous SHIPS 3-D Tomography Studies	101
4.3	Analysis of 3-D Velocity Model	102
4.4	Analysis of Horizontal Velocity Slices	103
4.4.1	Horizontal Velocity Slice at 1 km Depth	103
4.4.2	Horizontal Velocity Slice at 3 km Depth	104
4.4.3	Horizontal Velocity Slice at 5 km Depth	106
4.4.4	Horizontal Velocity Slice at 7 km Depth	106
4.4.5	Horizontal Velocity Slice at 9 km Depth	109
4.4.6	Horizontal Velocity Slice at 11 km Depth	109
4.5	Analysis of Profile Sections	113
4.5.1	Interpretation of Profile Section - P1	113
4.5.2	Interpretation of Profile Section - P2	115
4.5.3	Interpretation of Profile Section - P3	115
4.5.4	Interpretation of Profile Section - P4	118
4.5.5	Interpretation of Profile Section - P5	118
4.6	Interpretation of Isovelocity Surfaces	122
4.6.1	Interpretation of 5.5 km/s Isovelocity Surface	122
4.6.2	Interpretation of 6.0 km/s Isovelocity Surface	124
4.7	Summary	127
5	Interpretation of Deep Crustal Structure	129
5.1	Introduction	129
5.2	Previous Studies	129
5.3	Margin Parallel and Perpendicular Lines	136

5.3.1	Interpretation of Line S1	138
5.3.2	Interpretation of Line S2	154
5.3.3	Interpretation of Line S3	154
5.3.4	Interpretation of Line S4	155
5.3.5	Interpretation of Line S5	156
5.3.6	Interpretation of Line S7	156
5.3.7	Interpretation of Line D4	157
5.3.8	Interpretation of Line D5	157
5.3.9	Interpretation of Line D7	158
5.3.10	Interpretation of Line D10	158
5.3.11	Interpretation of Line D12	159
5.3.12	Interpretation of Line D13	159
5.3.13	Interpretation of Line D15	160
5.4	Interpretation of Regional Geology	160
5.4.1	Sedimentary Basins	160
5.4.2	Coast Plutonic Complex	161
5.4.3	Wrangellia	161
5.4.4	Pacific Rim Terrane	167
5.4.5	Crescent Terrane	168
5.4.6	Olympic Core Rocks	168
5.4.7	Mafic/Ultramafic Units	169
5.4.8	Continental Forearc Mantle	171
5.4.9	Oceanic Crust and Mantle	171
5.4.10	Seismicity Correlation With Structure	172
5.5	Summary	175
6	Discussion and Conclusions	177
6.1	Suggestions for Further Work	179

References	181
Appendix A Pseudo Code for Controlled Source Tomography	192
Appendix B Pseudo Code for Checkerboard Tests	194
Appendix C Pseudo Code for Earthquake Tomography	196
Appendix D CD-ROM Contents	197

List of Figures

1.1	Regional tectonic setting of the western British Columbia and Wash- ington margin	6
1.2	Major geological features in the study area.	8
1.3	Sedimentary basin and fault map	10
1.4	Seismicity map of western margin of British Columbia and Washington	13
2.1	Location map of SHIPS (1998) shot lines and receivers	26
2.2	Location map of SHIPS shot lines and receivers in the study area . .	28
2.3	Location map of the shot line segments used in this study	29
2.4	Seismogram of line 1 recorded at receiver CA04	30
2.5	Seismogram of line 4A recorded at receiver CA04	31
2.6	Seismogram of line 4B recorded at receiver CA04	31
2.7	Seismogram of line 5A recorded at receiver CA04	32
2.8	Seismogram of line 5B recorded at receiver CA04	32
2.9	Seismogram of line 6A recorded at receiver CA04	33
2.10	Seismogram of line 6B recorded at receiver CA04	33
2.11	Starting 1-D velocity model	35
2.12	Travel-time misfit in starting and final velocity model	37
2.13	Convergence of RMS travel-time misfit, normalised χ^2 and λ	38
2.14	Variation in perturbation, horizontal and vertical roughness	39
2.15	Starting velocity model	41
2.16	Perturbation velocity model	42
2.17	Final velocity model	43
2.18	Ray density in the final velocity model	46
2.19	Derivative sum in the final velocity model	47

2.20	Checkerboard test input anomaly pattern for 20 km grid size	48
2.21	Checkerboard test recovered anomaly pattern for 20 km grid size . . .	49
2.22	Semblance values for 20 km grid size	50
2.23	Checkerboard test input anomaly pattern for 30 km grid size	51
2.24	Checkerboard test recovered anomaly pattern for 30 km grid size . . .	52
2.25	Semblance values for 30 km grid size	53
3.1	Synthetic study area	60
3.2	True velocity model used in the synthetic study	61
3.3	Location of earthquakes and receivers used in the synthetic study . .	62
3.4	Starting velocity model for synthetic study	63
3.5	Final velocity model from the synthetic study	64
3.6	True, starting and relocated synthetic earthquake locations (4 km depth)	65
3.7	True, starting and relocated synthetic earthquake locations (8 km depth)	66
3.8	True, starting and relocated synthetic earthquake locations (12 km depth)	67
3.9	Final velocity model without joint hypocentral parameter estimation	68
3.10	Difference between true velocity model and final velocity model with joint hypocentral parameter estimation	69
3.11	Difference between true velocity model and final velocity model without joint hypocentral parameter estimation	70
3.12	Location of earthquakes used in the tomographic inversion	73
3.13	The earthquake locations projected on a vertical plane	74
3.14	1-D Starting velocity model	75
3.15	Relocated location of earthquakes	76
3.16	Relocated earthquake locations projected on a vertical plane	77
3.17	Travel-time misfit in starting and final model	78
3.18	Convergence plot of RMS travel-time misfit, normalised χ^2 , and λ . .	79

3.19	Variation in perturbation, horizontal and vertical roughness	80
3.20	Starting velocity model	83
3.20	Starting velocity model	84
3.21	Perturbation velocity model	85
3.21	Perturbation velocity model	86
3.22	Final velocity model	87
3.22	Final velocity model	88
3.23	Ray coverage in the final velocity model	89
3.23	Ray coverage in the final velocity model	90
3.24	Checkerboard test input anomaly pattern for 30 km grid size	91
3.25	Checkerboard test recovered anomaly pattern for 30 km grid size	92
3.26	Semblance values for 30 km grid size	93
3.27	Checkerboard test input anomaly pattern for 40 km grid size	94
3.28	Checkerboard test recovered anomaly pattern for 40 km grid size	95
3.29	Semblance values for 40 km grid size	96
3.30	Checkerboard test input anomaly pattern for 50 km grid size	97
3.31	Checkerboard test recovered anomaly pattern for 50 km grid size	98
3.32	Semblance values for 50 km grid size	99
4.1	Horizontal slice plot of SHIPS velocity model at 1 km depth	105
4.2	Horizontal slice plot of SHIPS velocity model at 3 km depth	107
4.3	Horizontal slice plot of SHIPS velocity model at 5 km depth	108
4.4	Horizontal slice plot of SHIPS velocity model at 7 km depth	110
4.5	Horizontal slice plot of SHIPS velocity model at 9 km depth	111
4.6	Horizontal slice plot of SHIPS velocity model at 11km depth	112
4.7	Plot showing the locations of the vertical profile sections	114
4.8	Vertical velocity section P1	116
4.9	Vertical velocity section P2	117

4.10	Vertical velocity section P3	119
4.11	Vertical velocity section P4	120
4.12	Vertical velocity section P5	121
4.13	Isovelocity surface map for 5.5 km/s	123
4.14	Isovelocity surface map for 6.0 km/s	125
4.15	Gravity anomaly map	126
5.1	Earthquake data from 1984–2000.	133
5.2	Crustal earthquakes from 1984–2000	134
5.3	Wadati-Benioff earthquakes from 1984–2000	135
5.4	Location map of margin parallel lines	139
5.5	Location map of margin perpendicular lines	140
5.6	Vertical velocity slice along line S1	141
5.7	Vertical velocity slice along line S2	142
5.8	Vertical velocity slice along line S3	143
5.9	Vertical velocity slice along line S4	144
5.10	Vertical velocity slice along line S5	145
5.11	Vertical velocity slice along line S7	146
5.12	Vertical velocity slice along line D4	147
5.13	Vertical velocity slice along line D5	148
5.14	Vertical velocity slice along line D7	149
5.15	Vertical velocity slice along line D10	150
5.16	Vertical velocity slice along line D12	151
5.17	Vertical velocity slice along line D13	152
5.18	Vertical velocity slice along line D15	153
5.19	Isovelocity surface at 5.5 km/s	162
5.20	Isovelocity surface at 6.0 km/s	163
5.21	Vertical velocity slice along line EW1	164

5.22	Vertical velocity slice along line NS1	165
5.23	Vertical velocity slice along line EW2	166
5.24	Vertical velocity slice along line S3	170
5.25	Depth to top of JdF crust	173
5.26	Vertical velocity slice along line D7	174

Acknowledgments

I could successfully complete this dissertation work due to the excellent help provided by a number of people. I am thankful to Dr. Stan Dosso for providing guidance and helping me stick to a tight time line. I would like to especially thank Dr. Roy Hyndman without whose unflagging support, this thesis would not exist. I appreciate the assistance provided by my committee members Dr. Ross Chapman and Dr. George Spence. I sincerely acknowledge Dr. Colin Zelt for helping me with the technical details of his 3-D tomography code and for making my stay at Rice University a pleasant experience. I am thankful to Dr. Gary Rogers for providing the earthquake database of southwestern British Columbia. I sincerely acknowledge the efforts of the SHIPS team members for collecting and distributing an excellent data set.

I owe a great deal to my friend Ruben Veefkind for being a great source of inspiration throughout my research and for spending long hours discussing the tomographic velocity models. It's been a great pleasure working with Michael Riedel at the seismology lab and also spending quality time at Felicitas! And then there are all the other people who have made Victoria a very special place over the past three years: Gloria Lopez, Vanessa Corre, Sheri Molnar, Hibak Hersi, David Mate, Sean Bailey, Steve Bloomer, Magnus Eek, Samantha Gray, Ivana Novosel, Richard Fitton, Johanna Hoehne, Lucinda Leonard, Joe English, Lisa Wolynech, Claire Currie and Maiclaire Bolton.

I am thankful to my family for their emotional support throughout this long process; especially to my mother and father for being a great source of inspiration; Lakshmi Mahesh and Mahesh Ramachandran for their loving care. Saratha Mahesh and Emily Oatney take a special mention for making me look forward and keep going when the going got tough!

I am indebted to the Oil and Natural Gas Corporation, India for granting me study leave to pursue this Ph.D. at the University of Victoria.

To

My Parents

*‘Civilisation exists by geologic consent,
subject to change without notice’*

Will Durant
Philosopher and Historian
(1885-1981)

Chapter 1

Introduction

1.1 Motivation for the Study

The Cascadia subduction zone of the west coast of British Columbia and Washington is an earthquake prone area. Two major tectonic processes are responsible for this earthquake activity. The first is the active subduction of the Juan de Fuca plate beneath the North American plate. Potentially dangerous megathrust earthquakes ($M > 8$) have occurred in the past at irregular intervals averaging about 600 years, the last having occurred about 300 years ago (Hyndman 1995a). Earthquakes also occur within the subducting plate due to the intraslab stress, downward pull on the slab, bending stress and ridge push. This process has resulted in several damaging earthquakes on the Cascadia margin, e.g. the Olympia earthquake (1949, $M_w = 7.1$, depth = 53 km), the Seattle earthquake (1965, $M_w = 6.8$, depth = 67 km), and the Nisqually earthquake (2001, $M_w = 6.8$, depth = 52.4 km).

Secondly, the stress regime in southwestern British Columbia and northwestern Washington is margin parallel (Mulder 1995; Wang *et al.* 1995). The upper crustal earthquakes in this region occur due to the margin parallel compressive stress. The earthquake activity in the urban corridor adjacent to sedimentary basins, including the cities of Vancouver, Seattle, and Tacoma, poses great threat to human life and property, mainly due to soil liquefaction and ground motion amplification. A proper mapping of the subsurface geology and tectonics is essential for better earthquake hazards planning and damage reduction efforts.

Given the socio-economic impact of earthquakes, studies aimed at understanding earthquake activity are of major importance. This thesis work is focussed towards

mapping the subsurface seismic velocity structure in the area covering southwestern British Columbia and northwestern Washington by applying seismic tomographic inversion to first arrival travel-time data. The constructed velocity structure is interpreted to map the shallow and deep crustal structure of the North American plate and the geometry of the subducting Juan de Fuca plate. Seismogenic zones are identified by correlating earthquake activity with three-dimensional velocity structure and known surface fault locations.

1.2 Seismic Tomography

Estimation of the seismic velocity structure of the Earth's crust and upper mantle from travel-time data has advanced greatly in recent years. Forward modelling trial-and-error methods have been superseded by tomographic methods which allow more objective analysis of large two-dimensional (2-D) and three-dimensional (3-D) refraction and/or reflection data sets. The medical community used the word 'tomography' to describe 2-D image reconstruction from line integral measurements of X-ray intensity along known ray paths. However, geophysicists use seismic tomography to describe 2-D and 3-D imaging based on inversion for physical properties along a ray path (e.g. travel-time tomography, attenuation tomography). The fundamental purpose of travel-time tomography is to determine the velocity structure of a medium by analysing the time it takes for a wave generated at a source point within the medium to arrive at a distribution of receiver points.

Travel-time tomography is a non-linear inverse problem. In linearising the travel-time tomography problem, one makes use of Fermat's principle, which implies that ray paths are stationary paths, that is, for small changes in travel-time, the ray paths remain approximately the same. Thus travel-times are more sensitive to the velocities encountered along the paths than to the paths themselves. In this case

the ray propagation paths are presumed without exactly knowing the velocity. The above assumption no longer applies to situations where structures with large velocity contrasts exist in the subsurface. Nonlinear tomography is comprised of repeated applications of linearised inversion, with each application achieving a better fit to the data until convergence is reached. The complexity in this class of problems is due to the extra burden of travel-time computation and ray tracing at each linearised step.

1.3 First Arrival 3-D Travel-time Tomography

In first arrival travel-time tomography, observed first arrival times from experiments with a spatial distribution of sources and receivers, are inverted for the velocity structure of the earth's subsurface in three dimensions. Mapping the subsurface in three dimensions is required to provide a realistic picture of the subsurface since the velocity structure is seldom sufficiently laterally homogeneous to be mapped using a 2-D approach.

In the first seismic tomography study, Aki *et al.* (1974) reported the results for the earth structure beneath the San Andreas fault zone by inverting teleseismic P arrival time data. Aki and Lee (1976) extended this method to data from local earthquakes. The inverse approach to velocity structure determination from travel-times was termed 'tomography' by Clayton and Comer (1983). With the introduction of iterative matrix solvers, the method was applied to solve for a large number of model parameters. Humphreys and Clayton (1988) applied direct inversion and the back-projection tomographic method and found both methods to be comparable in their ability to reconstruct the subsurface velocity structure. Zhao (1990) formulated earthquake tomography as a linearised inverse problem by direct inversion and by the iterative algorithm LSQR (Paige and Sanders 1982) and found that this method gave satisfactory results (Aki 1993).

Model parameterisation of the subsurface velocity structure has been approached in a variety of ways by different researchers. Aki *et al.* (1974) parameterised the subsurface into a number of rectangular constant velocity blocks. Crosson (1976) applied a 1-D layered model parameterisation to invert earthquake arrival times. Thurber (1983) used velocities interpolated between grid nodes to invert local earthquake and explosion travel-times. Hammer *et al.* (1994) employed a model parameterisation that uses a series of continuous functions which is well suited to problems with sparse ray coverage, and required only about 100 arrival times to study the velocity structure of oceanic crust. Toomey *et al.* (1994) referred to their method as an ‘adaptive inverse modelling tool,’ owing to the relatively large amount of prior information incorporated into the inversion. The main features of their method are the jumping strategy and regularisation in the form of vertical and horizontal smoothness constraints. Zelt and Barton (1998) applied regularised inversion as well as back-projection to study Faroe Basin data.

An important difference exists in the inverse methodology applied to active source data and earthquake data. In case of active source data, the location of the source and the receiver are known *a priori*. However the hypocentral parameters (location in space and origin time) of earthquakes are not known. The observed earthquake arrival times at a network of stations are initially inverted for hypocentral parameters using a 1-D velocity model. The hypocentral parameters so obtained are used as a starting model in an inversion for both hypocentral location and velocity structure. Where available, active source data can be jointly inverted with earthquake data. Generally the upper crustal structure exhibits strong lateral and vertical velocity variations. The active source data constrains well the upper crustal structure depending on the experimental geometry. With a well constrained upper crustal velocity structure, useful results can be obtained from earthquake data for the hypocentral parameters and the velocity structure of lower crust and upper mantle.

Most of the earlier 3-D tomographic methods were limited in their application

because of two factors. The first factor was the nonlinearity of the seismic travel-time problem. Many travel-time inversion methods avoided the fact that the ray paths depend on the unknown velocity structure by assuming that the velocity variations are small enough that the path variation is negligible. This limited the type of earth structures that could be imaged. Some tomographic methods accounted for the nonlinearity by iteratively ray tracing and performing linearised inversions. However accurate forward modelling and linear inversions are both computationally intensive. The second limitation of the earlier tomographic methods was that the computational cost limited the spatial resolution of the model. The inversion required solving a system of linear equations that relate the travel-times to the model parameters. In order to obtain a model parameterisation capable of resolving the structure illuminated by the data, the matrix inversion became computationally time consuming. However, modern computer systems with their large storage devices and high computational speed now have the capability to handle large matrix inversions.

1.4 Geology of Southern Vancouver Island and Adjoining Areas

In this section, a description of the regional geology and tectonics providing background to the tomographic inversion and interpretation is presented.

On the western margin of North America, a series of Pacific island arcs carried north and east on the Pacific plate collided with the North American plate. About 200 Ma the Intermontane superterrane, mostly made up of sedimentary and volcanic rocks, collided with the North America plate (Fig. 1.1). Around mid-Cretaceous time, the last major collisional episode emplaced the Insular Superterrane against the existing continental boundary represented by the Intermontane superterrane, and generated the mid-Cretaceous to early Tertiary intrusive rocks of the Coast Belt over the region of the suture (Monger *et al.* 1982). The two superterrane underlie

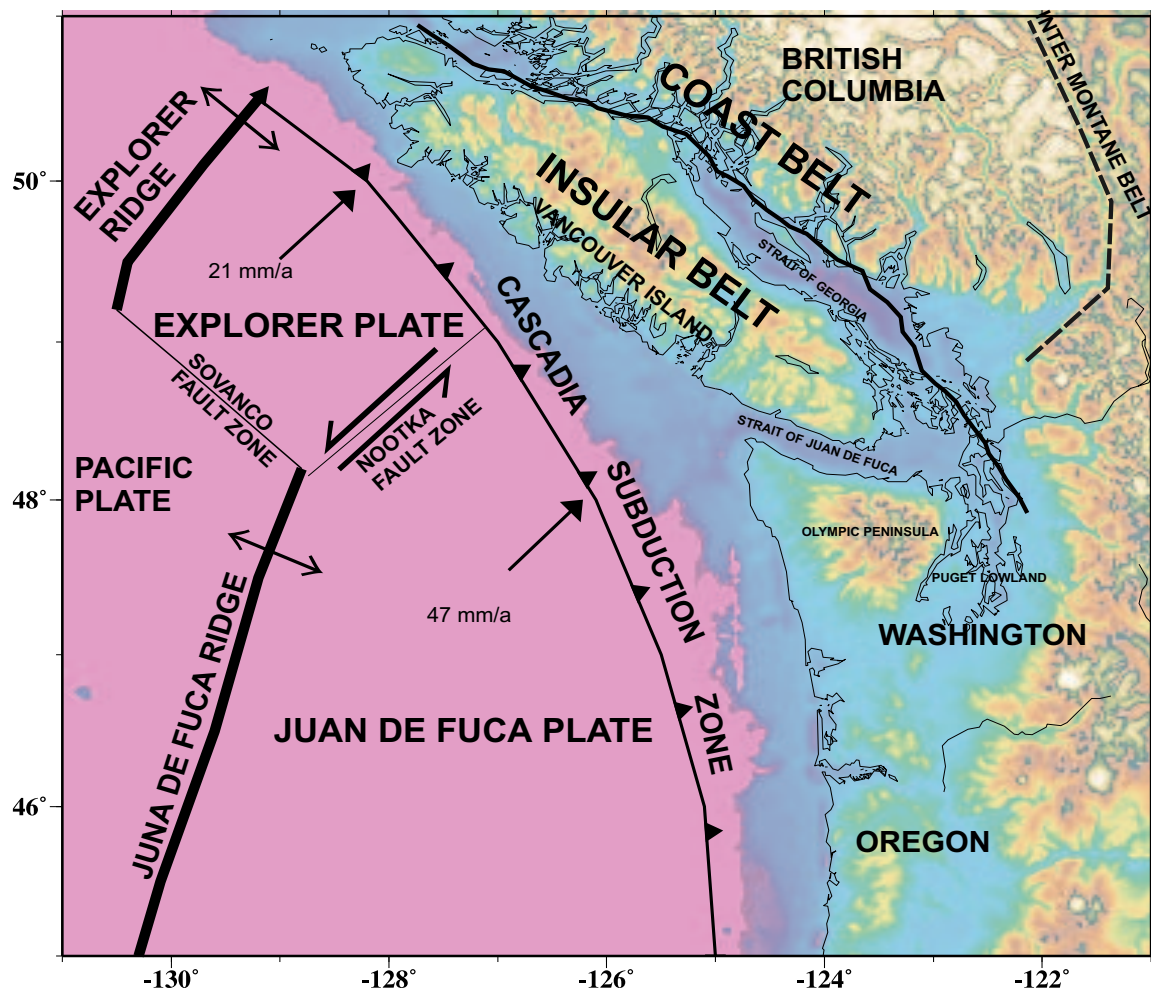


Figure 1.1 Regional tectonic setting of the western British Columbia and Washington margin.

the Intermontane and Insular belts, respectively. The Insular Belt comprises the Wrangellia Terrane and the Alexander Terrane. Vancouver Island is dominated by Wrangellia rocks, a package of Devonian through Lower Jurassic igneous sequences and sedimentary successions (Fig. 1.2). The Coast Belt was likely initiated when the Insular superterrane was thrust onto the western margin of North America. The Coast Belt lies to the east of Wrangellia and straddles the mid-Cretaceous suture zone between the Insular and Intermontane superterranes. The low velocity sediments of the Georgia basin have been mainly deposited along this suture. The structure of these belts is considered to be a stack of northeast dipping underthrust sheets (England and Bustin 1998). Much of the geological structure and overall character of present British Columbia developed during this period. Along the west coast and the southern part of the Island, outcrops of the small Pacific Rim Terrane, in contact with Wrangellia rocks, are found along the San Juan and Survey Mountain faults. The Crescent Terrane outcrops on the southern tip of the Vancouver Island and northwestern Washington. In southern Vancouver Island the Leech River fault delineates the contact between the Pacific Rim Terrane and Crescent Terrane.

Wrangellia rocks of the Insular Superterrane, named after the Wrangell Mountains of southern Alaska, extend from Vancouver Island to southern Alaska (Muller 1977). Based on paleomagnetic data, these rocks originated far to the south of its present position (Irving 1985). The lowest unit, designated a 'sediment-sill' unit, comprise up to 200 m of shale and siltstone. These sedimentary rocks, intruded by numerous basic sills, overly the Upper Paleozoic sedimentary rocks of the Sicker Group. The Karmutsen Formation of the Vancouver Group overlies the Sicker Group. The Karmutsen is divided into three units: a 2500 m thick basal member composed of pillow lava; a 600-110 m thick pillow breccia in the middle; and a 3000 m thick upper member composed of basalt flows with minor amounts of pillow lava and some sedimentary layers. The Karmutsen is overlain at some places by the limestone of the Quatsino Formation. The Triassic Vancouver Group is overlain by the Jurassic volcanics of the

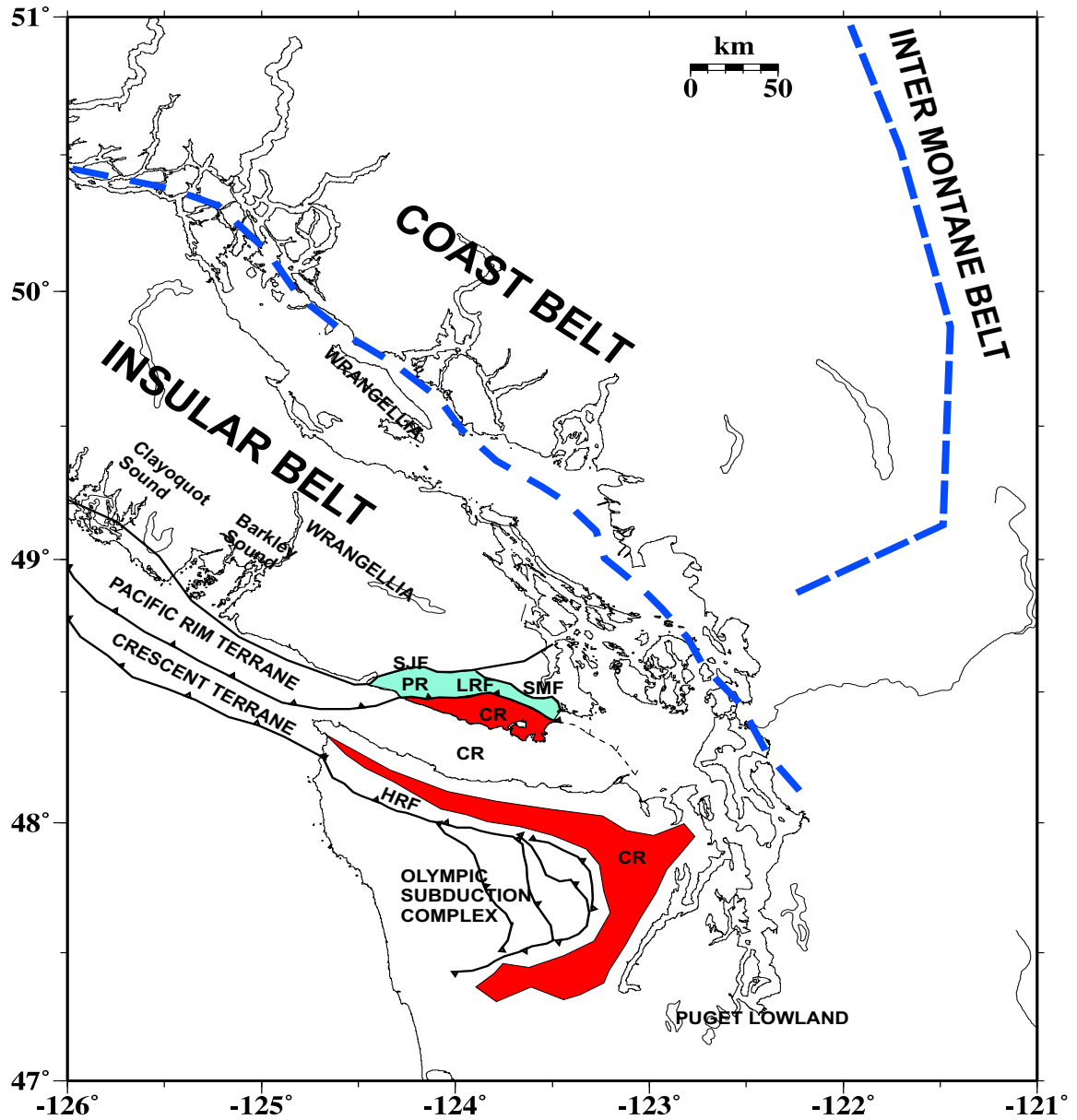


Figure 1.2 Major geological features in the study area. PR - Pacific Rim Terrane; CR - Crescent Terrane; LRF - Leech River fault; SJF - San Juan fault; SMF - Survey Mountain fault; HRF - Hurricane Ridge fault.

Bonanza Group. Extensive igneous intrusions cut through Wrangellia assemblages on Vancouver Island. Metamorphic complexes are exposed on the west coast and southern part of the Island. The collision with North America resulted in the folding and uplifting of Wrangellia and the formation of the Cowichan Fold and Thrust Belt (CFTB) as shown in Fig. 1.3. No pre-Tertiary rocks of continental-margin affinity are preserved in place along the southern Vancouver Island margin. Paleomagnetic results from Wrangellia suggest that any sediments accumulated upon this margin have been transported northward by late-Cretaceous transform-fault motion (Irving 1985). The surface contact between the Coast Belt and the Wrangellia Terrane occurs near the eastern edge of the Strait of Georgia.

The Pacific Rim Terrane and Crescent Terrane were the last to join the continent and reached their present locations during late Cretaceous and Tertiary Periods (Johnson 1984). The mainly meta-sedimentary Mesozoic Pacific Rim Terrane and the volcanic Eocene Crescent Terrane lie along the west coast and southern end of Vancouver Island. The emplacement of Pacific Rim Terrane and Crescent Terrane against and beneath the Insular Superterrane is assumed to have occurred during the same tectonic event, at about 42 Ma, although the Crescent Terrane may have first underthrust the Pacific Rim (PR). The Pacific Rim Terrane comprises three components acquired on a continental margin setting. The first is a melange of disrupted mudstone, chert, sandstone, conglomerate and volcanics. The other two components are the Leech River Formation and Pandora Peak Unit, exposed on southern Vancouver Island and comprising schistose greywacke, slate, and higher grade metasediments as well as unmetamorphosed sediments and metavolcanics. In southern Vancouver Island, the Pacific Rim Terrane is separated from Wrangellia by the San Juan fault and Survey Mountain fault system. The Pacific Rim Terrane is also exposed in a narrow strip along the central west coast of the Island, bound to the east by the Westcoast fault (Fig. 1.3). Mafic rocks of the Eocene Crescent Terrane which form the basal part of the Olympic Mountain succession composed of basalt, diabase and

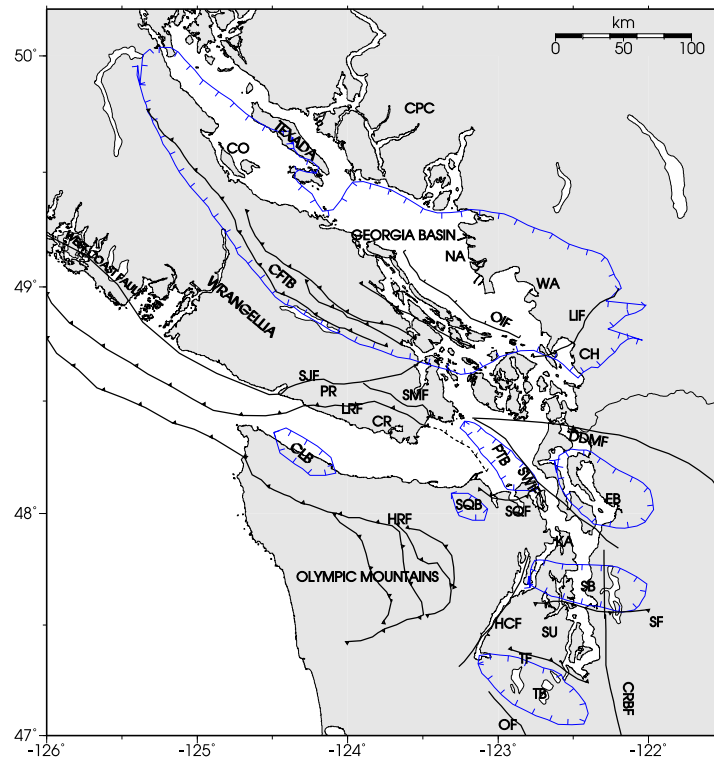


Figure 1.3 Sedimentary basin and fault Map. Major geologic features taken from Muller (1977), England and Bustin (1998), Zelt *et al.* (2000), Brocher *et al.* (2001), and Wagnor *et al.* (2001). CFTB-Cowichan Fold and Thrust Belt; CH-Chuckanut subbasin; CLB-Clallum basin; CO-Comox subbasin; CPC-Coast Plutonic Complex ; CRBF-Coast Range boundary fault; CR-Crescent Terrane; DDMF-Darrington-Devils Mountain fault; EB-Everett basin; HCF-Hood Canal fault; HRF-Hurricane Ridge fault; LIF-Lummi Island fault; LRF-Leech River fault; NA- Nanaimo subbasin; OF-Olympia fault; OIF-Outer Islands fault; PR-Pacific Rim Terrane; PTB-Port Townsend basin; SB-Seattle basin; SF-Seattle fault; SJF-San Juan fault; SMF-Survey Mountain fault; SQB-Sequim basin; SQF-Sequim fault; SU-Seattle uplift; SWIF-southern Whidbey Island fault; TB-Tacoma basin; TF-Tacoma fault; WA-Whatcom subbasin.

gabbro, are considered to be correlative to the Metchosin volcanics of southern Vancouver Island (Muller 1980). The Metchosin volcanics consist of an estimated 3000 m of pillow lavas, breccias and minor silicious tuffs, succeeded by 1000 m of layered amygdaloidal flows. At one place there is a minor limestone lens at the transition of the pillow lavas to flows and early Eocene age is indicated (Muller 1980). The basalts of the lower part of the formation are submarine and of partly nearshore origin as indicated by the presence of well preserved gastropods. An ophiolitic succession is observed, except that ultramafic rocks are absent. Massey (1986) proposed that the terrane formed as new oceanic crust in a marginal basin.

The Juan de Fuca plate is converging with the North American margin at a relative rate of 47 mm/a directed N56°E (Riddihough and Hyndman 1991). The modern accretionary complex has formed beneath and against the Crescent Terrane by scraping off the incoming sediments on the subducting Juan de Fuca plate (Davis and Hyndman 1989). The forearc Tofino basin formed by the deposition of Eocene to Recent marine clastic sediments over the Pacific Rim and Crescent Terrane and the inner portion of the modern accretionary wedge and covers most of the continental shelf (Hyndman *et al.* 1990). The subduction process has created the Olympic Subduction Complex to the south of Vancouver Island (e.g. Brandon and Calderwood 1998).

To the south of Vancouver Island, the Strait of Juan de Fuca with a thick column of sediment lies in the synclinal depression formed by the Crescent Terrane. To the east of Vancouver Island, the Strait of Georgia is a forearc basin which straddles the boundary of the Insular and Coast belts. To the east of the Olympic Subduction Complex, the Puget Lowland is a forearc basin in continuity with the Strait of Georgia to the north. The portion of Crescent Terrane east of the Olympic Subduction Complex is tilted to the east by the uplift of the accretionary sediments in the complex (e.g. Brandon and Calderwood 1990).

1.5 Seismicity

A map of the seismicity on the margin of southwestern British Columbia and northwestern Washington is shown in Fig. 1.4. The earthquakes occur in two zones, the deeper Wadati-Benioff seismicity in the subducting Juan de Fuca plate (e.g. Rogers 1983; Crosson and Owens 1987) and shallower earthquakes in the North American continental crust (e.g. Wang *et al.* 1995). Small to moderate size earthquakes occur within the continental upper crust. These earthquakes are concentrated in southwestern British Columbia and in the Puget Sound region. They are limited to the upper 30 km of the continental crust, constrained by the maximum temperature for crustal earthquake failure of about 350° C (Hyndman and Wang 1993). Generally, no correlation of surface faulting with seismicity has been reported, except for the probable association of the 1946, $M = 7.3$ event with the Beaufort Range fault in central Vancouver Island (e.g. Hyndman 1995).

1.6 Outline of Thesis

This thesis applies nonlinear seismic tomography to controlled source and earthquake data for southwestern British Columbia and northwestern Washington, and interpreting the results in terms of subsurface geological and structural features.

The theory of nonlinear seismic tomography as applied to controlled source seismic data is reviewed in Chapter 2. Data processing and tomographic inversion of the 1998 Seismic Hazards Investigation in Puget Sound (SHIPS) experiment are presented. The constructed velocity model is evaluated for model resolution using checkerboard tests and derivative sum method.

In Chapter 3, the theory of nonlinear earthquake tomography is reviewed and an algorithm is developed for joint estimation of hypocentral parameters and velocity structure. The algorithm is tested on a synthetic data set for performance evaluation.

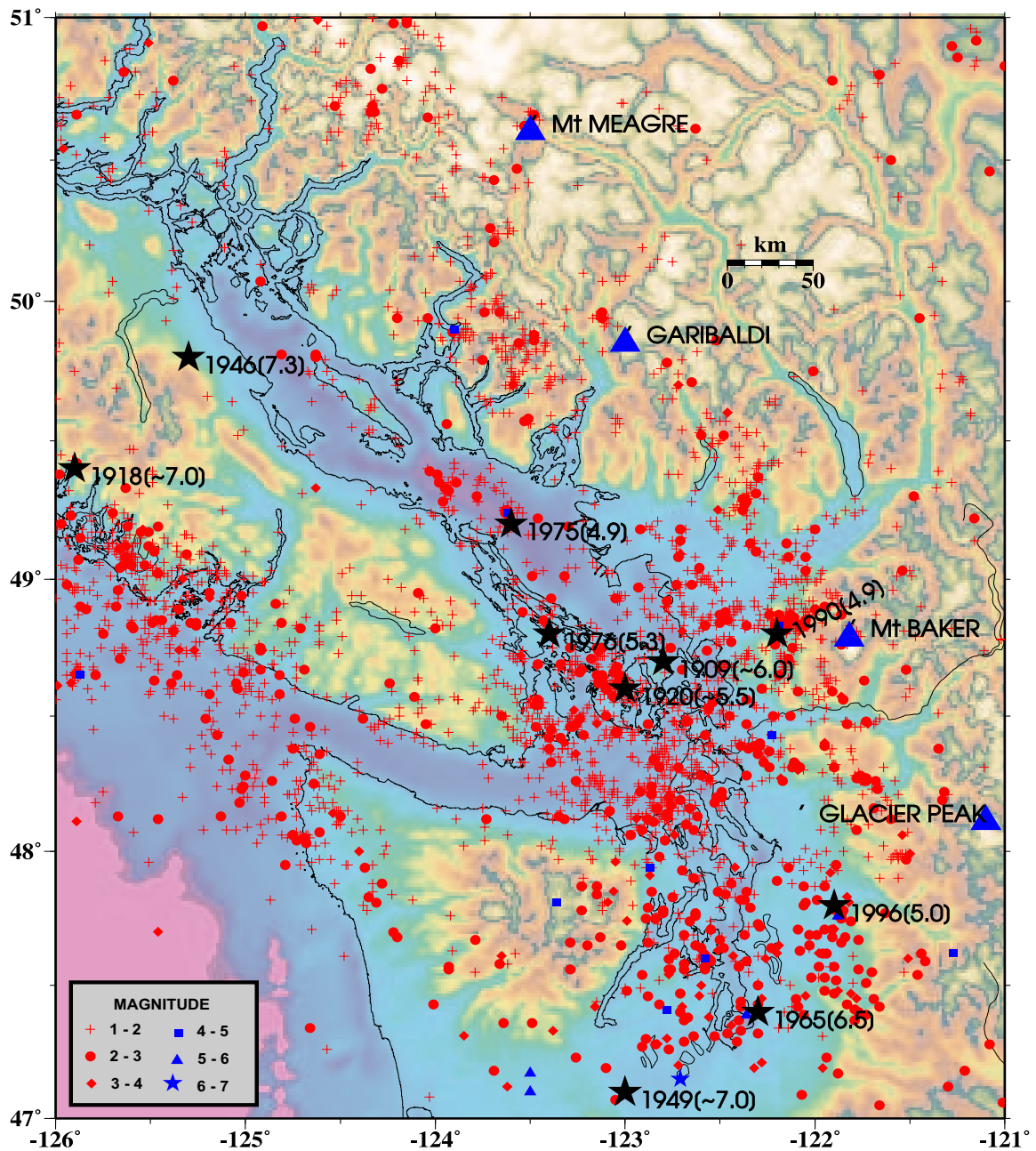


Figure 1.4 Seismicity map of western margin of British Columbia and Washington from 1984–2000.

The algorithm is then applied to a simultaneous inversion of controlled source data from the SHIPS experiment and earthquake data from southwestern British Columbia and northwestern Washington. Model resolution tests are conducted on the resulting velocity model.

Interpretation of upper crustal features is considered in Chapter 4 by analysing the velocity model constructed using controlled source tomography in Chapter 2. Structure and geology of the upper crust are delineated to a depth of 12 km where appropriate ray coverage exists. Sedimentary basins are mapped and maximum sediment thickness is interpreted. Earthquake activity in the upper crust is analysed and seismogenic zones are associated with mapped structural features.

In Chapter 5, the interpretation of the velocity model obtained from simultaneous tomographic inversion of earthquake and controlled source data is presented. The crustal and sub-crustal features are mapped and interpreted for their tectonic significance. The subducting Juan de Fuca oceanic crust and mantle are mapped. Velocity discontinuities are associated with known fault locations and correlated with earthquake activity. Mafic/ultramafic units are identified at deeper levels above the subducting plate.

Appendix A outlines the computational sequence for the nonlinear seismic tomography method discussed by Zelt and Barton (1998). Appendix B gives the computational sequence for the checkerboard resolution tests used for estimating model resolution. Appendix C outlines the computational sequence for earthquake tomography for joint estimation of hypocentral and velocity parameters. In Appendix D the constructed velocity models, horizontal/vertical slice plots, and isovelocity surface plots are provided on a CD-ROM.

Chapter 2

Controlled Source Tomography

2.1 Introduction

Tomographic inversion of first arrival travel-time data is a nonlinear problem since both the velocity of the medium and ray paths in the medium are unknown, and the solution is typically obtained by repeated application of linearized inversion. Regularisation of the nonlinear problem reduces the ill-posedness inherent in the tomographic inversion due to the under-determined nature of the problem and the inconsistencies in the observed data. The regularised inverse problem is solved such that the data are fit according to their observed uncertainties while solving for model parameter estimates that conform to a desired *a priori* measure of model structure. The resolution of the estimated model parameters in nonlinear tomography is accessed by studying the ray density and checkerboard test results. The theory pertaining to regularised first arrival nonlinear travel-time tomography and the checkerboard tests is detailed in this chapter, with application to the SHIPS data set.

2.2 Theory: Controlled Source Tomography

2.2.1 Linearisation

Seismic surveys based on explosive, vibrator or air-gun sources and receivers on land or sea have the advantage of having defined recording geometry, *i.e.*, the source and receiver positions are known *a priori*. In such a case, the travel-time t of a seismic arrival can be written as

$$t = \int_{l[m(\mathbf{r})]} m(\mathbf{r}) dl, \quad (2.1)$$

where $m(\mathbf{r})$ is the slowness (reciprocal of velocity) field of the medium, defined as a function of the 3-D position vector \mathbf{r} . The relationship between t and m is nonlinear, as the integral is performed over the ray path $l[m(\mathbf{r})]$, which is dependent on the slowness of the medium. The relationship is linearised by considering a small perturbation of the slowness about a reference slowness field of the medium $m_o(\mathbf{r})$. The modified travel-time expression is given by

$$t = \int_{l[m_o(\mathbf{r})+\delta m(\mathbf{r})]} m_o(\mathbf{r}) dl + \int_{l[m_o(\mathbf{r})+\delta m(\mathbf{r})]} \delta m(\mathbf{r}) dl, \quad (2.2)$$

where $\delta m(\mathbf{r})$ is the slowness perturbation. Using Fermat's principle of ray path stationarity with respect to slowness, the integral over $l[m_o(\mathbf{r}) + \delta m(\mathbf{r})]$ can be approximated by an integral over $l[m_o(\mathbf{r})]$ in the reference slowness field of the medium. The first integral then approximately equals t_o , the travel-time in the reference slowness field. The travel-time perturbation is then written as

$$\Delta t = t - t_o = \int_{l[m_o(\mathbf{r})]} \delta m(\mathbf{r}) dl. \quad (2.3)$$

Since the ray path $l[m_o(\mathbf{r})]$ and travel-time t_o can be calculated for the reference slowness model, equation (2.3) defines a linear relationship which is a reasonable approximation between the travel-time residual and the slowness perturbation near the reference slowness field of the model. By adopting a discrete parameterisation of the slowness structure, equation (2.3) can be written as

$$\Delta t = \sum_{i=1}^M \frac{\partial t(\mathbf{m}_o)}{\partial \mathbf{m}_i} \Delta \mathbf{m}_i, \quad (2.4)$$

where t is the travel time, \mathbf{m}_i are the model slowness parameters, and M is the number of model parameters. The partial derivative of travel-time with respect to slowness is the length of the path influenced by the model parameter. This relationship is employed in an iterative inversion scheme to find a final slowness model.

2.2.2 Regularised Inversion

Regularisation deals with the ill-posedness of the inverse problem. The under-determined part of the problem is controlled by providing *a priori* knowledge on the physical solution in the form of additional constraints that the solution must satisfy (Jackson 1979; Tarantola and Valette 1982). The final model is constrained to fit the data and also to satisfy some additional property. For tomography, this property is selected such that the final model is as smooth as possible. This concept is physically meaningful as smooth models are sought that include only structure that is required to fit the data according to its uncertainty (Constable *et al.* 1987). The motivation for seeking a smooth model is that features present in the model should be essential to match the observations. Such a class of models are referred to as minimum structure models. There are also several physical reasons for choosing the smooth models in ray-based travel-time tomography problems (Zelt and Barton 1998): (i) infinite-frequency ray methods are valid only for smooth media, (ii) travel-times constrain only the long wavelength model features since the data represent integrals through the model, and (iii) the linearisation assumption of stationary ray paths is more likely to be satisfied for smooth models.

The amount of structure in the estimated model parameters is measured in terms of roughness. In seismic tomography, second spatial derivatives are employed to quantify the model roughness (Lees and Crosson 1989). In this kind of regularised inversion, an objective function is minimized which includes norms that measure model roughness and data misfit. A tradeoff parameter is selected that provides the model with the least structure for a given level of data misfit. For Gaussian noise, the acceptable data misfit is set to the expected value for the χ^2 misfit statistic, i.e. $\langle \chi^2 \rangle = N$, where N is the number of data. The normalised χ^2 is defined as $\chi^2/(N - 1)$ where N is the number of data (Zelt and Barton 1998). In the present study, the acceptable data misfit is obtained at a normalised χ^2 value of one. The

concepts of linearisation and regularisation are implemented in matrix notation as follows.

From Shaw and Orcutt (1985), a forward problem is described by

$$\mathbf{t} = G(\mathbf{m}), \quad (2.5)$$

where \mathbf{t} represents the vector of measured data and G represents the functional which operates on the model \mathbf{m} to produce the data. In travel-time tomographic inversion, the relationship in the above equation is nonlinear, and represents computation of travel-times. Assuming that an initial model \mathbf{m}_o is ‘close’ to the real earth model \mathbf{m} , the problem can be linearised by expanding the observed travel-times in Taylor series about model \mathbf{m}_o

$$G(\mathbf{m}) = G(\mathbf{m}_o) + \mathbf{L}\Delta\mathbf{m} + O\|\Delta\mathbf{m}^2\|, \quad (2.6)$$

where \mathbf{L} is the partial derivative matrix of the functional G at \mathbf{m}_o , $\Delta\mathbf{m}$ is the model correction vector. Discarding the nonlinear term $O\|\Delta\mathbf{m}^2\|$, the linearisation can be expressed as

$$\mathbf{L}\Delta\mathbf{m} \approx G(\mathbf{m}) - G(\mathbf{m}_o) = \mathbf{t} - G(\mathbf{m}_o). \quad (2.7)$$

The left-hand side of the above equation (2.7) is a matrix product and the right-hand is a data residual vector.

Applying a modification to equation (2.7), as given by Shaw and Orcutt (1985), by adding \mathbf{Lm}_o to both sides of equation (2.7):

$$\mathbf{L}\Delta\mathbf{m} + \mathbf{Lm}_o \approx \mathbf{t} - G(\mathbf{m}_o) + \mathbf{Lm}_o. \quad (2.8)$$

Substituting $\mathbf{m} = \Delta\mathbf{m} + \mathbf{m}_o$ in equation (2.8):

$$\mathbf{Lm} \approx \mathbf{t} - G(\mathbf{m}_o) + \mathbf{Lm}_o. \quad (2.9)$$

The important difference between equation (2.7) and (2.9) is that equation (2.9) is solved for the model \mathbf{m} , and not for a correction vector $\Delta\mathbf{m}$. This allows constraints

to be applied to the model itself rather than to the model correction. Applying smoothness constraints to equation (2.7) leads to the system of equations:

$$\begin{pmatrix} \mathbf{L} \\ \lambda \mathbf{C} \end{pmatrix} \Delta \mathbf{m} = \begin{pmatrix} \mathbf{t} - G(\mathbf{m}_o) \\ 0 \end{pmatrix}, \quad (2.10)$$

where \mathbf{C} is the regularisation operator (discussed below) and λ is the tradeoff parameter that controls data misfit to model roughness. The regularised inverse problem that solves equation (2.10) is known as the creeping approach (Backus and Gilbert 1967; Parker 1985) which is solved for model perturbation $\Delta \mathbf{m}$ and also constrains $\Delta \mathbf{m}$ during the inversion. The disadvantage of the creeping approach is that the final model possesses no special properties and is simply a sum of smooth deviations from the starting model (Shaw and Orcutt 1985).

Alternatively applying smoothness constraints to equation (2.9) gives the system of equations:

$$\begin{pmatrix} \mathbf{L} \\ \lambda \mathbf{C} \end{pmatrix} \mathbf{m} = \begin{pmatrix} \mathbf{t} - G(\mathbf{m}_o) \\ 0 \end{pmatrix} + \begin{pmatrix} \mathbf{L} \mathbf{m}_o \\ 0 \end{pmatrix}. \quad (2.11)$$

Equation (2.11) can be solved for the new model \mathbf{m} and places constraints on \mathbf{m} . This method is known as the jumping approach (Parker 1985). In the jumping approach, a suitable norm of the model is set to be minimised, which can result in the final model having properties such as flatness or smoothness.

In seismic tomography, the number of parameters needed to represent a realistic model often exceeds the number of data points. When the dimensions of the model space exceed that of data space, the regularisation plays a prominent role in obtaining a meaningful solution. Toomey *et al.* (1994) applied tomographic inversion for imaging the East Pacific Rise using horizontal and vertical smoothing as regularisation constraints. They called such an approach as ‘the adaptive inverse modelling tool.’

The final model obtained using this approach was referred to as ‘the preferred model,’ since regularising constraints were used in the inversion process. As the variation of velocity in the lateral and vertical directions is usually different, the horizontal and vertical smoothing operators are implemented separately in the inversion algorithm.

Zelt and Barton (1998) applied a similar tomographic inversion to determine the 3-D velocity structure from first arrival travel-time data. Their tomographic method implemented regularising constraints by penalising total model roughness and used the ‘jumping’ strategy. The objective function Φ minimised at each iteration is given by

$$\Phi(\mathbf{m}) = \Delta \mathbf{t}^T \mathbf{C}_d^{-1} \Delta \mathbf{t} + \lambda [\mathbf{m}^T \mathbf{C}_h^{-1} \mathbf{m} + s_z \mathbf{m}^T \mathbf{C}_v^{-1} \mathbf{m}] , \quad (2.12)$$

where \mathbf{m} is the slowness model vector; $\Delta \mathbf{t}$ is the travel-time data residual vector; \mathbf{C}_d is the data covariance matrix describing the errors in the observations; \mathbf{C}_h and \mathbf{C}_v are the horizontal and vertical roughening matrices, respectively; λ is the trade-off parameter; and s_z sets the relative importance of maintaining horizontal to vertical model smoothness. Following Zelt and Barton (1998), this leads to the system of equations

$$\begin{bmatrix} \mathbf{C}_d^{-1/2} \mathbf{L} \\ \lambda \mathbf{C}_h \\ s_z \lambda \mathbf{C}_v \end{bmatrix} \Delta \mathbf{m} = \begin{bmatrix} \mathbf{C}_d^{-1/2} \Delta \mathbf{t} \\ -\lambda \mathbf{C}_h \mathbf{m}_o \\ -s_z \lambda \mathbf{C}_v \mathbf{m}_o \end{bmatrix} , \quad (2.13)$$

where \mathbf{L} is the partial derivative matrix with elements $L_{ij} = \frac{\partial t_i}{\partial m_j}$ equal to the length of the i th ray in the j th cell of the slowness model, \mathbf{m}_o represents the current slowness model, $\Delta \mathbf{m}$ is the slowness perturbation, and $\mathbf{m} = \mathbf{m}_o + \Delta \mathbf{m}$.

For data errors that are assumed to be uncorrelated, the data covariance matrix \mathbf{C}_d is a diagonal matrix with elements σ_i^2 representing the variance of the i^{th} travel-time measurement. The roughening matrices \mathbf{C}_h and \mathbf{C}_v contain the 2-D and 1-D second derivative finite difference operators that measure the model roughness in the horizontal and vertical directions. Each row of the regularisation operator in the horizontal direction \mathbf{C}_h contains the five nonzero elements of the Laplacian operator

$$\mathbf{C}_h = \begin{bmatrix} \vdots & \\ \dots & 0 & 1 & 0 & \dots & 0 & 1 & -4 & 1 & 0 & \dots & 0 & 1 & 0 & 0 & \dots \\ \dots & 0 & 0 & 1 & 0 & \dots & 0 & 1 & -4 & 1 & 0 & \dots & 0 & 1 & 0 & \dots \\ \vdots & \end{bmatrix}. \quad (2.14)$$

Each row of the regularisation operator in the vertical direction \mathbf{C}_v has three non-zero elements equal to -2 , 1 , and 1 , where the elements correspond to a central cell and the two adjacent cells in the z direction. The vertical roughening matrix is

$$\mathbf{C}_v = \begin{bmatrix} \vdots & & \\ \dots & 0 & 1 & 0 & \dots & 0 & 0 & -2 & 0 & 0 & \dots & 0 & 1 & 0 & 0 & \dots \\ \dots & 0 & 0 & 1 & 0 & \dots & 0 & 0 & -2 & 0 & 0 & \dots & 0 & 1 & 0 & \dots \\ \vdots & & \end{bmatrix}. \quad (2.15)$$

For M model parameters, \mathbf{C}_h provides M additional constraint equations.

The system of equations (2.13) is sparse and often has less than one percent nonzero elements. This system is solved using the LSQR variant of the conjugate gradient algorithm (Paige and Sanders 1982), which is an efficient iterative matrix solver introduced to seismic tomography by Nolet (1987). The computational sequence Zelt and Barton (1998) use for first-arrival travel-time tomography algorithm is given in Appendix A. The two free parameters to be decided for a given inversion are λ and s_z . The parameter s_z is initially tested for a range of values and is subsequently held fixed throughout a given inversion. The parameter λ acts as the trade-off parameter between data misfit and model smoothness. For large values of λ , model smoothness is emphasized over fitting the data. As the value of λ decreases, the relative importance of fitting the data increases. During the inverse procedure, the parameter λ is tested over a range of values by slowly decreasing it from a starting value. For any λ , the model that achieves the least data misfit $\Delta \mathbf{t}^T \mathbf{C}_d^{-1} \Delta \mathbf{t}$ is selected as the best model for that iteration. The starting value of λ and the reduction factor have to be chosen such that small steps are taken in the model space in order for the linearisation assumption to be honored. Also the linearisation assumption makes it necessary to select a proper starting velocity model so that only small perturbations are necessary to arrive at the final model, *i.e.* the starting model should be reasonably close to the final model. The L_2 norm of the perturbation and the roughness of a given velocity model are numerically quantified (Zelt and Barton 1998) to understand the variation of these parameters at the various stages of the inversion. Representing the velocity model with I, J, K nodes (discrete velocity values at equal spacing) in the x, y, z directions, the perturbation P of a specified velocity model with respect to the the starting model is given by

$$P = \sqrt{\frac{1}{\bar{M}} \sum_{i=1}^I \sum_{j=1}^J \sum_{k=1}^K \left[\frac{v_{i,j,k} - v_{i,j,k}^b}{v_{i,j,k}^b} \right]^2}, \quad (2.16)$$

where $v_{i,j,k}^b$ and $v_{i,j,k}$ represent the velocity of the node in the starting model and the solution model. \bar{M} is the number of nodes in the model sampled by the data (nodes with ray coverage). The amount of structure in a given model can be computed by the L_2 norm of the horizontal roughness R_h and the vertical roughness R_v , given by

$$R_h = \sqrt{\frac{1}{\bar{M}} \sum_{i=1}^I \sum_{j=1}^J \sum_{k=1}^K \left[\frac{4v_{i,j,k} - v_{i+1,j,k} - v_{i-1,j,k} - v_{i,j+1,k} - v_{i,j-1,k}}{v_{i,j,k}} \right]^2}, \quad (2.17)$$

$$R_v = \sqrt{\frac{1}{\bar{M}} \sum_{i=1}^X \sum_{j=1}^Y \sum_{k=1}^Z \left[\frac{2v_{i,j,k} - v_{i,j,k+1} - v_{i,j,k-1}}{v_{i,j,k}} \right]^2}. \quad (2.18)$$

The computed values of P , R_h and R_v are used in comparing the final model solutions for different starting models and/or for different values of the parameter s_z .

2.2.3 Resolution and Checkerboard Tests

In evaluating models obtained by inversion, it is important to consider model resolution, that is, how well individual model parameters are determined. In the case of perfect model resolution, each model parameter is determined independently from all other model parameters. As resolution decreases, averages of neighboring parameters can be estimated but not the individual parameters themselves. In linear inverse theory, resolution is quantified in terms of a closed-form expression for the resolution matrix (e.g. Menke 1989), with i^{th} row of the matrix indicating the resolution of the i^{th} parameter. However, for nonlinear inverse problems, a linear analysis may not be appropriate.

Resolution in nonlinear tomography depends on the signal band width, the source receiver distribution, and the velocity structure (Parsons *et al.* 1996). The common

methods employed to evaluate the resolution of the final model are ray hit count analysis, the derivative sum method, and the checkerboard test. The simplest form of quantifying resolution is the ray hit count analysis. In this analysis, the number of rays passing through a given cell are examined, and reasonable resolution is inferred for regions with greater ray coverage. A more appropriate measure is given by the derivative sum of the seismic ray paths in the model parameter cells (Toomey *et al.* 1994) . The derivative sum is the sum of all ray path lengths within a model cell given by

$$DS(m_i) = \sum_{k=1}^R \frac{\partial T_k}{\partial m_i}, \quad (2.19)$$

where R is the number of rays through the cell. This is a more meaningful measure of ray path effect than simply counting the number of rays passing through the cell.

In previous tomographic studies, checkerboard tests have been successfully employed to assess lateral model resolution (Humphreys and Clayton 1990; Hearn and Ni 1994; Zelt and Barton 1998). In this test, a synthetic velocity model is generated by the addition of a laterally alternating anomaly pattern of positive and negative squares to the final model. The source-receiver geometry of the experiment is used to compute travel-times for this synthetic velocity model. Gaussian noise with a standard deviation equal to the pick uncertainties in the field data is added to the computed travel-times. This synthetic travel-time data are then inverted using the final model previously obtained from the real data as the starting model. The computation sequence for the checkerboard test is given in Appendix B. By assessing the recovered anomaly pattern, an estimate of the ability of the data to resolve anomalies with a lateral dimension equal to the size of the anomaly pattern can be obtained throughout the model. A reasonable ray coverage will generally enable the recovery of the alternating anomaly pattern. Regions of poor ray coverage typically result in a smooth non-alternating recovered pattern due to the horizontal smoothing included in the inversion. Semblance values measuring the correlation between the input and

recovered patterns can be used to classify areas of reasonable lateral resolution. Semblance is given by

$$S = \frac{1}{2} \frac{\sum_{i=1}^I \sum_{j=1}^J \sum_{k=1}^K [vt_{i,j,k} + vr_{i,j,k}]^2}{\sum_{i=1}^I \sum_{j=1}^J \sum_{k=1}^K [vt_{i,j,k}^2 + vr_{i,j,k}^2]}, \quad (2.20)$$

where $vt_{i,j,k}$ and $vr_{i,j,k}$ represent the velocity of the node in the input checkerboard model and the recovered checkerboard model, respectively; and (I, J, K) represents the size of the semblance window. These semblance values are referred to as ‘resolvability’ since they indicate the ability of the final model to resolve features of a particular size (Zelt and Barton 1998).

2.3 Seismic Hazards Investigation of Puget Sound (SHIPS)

The objective of the 1998 SHIPS survey was to obtain new 3-D structural control on the seismogenic zones and Cenozoic basins in southwestern British Columbia and northwestern Washington, and to determine compressional and shear wave velocity information for the sedimentary basin fill of the Fraser Delta and the Tacoma, Seattle, and Everett Basins (Brocher *et al.* 1998). The SHIPS experiment recorded data from a total of 33,000 air-gun shots fired in the waterways of the Strait of Georgia (SG), the Strait of Juan de Fuca (SJF), and the Puget Sound (PS), split into 11 shot lines (Fig. 2.1). The air-gun shots were recorded at 257 temporary land-based Reftek stations and ocean-bottom seismometers at offsets from 1 to 370 km (Brocher *et al.* 1998). The digital Reftek stations deployed on land consisted of a Data Acquisition System (DAS), internal oscillator and internal or external Global Positioning System (GPS) receiver, seismometer, hard disk for data storage and battery pack. The Reftek stations consisted of 3-component seismometers. The data were recorded at a sample rate of 100 Hz. The clock time and positional data of the recording station were recorded simultaneously with the seismic data.

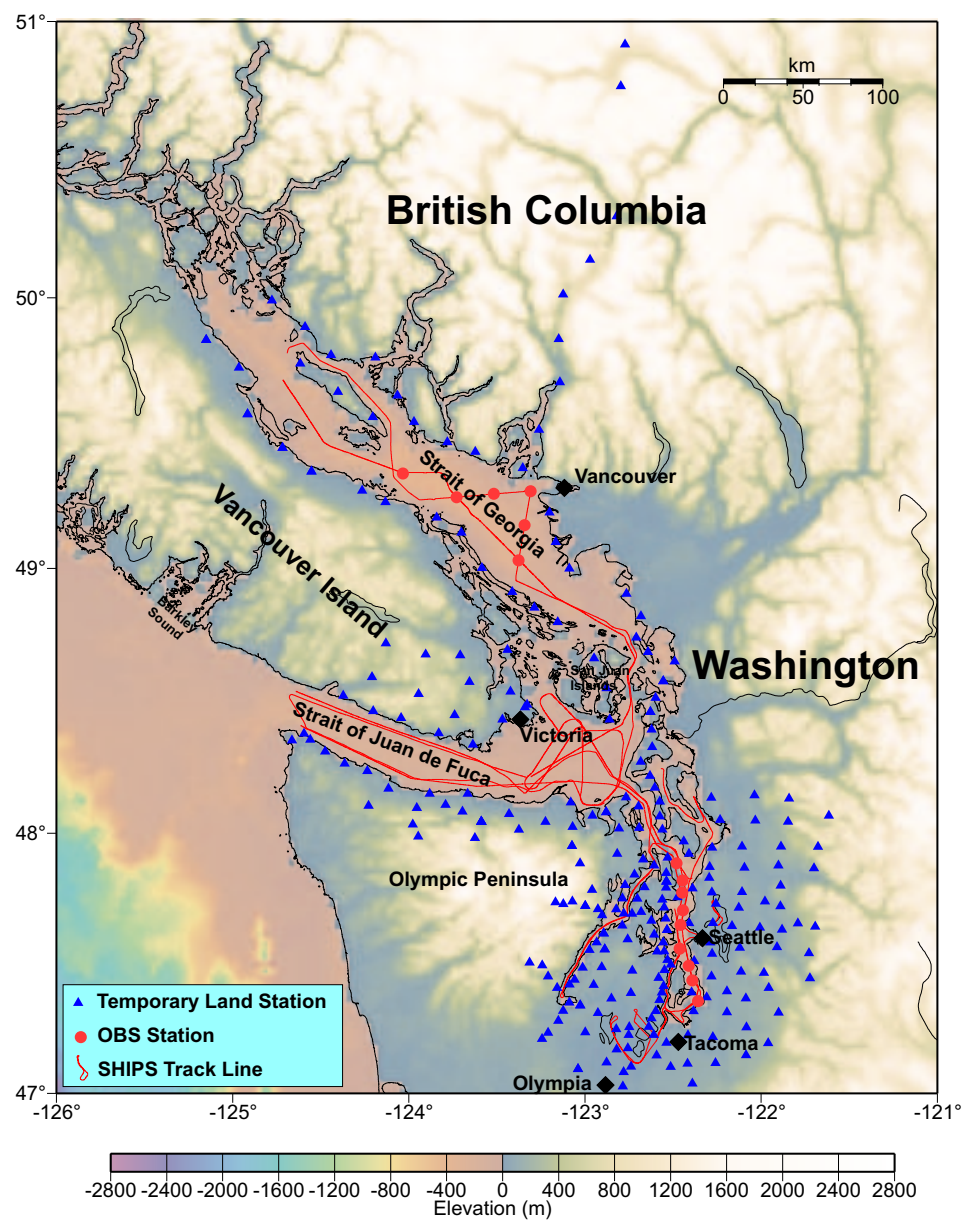


Figure 2.1 Location map of SHIPS (1998) shot lines and receivers.

The Reftek receiver locations were distributed widely over southwestern British Columbia and northwestern Washington as shown in Fig. 2.1. Line 1 was shot in Lake Washington, lines 2, 3 and 9 were shot in PS and Hood Canal, lines 4, 7 and 8 were shot in SJF, and lines 5 and 6 were shot in SG. Lines 10 and 11 were shot at the junction of SJF, SG and PS. Wide-angle recording was the focus of the first part of the experiment. A large air-gun array, consisting of 16 individual air-guns (total volume of 110 liters), was used to shoot lines 1 to 5 with a shot interval of 40 s (equivalent to ~ 90 m). The rest of the lines were shot with a smaller 13 air-gun array (total volume 79 liters) with a shot interval of 20 s (equivalent to ~ 50 m). In this part of the experiment, near-vertical incidence reflection data were recorded with a towed 2.4 km long, 96 channel digital streamer. The location accuracy of air-gun shots was estimated at 40 m. Many Reftek receivers were deployed laterally off the shot lines to provide three dimensional coverage of the area. The location accuracy of Reftek stations was within 50 m and elevation accuracy was within 20 m (Brocher *et al.* 1998). The air-gun array was towed at depths of 8 to 10 m and the air-gun shot locations represent the midpoint of the air-gun array. Air-gun firing times were determined from the air-gun fire command time that was measured using a GPS clock and are accurate to 1 ms.

2.4 Tomographic Inversion of SHIPS Data

The area chosen for 3-D tomographic inversion falls between latitude $47^{\circ}40'$ N to 50° N and longitude $122^{\circ}15'$ W to $125^{\circ}15'$ W in southwestern British Columbia and northwestern Washington (Fig. 2.2). Four shot-lines were processed for picking first arrival travel-times (Fig. 2.3). The receiver locations were distributed over southern Vancouver Island, the western and eastern boundaries of SG, and the northern and southern boundaries of SJF, as shown in Fig. 2.2.

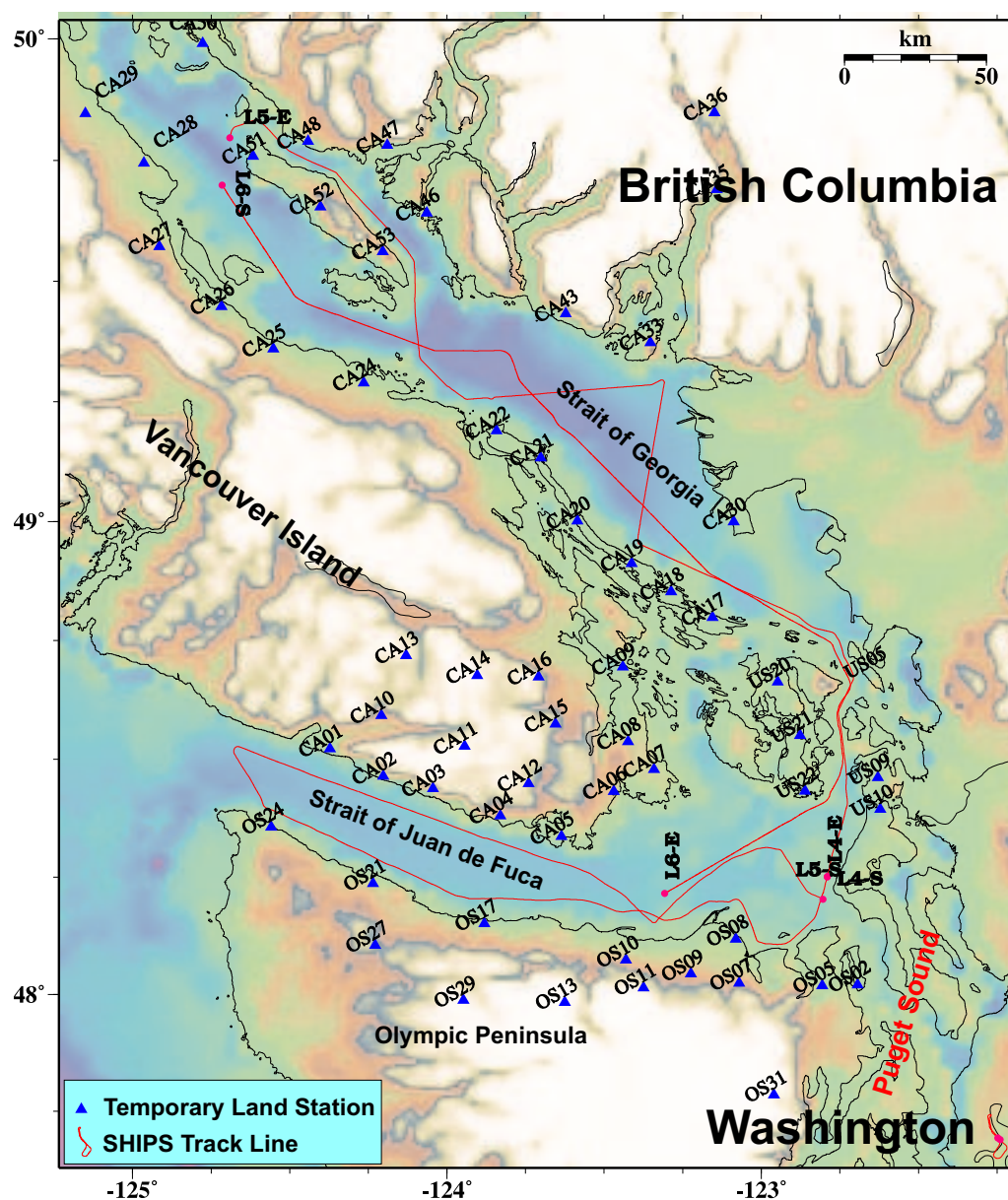


Figure 2.2 Location map of SHIPS shot lines and receivers in the study area.

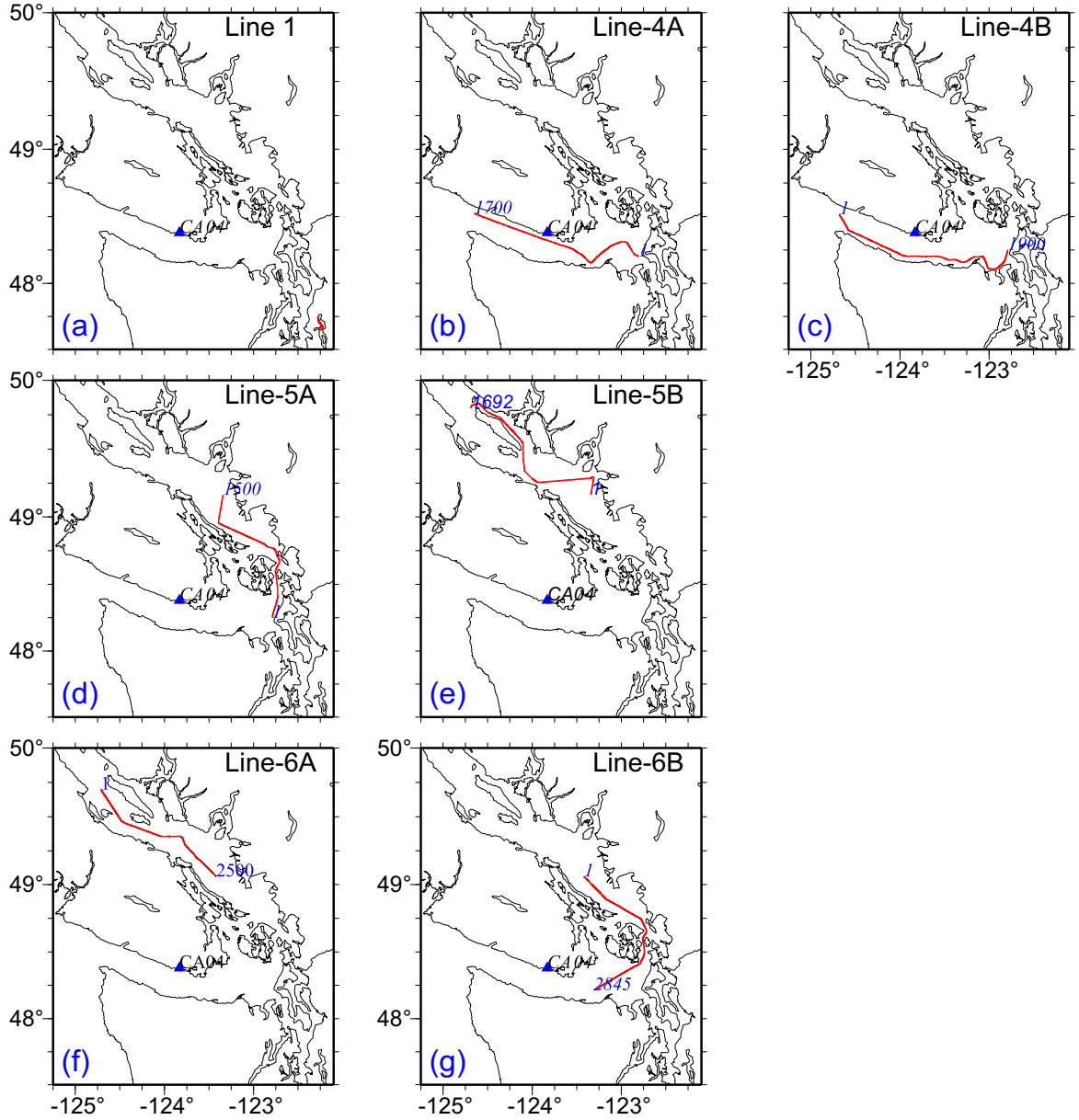


Figure 2.3 Location map of the shot line segments used in this study. Location of receiver CA04 is shown by the blue triangle. The time sections recorded by CA04 are shown in Figs. 2.4 to 2.10.

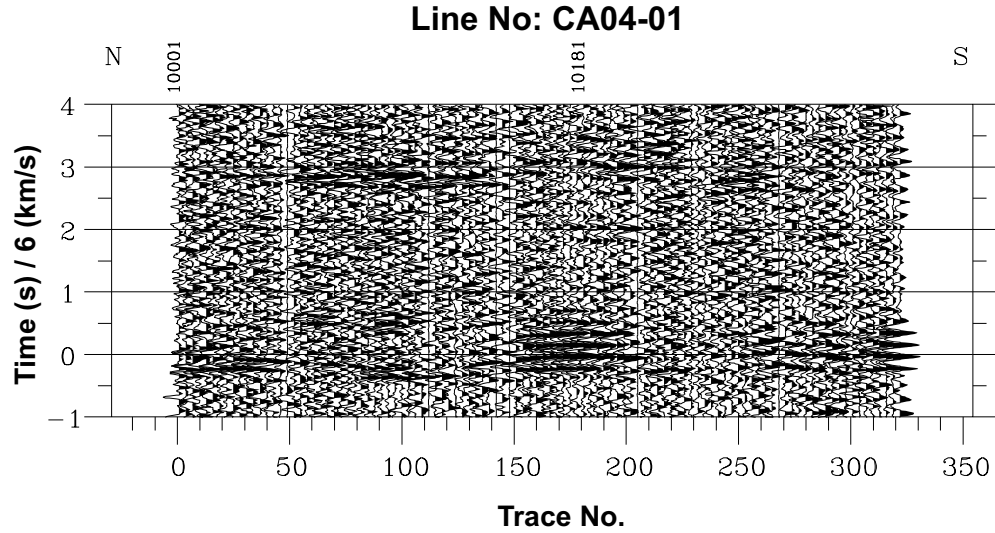


Figure 2.4 Seismogram of line 1 (Lake Washington) recorded at receiver CA04. Data are plotted with a reducing velocity of 6 km/s. The location of the line is shown in Fig. 2.3a.

The processing of the raw data was carried out in three steps. In the first step, the SEG-Y header keywords were verified for correctness. The SEG-Y header keywords for shot-time, receiver locations, and angle conversion factor were set to the correct value. After this correction, the offset distance between shot and receiver was computed for the new values of receiver location and angle conversion factor. Although the initial SEG-Y data had a record time window of 90 s, a record length of 40 s captures first arrival events for offsets up to 200 km. In the present study, first arrival events from offsets up to 175 km only have been included in the inversion to avoid inclusion of events from wide angle reflections. In the second step of processing, the shot-lines were trimmed to a time window of 40 s after the shot time. In the third step of processing a band pass filter of 4-15 Hz was applied since the time sections had observable high frequency noise which masked the first breaks in many places. This enhanced the time sections for first break identification and picking.

To illustrate some of the major features of the data, processed time sections of

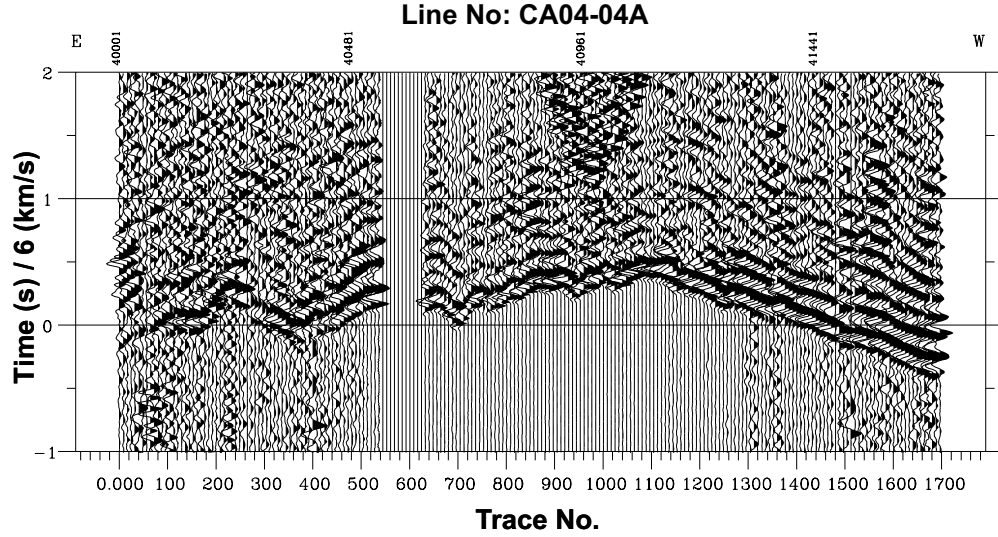


Figure 2.5 Seismogram of line 4A recorded at receiver CA04. Data are plotted with a reducing velocity of 6 km/s. The location of the first trace (1) and the last trace (1700) are shown in Fig. 2.3b.

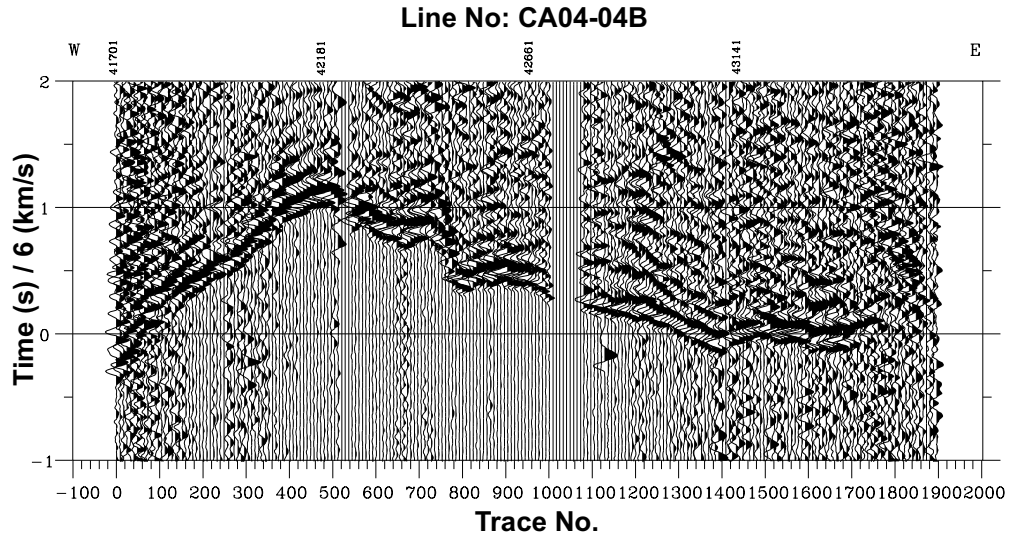


Figure 2.6 Seismogram of line 4B recorded at receiver CA04. Data are plotted with a reducing velocity of 6 km/s. The location of the first trace (1) and the last trace (1900) are shown in Fig. 2.3c.

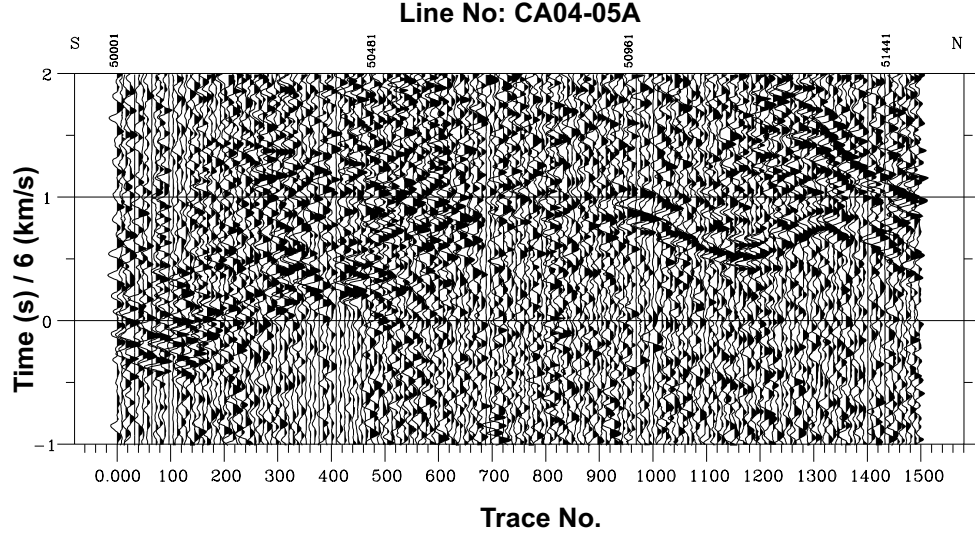


Figure 2.7 Seismogram of line 5A recorded at receiver CA04. Data are plotted with a reducing velocity of 6 km/s. The location of the first trace (1) and the last trace (1500) are shown in Fig. 2.3d.

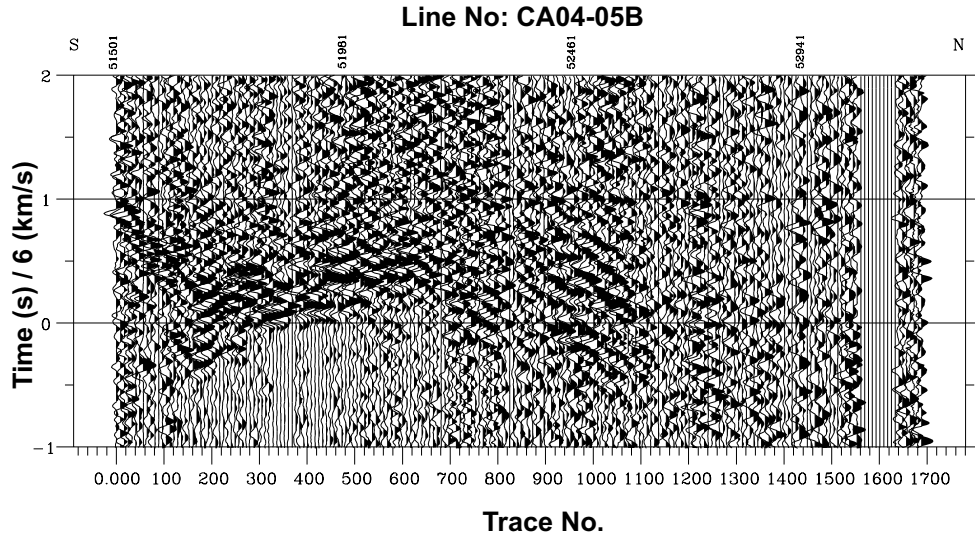


Figure 2.8 Seismogram of line 5B recorded at receiver CA04. Data are plotted with a reducing velocity of 6 km/s. The location of the first trace (1) and the last trace (1690) are shown in Fig. 2.3e.

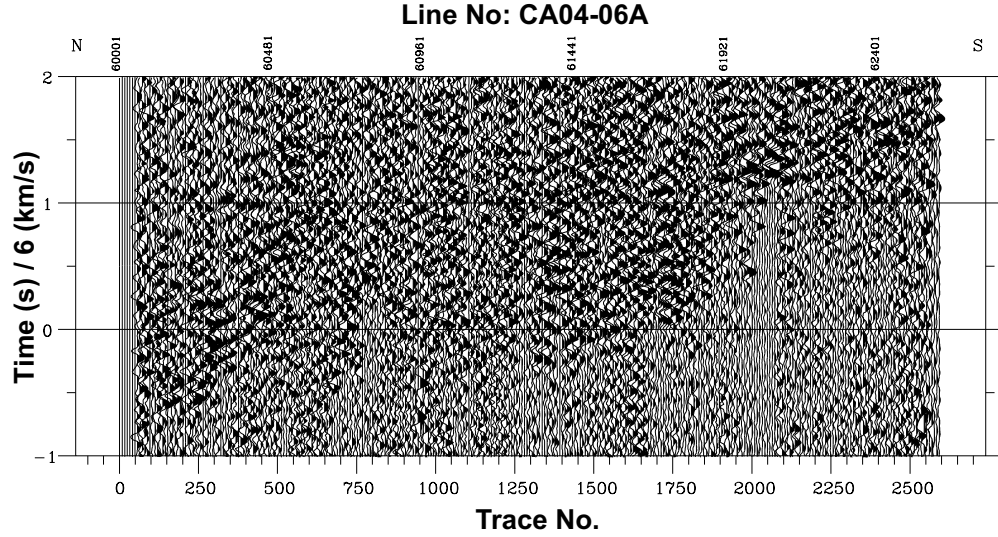


Figure 2.9 Seismogram of line 6A recorded at receiver CA04. Data are plotted with a reducing velocity of 6 km/s. The location of the first trace (1) and the last trace (2600) are shown in Fig. 2.3f.

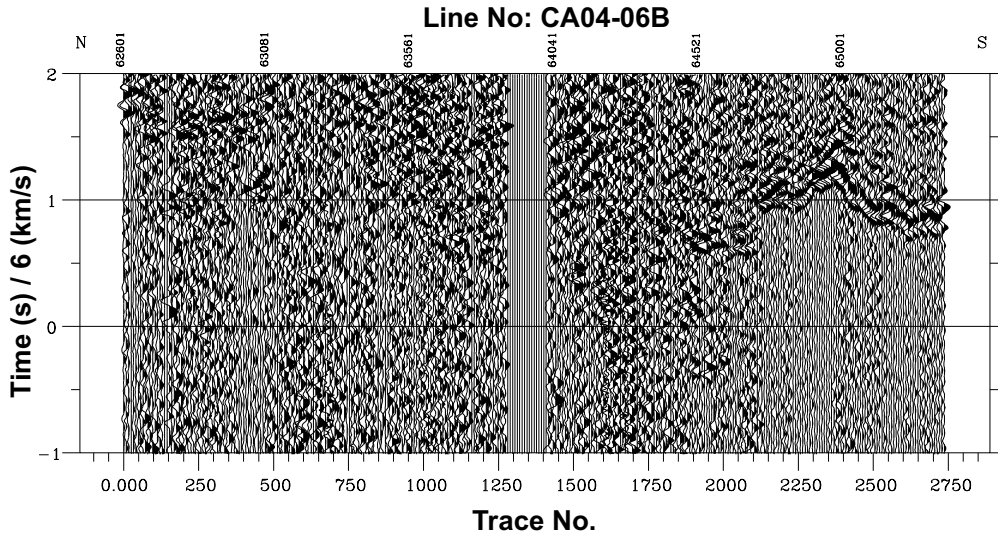


Figure 2.10 Seismogram of line 6B recorded at receiver CA04. Data are plotted with a reducing velocity of 6 km/s. The location of the first trace (1) and the last trace (2750) are shown in Fig. 2.3g.

lines 1, 4, 5 and 6, recorded by station CA04 (Fig. 2.3) are discussed below. Line 1, shown in Fig. 2.4, is a small line shot in Lake Washington and has medium signal to noise ratio (S/N). Lines 4A and 4B shown in Figs. 2.5 and 2.6 were shot in SJF and with high S/N. The difference in first arrival times between lines 4A and 4B show the strong velocity variations in the subsurface. Lines 5A and 5B, shown in Figs. 2.7 and 2.8, from SG have medium S/N for most parts of the line. Lines 6A and 6B, shown in Figs. 2.9 and 2.10, shot in the SG have systematic noise and the S/N is medium to low for receivers from medium to large offset.

First arrival events were identified and picked manually on all record sections. Lines 1, 4, 5, and 6 contain 12457 shots. Approximately 175,000 first arrival picks were made from 58 receivers. On average this amounts to, 3017 picks/station, or 24% of the available shots. Line 1 recorded by receivers on the Olympic Peninsula and southern Vancouver Island provided reasonable travel-time picks. Line 4 recorded by receivers in southern Vancouver Island, Olympic Peninsula and portions of mainland British Columbia also provided high quality travel-time picks. Lines 5 and 6 produced medium quality picks, mostly from the receivers on southern Vancouver Island. To assign pick uncertainties, events from different offsets recorded at the various receivers in the study region were analysed manually. Pick uncertainties of 50, 70, and 90 ms were assigned to the picks having first arrival travel-times of less than 10 s, 10-15 s, and greater than 15 s, respectively.

The velocity model for both the forward and inverse steps was parameterised by a node/cell spacing of $(1 \times 1 \times 1)$ km in (x, y, z) directions. The velocity model dimensions were $(220 \times 220 \times 22)$ km. The top of the model was set to 1 km above sea-level to allow the positioning of receivers at their actual elevations in the velocity model. However the results reported were standardised with respect to mean sea level. A 1-D starting model was constructed that best fits the time-distance plot and minimises the RMS travel-time misfit by computing the finite difference travel-times for the starting 1-D model (Fig. 2.11). The travel-time misfit for the picks in the

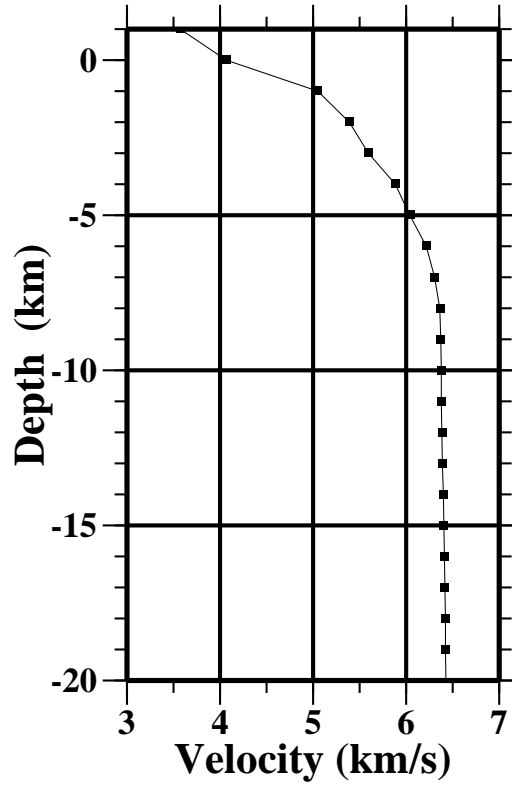


Figure 2.11 Starting 1-D velocity model.

starting model is shown in Fig. 2.12. The large differences observed in the travel-time misfit for the same range of offsets can be explained by the local geology of the area. In SJF, low velocity sediments are juxtaposed against high velocity basaltic and gabbroic Crescent Terrane, and in SG, the low velocity sediments contrast with high velocity Wrangellia rocks. This is a typical study area with large lateral velocity contrasts.

Given a velocity model, computation of travel-times is the forward step of the inversion problem. Vidale's method (Vidale 1990) calculates first-arrival travel-times on a uniform grid by solving the Eikonal equation using the finite difference (FD) method. The method was modified by Hole and Zelt (1995) for handling large velocity

contrasts and is the most widely used algorithm for travel-time computation in travel-time tomography (Zelt and Barton 1998). The velocity model defined at the nodes of the uniformly spaced grid is used to compute the travel-times at the nodes of the grid employing the FD approach. The travel-time at a receiver location is then obtained by linear interpolation of the travel-times at the eight surrounding grid nodes. To compute the ray path length, L_{ij} , the steepest gradient direction from the receiver to the source is traced in the travel-time grid generated by FD method.

The inversion procedure was initially run in the test mode to determine the optimum value of the parameter s_z that controls the ratio of horizontal to vertical smoothing in equation 2.12. After visually inspecting the final models obtained for smoothness and continuity in lateral and vertical directions, s_z was set to a value of 0.25 which implies a horizontal to vertical smoothing ratio of 4:1. This value of s_z was then held fixed throughout the inversion. During the testing process a few outliers were identified and removed from the data. These outliers, due to the errors at the time of manual picking, amounted to less than one percent of the data used in the inversion. The RMS travel-time residual for the starting model for 1.7×10^5 picks was 549 ms for a normalized χ^2 of 73 (Figs. 2.13a and 2.13b). The starting λ value was set to 100 (Fig. 2.13c). During the tomographic inversion, three λ values were tested for each iteration. The model corresponding to the λ value with the best normalised χ^2 misfit was selected. This model was then used as the starting model for the next iteration and the inversion process was continued. After six iterations, a normalised χ^2 of 1.04 was achieved (Figs. 2.13b).

The RMS travel-time residual in the final model was 76 ms for a final λ value of 4.4. The total number of model nodes in the forward computation was 1.3×10^6 , and the number of model cells in the inverse computation was 1.2×10^6 . The number of nonzero elements in the slowness kernel was approximately 1.9×10^7 for 1.7×10^5 observations. The number of constraint equations was 2.5×10^6 and the number of nonzero elements was 2.8×10^7 which was approximately 0.001% of the total elements

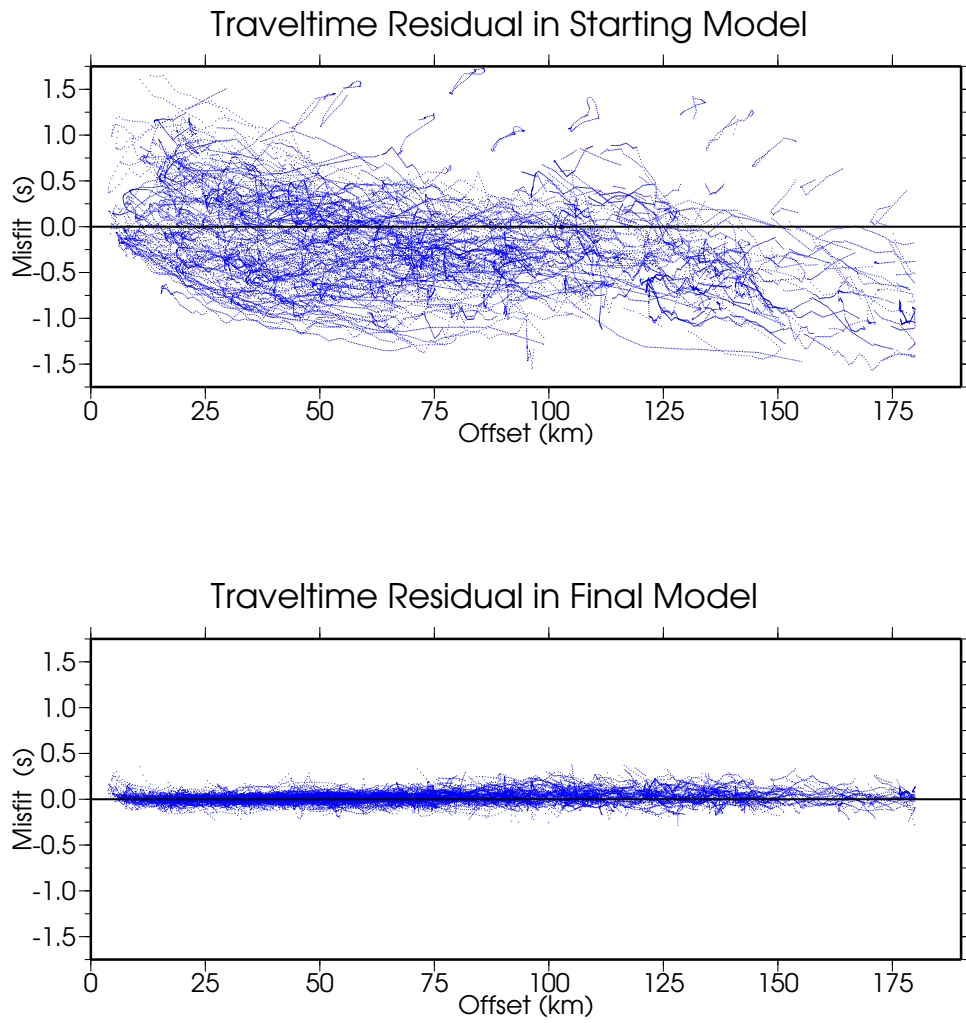


Figure 2.12 Travel-time misfit in starting model (above), and final model (below).

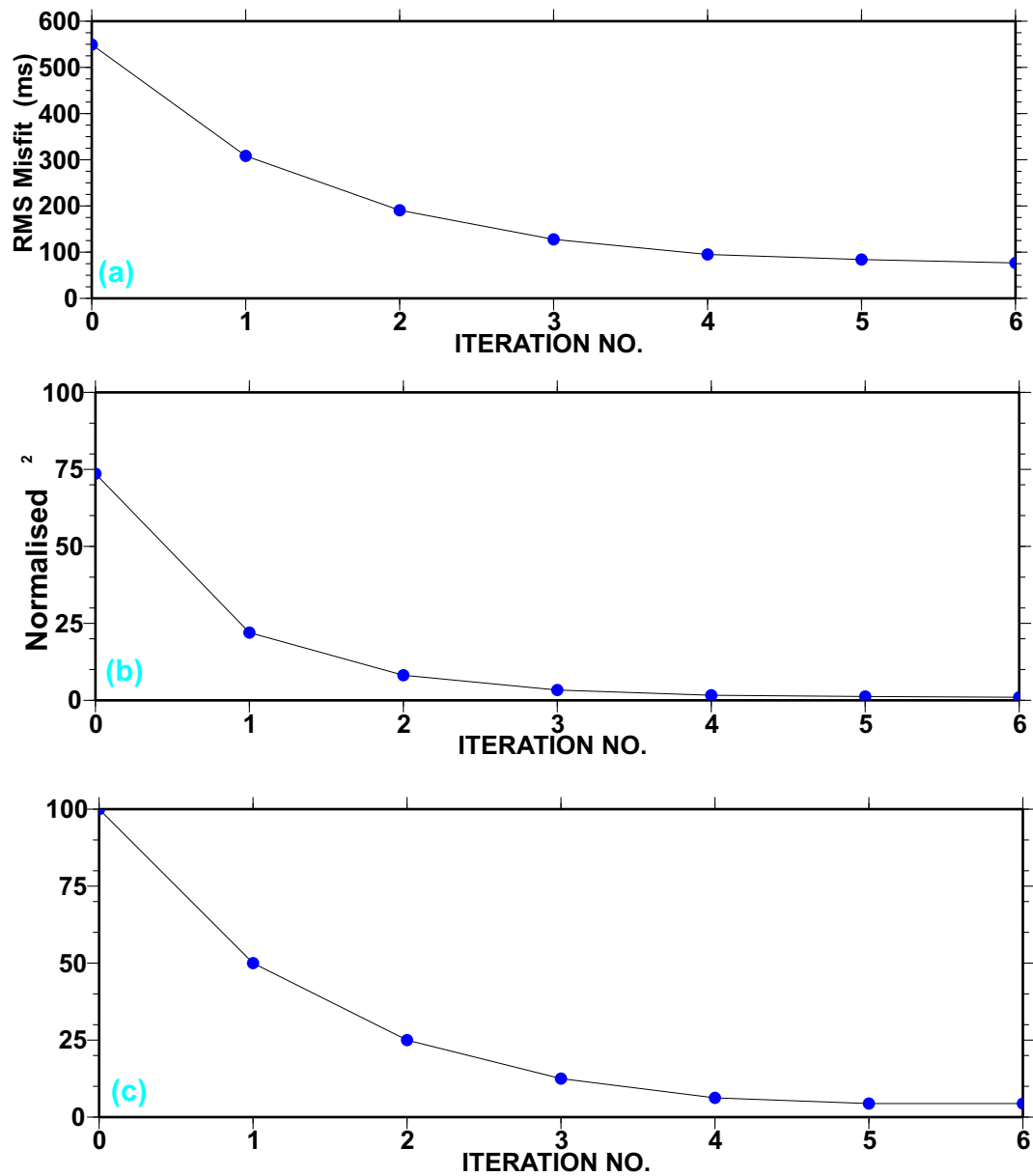


Figure 2.13 Convergence of (a) RMS travel-time misfit, (b) $normalised\chi^2$ and (c) λ .

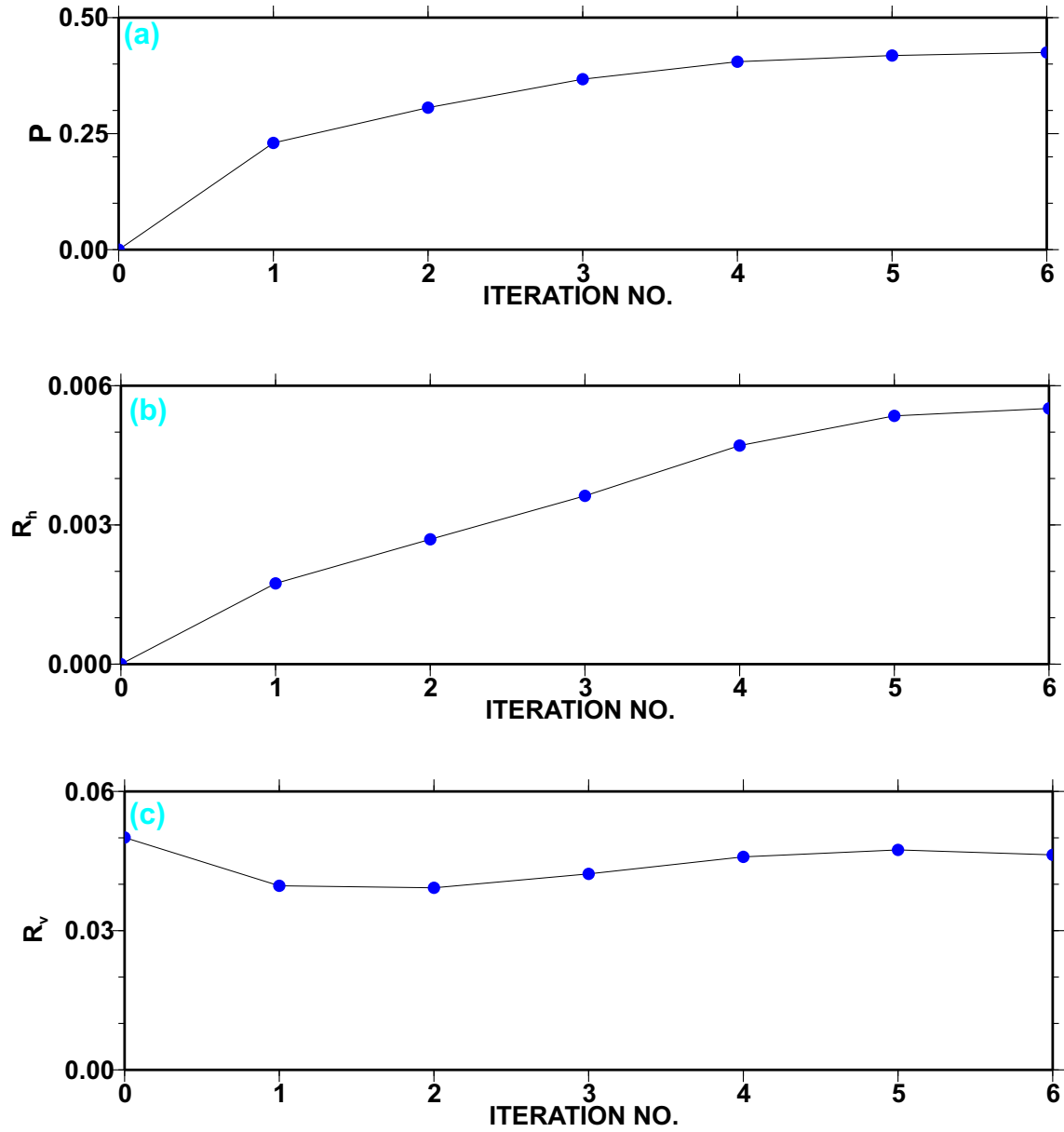


Figure 2.14 Variation in (a) perturbation P , (b) horizontal roughness R_h , and (c) vertical roughness R_v .

in the sparse matrix. The travel-time misfit with offset in the final model is observed to be uniform over the entire range of offset as shown in Fig. 2.12. The perturbation (P) and horizontal roughness (R_h) increase steadily as the inversion converges to the final model (Figs. 2.14a and 2.14b). However the vertical roughness remains approximately constant throughout the inversion at a value similar to that of the 1-D starting model (Fig. 2.14c). The values of the trade off parameter s_z and the node/cell size control the amount of horizontal and vertical roughness in the final model. Changing one or both of these parameters will result in a model with somewhat different structure and resolution. The type of structure and the resolution in the output model depends on the, (i) the quality, density and distribution of the data, (ii) the parameterisation of the model, and (iii) the subsurface velocity structure.

The starting velocity model is shown in Fig. 2.15 in terms of constant depth slices from 1 to 12 km depth. The total perturbation applied to the starting model to obtain the final model is shown in Fig. 2.16. Ray tracing is performed in the final velocity model to identify the cells with ray coverage; model parameters are plotted only for cells with ray coverage. The perturbation model brings out the locations where strong velocity perturbations to the starting model have been applied. Significant perturbations are found to occur at the locations of known geologic features such as the high velocity Crescent Terrane and the basinal part of SJF and SG. The final velocity model, shown in Fig. 2.17, clearly outlines the Crescent Terrane in Southern Vancouver Island. Regions with strong velocity perturbation (Fig. 2.16) coincide with regions of large ray coverage (Fig. 2.18). Also, the basinal structure of SJF and SG stand out clearly in this model. The structure of the final velocity model is examined in detail in Chapter 4.

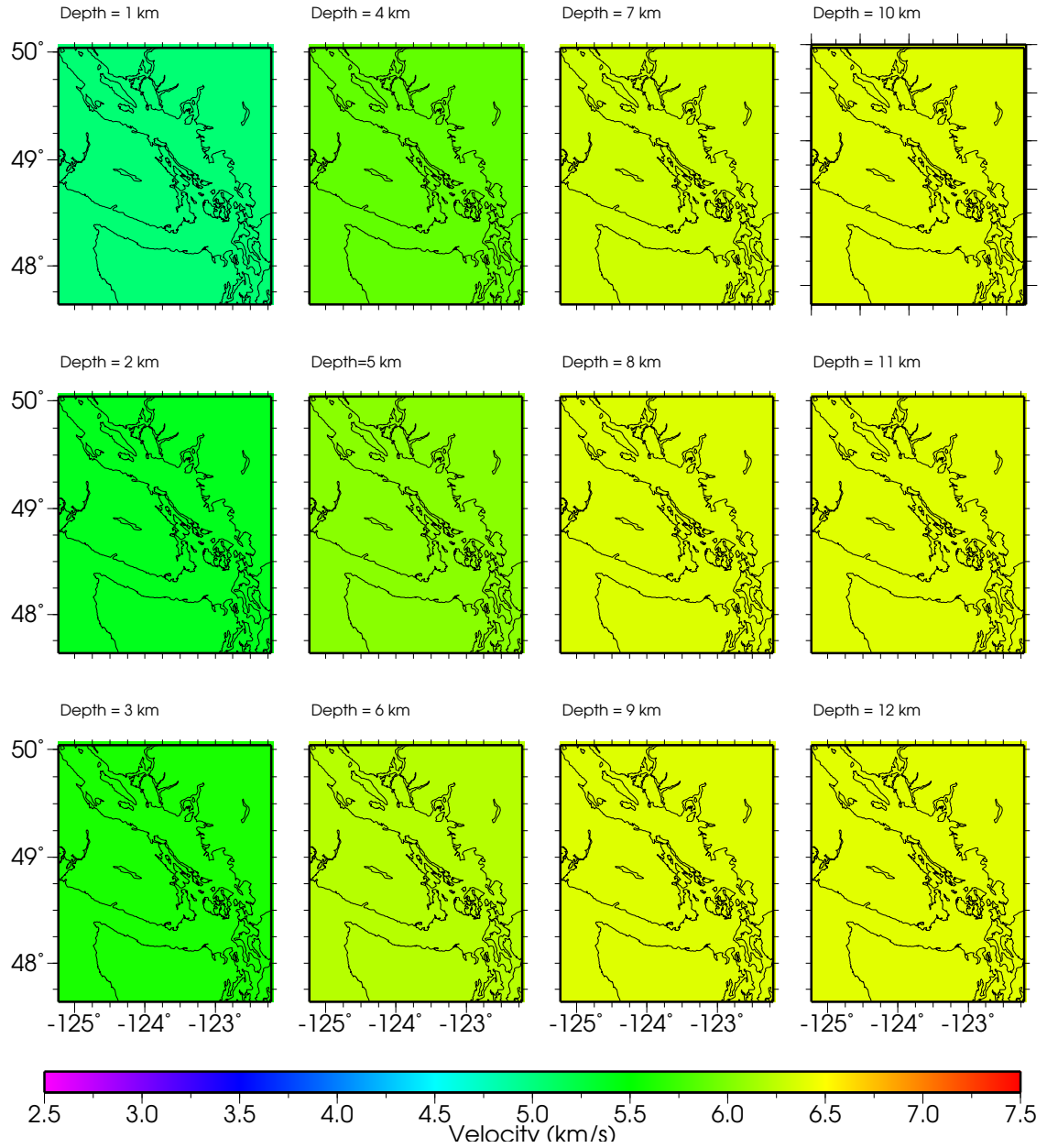


Figure 2.15 Depth slices of starting velocity model.

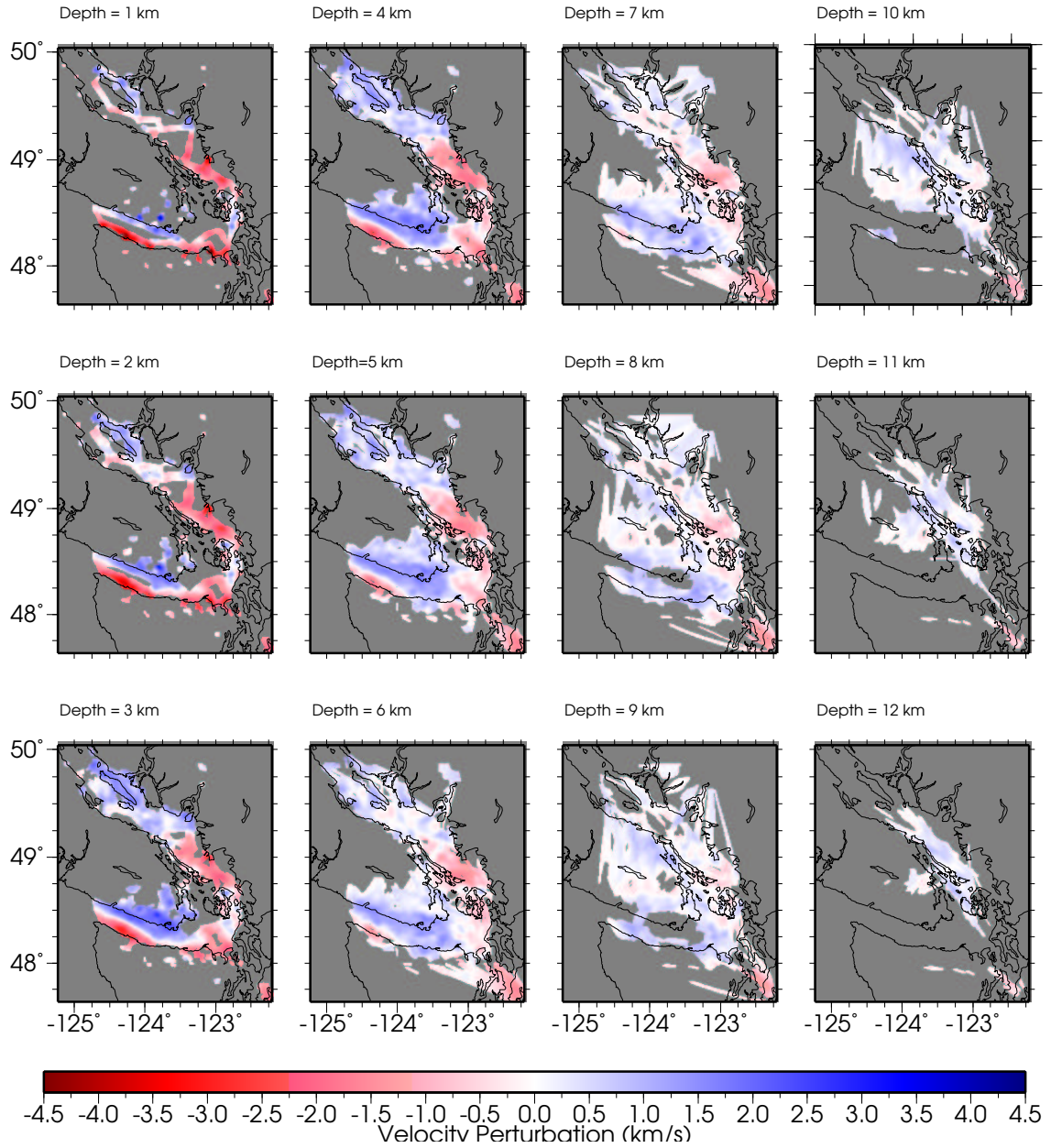


Figure 2.16 Depth slices of perturbation velocity model.

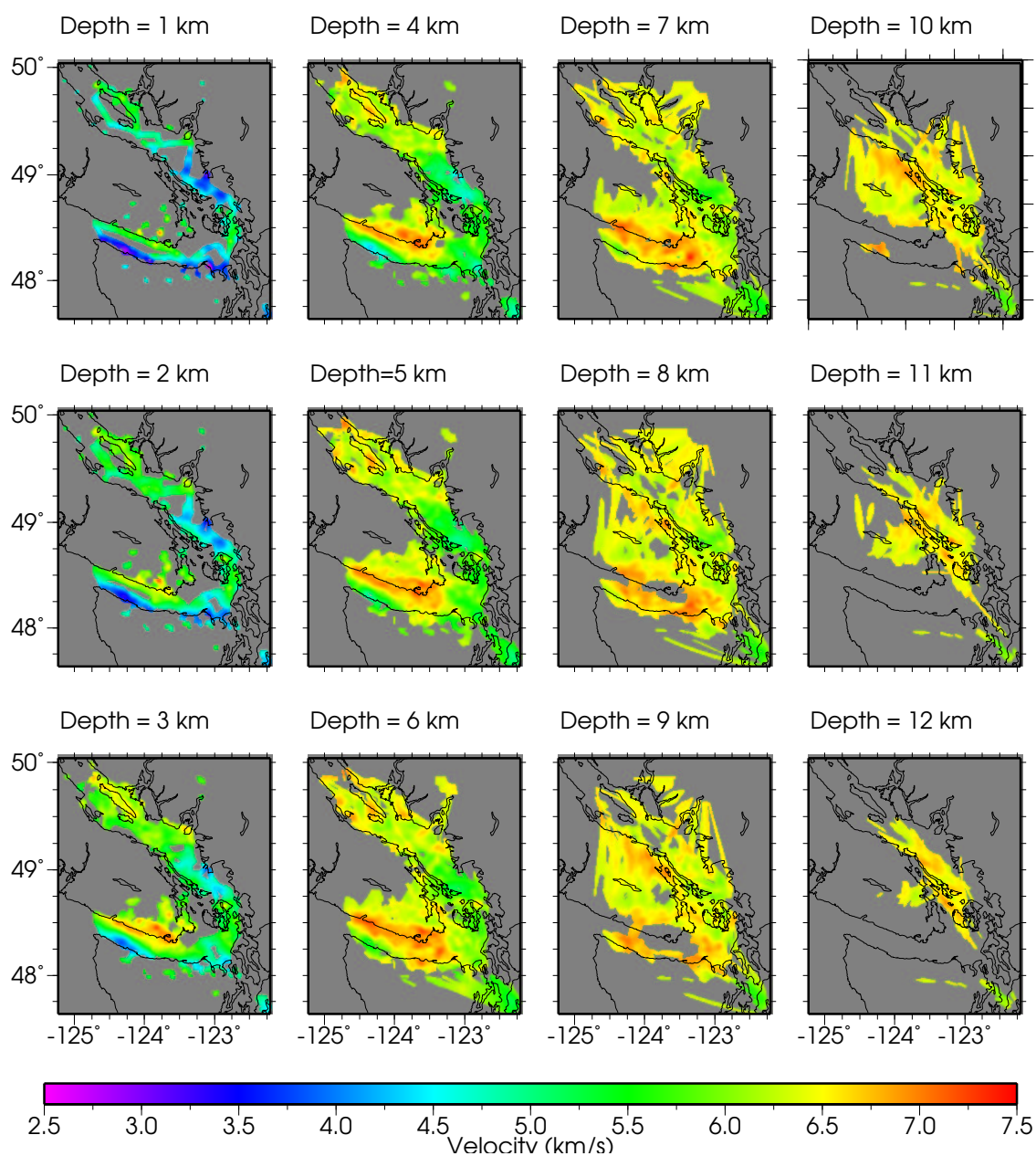


Figure 2.17 Depth slices of final velocity model

2.5 Ray Coverage and Checkerboard Tests

Ray coverage varies with depth and peaks at 5 km depth (Fig. 2.18). The ray coverage constrained approximately 14% of the model. In SG and SJF the ray coverage is sufficient to clearly map the thickness of low velocity sediments and associated structural features. Due to the geometry of the SHIPS experiment, the ray coverage at depths shallower than 3 km is confined mostly to SJF and SG. Ray coverage in southern Vancouver Island progressively increases downward to a maximum depth of 10 km. Strong ray focussing is observed where the high velocity Crescent Terrane is close to the surface in southern Vancouver Island. In SG, reasonable ray coverage is observed at all levels down to a depth of 12 km which brings out the basin structure clearly. The derivative sum plots in Fig. 2.19 shows the ray path length effect in the construction of the final velocity model. This plot resembles the ray hit count plot in most parts of the study area indicating that the ray hit count and the derivative sum have similar contribution for these cells; however, differences can be observed in SG and SJF. The geometry of the data acquisition and the model parameterisation during tomography controls the similarity between the derivative sum plot and the ray hit count plot.

Lateral resolution was tested using two checkerboard grid sizes of 20 km and 30 km. The optimum low cut of the lateral resolution is expected to be within this range considering the experimental geometry of the receiver positions which were separated at an average spacing of 15 km. The input anomaly pattern for a grid size of 20 km is shown in Fig. 2.20. The recovered anomaly pattern for the 20 km grid size is shown in Fig. 2.21. Semblance values, as described by Zelt and Barton (1998), were computed for a window size of $(10 \times 10 \times 6)$ km and are shown in Fig. 2.22. The recovery of the alternating anomaly pattern for the 20 km grid pattern is reasonable in most parts of the study area, as indicated by semblance values of 0.7 and above. The results for a checkerboard grid size of 30 km are shown in Figs. 2.23,

2.24 and 2.25. The recovery of the alternating anomaly pattern and the semblance values indicate reasonable lateral resolution for the 30 km grid. The overall results of the checkerboard test imply lateral resolution of features of extent 20 km and above in the final velocity model.

2.6 Summary

This chapter reviewed the theory of nonlinear 3-D tomography for first-arrival travel-time data. The jumping and creeping approaches to regularisation for stabilising ill-posed inversions were discussed. Solutions with ‘minimum structure’ are favored as they provide physically meaningful models. SHIPS experimental data were preprocessed and nearly 175,000 first arrivals picks were made. Three dimensional tomographic inversion of SHIPS data was performed and the results were evaluated by ray hit count analysis, the derivative sum method, and checkerboard tests. The travel-time misfit reduced from 549 ms for the starting model to 76 ms for the final model after 6 iterations, with a corresponding reduction in the normalised χ^2 values from 73 to 1.04. Checkerboard results imply lateral resolution at spatial scales of 20 km and above.

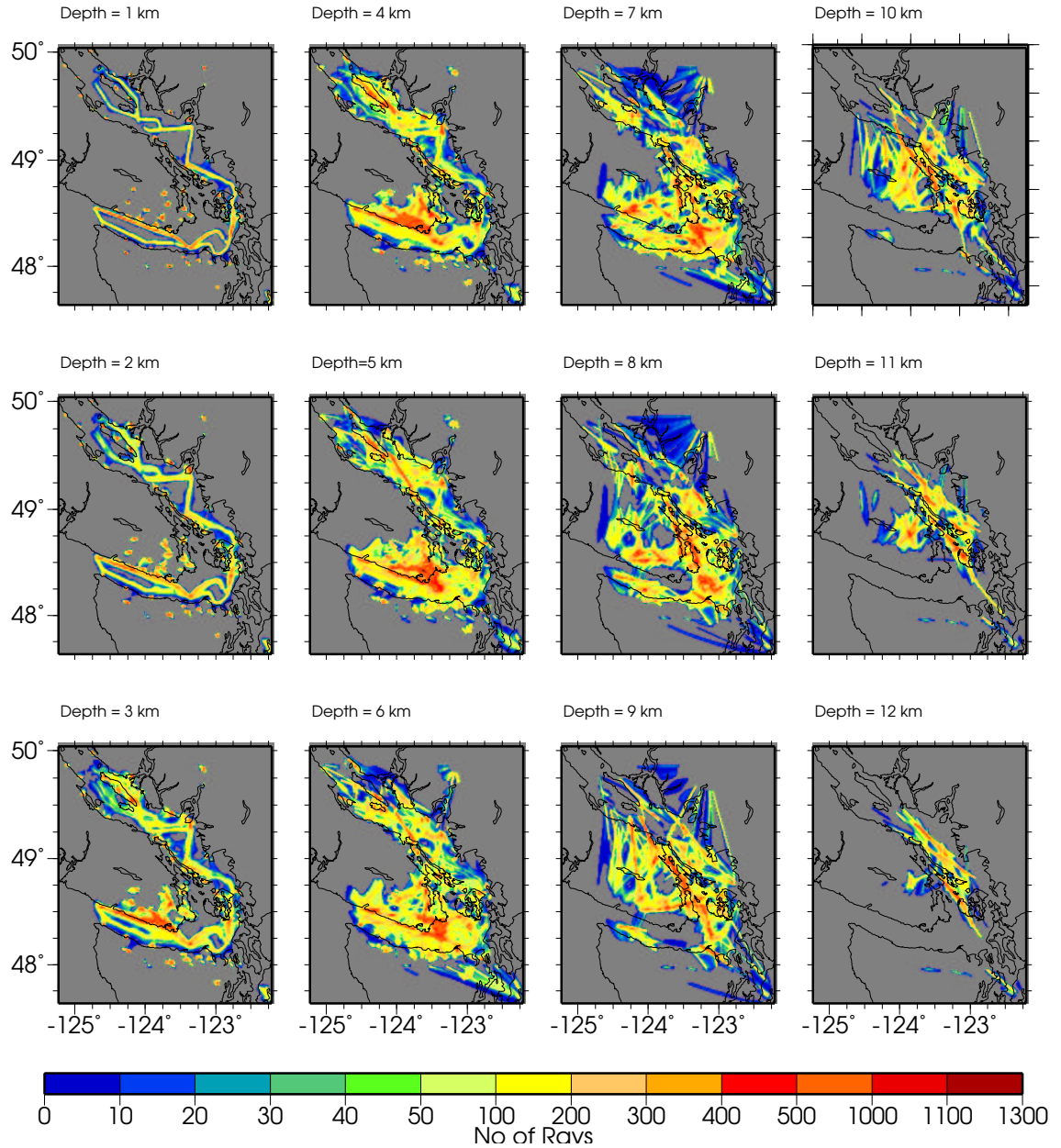


Figure 2.18 Depth slices of ray density in the final velocity model.

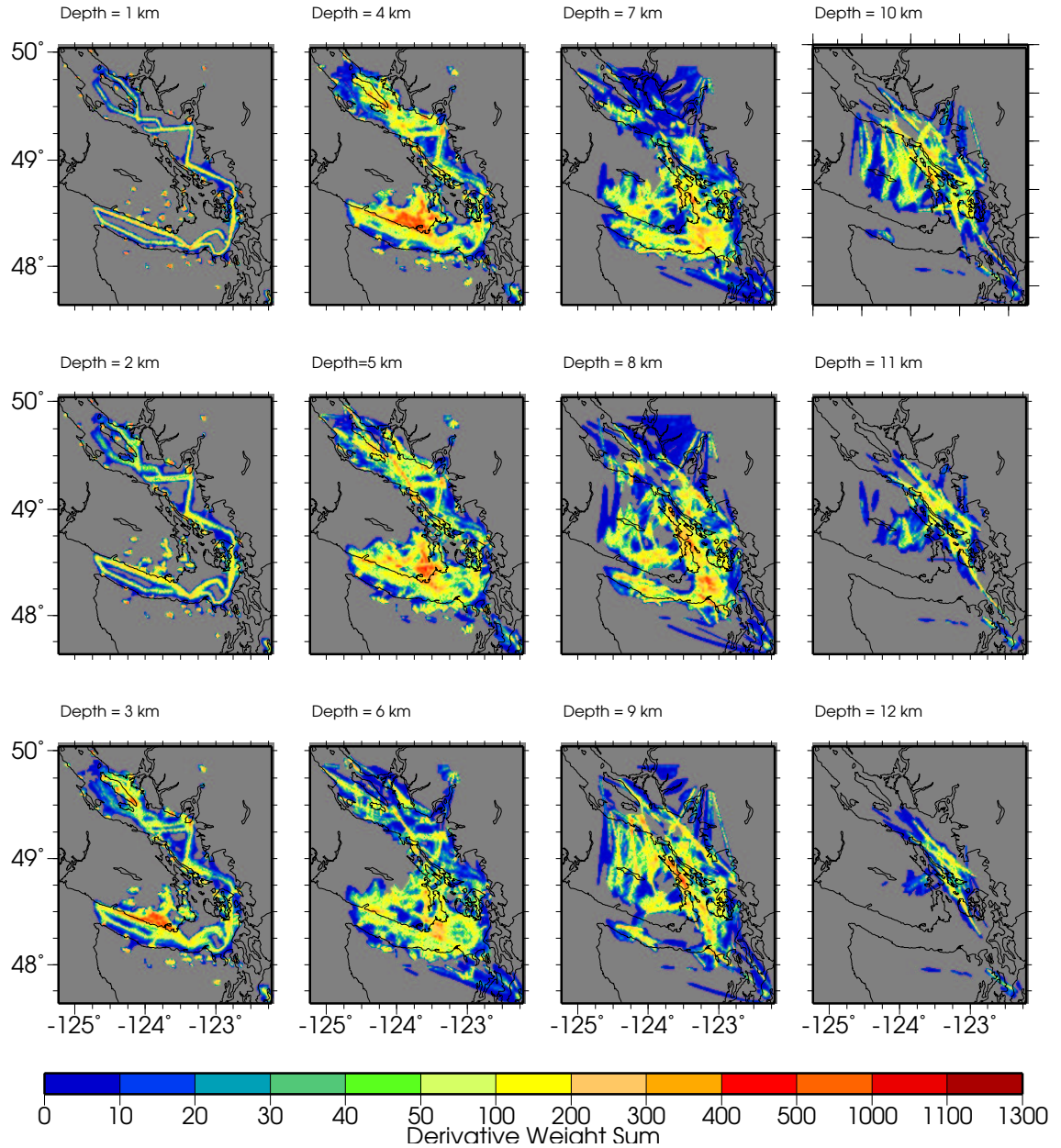


Figure 2.19 Depth slices of derivative sum in the final velocity model.

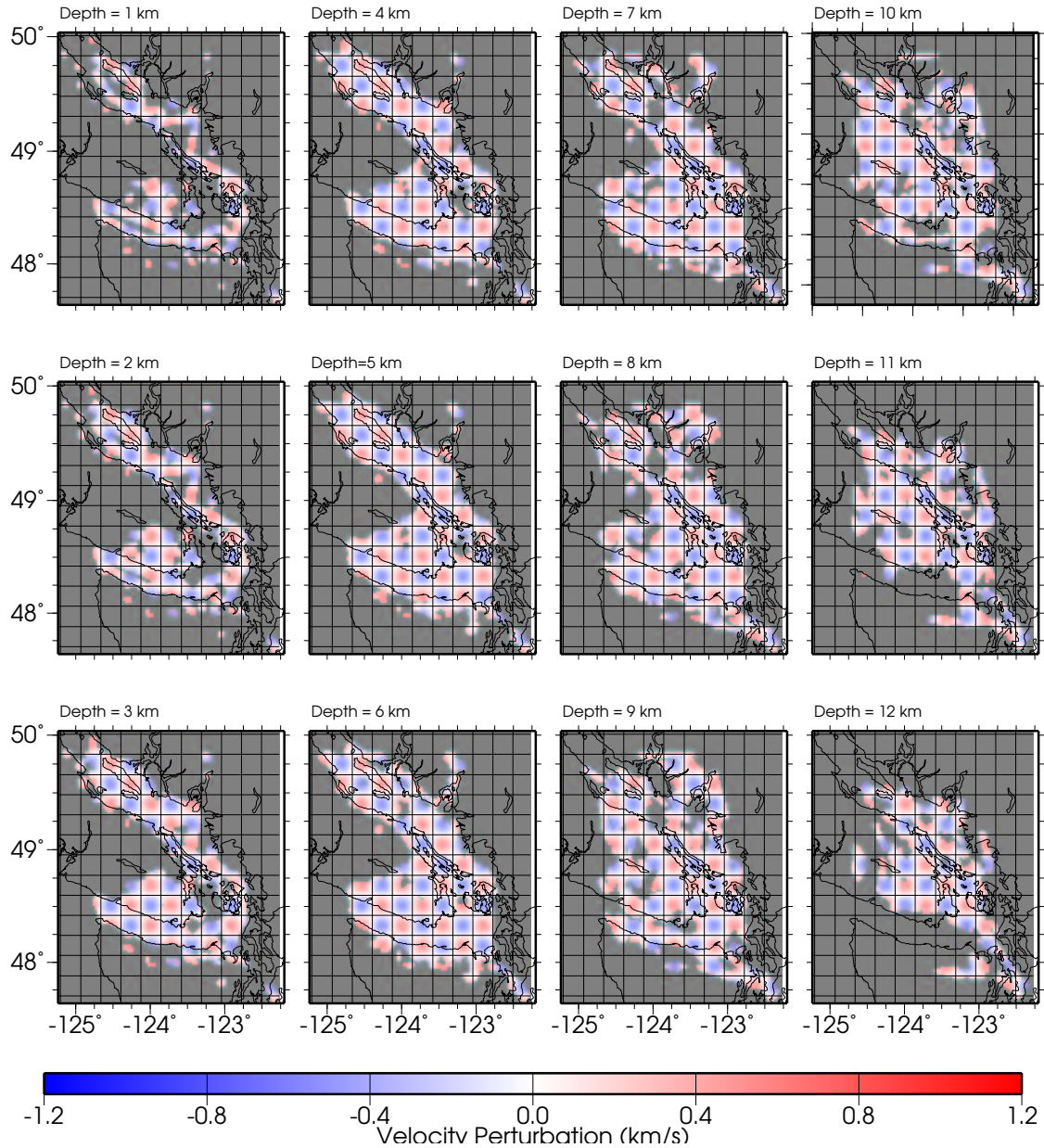


Figure 2.20 Depth slices of checkerboard test input anomaly pattern for 20 km grid size.

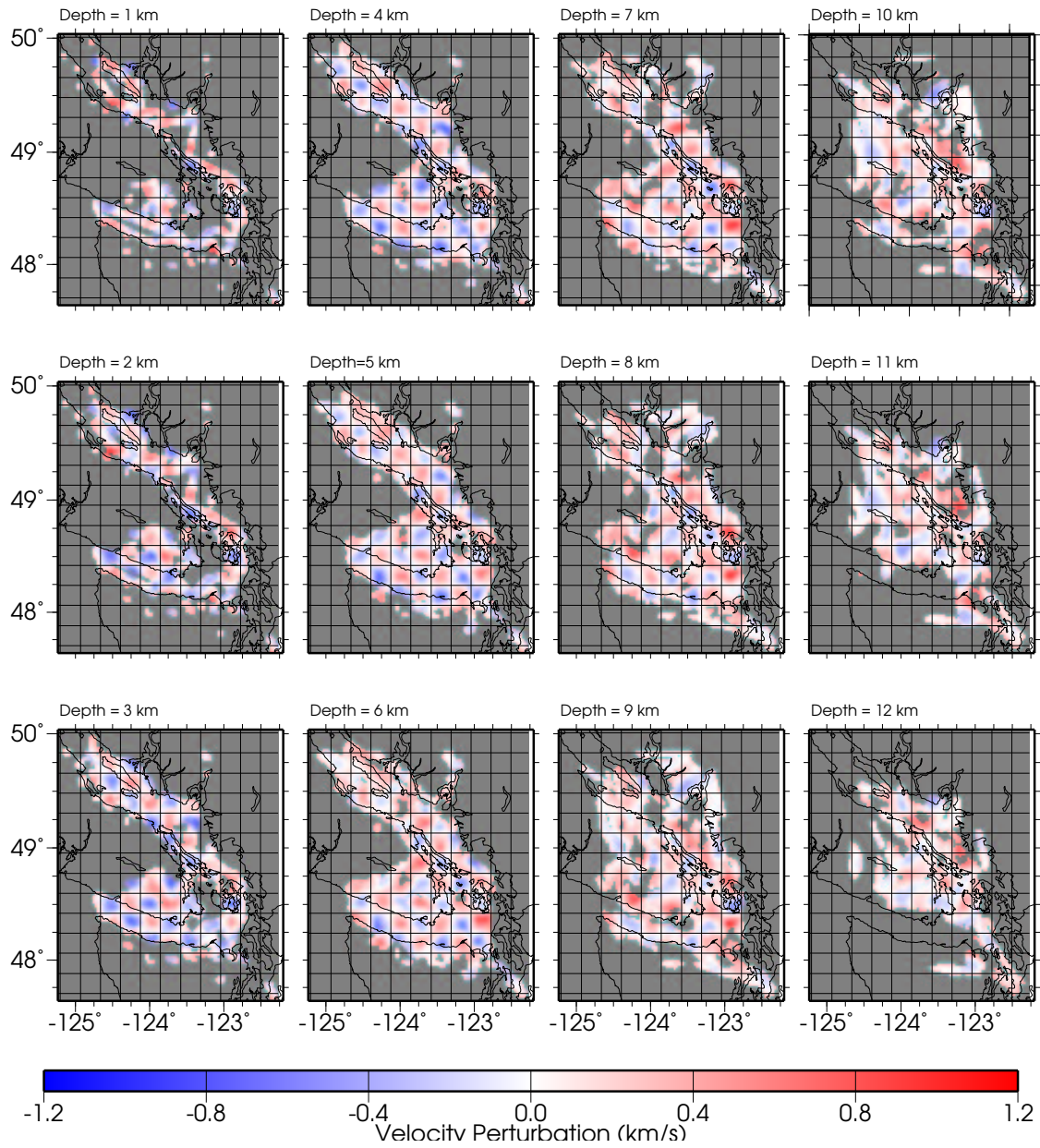


Figure 2.21 Depth slices of checkerboard test recovered anomaly pattern for 20 km grid size.

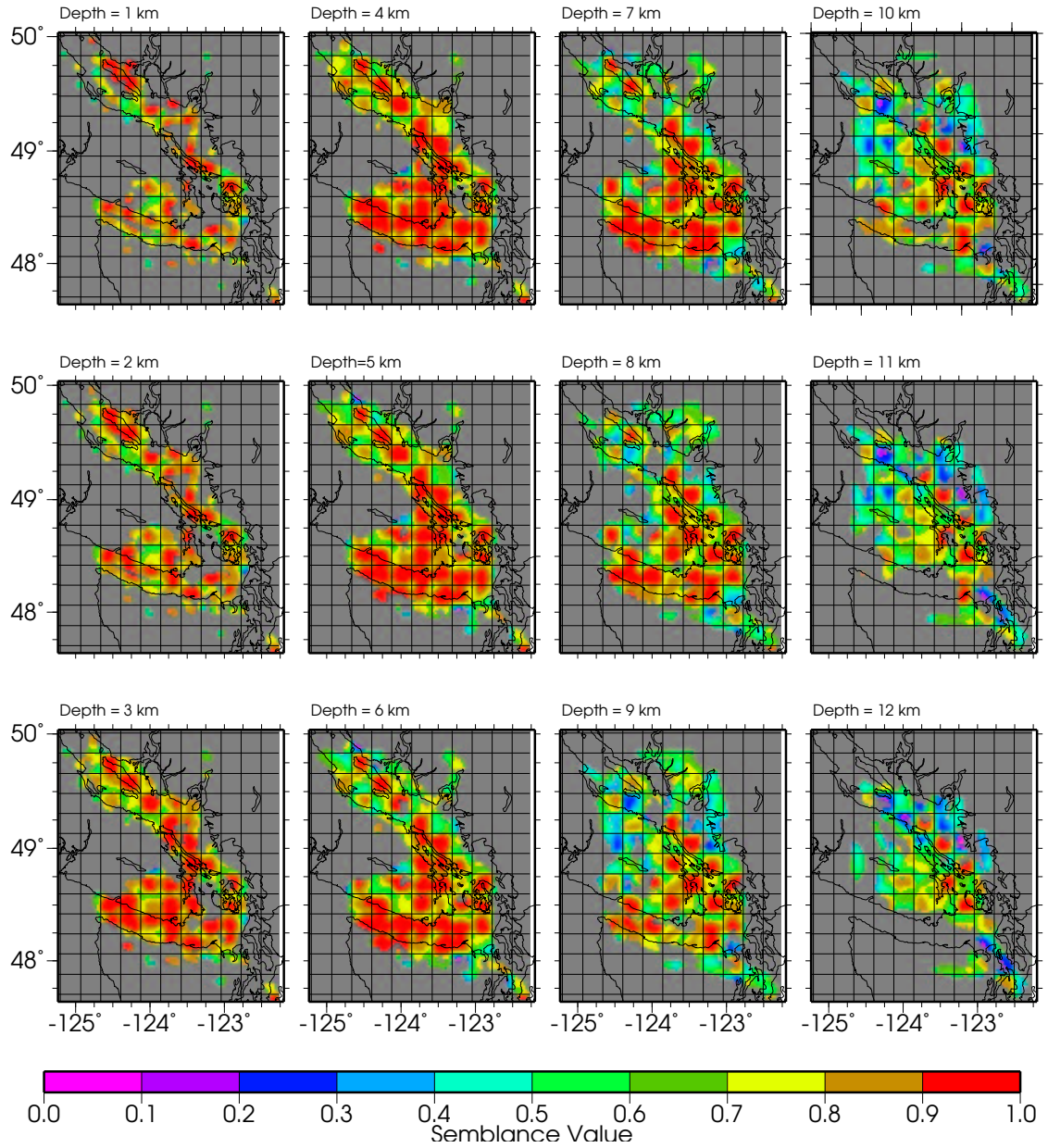


Figure 2.22 Depth slices of semblance values for 20 km checkerboard grid size.

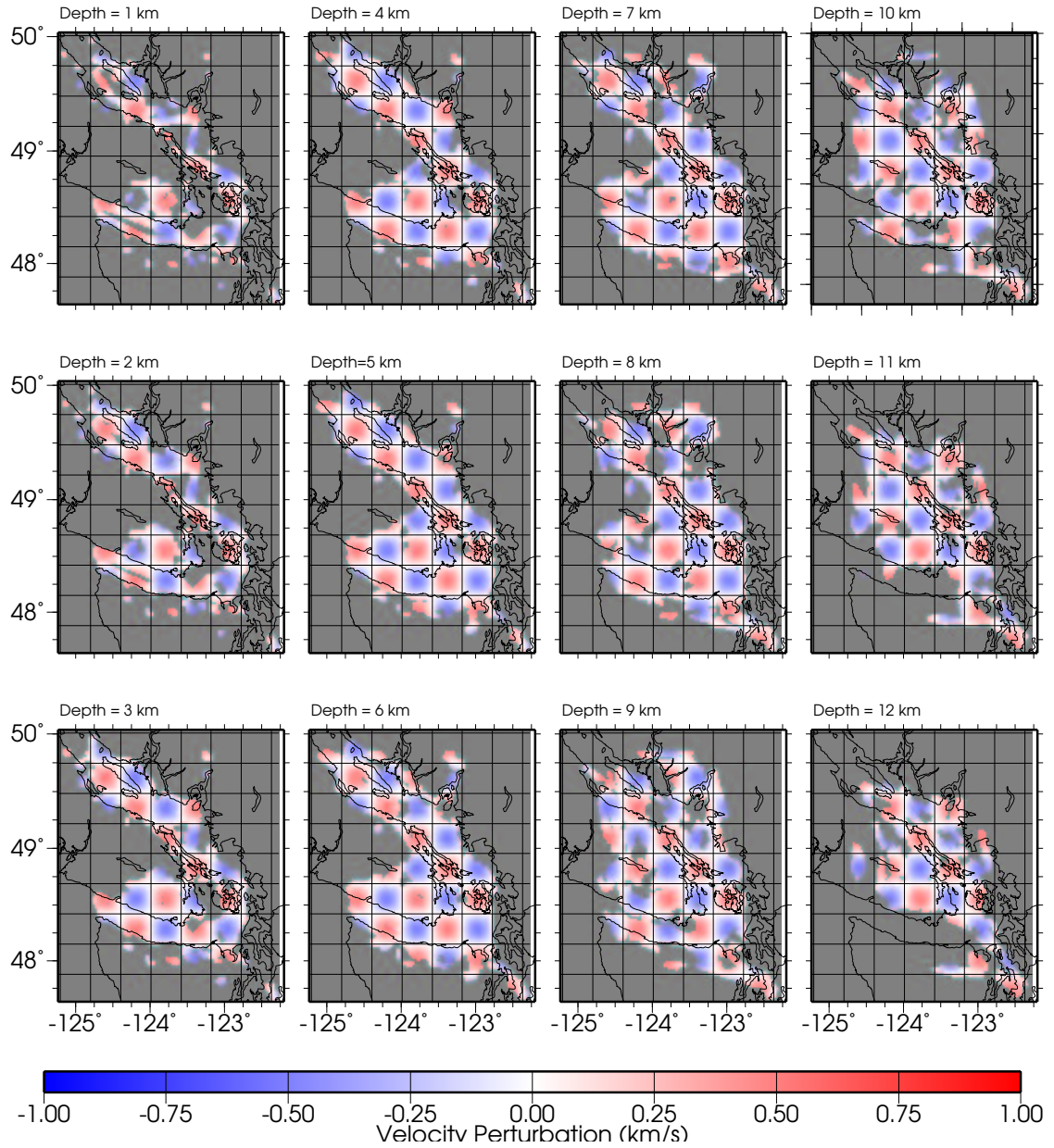


Figure 2.23 Depth slices of checkerboard test input anomaly pattern for 30 km size.

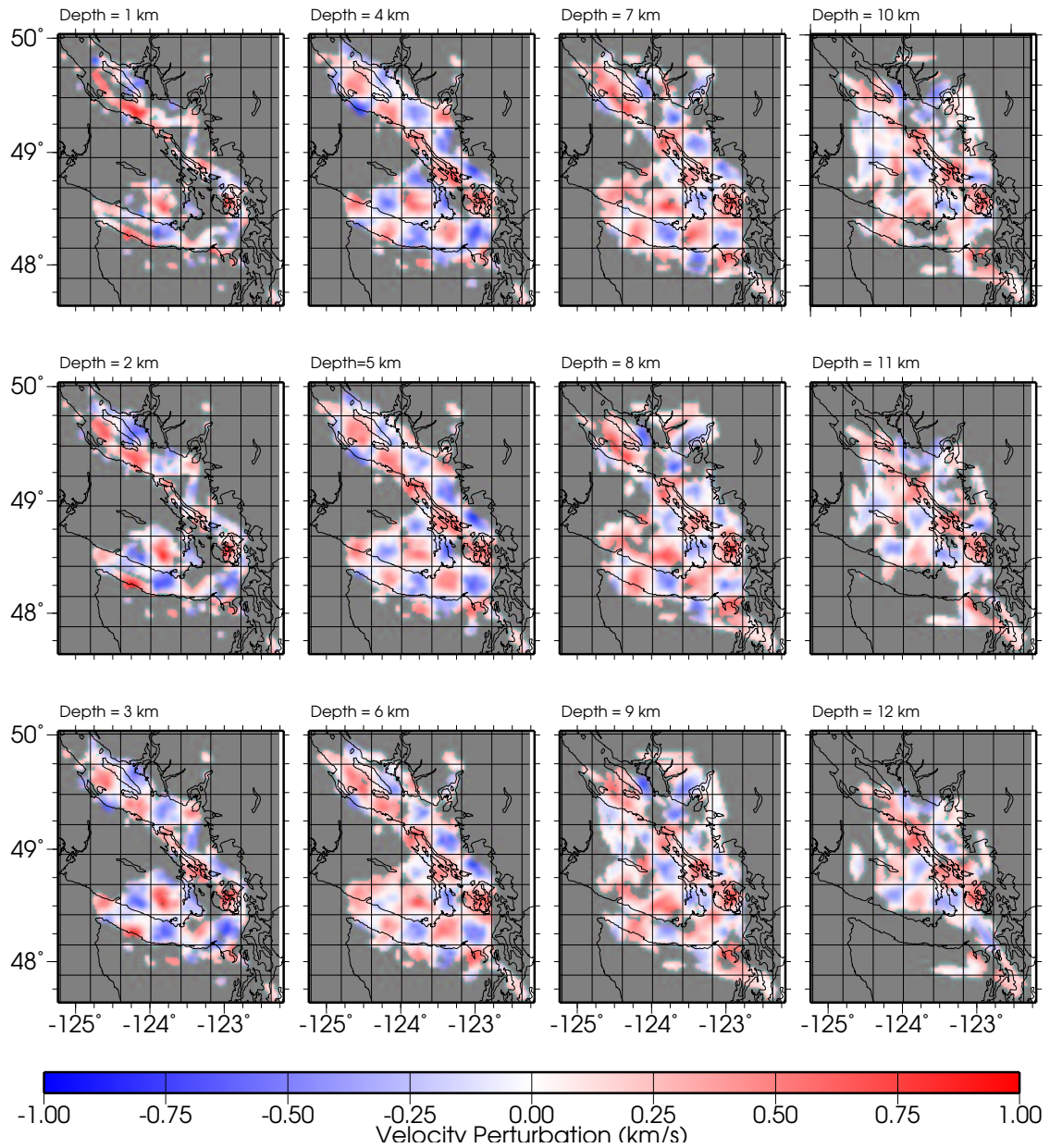


Figure 2.24 Depth slices of checkerboard test recovered anomaly pattern for 30 km grid size.

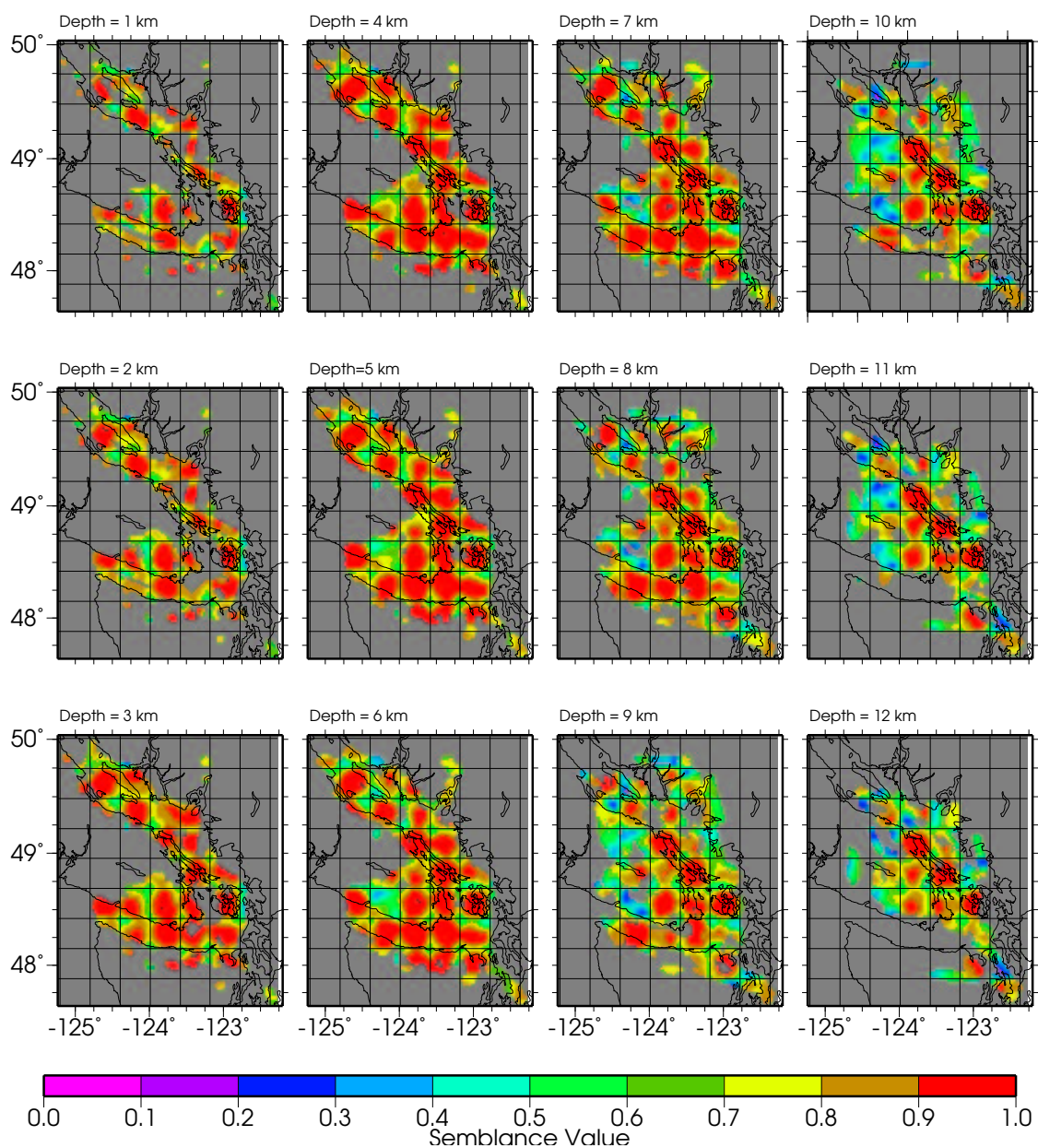


Figure 2.25 Depth slices of semblance values for 30 km checkerboard grid size.

Chapter 3

Earthquake Tomography

3.1 Introduction

Earthquake arrival times recorded at permanent recording stations contain information about hypocentral parameters and the velocity structure of the subsurface. Nonlinear 3-D tomography of earthquake arrival times constitutes the joint estimation of the earthquake hypocentral location and origin time and the subsurface velocity structure. In this chapter a method for joint estimation of hypocentral parameters and velocity structure is developed by modifying the controlled source tomography algorithm of Zelt and Barton (1998) described in Chapter 2. The modified algorithm is first applied to a synthetic data set to evaluate the results and algorithm performance. Subsequently, earthquake data from southwestern British Columbia, recorded by permanent recording stations located in British Columbia and Washington, are inverted for hypocentral parameters and velocity structure. The first arrival travel-time data from the SHIPS experiment are also included in this inversion to constrain the upper crustal velocity structure.

3.2 Theory: Earthquake Tomography

Earthquake tomography is similar to controlled source tomography but with the additional requirement to solve for the source position and origin time of the earthquake which are typically not known to sufficient accuracy. In early applications, when less computing power was available, the solution to this problem was obtained in two separate steps. In the first step, the hypocentral parameters were solved for

by employing the method of Geiger (1912) using inverse methods like damped least squares and singular value decomposition (e.g. Thurber 1986). In such methods, a 1-D starting velocity model is used to determine the hypocentral parameters with the velocity model fixed throughout the inversion procedure. These hypocentral parameters are then treated as fixed source locations and the velocity structure determined using the controlled source tomography algorithm. The velocity structure obtained by this method may not be close to the real earth model, since the hypocentral parameters were determined using a 1-D velocity model. In regions with strong lateral velocity contrasts, such as the fault zones where earthquakes occur, the results can be very poor. In order to obtain a reasonable solution, the hypocentral parameters must be jointly estimated with the velocity structure. Symons (1997) employed a complete joint inversion scheme using finite difference methods to compute travel-times. A similar approach has been developed independently in the present study by modifying the controlled source tomography algorithm of Zelt and Barton (1998) described in previous chapter.

The body wave travel-time T from an earthquake i to a seismic station j can be expressed as a path integral,

$$T_{ij} = \int_{l[m(\mathbf{r})]} m(\mathbf{r}) dl, \quad (3.1)$$

where m is the slowness field and dl is the element of path length. The actual observation is the arrival time t_{ij} , where

$$t_{ij} = T_{ij} + \tau_i, \quad (3.2)$$

and τ_i is the earthquake origin time. From a knowledge of the receiver locations and the observed arrival times, the slowness field of the subsurface, earthquake position coordinates (x, y, z) in the subsurface and origin time of the earthquakes are to be determined.

Given the arrival time t_{ij}^{obs} measured at station i of a network of I permanent recording stations for the j^{th} earthquake, the arrival time t_{ij}^{cal} is calculated using

a trial hypocentral location, origin time and an initial slowness model. The misfit between the observed and calculated arrival time is the residual Δt_{ij} . This residual is equated to the perturbation to be applied to the starting model of the hypocentral and slowness parameters by

$$\Delta t_{ij} = \int_{l[m(\mathbf{r})]} m(\mathbf{r}) dl + \sum_{k=1}^3 \frac{\partial T_{ij}}{\partial x_{jk}} \Delta x_{jk} + \Delta \tau_j, \quad (3.3)$$

where x_1, x_2, x_3 represent x,y,z, respectively. For J earthquakes and L velocity model parameters, the number of hypocentral parameters to be determined are $4J$ and the total number of parameters to be determined in the inversion are $L + 4J$. For a finite parameterisation of the slowness model the above equation can be written as

$$\Delta \mathbf{t}_{ij} = \sum_{l=1}^L \frac{\partial \mathbf{T}_{ij}}{\partial \mathbf{m}_l} \Delta \mathbf{m}_l + \sum_{k=1}^3 \frac{\partial \mathbf{T}_{ij}}{\partial \mathbf{x}_{jk}} \Delta \mathbf{x}_{jk} + \Delta \tau_j, \quad (3.4)$$

where m_l represent the L parameters of the slowness model. This system of equations can be represented in matrix form as

$$\begin{bmatrix} \frac{\partial T_{11}}{\partial m_1} & \dots & \frac{\partial T_{11}}{\partial m_L} & \frac{\partial T_{11}}{\partial x_{11}} & \frac{\partial T_{11}}{\partial x_{21}} & \frac{\partial T_{11}}{\partial x_{31}} & 1 & \dots & 0 & 0 & 0 \\ \frac{\partial T_{21}}{\partial m_1} & \dots & \frac{\partial T_{21}}{\partial m_L} & \frac{\partial T_{21}}{\partial x_{11}} & \frac{\partial T_{21}}{\partial x_{21}} & \frac{\partial T_{21}}{\partial x_{31}} & 1 & 0 & \dots & \dots & 0 & 0 \\ \vdots & \vdots & \vdots & \vdots & \vdots & \vdots & \vdots & \vdots & \vdots & \vdots & \vdots & \vdots \\ \frac{\partial T_{I1}}{\partial m_1} & \dots & \frac{\partial T_{I1}}{\partial m_L} & \frac{\partial T_{I1}}{\partial x_{11}} & \frac{\partial T_{I1}}{\partial x_{21}} & \frac{\partial T_{I1}}{\partial x_{31}} & 1 & 0 & \dots & \dots & 0 & 0 \\ \vdots & \vdots & \vdots & \vdots & \vdots & \vdots & \vdots & \vdots & \vdots & \vdots & \vdots & \vdots \\ \vdots & \vdots & \vdots & \vdots & \vdots & \vdots & \vdots & \vdots & \vdots & \vdots & \vdots & \vdots \\ \vdots & \vdots & \vdots & \vdots & \vdots & \vdots & \vdots & \vdots & \vdots & \vdots & \vdots & \vdots \\ \vdots & \vdots & \vdots & \vdots & \vdots & \vdots & \vdots & \vdots & \vdots & \vdots & \vdots & \vdots \\ \vdots & \vdots & \vdots & \vdots & \vdots & \vdots & \vdots & \vdots & \vdots & \vdots & \vdots & \vdots \\ \frac{\partial T_{1J}}{\partial m_1} & \dots & \frac{\partial T_{1J}}{\partial m_L} & 0 & \dots & \dots & 0 & 0 & \frac{\partial T_{1J}}{\partial x_{1J}} & \frac{\partial T_{1J}}{\partial x_{2J}} & \frac{\partial T_{1J}}{\partial x_{3J}} & 1 \\ \frac{\partial T_{2J}}{\partial m_1} & \dots & \frac{\partial T_{2J}}{\partial m_L} & 0 & \dots & \dots & 0 & 0 & \frac{\partial T_{2J}}{\partial x_{1J}} & \frac{\partial T_{2J}}{\partial x_{2J}} & \frac{\partial T_{2J}}{\partial x_{3J}} & 1 \\ \vdots & \vdots & \vdots & \vdots & \vdots & \vdots & \vdots & \vdots & \vdots & \vdots & \vdots & \vdots \\ \frac{\partial T_{IJ}}{\partial m_1} & \dots & \frac{\partial T_{IJ}}{\partial m_L} & 0 & \dots & \dots & 0 & 0 & \frac{\partial T_{IJ}}{\partial x_{1J}} & \frac{\partial T_{IJ}}{\partial x_{2J}} & \frac{\partial T_{IJ}}{\partial x_{3J}} & 1 \end{bmatrix} \begin{bmatrix} \Delta m_1 \\ \vdots \\ \Delta m_L \\ \Delta x_{11} \\ \Delta x_{21} \\ \Delta x_{31} \\ \Delta \tau_1 \\ \vdots \\ \Delta x_{1J} \\ \Delta x_{2J} \\ \Delta x_{3J} \\ \Delta \tau_J \end{bmatrix} = \begin{bmatrix} \Delta t_{11} \\ \Delta t_{21} \\ \vdots \\ \Delta t_{31} \\ \vdots \\ \Delta t_{I1} \\ \vdots \\ \Delta t_{1J} \\ \Delta t_{2J} \\ \Delta t_{3J} \\ \vdots \\ \Delta t_{IJ} \end{bmatrix}, \quad (3.5)$$

where $\frac{\partial \mathbf{T}_{ij}}{\partial \mathbf{m}_l}$ represent the partial derivatives of the l slowness model parameters ($l =$

1, L) and $\frac{\partial \mathbf{T}_{ij}}{\partial \mathbf{x}_{ij}}$ are the partial derivatives of the hypocenter location parameters for the j earthquakes ($j = 1, J$). Smoothing is applied similar to that in Chapter 2 by penalising total model roughness (Eqn. 2.9). The problem is underdetermined as the number of model parameters is more than the number of data. For a given velocity model travel-time cubes are generated for each receiver. The partial derivatives of the slowness model parameters equal to the path length of the rays in the cells are computed from the travel-time cubes. The partial derivatives of the hypocentral parameters are also computed from the travel-time cubes by computing the difference in travel-time at the earthquake source point for a unit disturbance in distance, in the respective directions. The computed slowness and hypocentral parameter updates are represented by $\Delta \mathbf{m}_l$ and Δx_{jk} respectively, and the computed earthquake origin time updates are given by $\Delta \tau_j$.

The seismic tomography problem can be formulated to simultaneously invert both controlled source and earthquake data. In general, data from controlled source experiments constrain well the upper crustal velocity structure due to the large number of ray paths and the *a priori* knowledge of source position and shot time. The largest lateral velocity variations usually exist in the upper few kilometers of the crust and it is difficult to constrain this structure using earthquake data. For a given study area with shallow velocity structure constrained by controlled source data, including earthquake data in the inversion extends the coverage to deeper structures. The spatial coverage and resolution of the deeper features in the final velocity model will depend on the spatial distribution of the earthquakes and the permanent recording stations. In joint inversion, the partial derivatives involving the hypocentral locations and origin time of the controlled source data are set to zero, since these parameters are known. The model is smoothed in a manner similar to that discussed in equation 2.12. The algorithm used for non-linear 3-D tomography of earthquake and controlled source data is presented in Appendix C and is discussed below.

3.3 Synthetic Case Study

A synthetic earthquake data set was constructed to test the robustness and efficiency of the modified algorithm in recovering the hypocentral and velocity parameters simultaneously. This geometry is used to test the inversion method, and not the experimental geometry. A test velocity model with a small volume of $(50 \times 50 \times 20)$ km was extracted from the velocity model constructed via the inversion of SHIPS data from a region close to the southern Vancouver Island with sharp vertical and lateral contrasts (Figs. 3.1), 3.2). This test model was specifically chosen to study the performance of the algorithm for complex geological structure. A total of 49 receivers with a station spacing of 8 km in x and y were used in the synthetic data generation (Fig. 3.3). Earthquake locations were uniformly distributed over planar surfaces at 4, 8 and 12 km depth. In each plane, 81 earthquake locations separated by 5 km in x and y were used to compute the synthetic travel-times. Gaussian noise with a standard deviation of 100 ms was added to the travel-times.

The starting model in earthquake tomography consisted of a 1-D velocity model (Fig. 3.4) and earthquake hypocentral parameters constructed by adding Gaussian perturbations to the actual locations used in the computation of the synthetic travel-time data. The procedure for non-linear 3-D tomography of earthquake data, given in Appendix C, differs from that for controlled source data in the model update step. For every iteration of the inversion step, the velocity model and the hypocentral parameters are updated. After the model update, partial derivatives are computed at each iteration. One value of the tradeoff parameter λ is tested for each iteration. The RMS travel-time misfit for approximately 1.2×10^4 rays in the starting model was 517 ms for a normalised χ^2 value of 24. The vertical to horizontal smoothing parameter s_z was set to 0.2 and the starting and final values of λ were 40 and 3.4. The final model was obtained after 22 iterations and the final value of RMS travel-time misfit was 111 ms for a normalised χ^2 value of 1.2. The reduction of RMS travel-time

misfit from initial 1-D model to final 3-D model was 79%. The RMS errors of the hypocentral location and origin time in the starting model were 2.77 km and 311 ms. The RMS error of the hypocentral location and origin time in the final model were 1.24 km and 108 ms.

All the major features observed in the true velocity model are recovered in the final velocity model (Fig. 3.5). The true, starting and relocated hypocentral locations at 4, 8, and 12 km depth planes are shown in Figs. 3.6, 3.7 and 3.8. The relocated hypocentral locations (shown as red dots) are much close to the true hypocentral locations (blue squares) than the starting locations (green diamonds). To illustrate the importance of hypocentral relocation in earthquake tomography, the synthetic data were inverted for velocity structure holding the hypocentral locations fixed at their starting values. The final velocity model for this inversion is shown in Fig. 3.9. This model does not show any of the features present in the true model, but rather includes spurious structure with high lateral velocity contrasts. Difference between the true velocity model and the final velocity model (Fig. 3.6) and the velocity model obtained with joint hypocentral relocation (Fig. 3.8) is shown in Fig. 3.10. Difference between the true velocity model and the final velocity model (Fig. 3.6) and the velocity model obtained without joint hypocentral relocation (Fig. 3.9) is shown in Fig. 3.11. The difference between Figs. 3.10 and 3.11 clearly brings out the necessity for performing joint inversion in the case of earthquake data.

3.4 Tomographic Inversion of Earthquake Data

The study area selected for earthquake tomography falls between between 126° W and 121° W, and 47° N and 51° N (Fig. 3.12). Earthquakes recorded by 46 permanent recording stations were selected for analysis. In total 1,650 earthquakes of magnitude greater than one, recorded between the years 1984 and 2000, and which were recorded

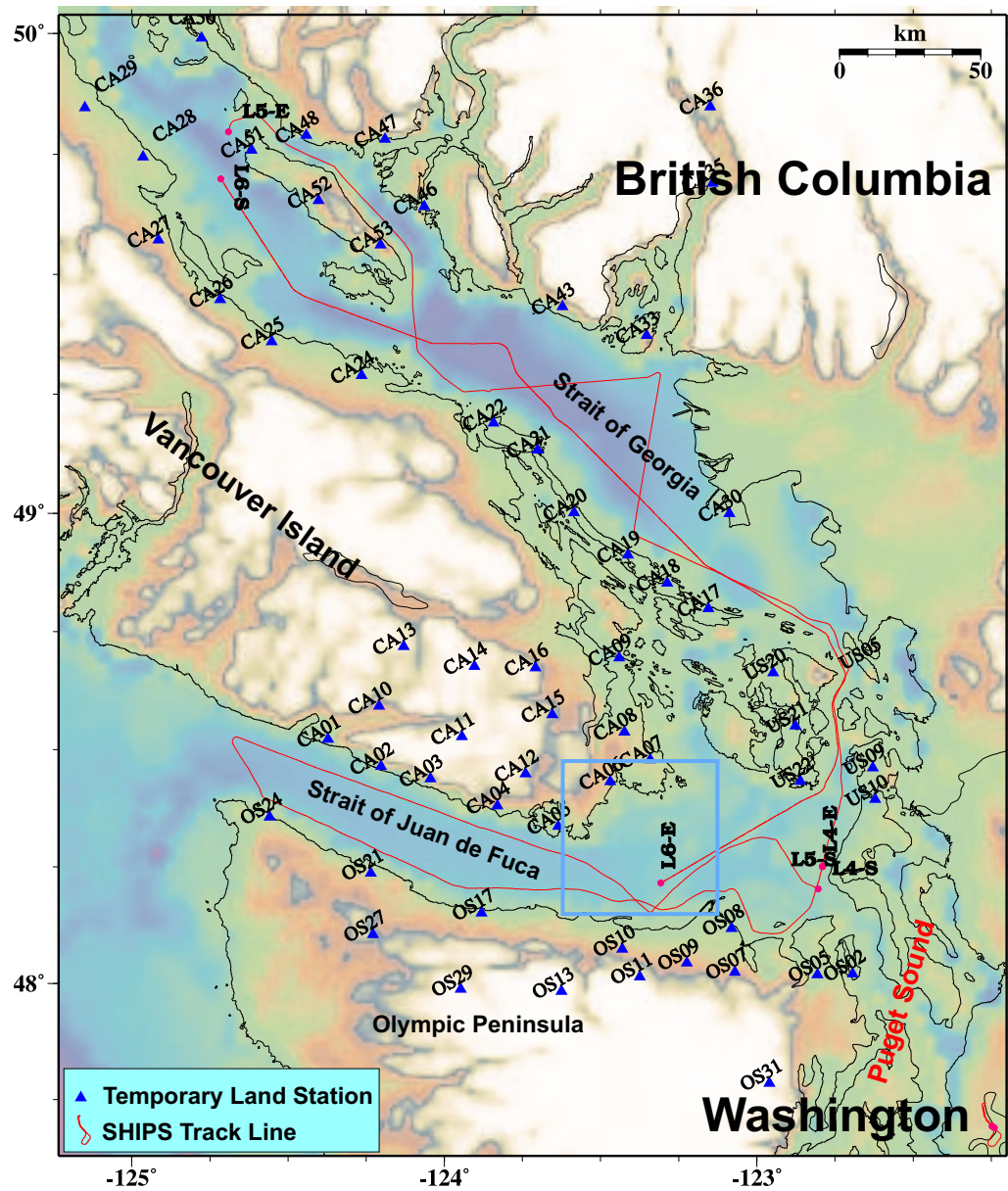


Figure 3.1 Synthetic study area close to southern Vancouver Island is shown by the blue box.

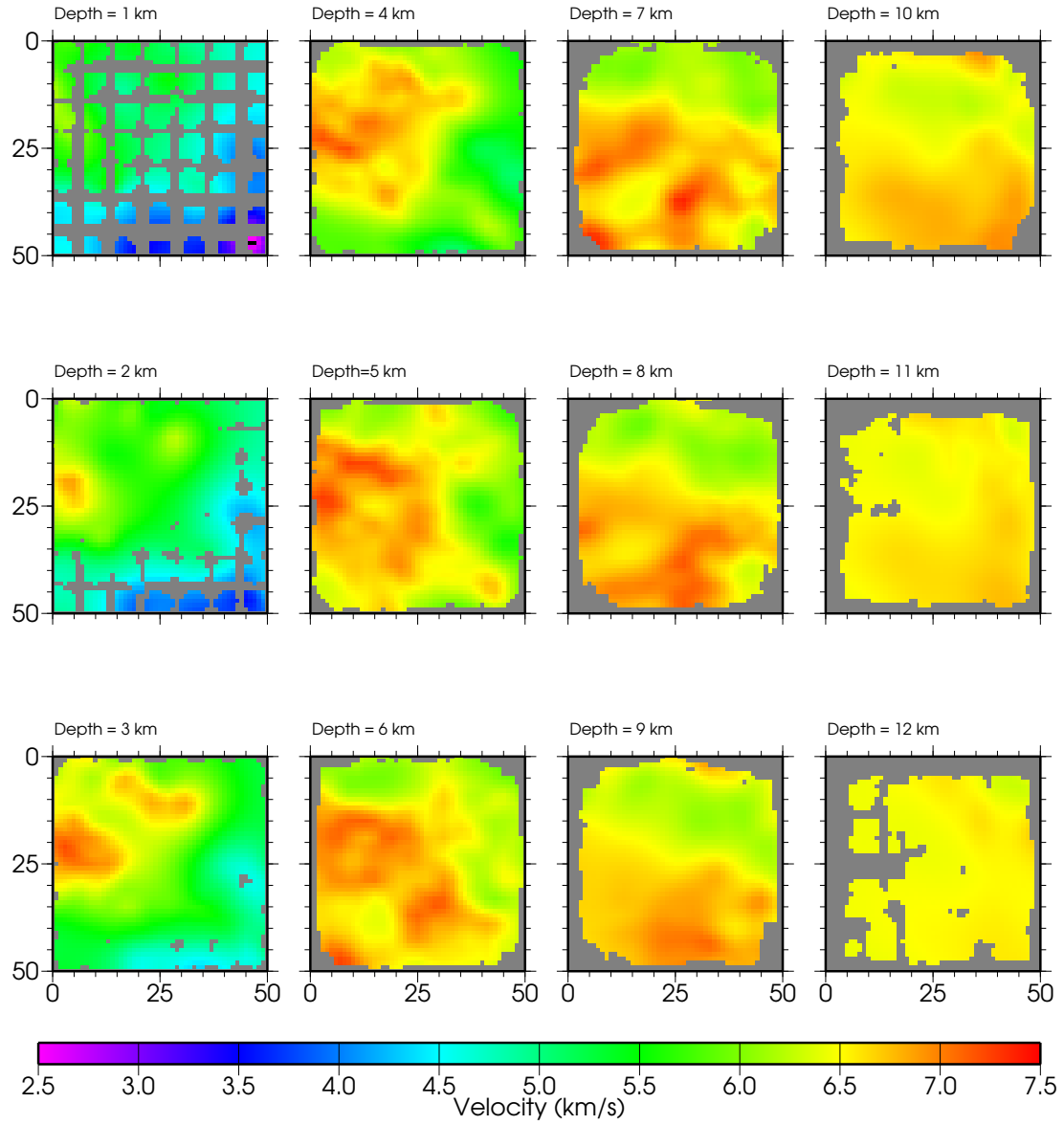


Figure 3.2 True velocity model used in the synthetic study.

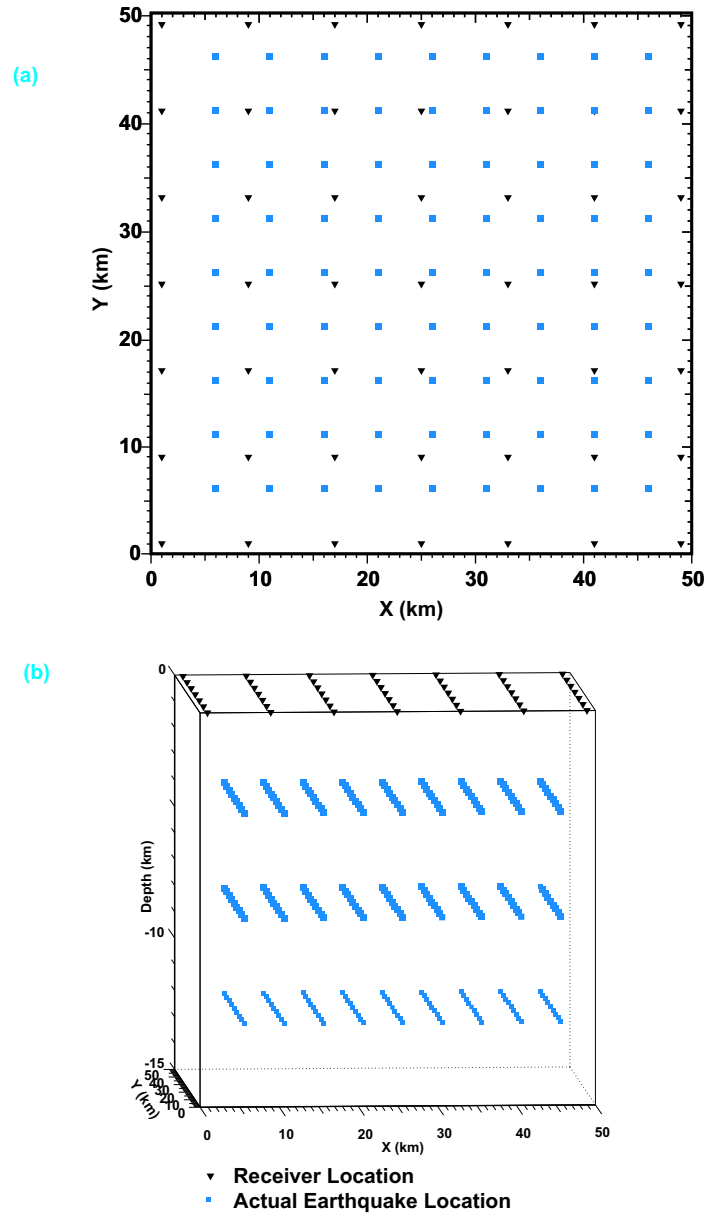


Figure 3.3 Location of earthquakes and receivers used in the synthetic study: (a) projected on to surface, (b) viewed in three dimensions.

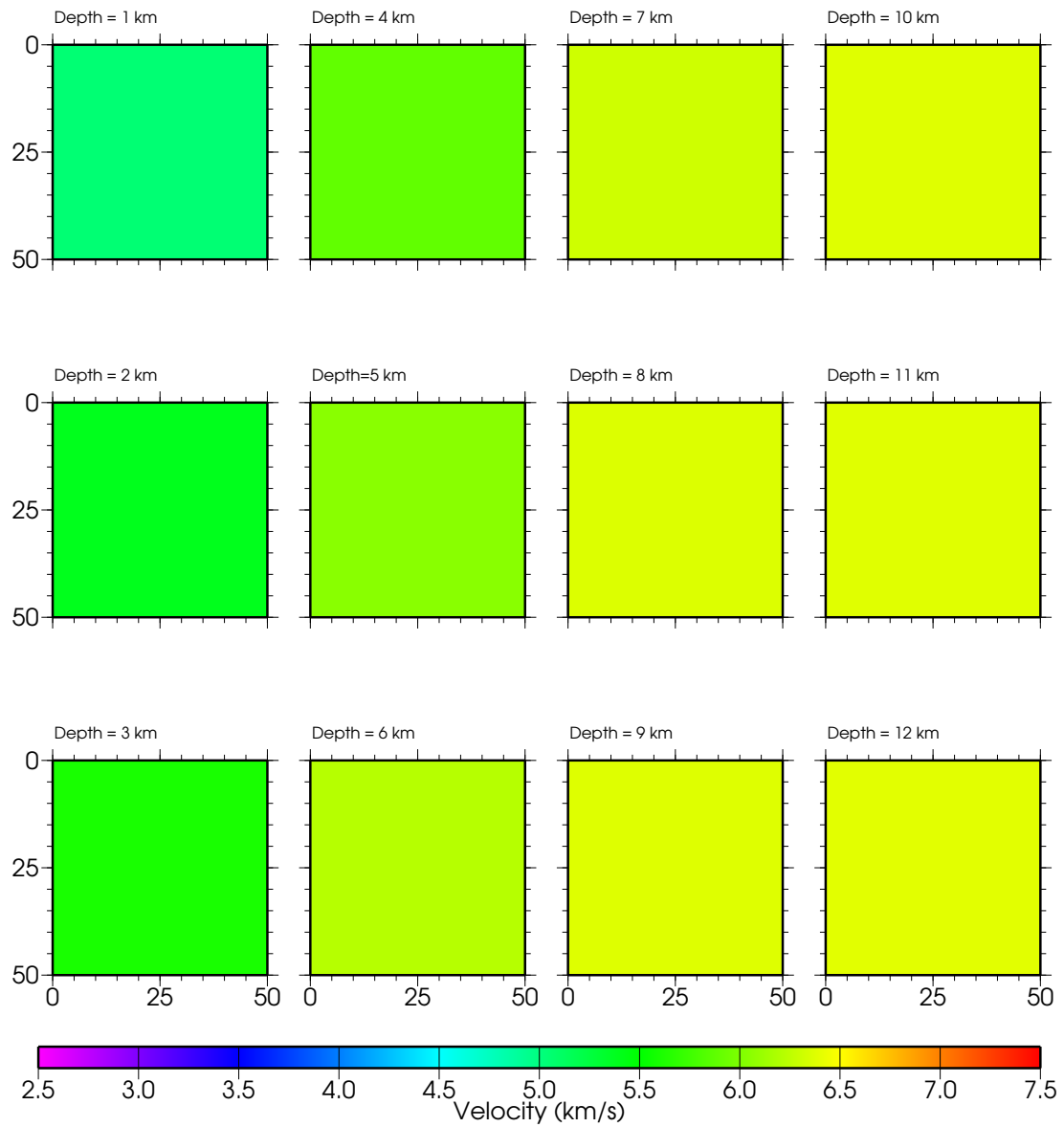


Figure 3.4 Starting velocity model for inversion of synthetic earthquake data.

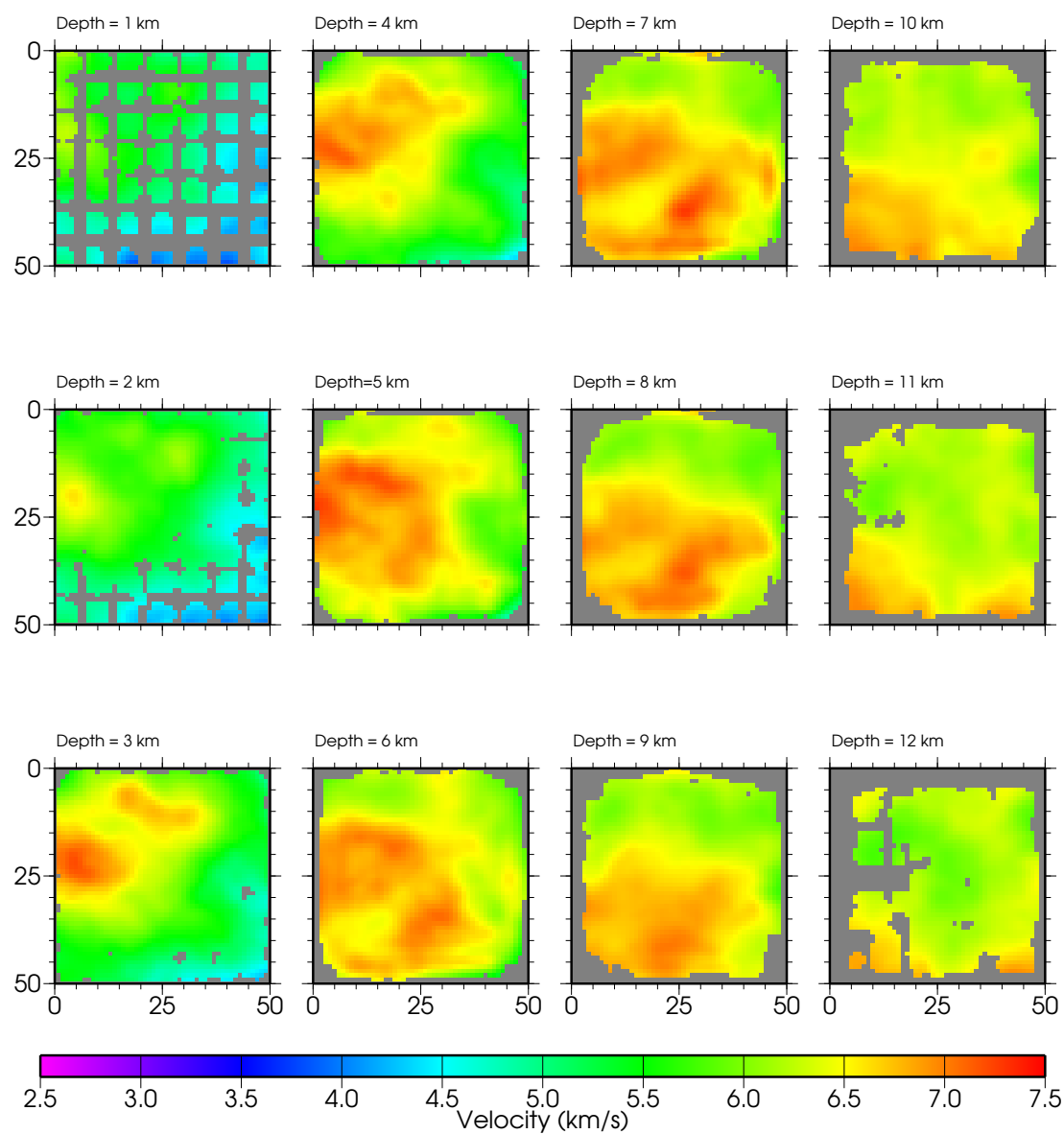


Figure 3.5 Final velocity model from the synthetic study.

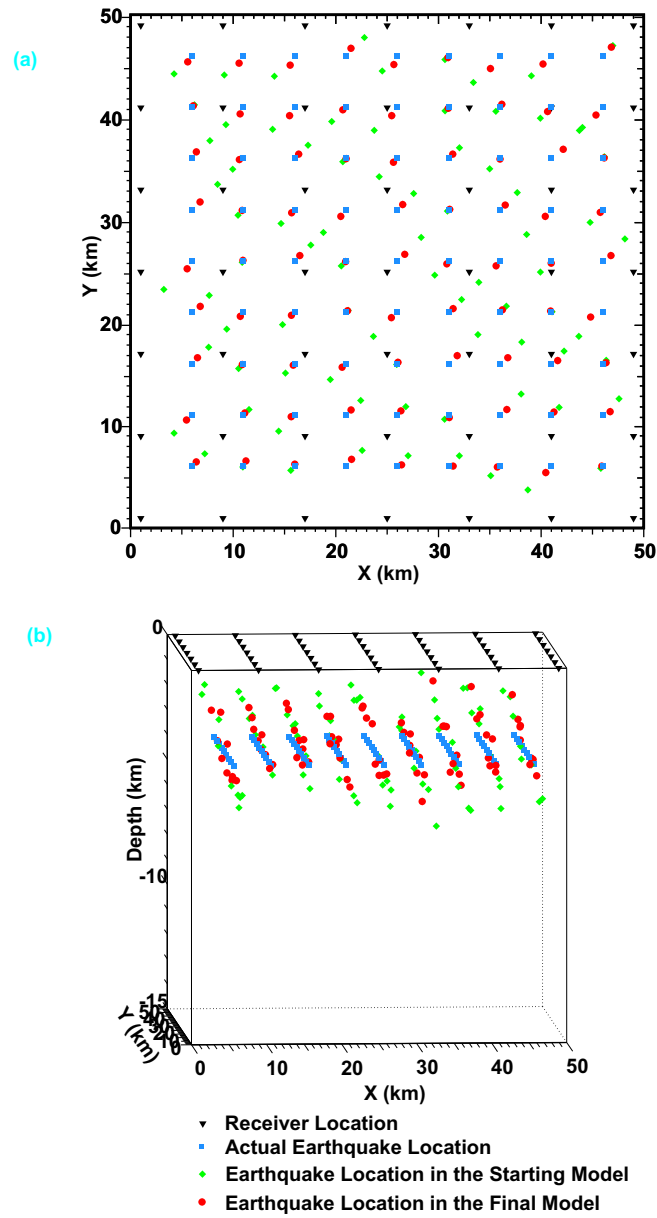


Figure 3.6 True, starting, and relocated earthquake locations at 4 km depth. (a) The earthquake locations are projected onto surface and (b) three dimensional view.

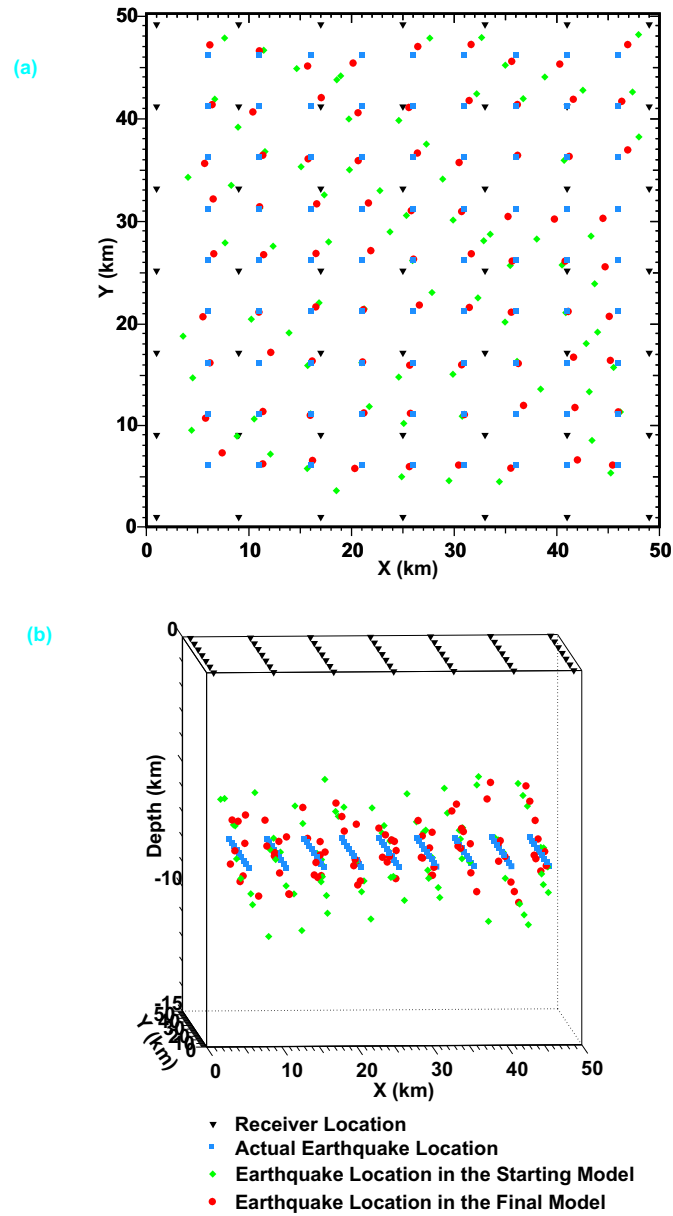


Figure 3.7 True, starting, and relocated earthquake locations at 8 km depth. (a) The earthquake locations are projected onto surface and (b) three dimensional view.

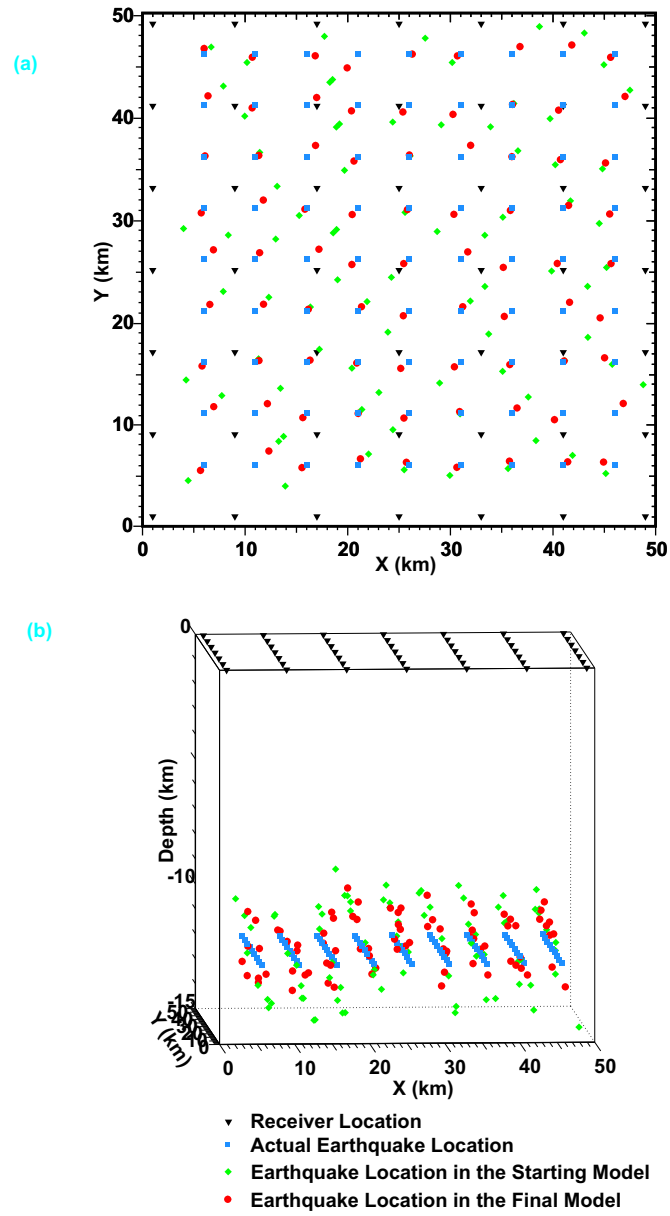


Figure 3.8 True, starting, and relocated earthquake locations at 12 km depth. (a) The earthquake locations are projected onto surface and (b) three dimensional view.

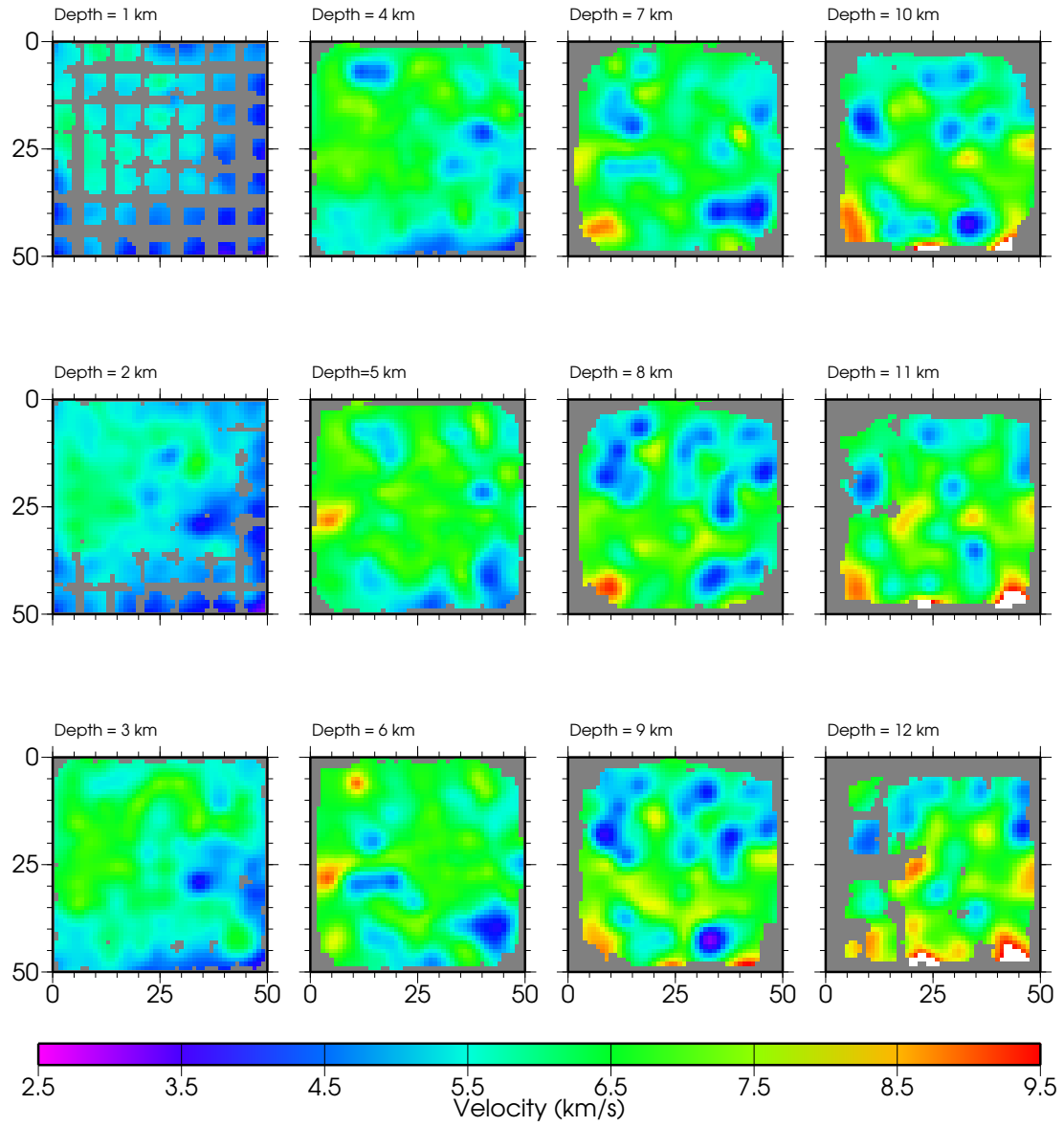


Figure 3.9 Final velocity model from the synthetic study without joint hypocentral parameter estimation.

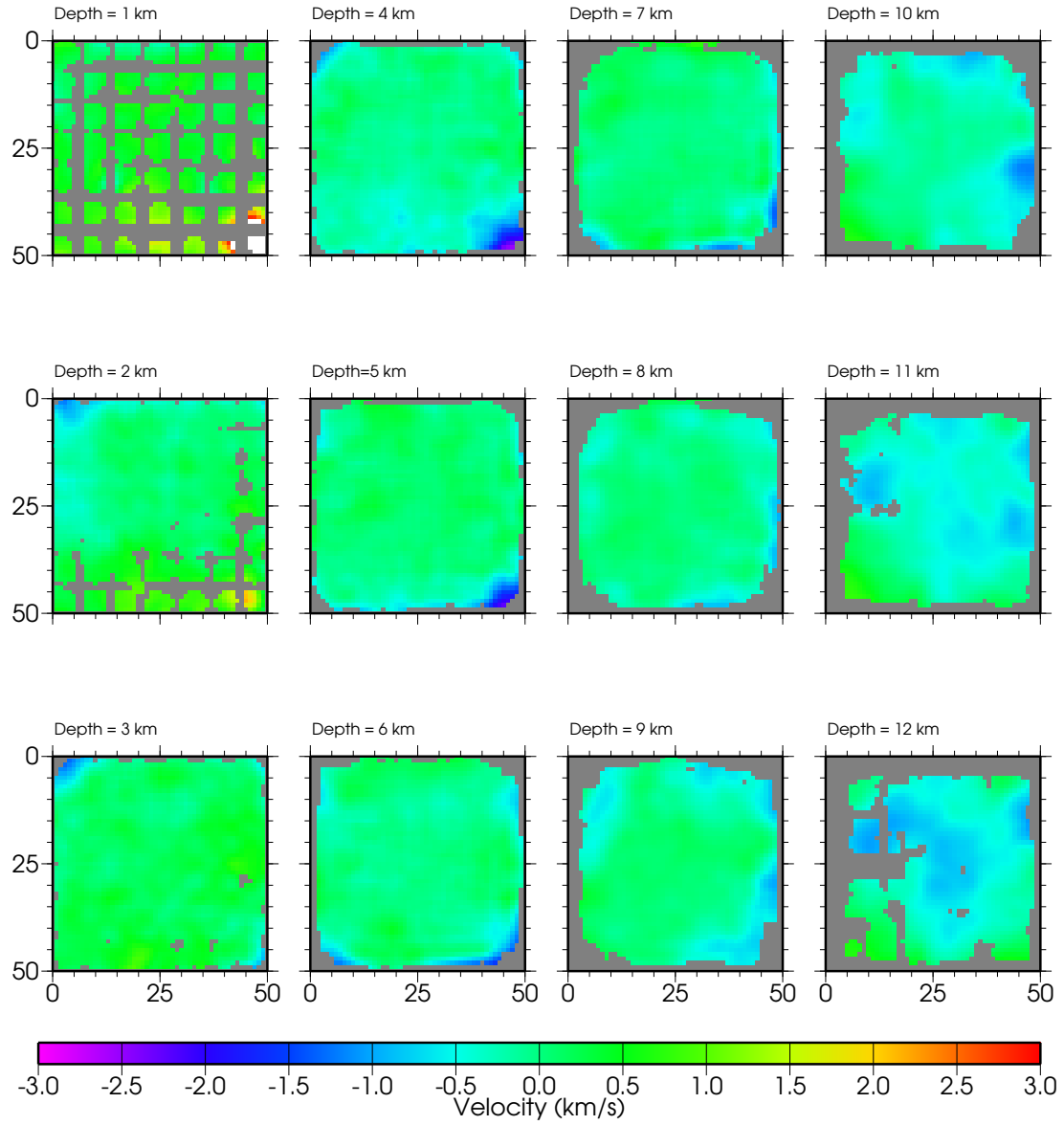


Figure 3.10 Difference between true velocity model and final velocity model constructed with joint hypocentral parameter estimation.

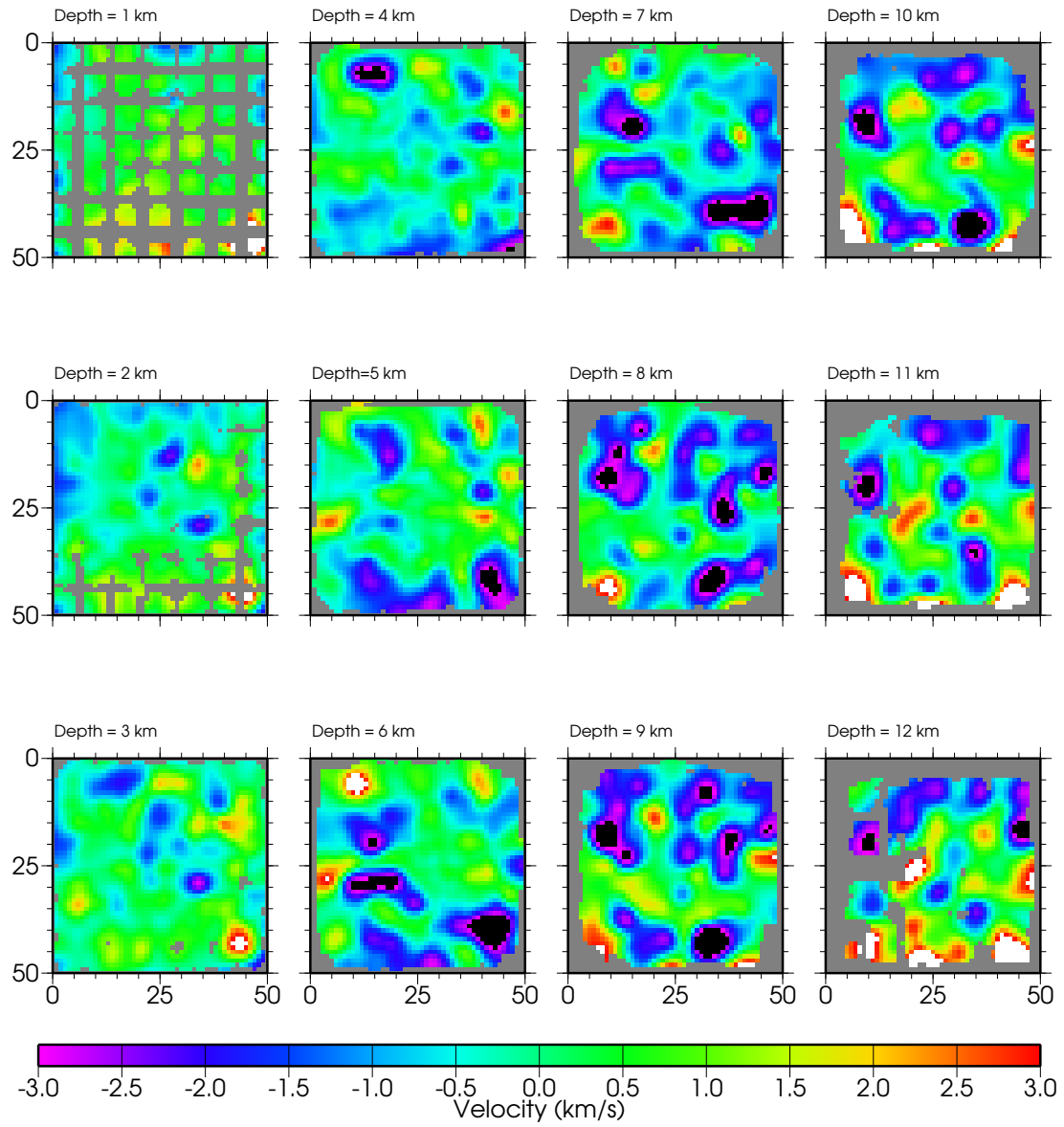


Figure 3.11 Difference between true velocity model and final velocity model constructed without joint hypocentral parameter estimation.

by a minimum of four permanent recording stations and $1 > M$ within the study area were selected as input data. Making these conditions more strict resulted in less number of earthquakes for the inversion and also the spatial distribution of the earthquakes was significantly affected. The total number of first arrival picks amounted to approximately 1.7×10^4 . The hypocentral parameter solutions were provided in the earthquake database obtained of the Pacific Geoscience Center, Geological Survey of Canada. Locations of the recording stations and earthquakes are shown in Fig. 3.12. Fig. 3.13 shows the plot of earthquakes projected on a vertical plane to show the distribution of the earthquakes with depth.

The initial hypocentral location and origin time were set as starting model parameters for the tomographic inversion. Approximately 3.5×10^4 first arrival travel-time picks from the SHIPS experiment, decimated at equal distances, were also included in the joint inversion. Only a fraction of the 175,000 SHIPS picks were used in this study due to computing limitations.

The velocity model was parameterised in the forward/inverse step by a node/cell spacing of $(3 \times 3 \times 3)$ km. The velocity model dimensions in (x, y, z) directions were $(360 \times 450 \times 93)$ km. The top of the model was set to 3 km above sea-level to position the receivers at their actual elevations in the velocity model. However the results reported were standardised with respect to mean sea level. The uncertainty in the earthquake travel-time observations was assigned a value of 100 ms. The uncertainty in the earthquake locations in each direction was assigned a value of 10 km. A 1-D starting velocity model was constructed that best fit the time-distance plot and minimised the RMS travel-time misfit (Fig. 3.14). The travel-time misfit for the picks in the starting model are shown in Fig. 3.17. The inversion procedure was run in test mode to determine the optimum value of the parameter s_z (horizontal to vertical smoothing). After visually inspecting the final models for smoothness and continuity in lateral and vertical directions, s_z was set to a value of 0.20 i.e. the smoothing in horizontal direction was set to five times more than that in vertical

direction. This value of s_z was then held fixed through out the inversion. One test run was conducted to identify and remove the travel-time observation outliers from the earthquake data.

After removing the outliers, 1435 earthquakes with approximately 1.6×10^4 travel-time picks and approximately 3.5×10^4 picks from the SHIPS experiment were used in the final inversion. The SHIPS travel-time picks are approximately two times the amount of earthquake picks. This ratio however will not affect the final velocity model as the data are fit according to their uncertainties. The updated hypocentral parameters from the test run were employed as the starting model for the final run of the joint inversion. The RMS travel-time residual in the starting model for approximately 5.0×10^4 picks was 479 ms for a normalized χ^2 of 19. The hypocentral and velocity parameters were updated during each iteration of the inversion, and ray tracing was performed to account for the change in hypocentral parameters. Small steps in λ were taken during inversion to ensure that the linearised formulation of the problem was honored. After 46 iterations, a normalised χ^2 close to 2 was achieved for an RMS travel-time residual of 120 ms. This solution was selected as no further improvement in the solution was observed. The total number of model nodes in the forward computations was 5.8×10^5 and the number of model cells in the inverse computations was 5.6×10^5 . The number of nonzero elements in the slowness kernel was approximately 2.1×10^6 for 5.1×10^4 observations. The number of constraint equations and nonzero elements were approximately 1.1×10^6 and 6.5×10^6 , respectively. Relocated locations of the earthquakes are shown in Fig. 3.15. Fig. 3.16 shows the plot of relocated earthquakes projected on a vertical plane.

The travel-time misfit with offset in the final model is shown in Fig. 3.17. The misfit is observed to be uniform over the entire range of offset for the SHIPS events (shown by blue dots) and the earthquake events (red dots). The convergence plots of RMS travel-time misfit, normalized χ^2 misfit and the trade-off parameter λ are shown in Fig. 3.18. Fig. 3.19 shows the variation in perturbation (P), horizontal roughness

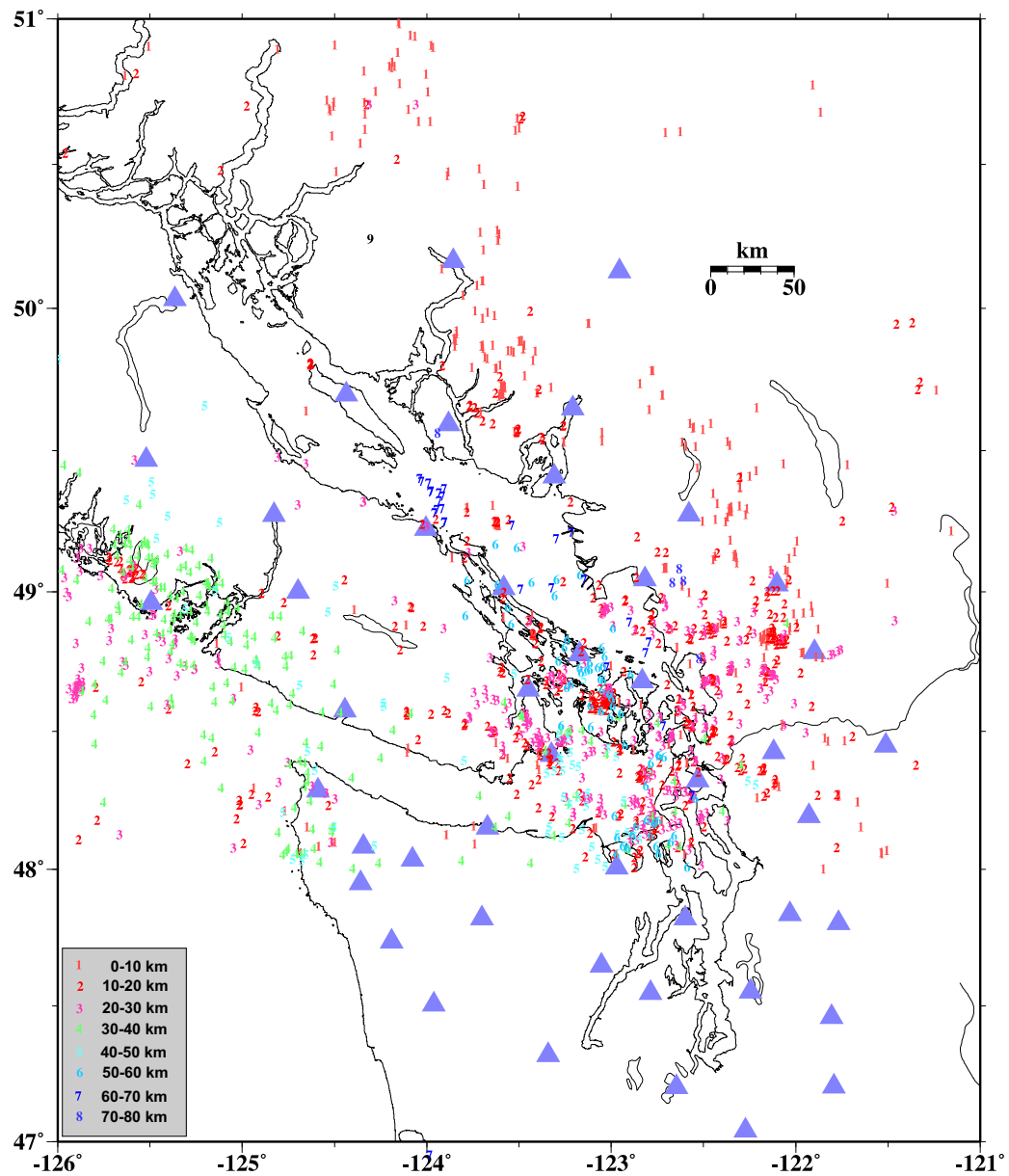


Figure 3.12 Location of earthquakes used in the tomographic inversion. Triangles indicate recording stations.

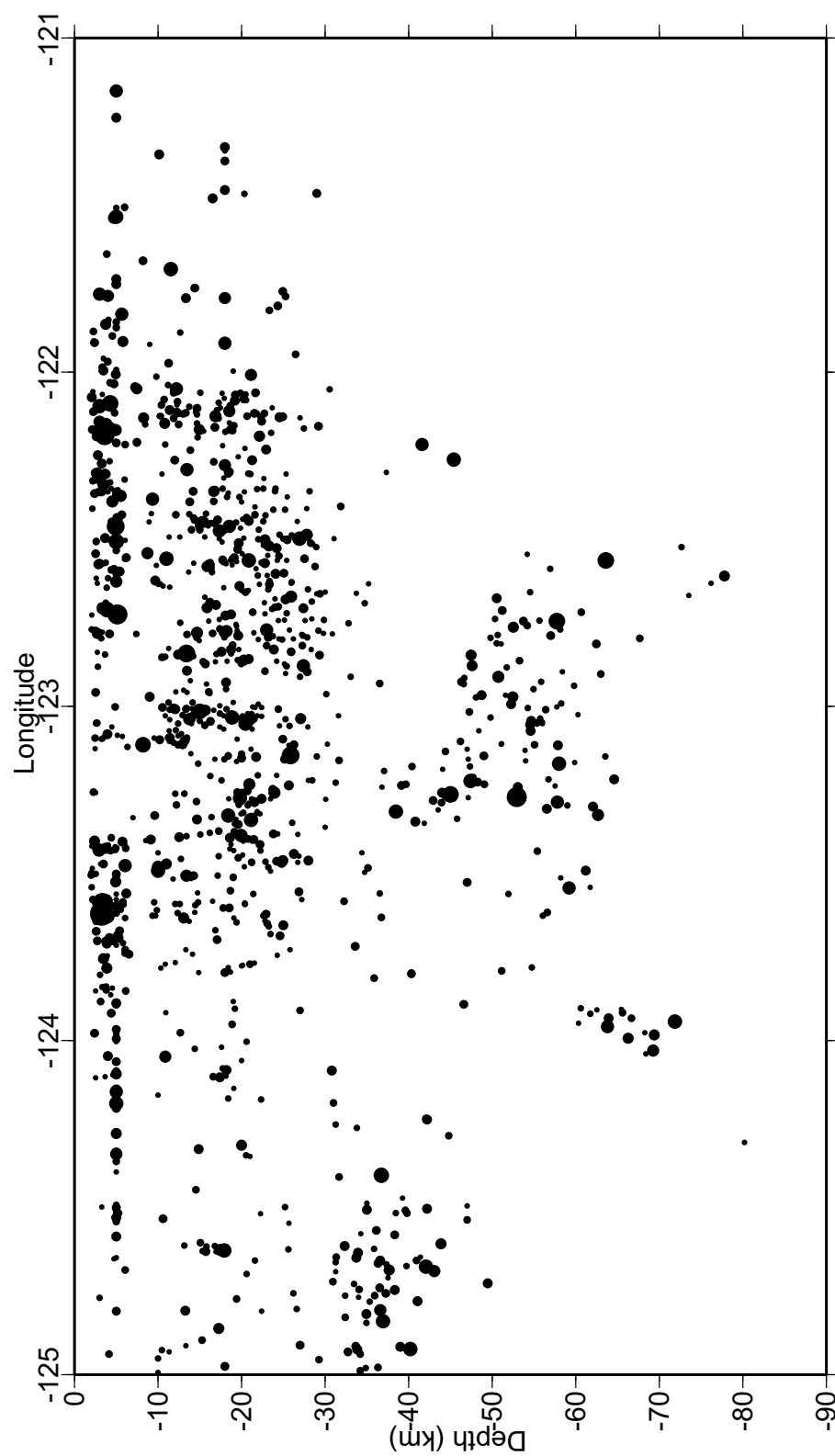


Figure 3.13 The earthquake locations projected on a vertical plane in the east west direction at latitude $48^{\circ}30'$.

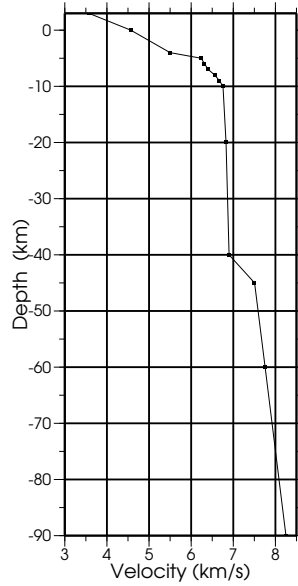


Figure 3.14 1-D starting velocity model.

(R_h) and vertical roughness (R_v) in the velocity models obtained at different stages of the inversion. The variation in vertical roughness (R_v) in the current inversion is observed to increase and this is possibly due to the 3 km cell size. A cell size of 1 km was used in the inversion of SHIPS data in Chapter 2. In coarser grids fitting data requires some additional roughness than in finer grids. At the start of inversion, for a large value of λ , the smoothness factor is dominant. However as λ value is decreased as the inversion progresses roughness is introduced such that the data can be fit according to the uncertainties. The increase in perturbation is small at the final stages of the inversion which indicates that the velocity model itself is not perturbed much. However the change in the values of horizontal and vertical roughness at the final stages of the inversion indicate that changes are made in structure of the velocity model that is necessary to fit the data.

The starting velocity model is shown in Fig. 3.20 in terms of constant depth slices from 1 to 69 km, at 3 km depth intervals. The total perturbation applied to the starting velocity model to obtain the final model is shown in Fig. 3.21 with model

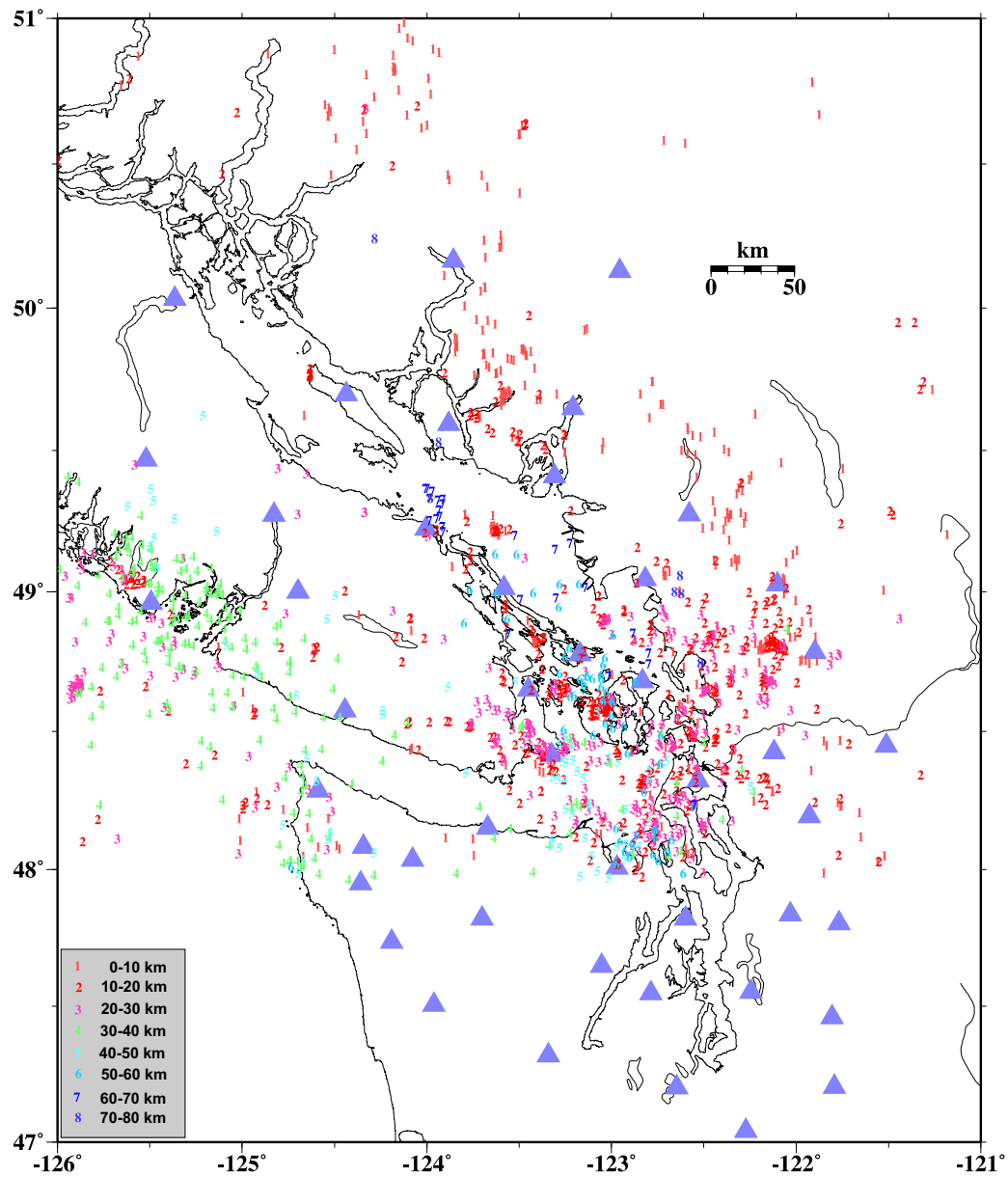


Figure 3.15 Relocated location of earthquakes used in the tomographic inversion. Triangles indicate recording stations.

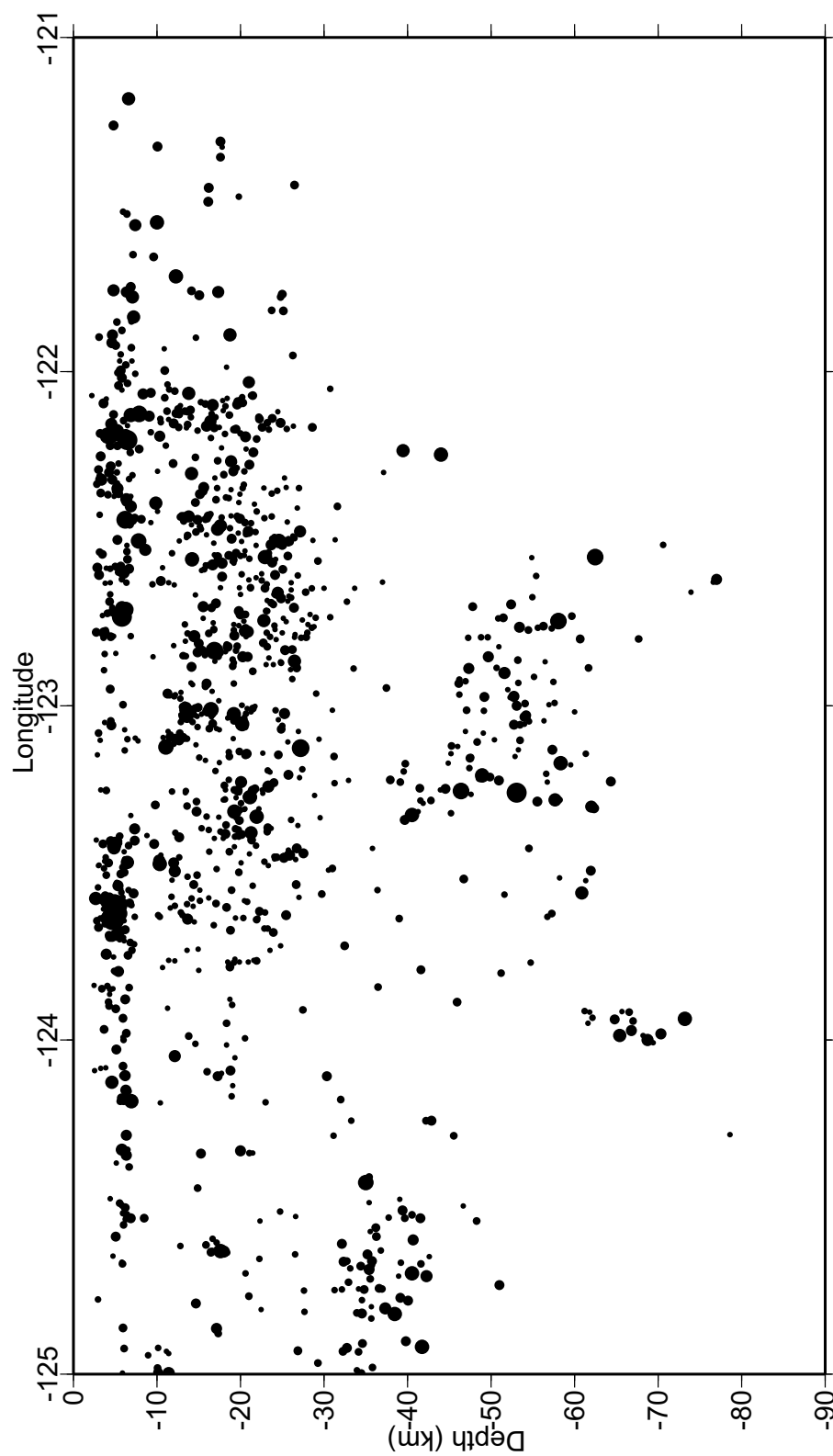


Figure 3.16 Relocated earthquake locations projected on a vertical plane in the east west direction at latitude $48^{\circ}30'$.

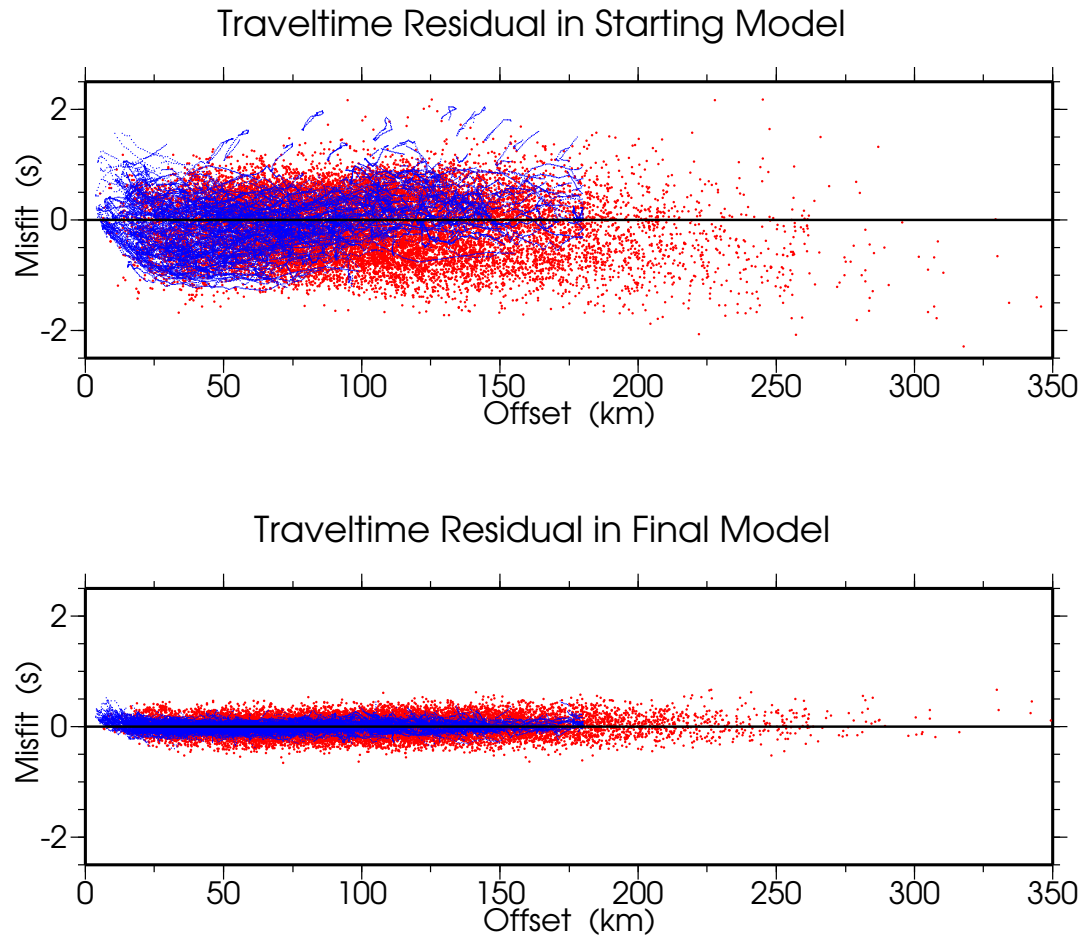


Figure 3.17 Travel-time misfit in starting model (above), and final model (below). The blue dots correspond to the SHIPS events and the red dots correspond to earthquake events.

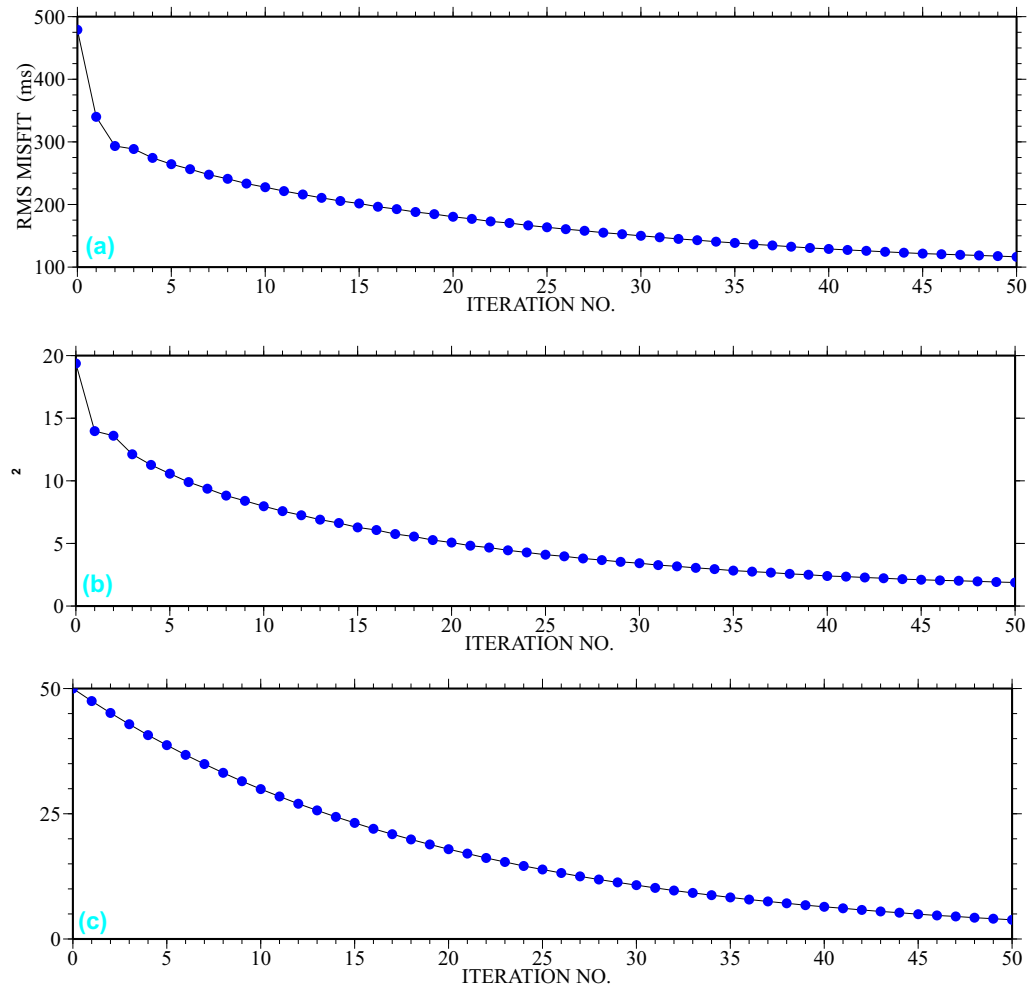


Figure 3.18 Convergence plot of (a) RMS travel-time misfit, (b) normalised χ^2 , and (c) λ .

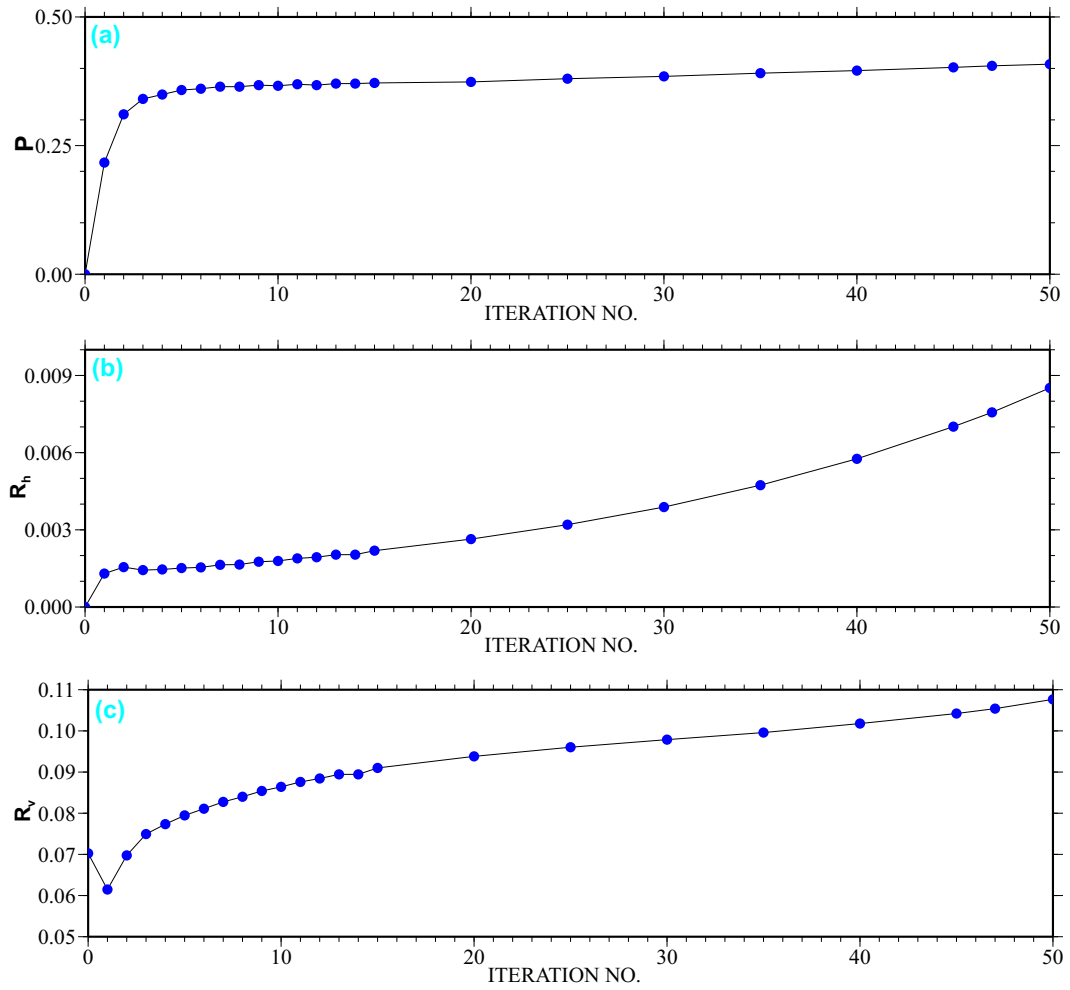


Figure 3.19 Variation in (a) perturbation P , (b) horizontal roughness R_h , and (c) vertical roughness R_v .

parameters plotted only for cells sampled by rays. Strong velocity perturbations are observed at shallow depths in the region of the high velocity Crescent Terrane and in the SJF and SG. This portion of the model is well constrained by the data from the SHIPS experiment. In the final velocity model, shown in Fig. 3.22, the high velocity Crescent Terrane in southern Vancouver Island, the basinal structures in the SJF and SG, the subducting oceanic crust, and the continental and oceanic mantle are clearly mapped. These features are interpreted in detail in Chapter 5.

3.5 Ray Coverage and Checkerboard tests

The ray coverage of the combined tomographic inversion is shown in Fig. 3.23. Reasonable ray coverage is observed in the shallow part of the velocity model. The ray coverage constrained approximately 1.0×10^5 model parameters out of a possible 5.8×10^5 . The maximum ray coverage is observed beneath southern Vancouver Island down to a depth of approximately 21 km. This portion of the model is well constrained by the SHIPS experiment data. The resolution is observed to vary from shallower to deeper parts of the model as the ray density varies at different depth levels. To access the ability of the data to resolve model features of a given size at different depth levels, checkerboard tests were carried out with three different grid sizes of 30, 40 and 50 km. Semblance plots between the input and output checkerboard anomaly patterns were computed for these three grid sizes.

The checkerboard input anomaly pattern, recovered anomaly pattern and semblance values for a grid size of 30 km are shown as depth slices at 6 km intervals in Figs. 3.24, 3.25 and 3.26, respectively. The semblance values indicate lateral resolution for features of 30 km size down to 21 km depth. The semblance values are low in the deeper part of the model. This is due to the fact that the amount of rays passing through the checkerboard blocks at deeper levels are not sufficient to resolve

the input structure. The checkerboard input anomaly pattern, recovered anomaly pattern and semblance values for a grid size of 40 km are shown in Figs. 3.27, 3.28 and 3.29, respectively. The semblance values indicate reasonable lateral resolution for features of 40 km size down to 33 km depth. The checkerboard input anomaly pattern, recovered anomaly pattern and semblance values for a grid size of 50 km are shown in Figs. 3.27, 3.28 and 3.29, respectively. Semblance values indicate adequate lateral resolution for features of 50 km size is inferred at all depth levels.

3.6 Summary

A method for nonlinear 3-D earthquake tomography problem for joint estimation of hypocentral parameters and velocity structure was developed in this chapter. The method was implemented by modifying the controlled source algorithm of Zelt and Barton (1998). The method was successfully tested on a synthetic earthquake data set. Earthquake data and SHIPS experiment data from southwestern British Columbia and northwestern Washington were simultaneously inverted for joint estimation of hypocentral parameters and velocity structure. The RMS travel-time misfit was reduced from 479 ms for the starting model to 120 ms for the final model after 46 iterations, with corresponding reduction in normalised χ^2 values from 19 to 2. Checkerboard tests conducted on the final velocity model imply reasonable lateral resolution at spatial scales of 30 km and above.

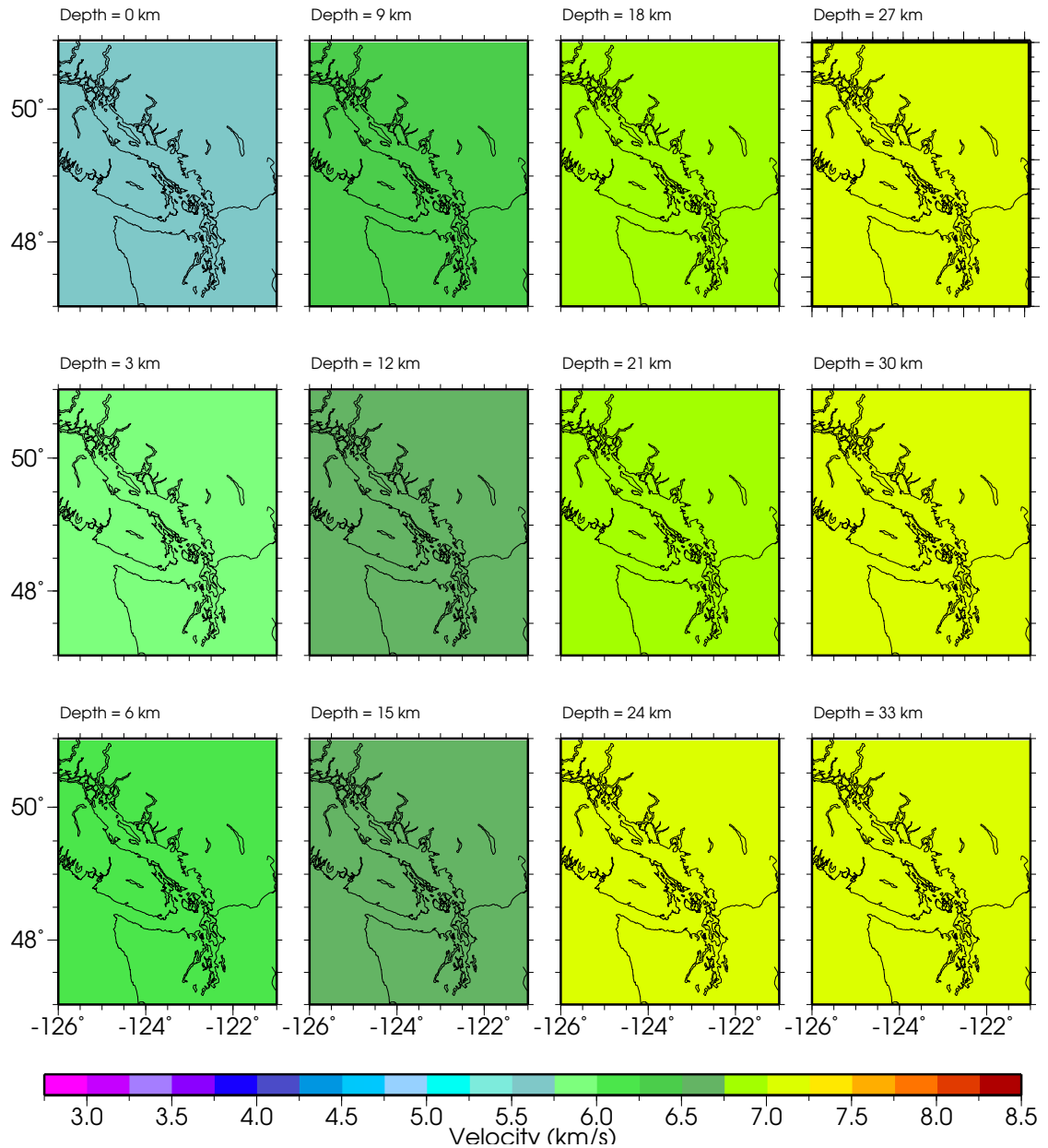


Figure 3.20 Depth slices of starting velocity model (continued on next page).

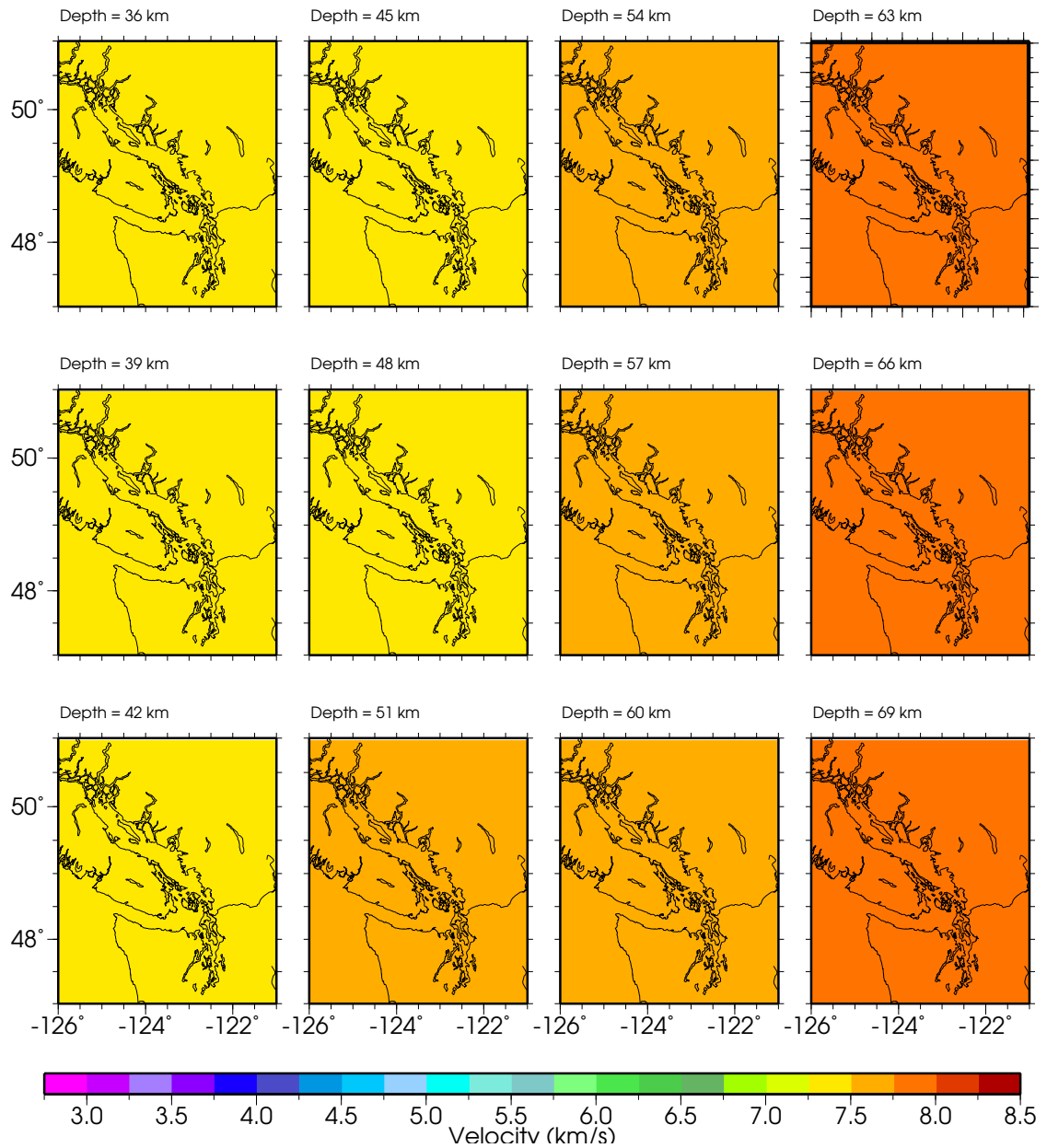


Figure 3.20 continued.

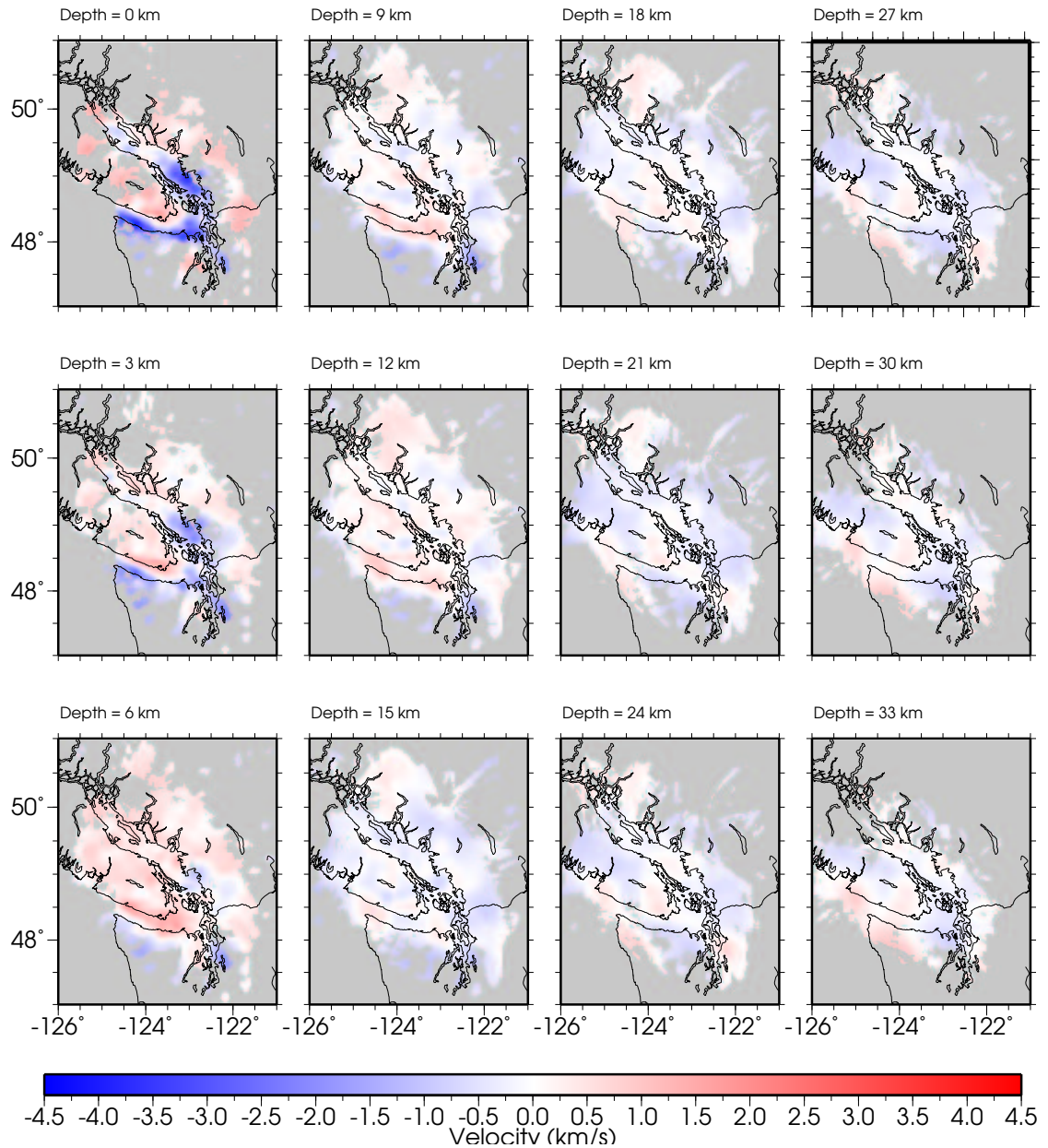


Figure 3.21 Depth slices of perturbation velocity model (continued on next page).

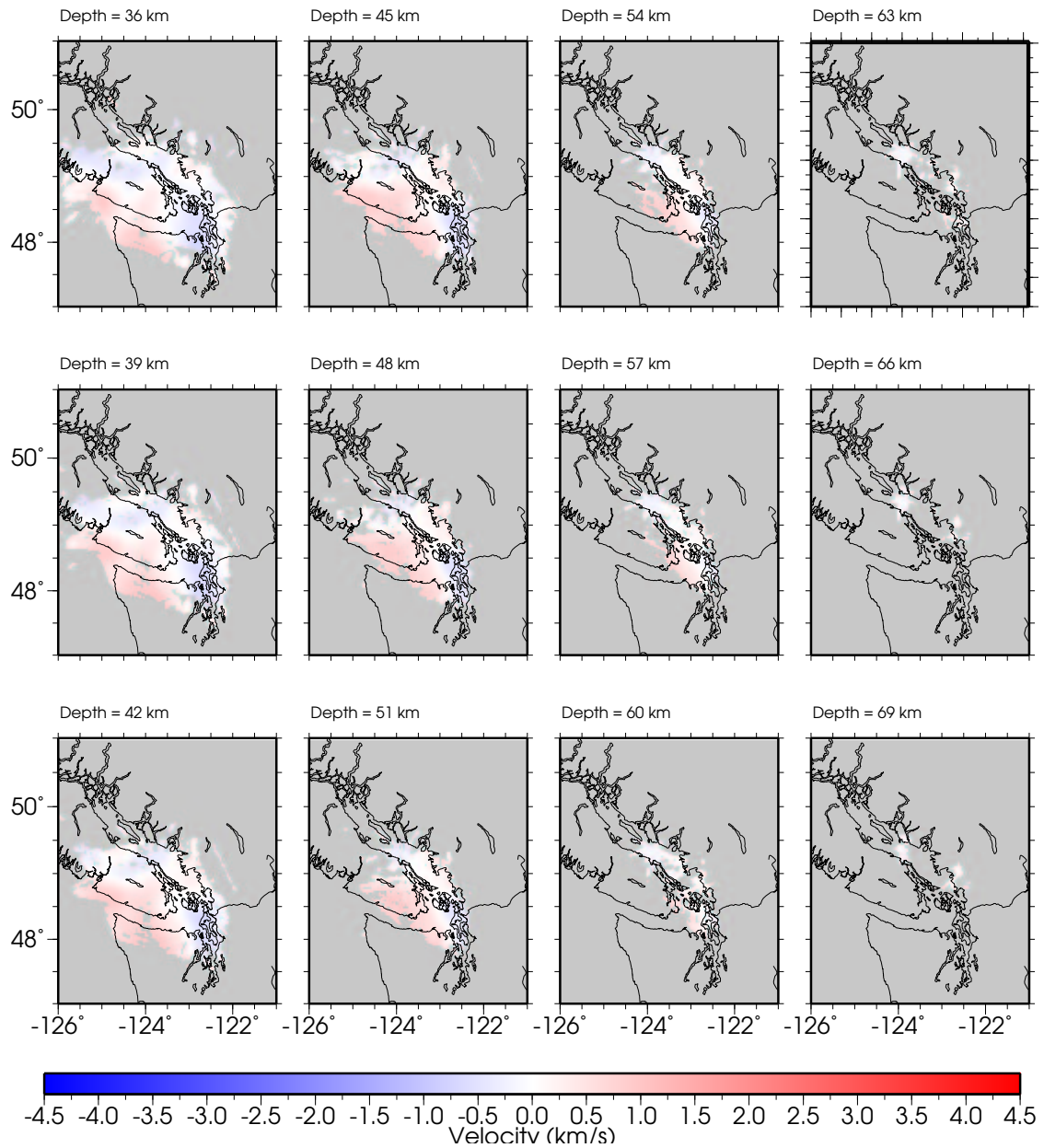


Figure 3.21 continued.

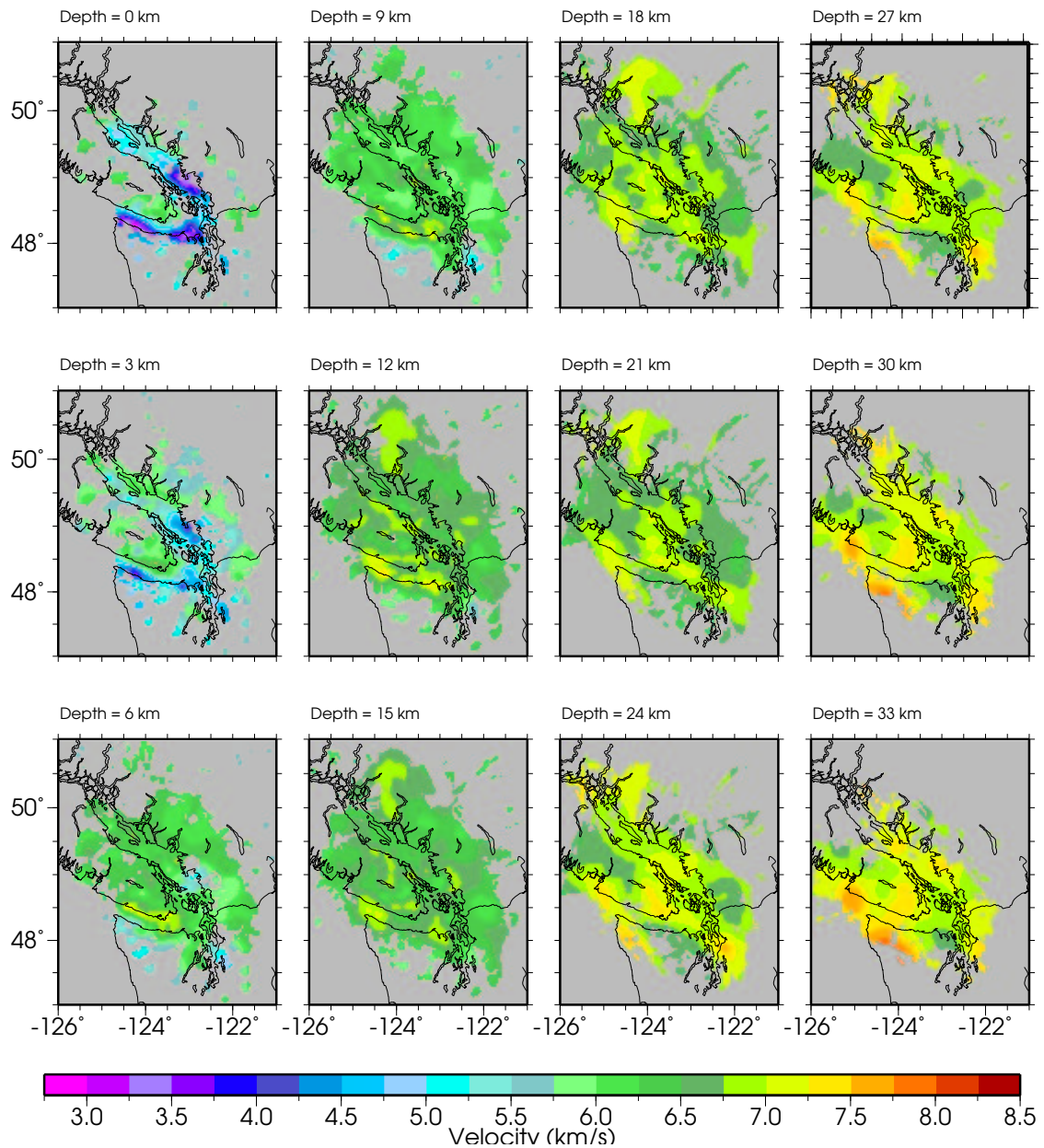


Figure 3.22 Depth slices of the final velocity model (continued on next page).

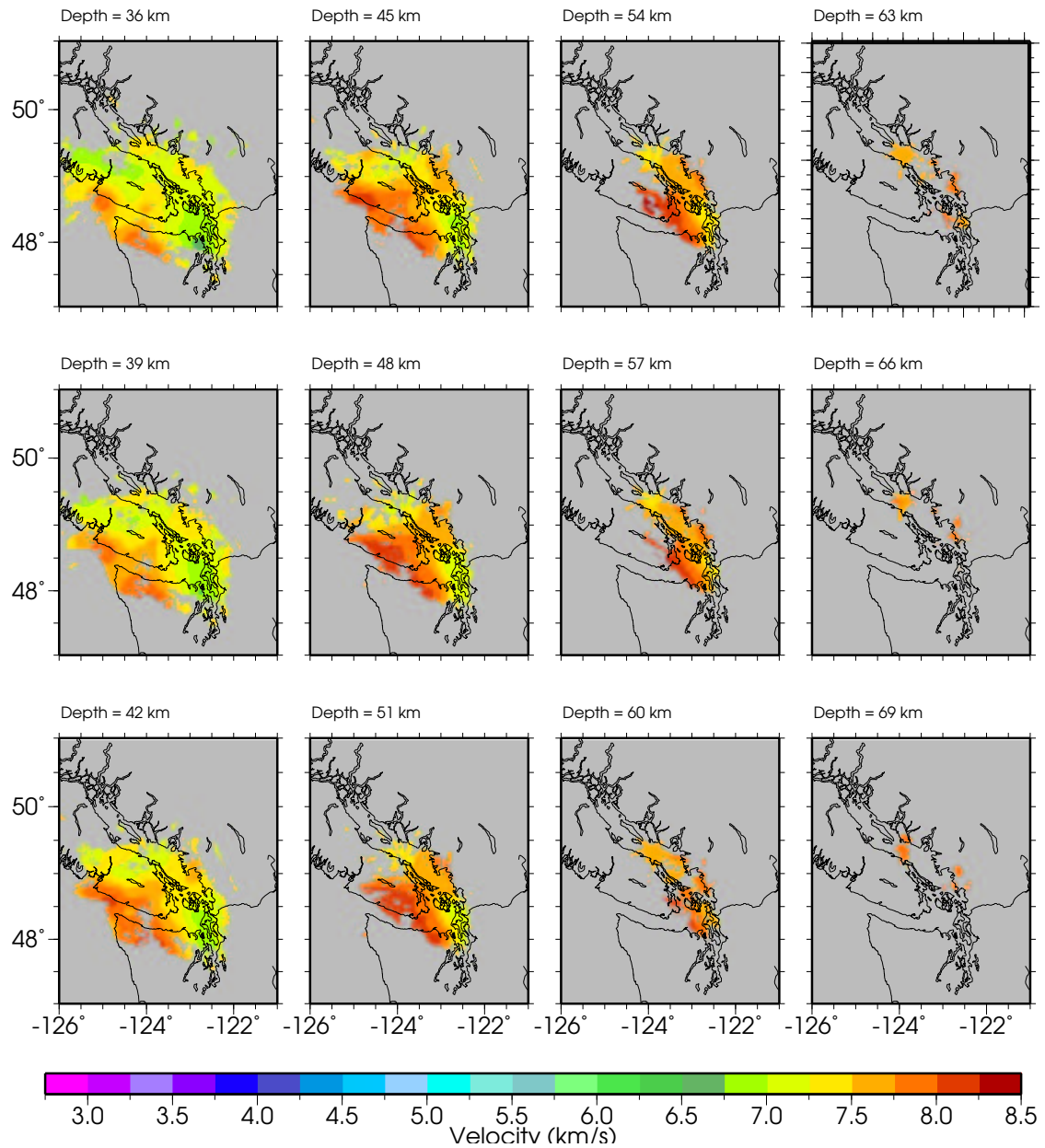


Figure 3.22 continued.

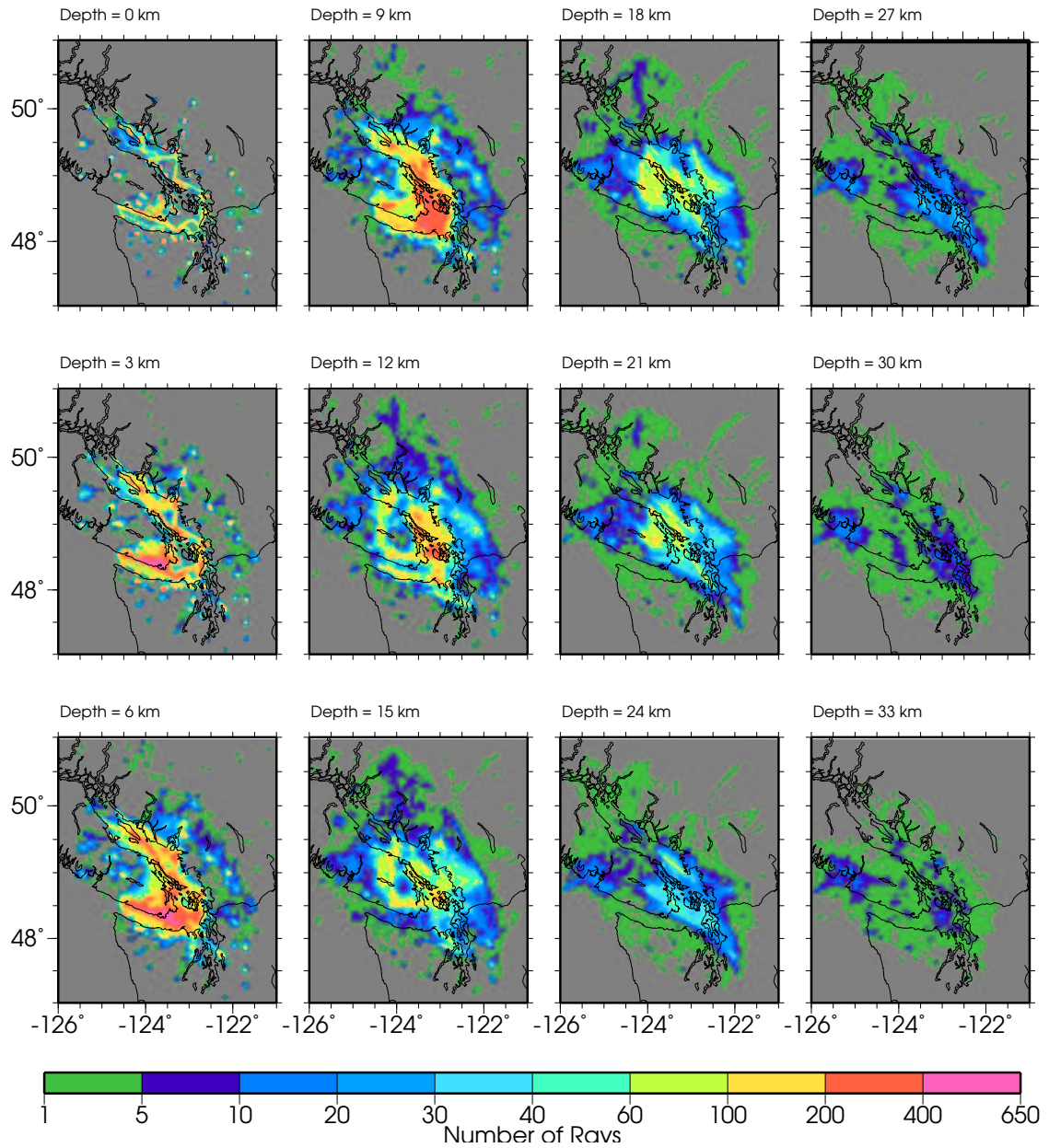


Figure 3.23 Depth slices of the ray coverage in the final velocity model (continued on next page).

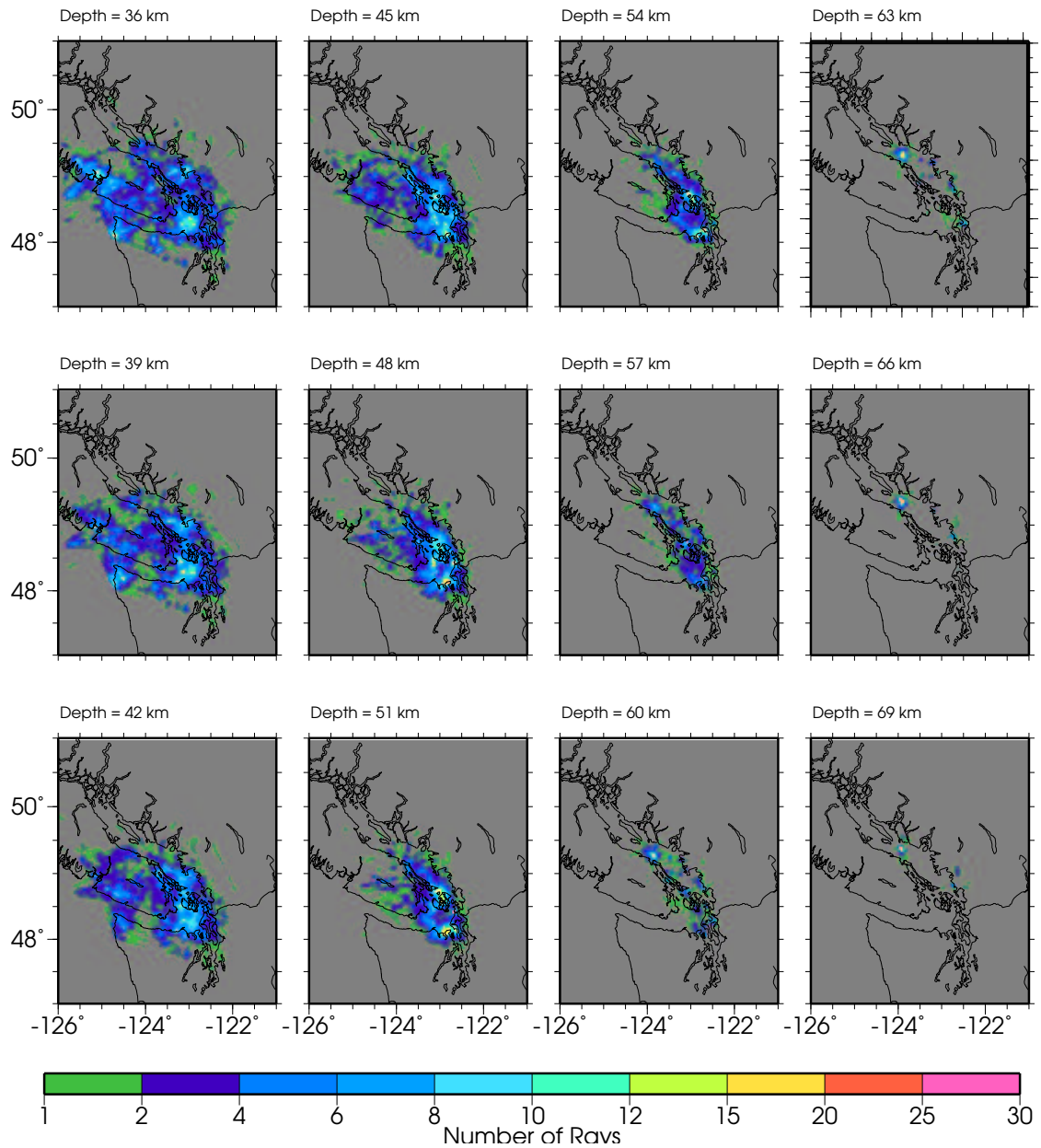


Figure 3.23 continued.

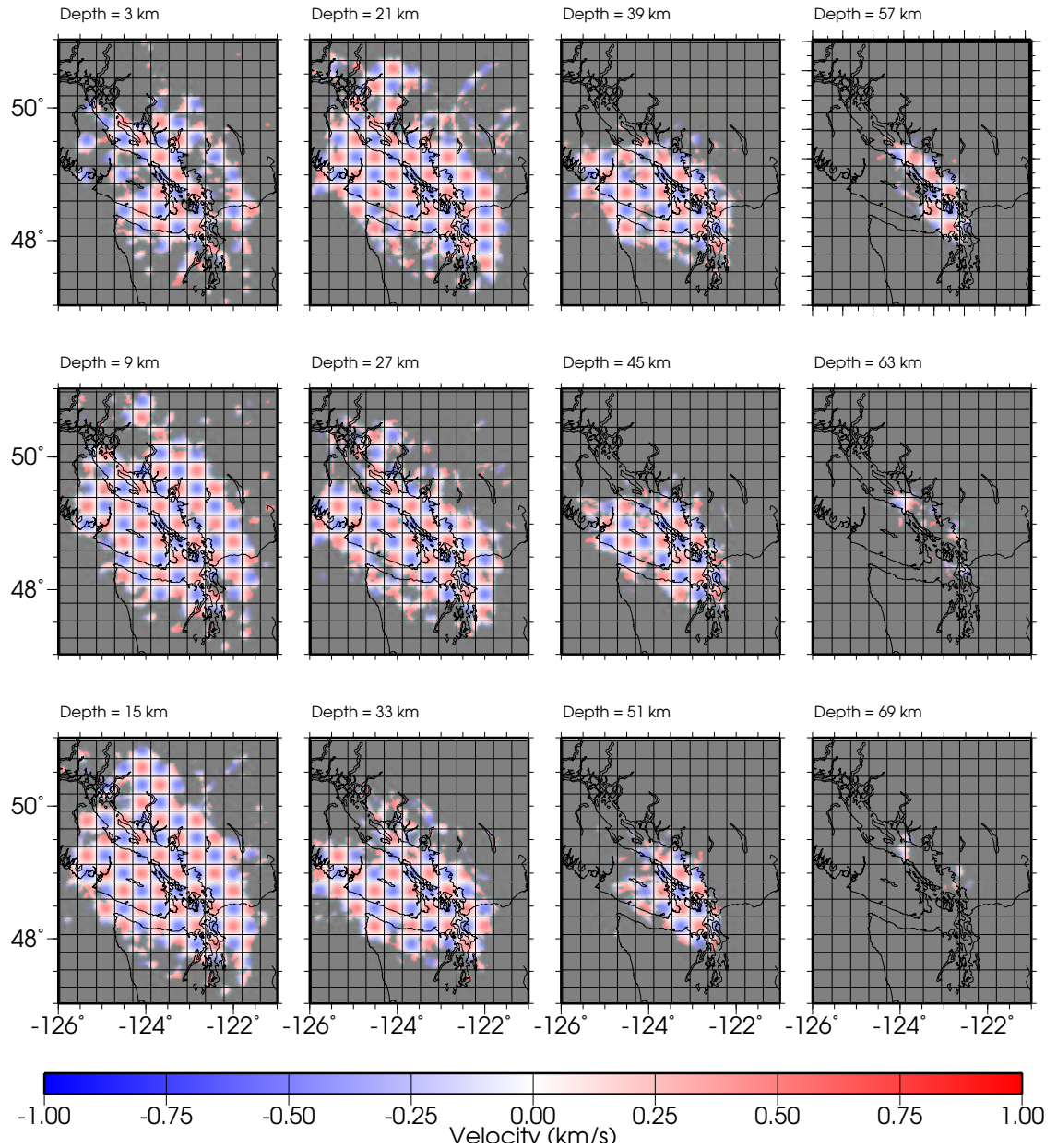


Figure 3.24 Depth slices of checkerboard test input anomaly pattern for 30 km grid size.

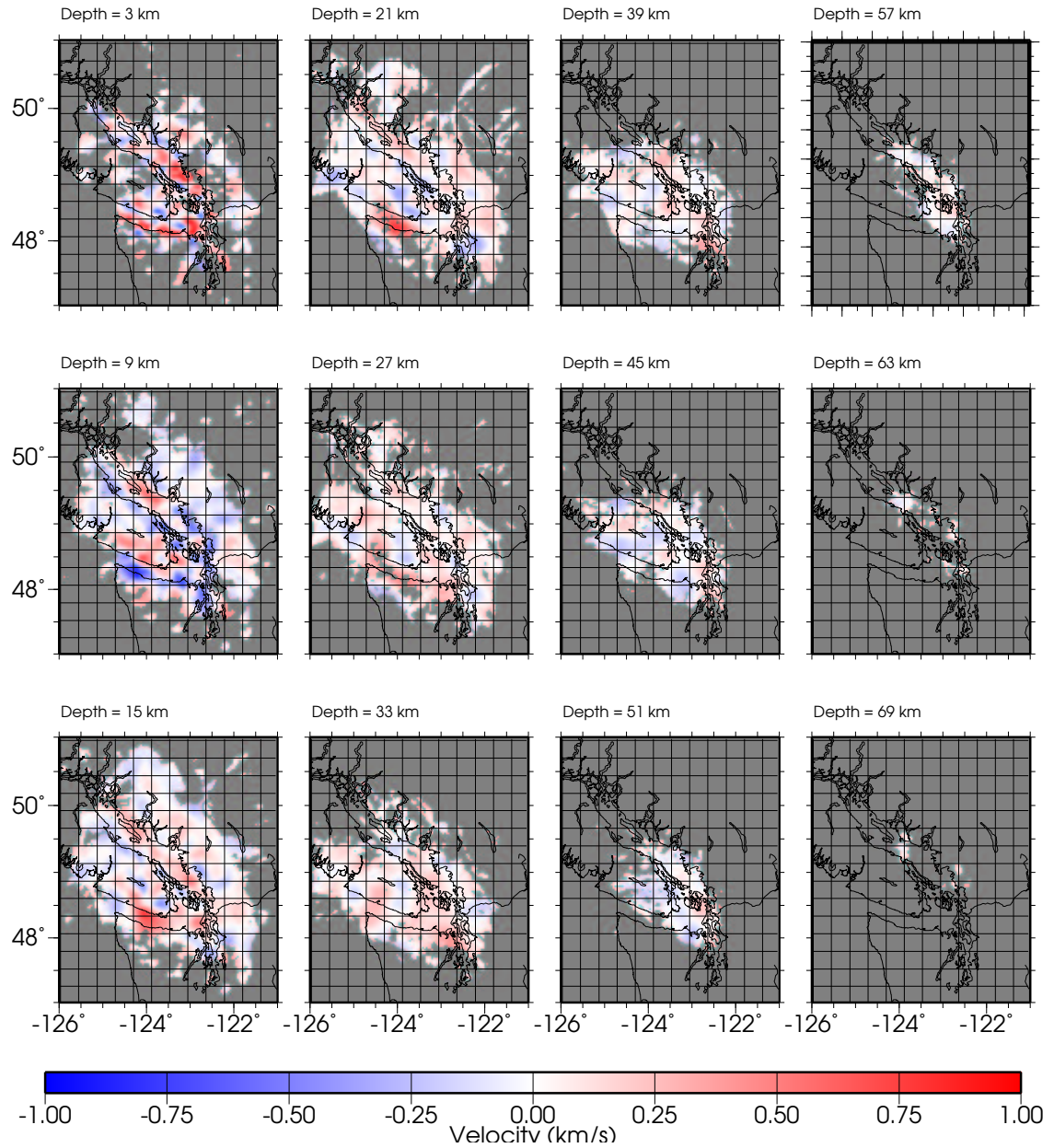


Figure 3.25 Depth slices of checkerboard test recovered anomaly pattern for 30 km grid size.

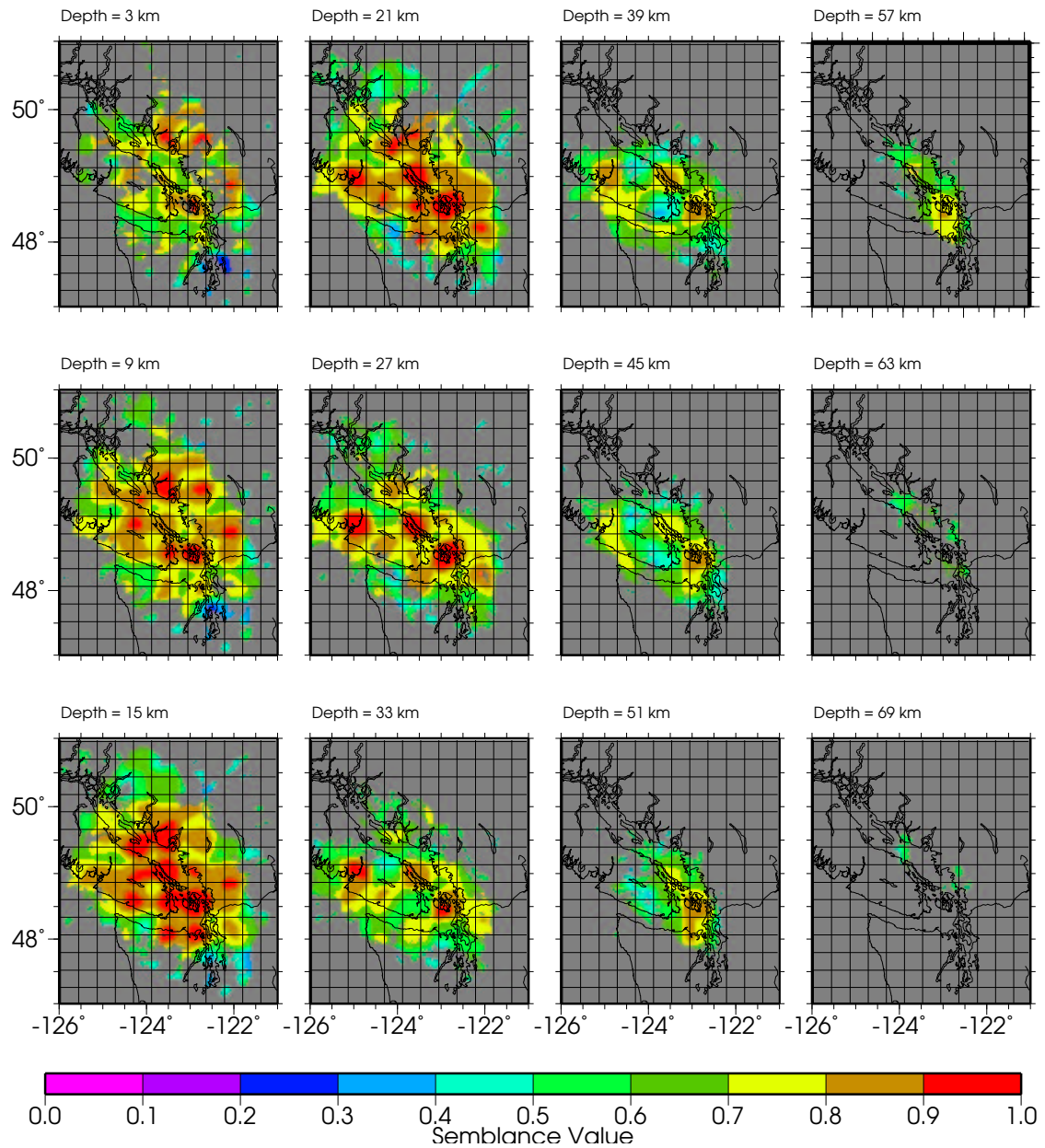


Figure 3.26 Depth slices of semblance values for 30 km grid size.

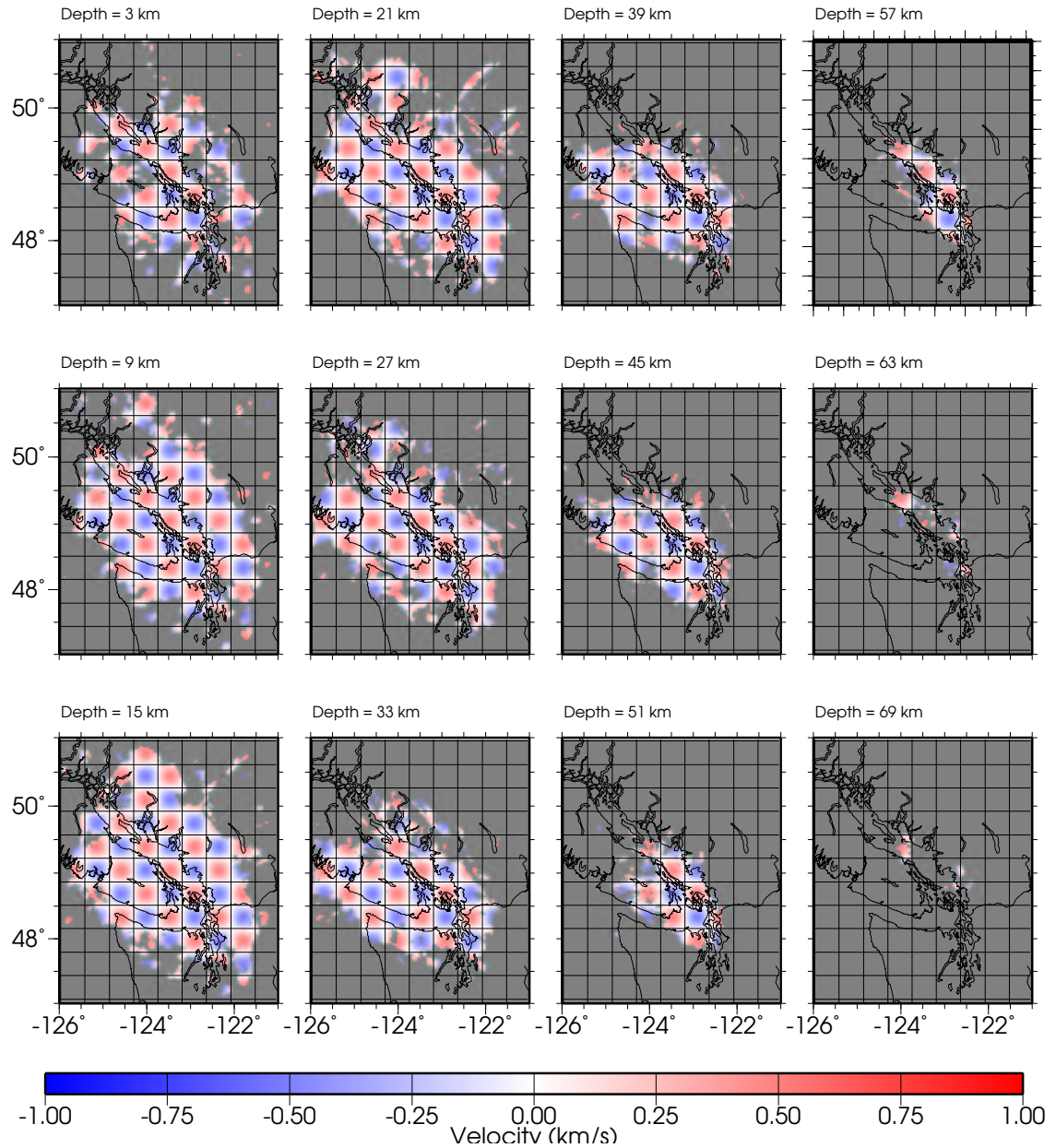


Figure 3.27 Depth slices of checkerboard test input anomaly pattern for 40 km grid size.

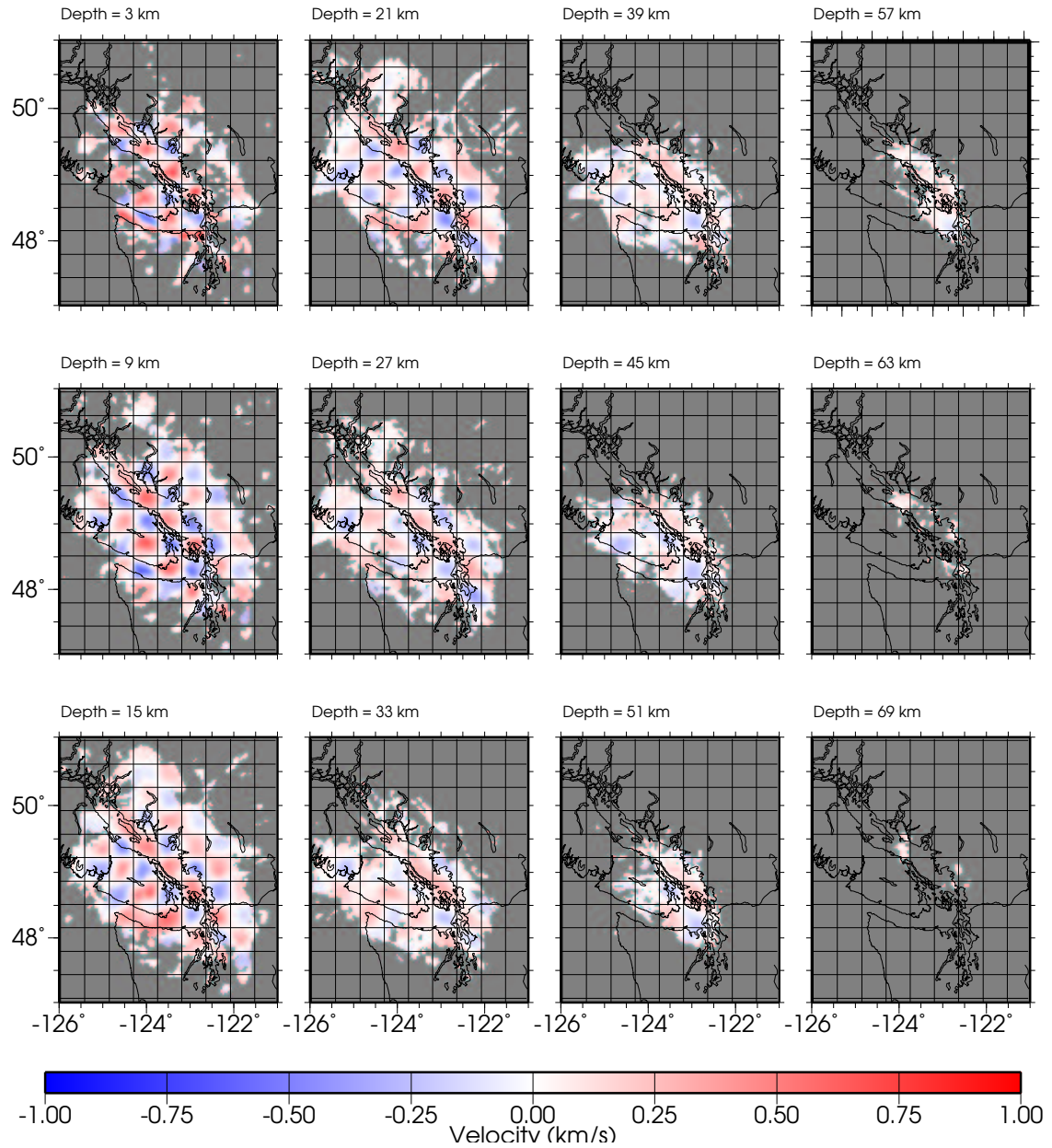


Figure 3.28 Depth slices of checkerboard test recovered anomaly pattern for 40 km grid size.

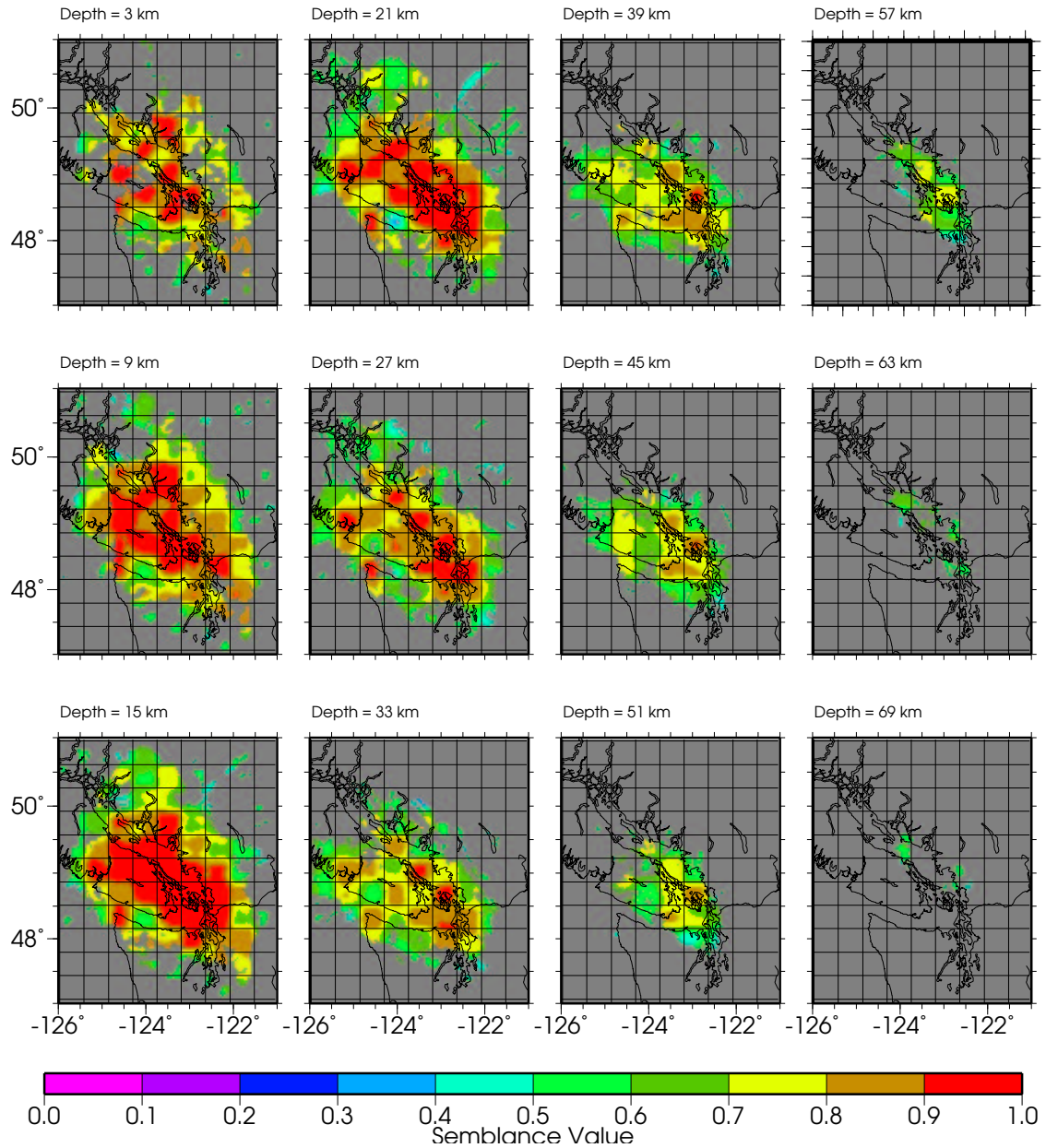


Figure 3.29 Depth slices of semblance values for 40 km grid size.

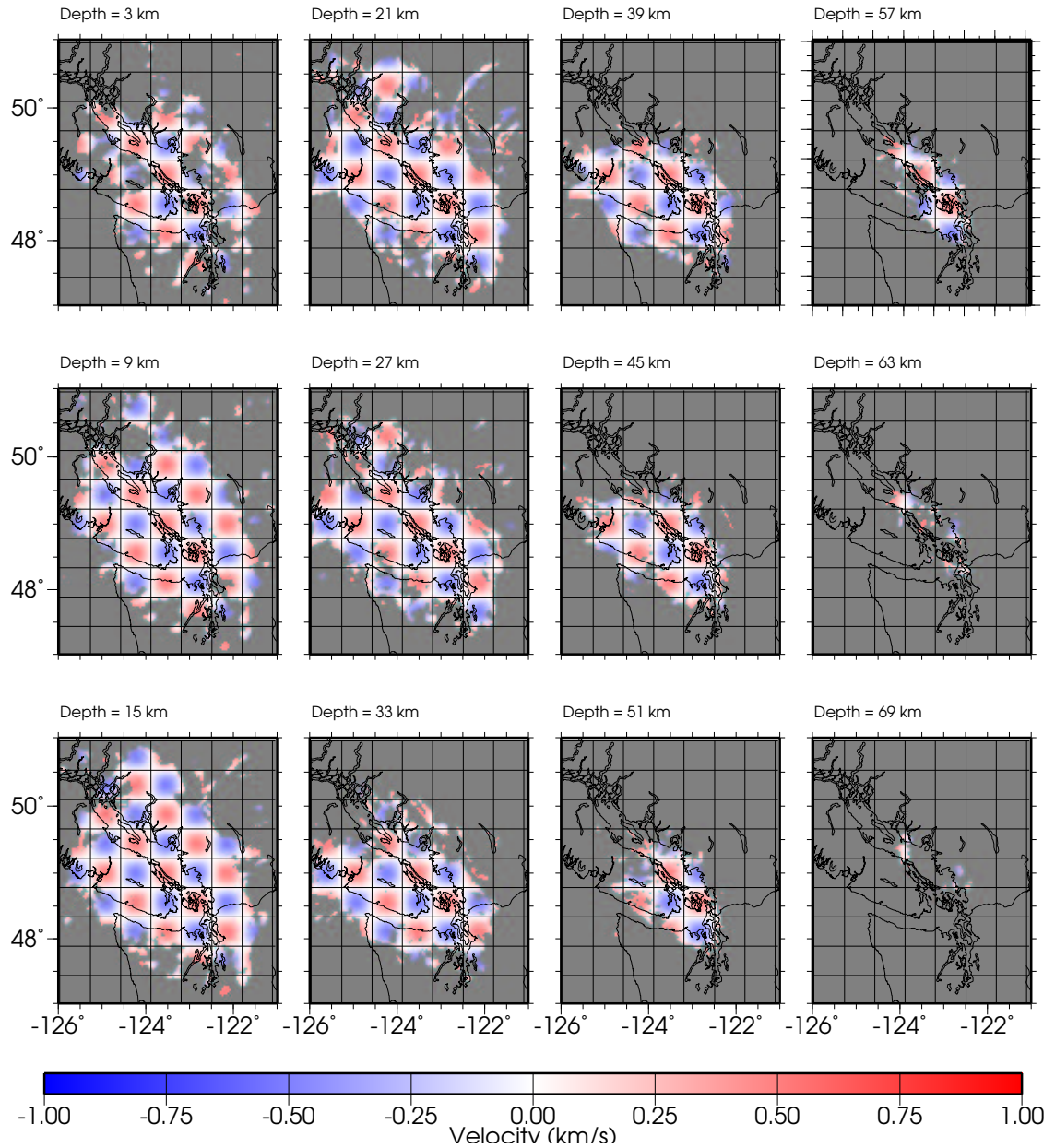


Figure 3.30 Depth slices of checkerboard test input anomaly pattern for 50 km grid size.

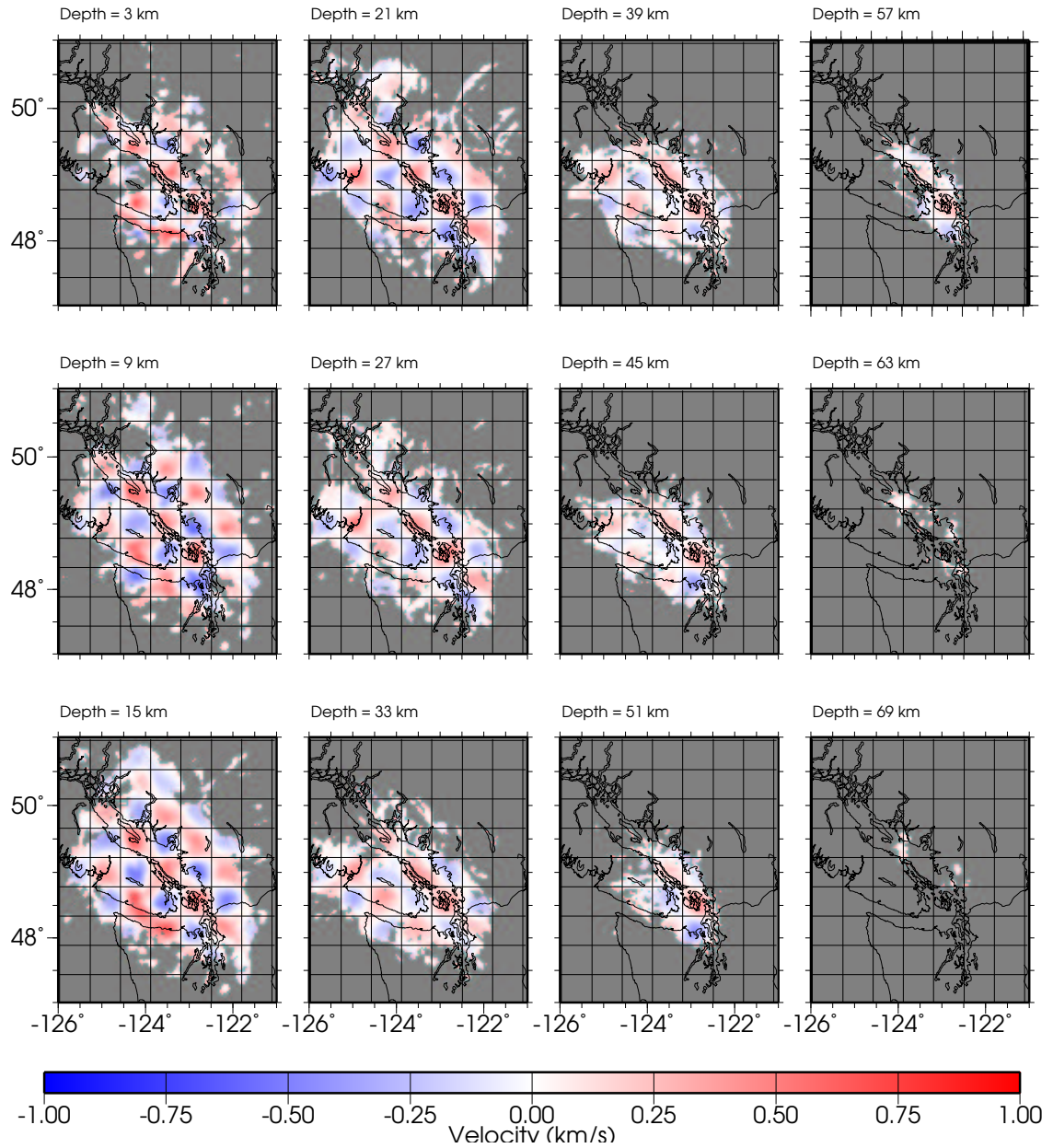


Figure 3.31 Depth slices of checkerboard test recovered anomaly pattern for 50 km grid size.

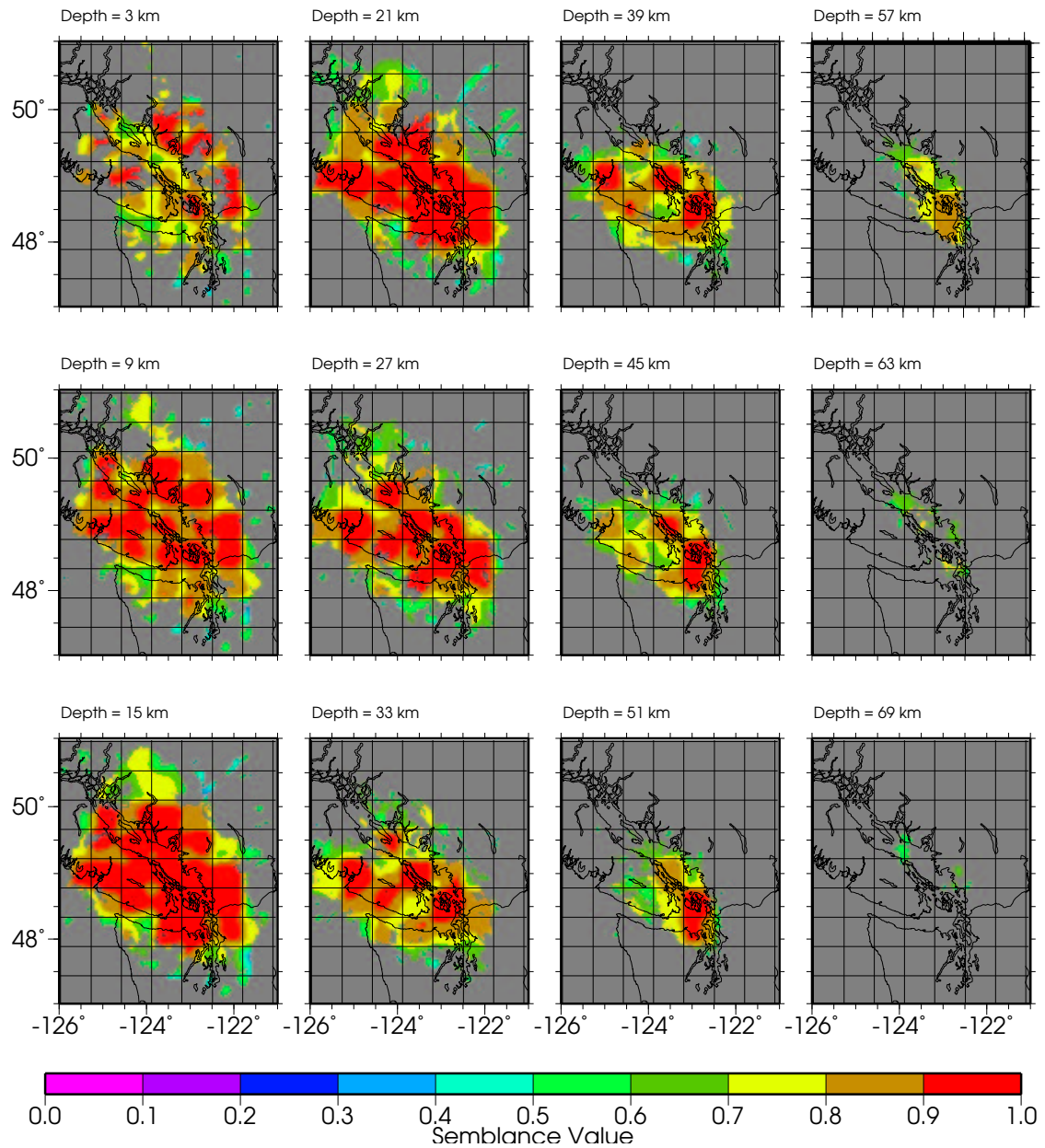


Figure 3.32 Depth slices of semblance values for 50 km grid size.

Chapter 4

Interpretation of Upper Crustal Structure

4.1 Introduction

In this chapter, the velocity model constructed from the tomographic inversion of first arrival travel-times from the SHIPS experiment, discussed in Chapter 2, is interpreted for upper crustal structure. Features observed in the velocity model are evaluated for meaningful correlation with known geologic units and fault locations. Horizontal depth slices are analysed for lateral continuity of the observed features. Five vertical profile sections extracted along major structural trends in the study area are interpreted by correlating velocity contrasts to structural contacts of the geologic units. The structural disposition and subsurface extension of the Crescent Terrane in the upper crust is mapped in the horizontal and vertical slices. Structural contacts are evaluated to identify seismogenic zones in the upper crust by correlating with earthquake occurrence along the profile sections. The contact between Wrangellia and the Coast Plutonic Complex is mapped on a NE-SW vertical cross section. The structural outlines of the Georgia basin, Clallum basin, and the Port Townsend basin with their maximum sediment thickness are mapped from isovelocity surface maps corresponding to 5.5 and 6.0 km/s. The isovelocity maps are correlated with gravity data for additional confirmation of the mapped sedimentary features. Recent earthquake activity over the past five years, well located in the upper 12 km of crust, is correlated with the observed features in the isovelocity maps. Structural contacts with associated seismic activity are mapped and discussed for tectonic significance.

4.2 Previous SHIPS 3-D Tomography Studies

Zelt *et al.* (2001) constructed a 3-D tomographic velocity model along the Strait of Georgia through tomographic inversion of SHIPS first arrival travel-times. This study was focussed in particular towards delineating the structure of the Georgia basin. A maximum sediment thickness of 8–9 km was observed in the southeastern Strait of Georgia. Towards the northeastern part of the strait the thickness of the sediment cover was 2–4 km. The sediment velocities observed in the northeastern part of Georgia basin were 4.5–6.0 km/s (Upper Cretaceous Nanaimo Group). In the southeastern Strait of Georgia, the sediment velocities ranged from 3.0–6.0 km/s. The reason for the lower velocities is explained by the additional presence of Tertiary and more recent sediments. Zelt *et al.* (2001) observed low velocities at shallow depths in the Karmutsen formation in the vicinity of Texada Island and suggested that these low velocities were due to weathering and fracturing.

South of the Georgia basin, Brocher *et al.* (2001) constructed a 3-D tomographic velocity model from SHIPS first arrival travel-times for the Puget Lowland down to a depth of 11 km. Their velocity model constrained the upper crustal structure and delineated four large, west to northwest trending low velocity basins (Tacoma, Seattle, Everett, and Port Townsend), separated by high velocity ridges. The tomographic model was used to refine the previously proposed fault zones as well as to identify structures that warranted additional study. They mapped a basinal structure in their velocity model bounded by the convergence of Darrington-Devils Mountain fault, southern Whidbey Island fault and Leech River fault and informally referred to it as the Port Townsend basin.

van Wagoner *et al.* (2001) constructed a 3-D velocity model from SHIPS first arrivals and earthquake data for the crust beneath the Puget Lowland. Their velocity model imaged the Sequim basin to the southwest of the Port Townsend basin. They identified high velocity regions (7.0–7.5 km/s) as Crescent Terrane and estimate the

thickness to be 20 km or more over much of their model area. They attributed the higher velocities to gabbro emplaced as part of the Crescent Terrane.

Trehu *et al.* (2001) constructed a tomographic velocity model for the upper crust in the region of the Strait of Juan de Fuca by inverting SHIPS first arrival travel-times. They identified a 5–7 km deep linear, northwest-trending basin beneath the southwestern shore of the Straits of Juan de Fuca.

4.3 Analysis of 3-D Velocity Model

The 3-D velocity model constructed from the SHIPS data in the present study covers the Strait of Juan de Fuca, southern Vancouver Island, the Strait of Georgia and a small segment in the northern Puget Sound region (Fig. 1.3). This velocity model creates a link between the models of Zelt *et al.* (2001) in the Strait of Georgia area and Brocher *et al.* (2001) in the Puget Sound area. Where ray paths are present, the velocity model is well constrained down to 12 km depth. However, below 7 km depth the number of velocity nodes with ray coverage decreases considerably. The velocity model is analysed primarily in terms of the spatial variation of the velocity structure rather than absolute velocity values. Nevertheless, geologic units are also interpreted on the basis of their gross velocity structure.

To make a generalised interpretation, previous studies provide a guide for the P wave velocities expected for the different geologic units. Zelt *et al.* (2001) considered velocities of 4.5–6.0 km/s to represent the Upper Cretaceous Nanaimo Group sediments in Strait of Georgia. In the southern Strait of Georgia velocities are lower due to the additional presence of Tertiary and more recent sediments, including glacial and modern Fraser River deposits. In general, velocities up to 5.5 km/s are considered to represent sedimentary rocks. Deep Cretaceous sediments of the Nanaimo basin are expected to have a higher velocity of up to 6.0 km/s due to consolidation.

The average P velocity values given by Christensen and Mooney (1995) for the suite of rocks found in the study area at depths less than 10 km are as follows: granite-granodiorite - 6.2 km/s; granite-gneiss - 6.1 km/s; slate - 6.1 km/s; basalt - 5.9 km/s; diabase - 6.7 km/s; gabbro - 7.1 km/s. Seismic velocities in deeper Wrangellia rocks vary from 6.4 to 6.75 km/s (McMechan and Spence 1983; Spence *et al.* 1985; Zelt *et al.* 2001). However, in the near subsurface, down to about 2 km depth, lower velocities from 5.5 to 6.0 km/s are expected in Wrangellia, due to weathering and fracturing (Zelt *et al.* 2001). The Pacific Rim Terrane, composed of sedimentary, metamorphic and volcanic rocks, has an expected velocity range of 6.0 to 6.2 km/s. Crescent Terrane rocks have measured P velocity ranging from 5.8 to 6.9 km/s in core samples from the Olympic Peninsula (Williams *et al.* 2000). van Wagoner *et al.* (2001) analysed borehole and laboratory measurement data for P wave velocities in Crescent Formation. They concluded that the expected range of velocity was 4.5–5.5 km/s for depths less than 5 km and 5.5–6.5 km/s at greater depth.

4.4 Analysis of Horizontal Velocity Slices

In this section, the horizontal velocity slices at 2 km intervals and at depths from 1 to 11 km are analysed for lateral continuity of geologic units and basin structure, and for correlation with known surface mapped fault boundaries.

4.4.1 Horizontal Velocity Slice at 1 km Depth

At the western end of the Strait of Juan de Fuca, low velocity sediments are mapped over the Clallum basin at 1 km depth (Fig. 4.1). Low velocity sediments were also found in a basin at the eastern end of Juan de Fuca. This basin was previously identified in the velocity model of Brocher *et al.* (2001) who informally referred to it as Port Townsend Basin. In the southeastern portion of the Strait of Georgia, low

sediment velocities are mapped in the Nanaimo subbasin. At the northwestern end of the Strait of Georgia, close to Texada Island, sediment velocities are mapped in the Comox subbasin. The velocities in the northwestern part of the Strait of Georgia are in general higher than those observed in the southeast. Due to limited ray coverage in the shallow part of the velocity model, only a small area is mapped in southern Vancouver Island. South of the Leech River fault, Crescent Terrane (Metchosin Igneous Complex) is mapped with relatively higher velocities. The reasonable correlation of mapped velocities to the known geologic units gives confidence that the velocity model has recovered reliable subsurface information through tomographic inversion.

4.4.2 Horizontal Velocity Slice at 3 km Depth

In the 3 km depth slice, towards the western end of the Strait of Juan de Fuca, the Clallum basin trends clearly in a WNW-ESE direction, with velocities of 4.5 km/s and less indicating sediments to a depth of at least 3 km (Fig. 4.2). The sediments are underlain by the Crescent Terrane, which is prominently mapped in southern Vancouver Island with higher velocities of 7 km/s at shallow depth. In southern Vancouver Island, the high velocity Crescent Terrane has a northeasterly dip and is in contact with the relatively low velocity Pacific Rim Terrane. The low velocity Pacific Rim Terrane at this depth is clearly mapped between the Survey Mountain fault and the Leech River fault. Northeast of the Survey Mountain fault, a higher velocity zone is mapped which correlates with Wrangellia rocks. The Port Townsend basin is mapped by low velocities at the eastern edge of the Strait of Juan de Fuca, with the Southern Whidbey Island fault as the eastern boundary. The extension of the Leech River fault towards the south demarcates the western boundary of the Port Townsend basin. Between the Southern Whidbey Island fault and the Darrington-Devils Mountain fault, the observed velocities are relatively higher (5.5–6.0 km/s) than those associated with basin sediments. Northwest of San Juan Islands within

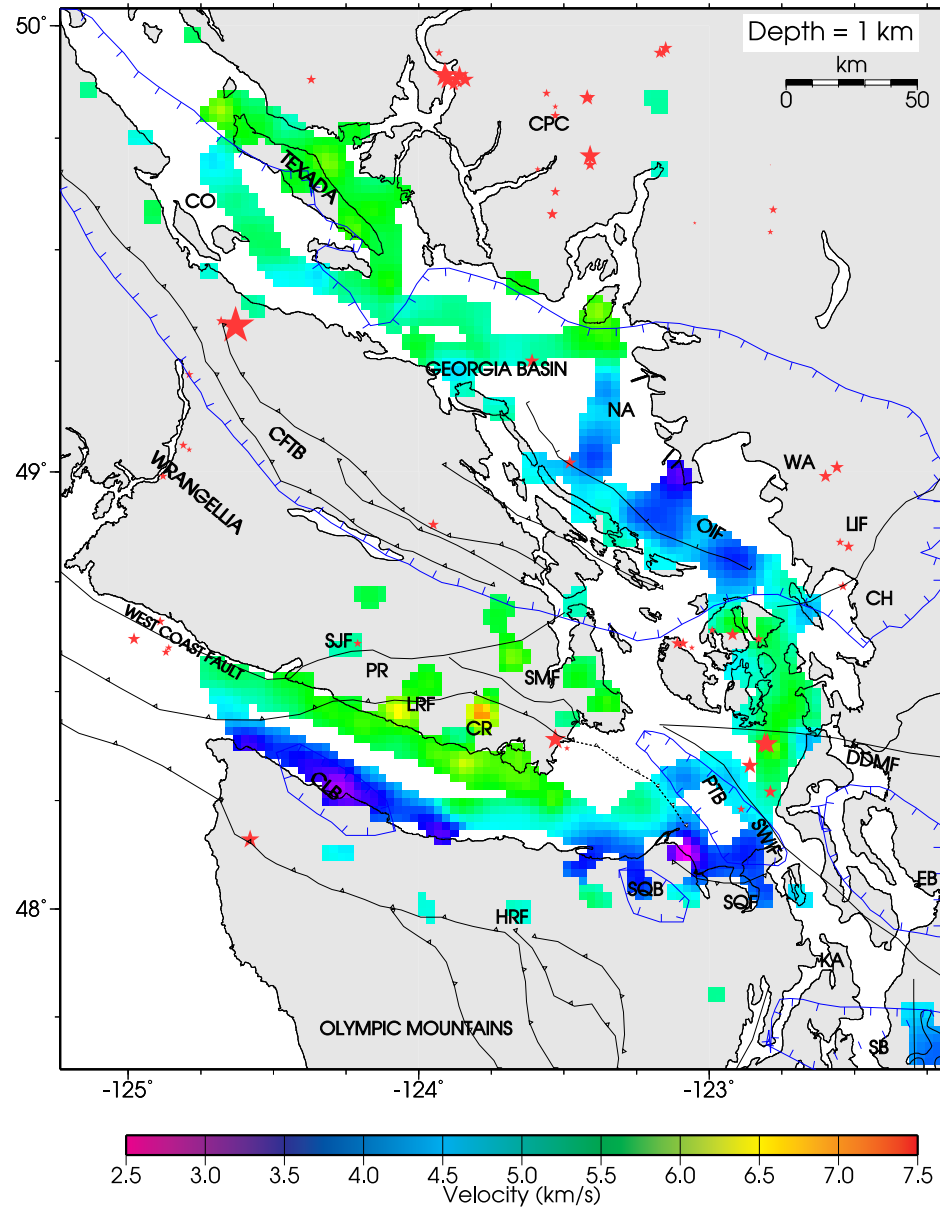


Figure 4.1 Horizontal slice plot of SHIPS velocity model at 1 km depth. Well located earthquake locations are shown as red stars. Abbreviations as in Fig. 1.3

the Cretaceous Nanaimo subbasin, the mapped velocities are less than 5.5 km/s and so within the expected range of sedimentary units. Higher velocity Wrangellia rocks (6.5–6.7 km/s) are mapped close to Texada Islands. A prominent difference in velocity structure of northwestern and southeastern Strait of Georgia, at this depth level, is identified.

4.4.3 Horizontal Velocity Slice at 5 km Depth

At 5 km depth, an east-west trending velocity high divides the northwest and southeastern parts of the Strait of Georgia (Fig. 4.3). Several highs appear in the northwestern segment of the Strait of Georgia, close to Texada Island. The Nanaimo subbasin is mapped with consolidated sediment velocities in the range of 5.0–5.5 km/s. Basement velocities are observed at the location of the Comox subbasin, indicating that the basin depth is less than 5 km. The vertical resolution of the depth to the basement is expected to be close to one cell size i.e. 1 km. The Crescent Terrane is well mapped by velocities of 6.5–7.0 km/s in southern Vancouver Island extending farther to the northeast at depth, and is laterally extensive at the eastern end of the Strait of Juan de Fuca. The north-south extent of Crescent Terrane, mapped at the eastern end of Strait of Juan de Fuca, is larger than that at the western end. Consolidated sediment velocities are still observed at this depth level in the Clallum basin. A part of the Seattle basin is mapped in the southeastern corner of the map.

4.4.4 Horizontal Velocity Slice at 7 km Depth

The maximum areal coverage for the SHIPS velocity model is observed at 7 km depth level (Fig. 4.4). A prominent E-W high is mapped clearly at the San Juan Islands. This marks the southern termination of the Nanaimo subbasin. A high velocity trend along the western margin of Strait of Georgia is also mapped clearly. Except for a small patch of low velocity observed in the Clallum basin, the full length

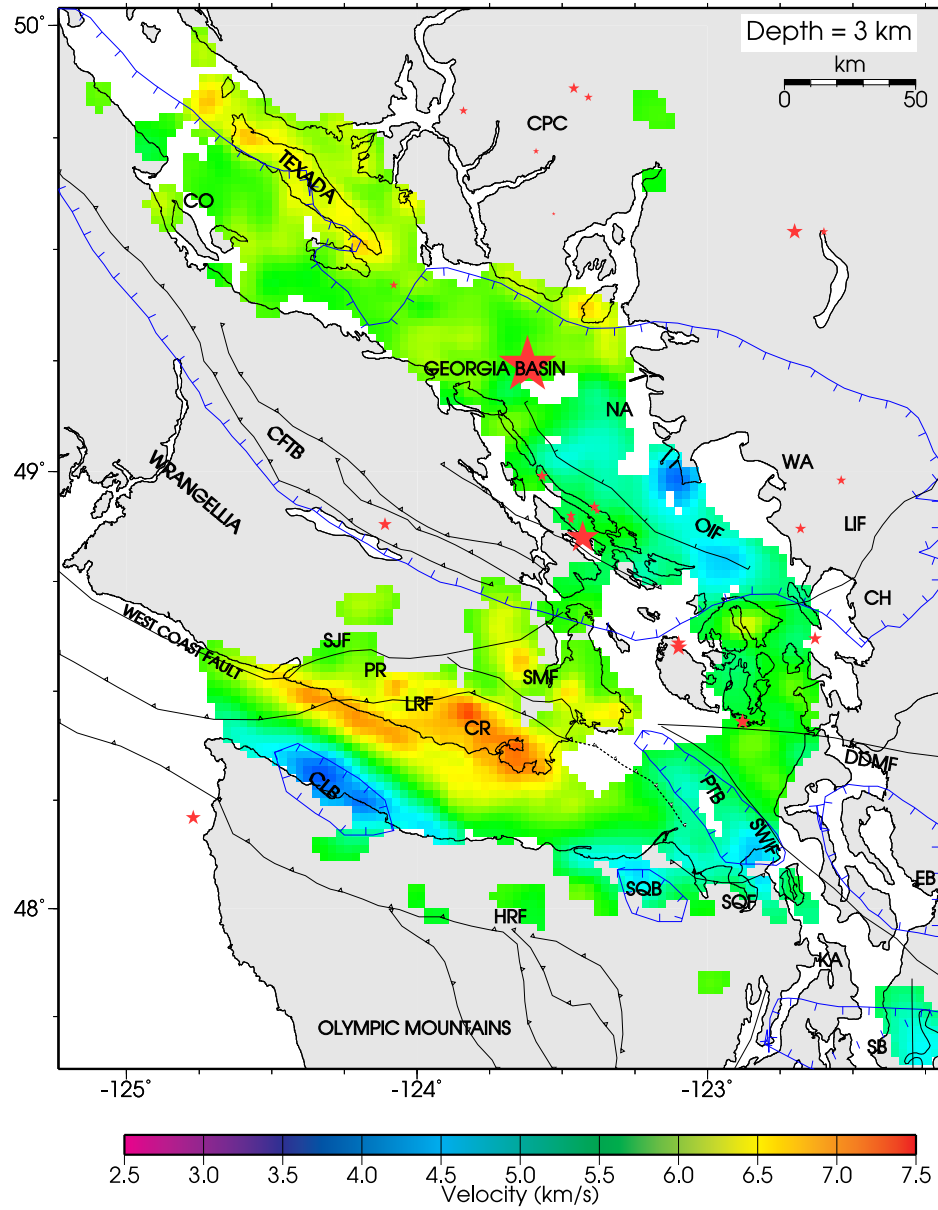


Figure 4.2 Horizontal slice plot of SHIPS velocity model at 3 km depth. Well located earthquake locations are shown as red stars. Abbreviations as in Fig. 1.3

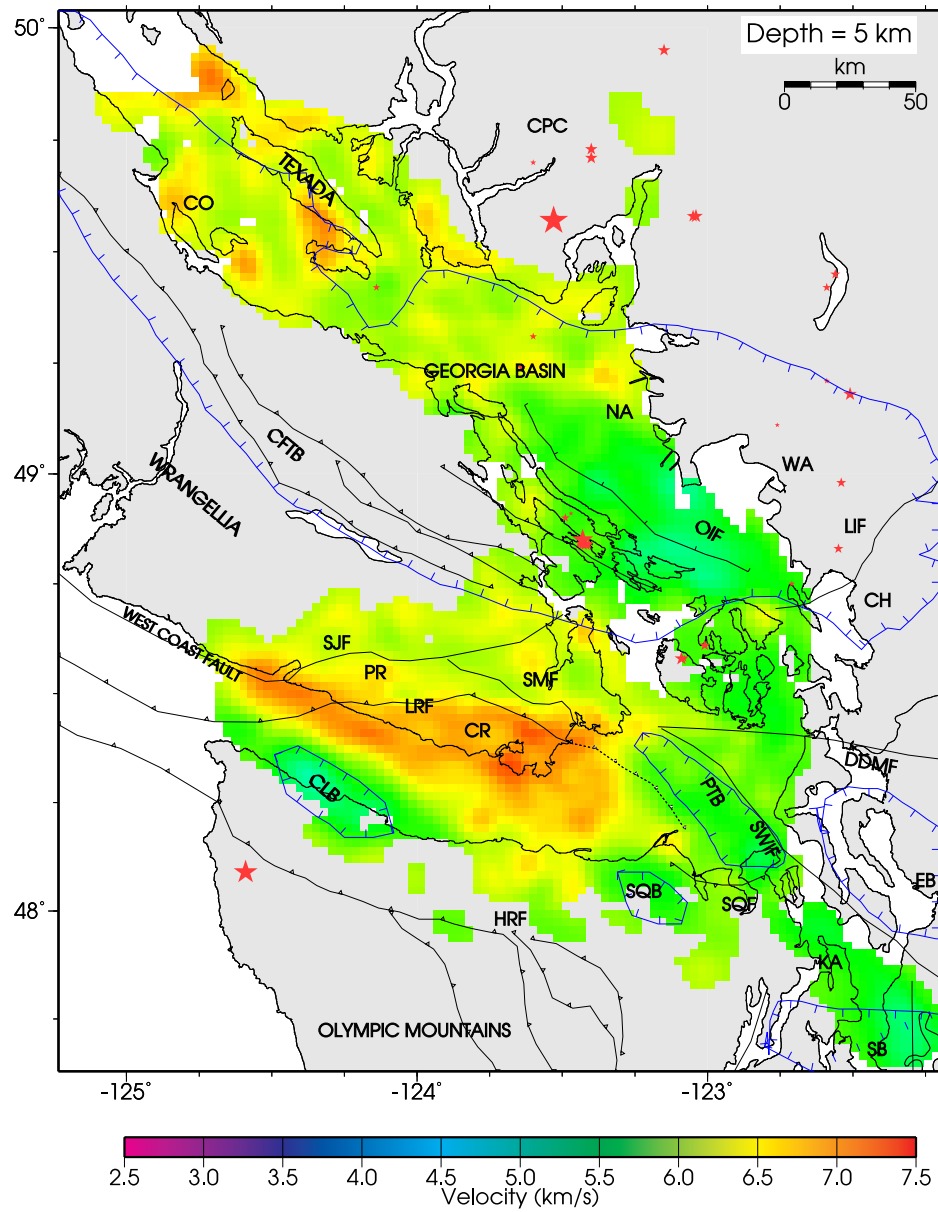


Figure 4.3 Horizontal slice plot of SHIPS velocity model at 5 km depth. Well located earthquake locations are shown as red stars. Abbreviations as in Fig. 1.3

of the Strait of Juan de Fuca is mapped with the high velocity of the mafic Crescent Terrane. At few places, however, lateral velocity contrasts within the Crescent Terrane are observed, indicating compositional/structural variation within the Crescent Terrane rocks.

4.4.5 Horizontal Velocity Slice at 9 km Depth

At 9 km depth level, the ray coverage in southern Vancouver Island is considerably decreased and the Crescent Terrane is mapped at only a few locations (Fig. 4.5). There are indications that the Crescent Terrane extends even deeper in the subsurface, but from the limited information available, the depth extent can not be mapped from this velocity model. These aspects are better constrained by the velocity model obtained from earthquake tomography and will be discussed in Chapter 5. A well marked alternating high-low velocity structure is mapped at the location of the San Juan Islands. The velocities observed in Wrangellia west of the CFTB are less than those observed to the east. This indicates a strong lithological boundary at this point in the subsurface.

4.4.6 Horizontal Velocity Slice at 11 km Depth

A significant velocity variation is observed across the CFTB at 11 km depth (Fig. 4.6). Towards the east the velocity values are higher than those towards the west. This indicates the continuation of the juxtaposition of different Wrangellia rocks at the CFTB zone observed in the previous depth slice. The velocity values observed on the eastern margin of the Strait of Georgia (~ 6.5 km/s) are considerably smaller than those on the western margin (~ 7.0 km/s). This may indicate the boundary between Wrangellia and the Coast Plutonic Complex.

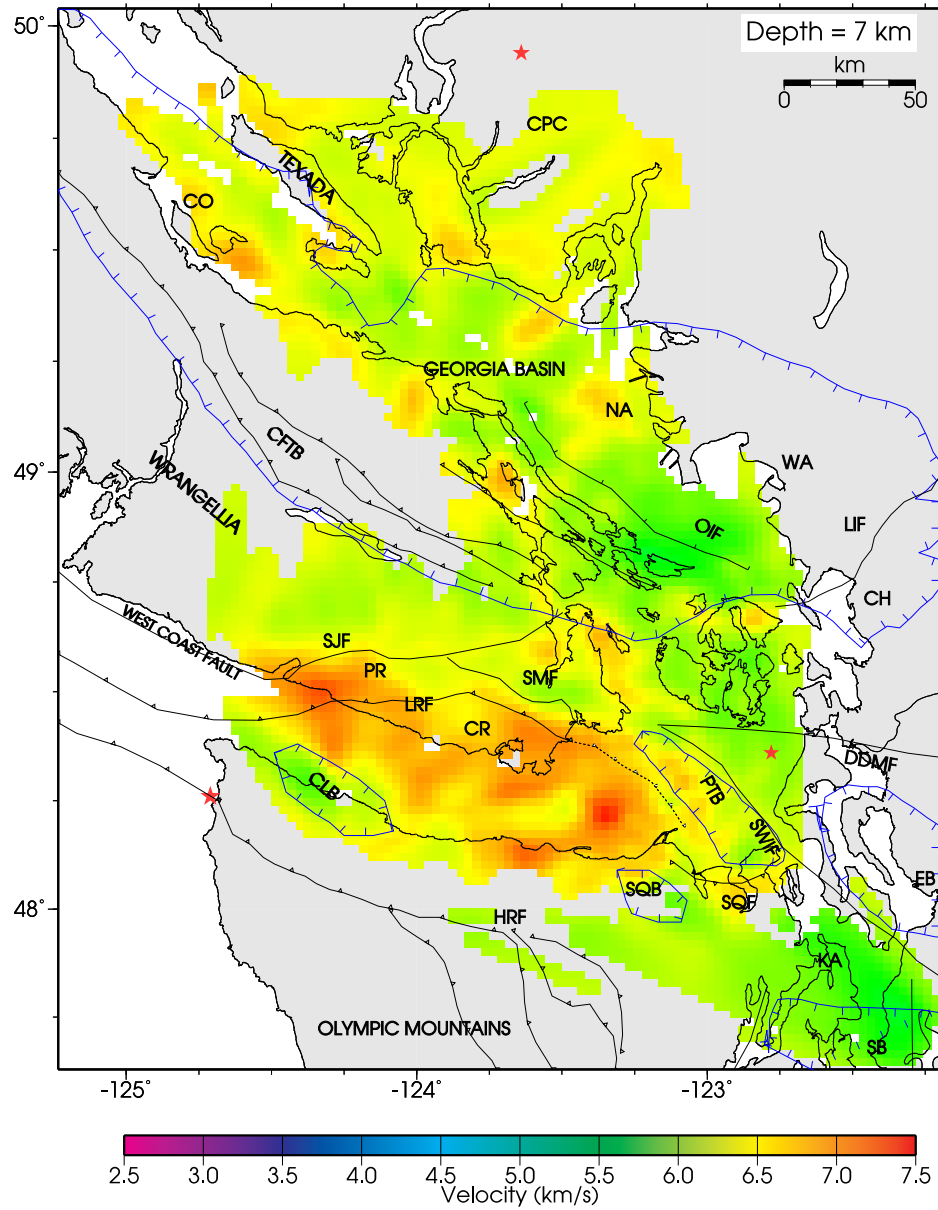


Figure 4.4 Horizontal slice plot of SHIPS velocity model at 7 km depth. Well located earthquake locations are shown as red stars. Abbreviations as in Fig. 1.3

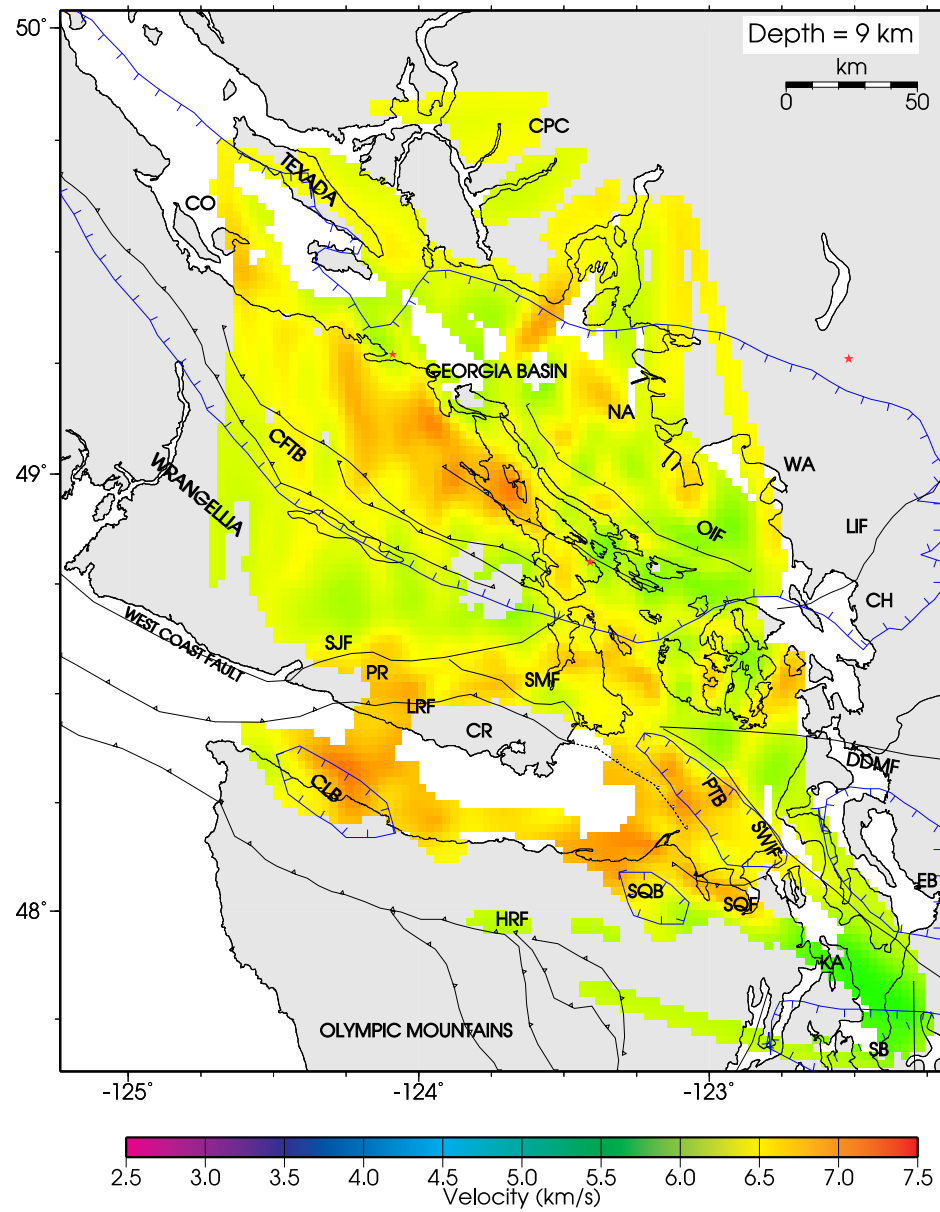


Figure 4.5 Horizontal slice plot of SHIPS velocity model at 9 km depth. Well located earthquake locations are shown as red stars. Abbreviations as in Fig. 1.3

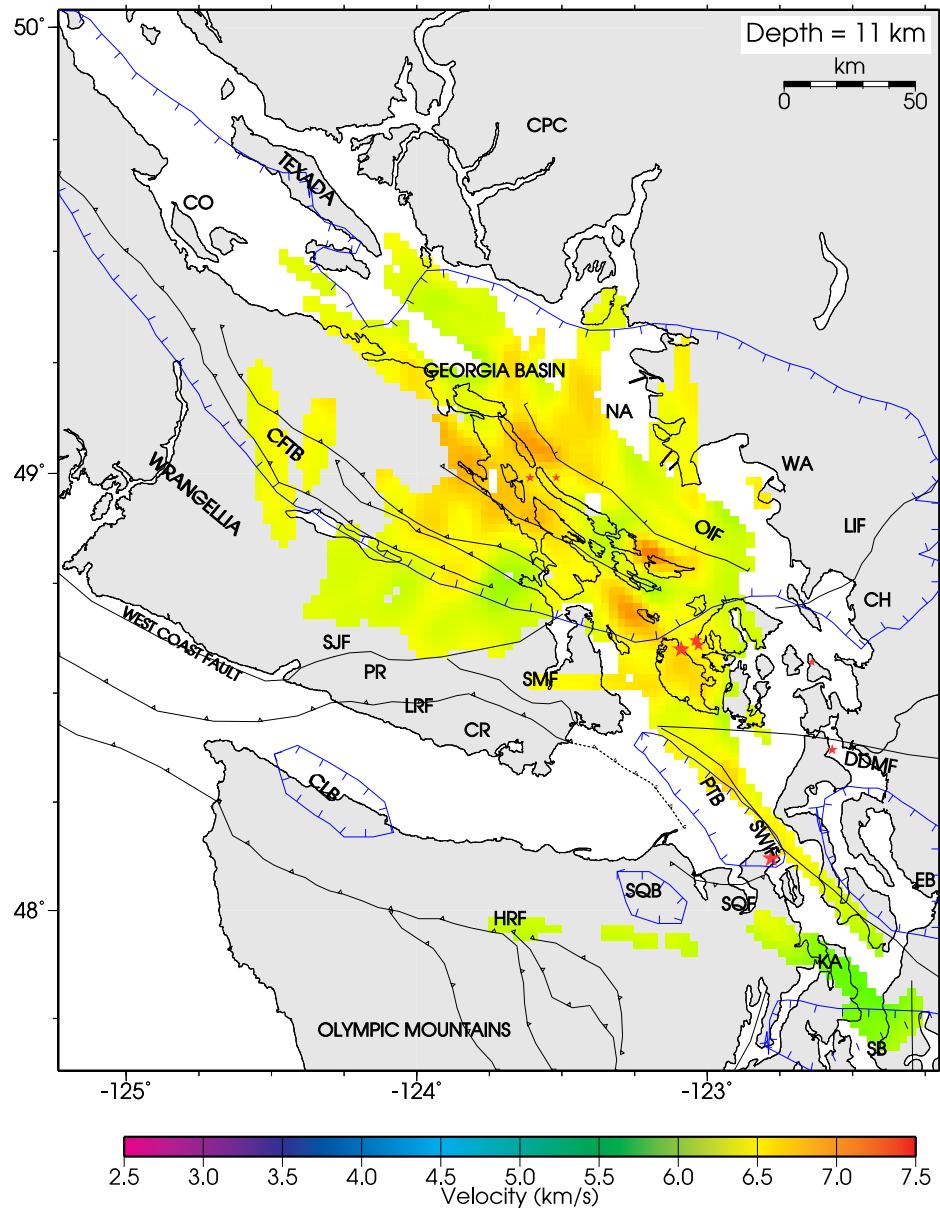


Figure 4.6 Horizontal slice plot of SHIPS velocity model at 11 km depth. Well located earthquake locations are shown as red stars. Abbreviations as in Fig. 1.3

4.5 Analysis of Profile Sections

The location of the five vertical sections generated along and across major structural and geologic features is shown in Fig. 4.7. On each of these sections well located earthquakes recorded for the past five years, within 5 km of the profile location, are plotted to identify active structural features (Source: Pacific Geoscience Centre, Geological Survey of Canada). The profile sections bring out the relationship between the different rock units in the subsurface and their structural attitude. All profiles are plotted with a vertical exaggeration of 3:1.

4.5.1 Interpretation of Profile Section - P1

Profile P1 is oriented NW-SE along the eastern margin of the Strait of Georgia and extends from Texada Island to Lummi Island (Fig. 4.8). The observed lateral velocity contrasts exhibit moderate to steep dips. Close to Texada Island, higher velocity Wrangellia rocks are mapped beneath a small basin. Earthquakes close to a profile distance of 50 km fall at the boundary of a dipping velocity contrast F1, which is a possible fault location. The dip of the fault is not well determined from the velocity model, but it appears to be vertical or sub-vertical. This location marks the northern termination of the thick sediments in the Nanaimo subbasin. South of this point, the depth of the basin is fairly uniform until a distance of 90 km. Strong earthquake activity is observed at this point and correlates well with a north dipping velocity contrast (F2). The depth of the basin increases towards the south; the maximum depth at ~ 160 km profile distance is between 6 km (5.5 km/s contour) and 8 km (6.0 km/s contour). The basement of the basin is expected to be represented by the 5.5 km/s contour or the 6.0 km/s contour. South of this point, the basin shallows and terminates against a velocity high east of the San Juan Islands.

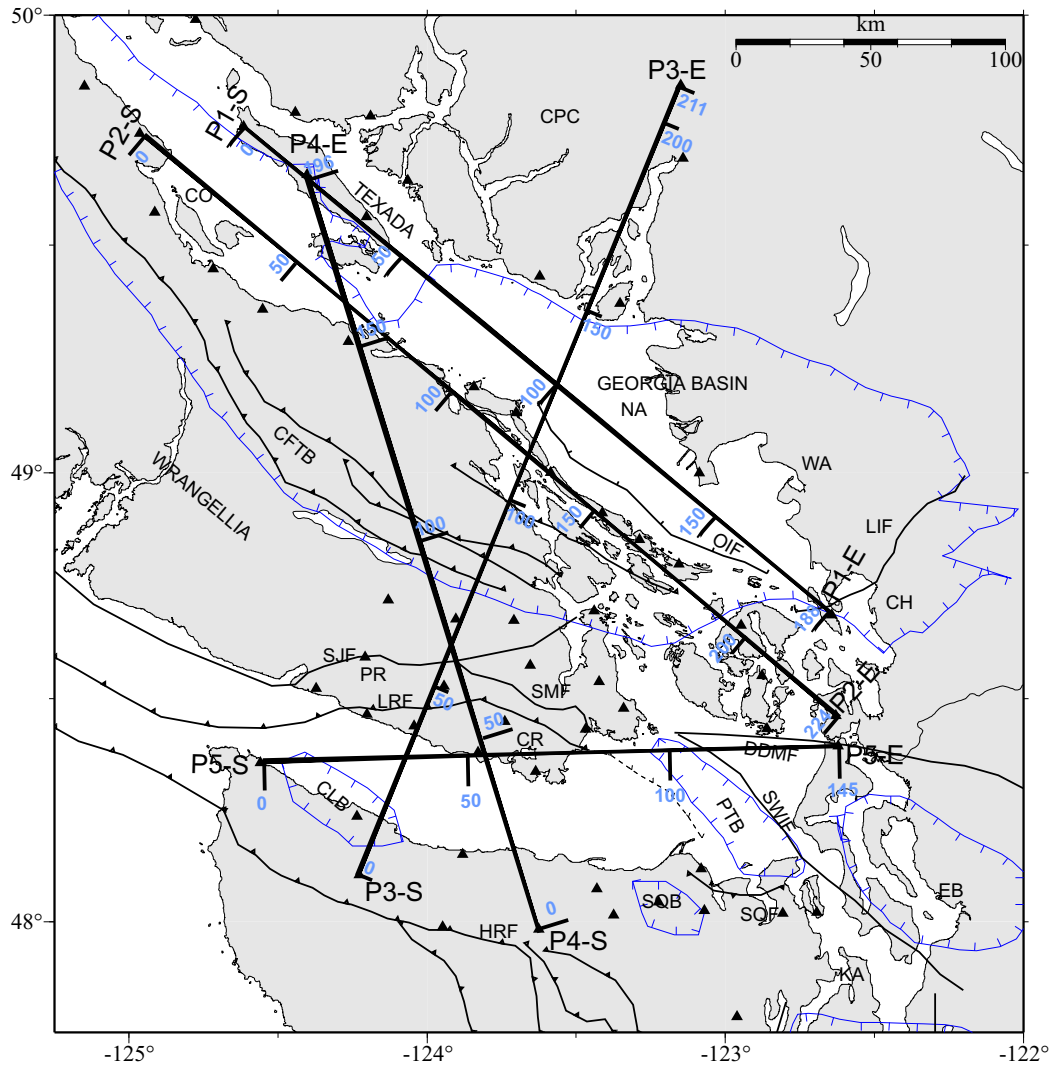


Figure 4.7 Location map of the vertical profile sections P1 (Fig. 4.8) to P5 (Fig. 4.12).
Triangles are recording stations.

4.5.2 Interpretation of Profile Section - P2

Profile P2 is located along the western margin of the Strait of Georgia from the Comox subbasin to south of the San Juan Islands (Fig. 4.9). The earthquake activity observed along this margin is higher than that on the eastern margin. The profile depicts strong lateral velocity contrasts with steep dips, dividing the basin into smaller units. The Comox subbasin, with approximately 4 km thick sediments, is clearly mapped. The basin geometry along this profile is more uneven than that observed on the eastern margin. The velocity contrast at F3 correlates with earthquake activity at 10 km depth. Two velocity contrasts at 140 and 150 km (F4 and F5) on the line correlate with the observed earthquake activity. The southern termination of the Georgia basin is sharply outlined by a velocity high beneath the San Juan Islands.

4.5.3 Interpretation of Profile Section - P3

Profile P3 is a NE-SW oriented section from the Olympic Peninsula to mainland British Columbia passing through southern Vancouver Island (Fig. 4.10). Clallum basin to the south is mapped with a maximum thickness of 5–6 km, with Crescent Terrane as the basement. The Crescent Terrane shallows in southern Vancouver Island and terminates laterally against the Pacific Rim terrane at the Leech River fault at F9. The velocities observed in the Crescent Terrane vary from 6.0 to 6.75 km/s indicating lithological variation. At depth, the subsurface outline of the Leech River fault is clearly mapped by the velocity contrast between the Pacific Rim Terrane and Crescent Terrane (F7). Due to the limited ray coverage, the Pacific Rim Terrane is mapped only at intermediate depth. The contact between the Pacific Rim Terrane and Wrangellia rocks at F8 is marked by a clear velocity contrast. Towards the northeast, base of the Nanaimo subbasin is mapped in the Strait of Georgia. Northeast of the Strait of Georgia, Wrangellia rocks are interpreted to be in contact with the Coast Plutonic Complex (F9). This contact is interpreted from the relatively lower velocities

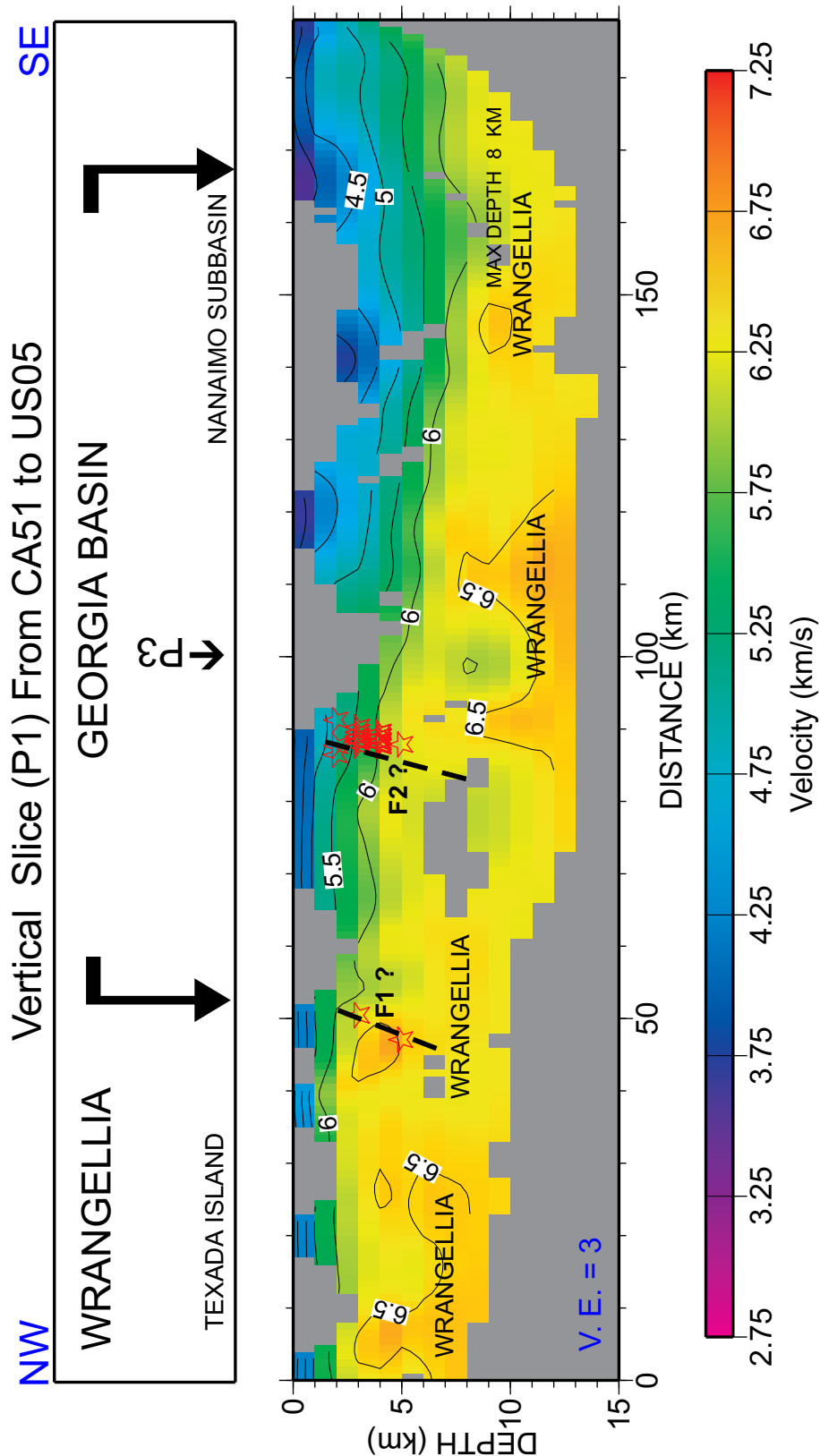


Figure 4.8 Vertical velocity section P1 along the eastern margin of Strait of Georgia. Well located earthquakes are shown as red stars.

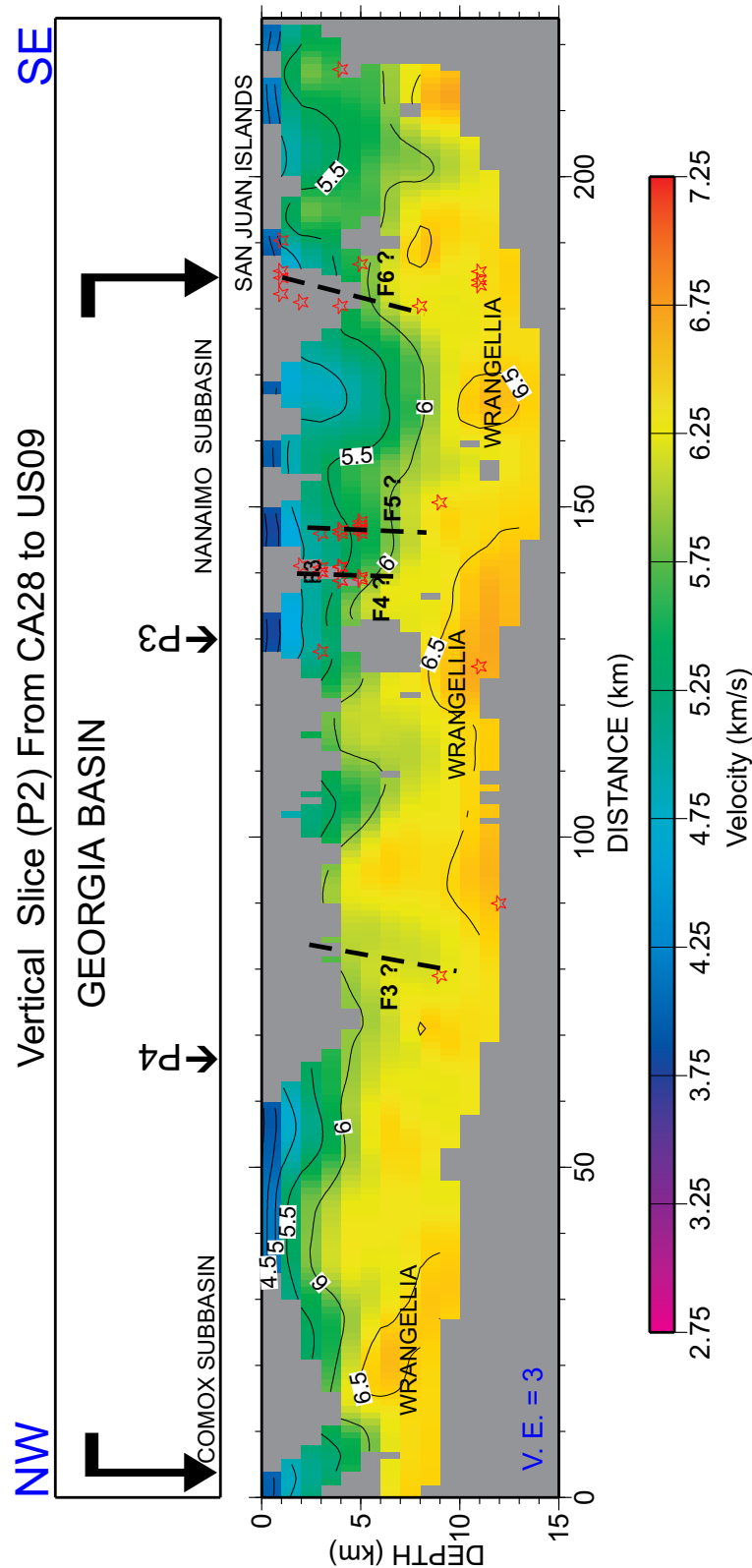


Figure 4.9 Vertical velocity section P2 along the western margin of Strait of Georgia. Well located earthquakes are shown as red stars.

(less than 6.5 km/s) observed on the eastern margin of the Strait of Georgia compared to those on the western margin (greater than 6.5 km/s) at the same depths.

4.5.4 Interpretation of Profile Section - P4

Profile P4 is a NW-SE section from the Olympic Peninsula to Texada Island (Fig. 4.11). In the southeast, Clallum basin is mapped with maximum depth of 4 km and is shallower than that observed on the profile P3. The Clallum basin is formed by the downwarping of the Crescent Terrane forming a synclinal structure with an E-W axis that plunges to the west. The contact of the Crescent Terrane with Pacific Rim Terrane at the Leech River fault is marked by a clear velocity contrast (F7). At the northwest end of the profile, the Wrangellia basement rocks beneath the Comox subbasin are mapped with velocities of 6.5 km/s and above (Spence and McLean 1998).

4.5.5 Interpretation of Profile Section - P5

Profile P5 is a W-E oriented section from the tip of the Olympic Peninsula to south of the San Juan Islands (Fig. 4.12). This profile passes through the Metchosin Igneous Complex mapped and detailed by Massey (1986). Higher velocities of 7 km/s occur at depths as shallow as 3 km, and their position correlates well with presence of exposed gabbroic rocks. *P* and *S* velocity measurement in the Crescent Formation near Olympia, Washington were from 5.88–6.94 km/s and 2.35–3.85 km/s, respectively (Williams *et al.* 2000). *P* wave velocity in gabbro is observed to vary from 7.0 to 7.2 km/s over the depth range from the surface to 10 km (Christensen and Mooney 1995). East of the Leech River fault, strong velocity contrasts with steep dip (F10 and F11) correlate with observed seismicity.

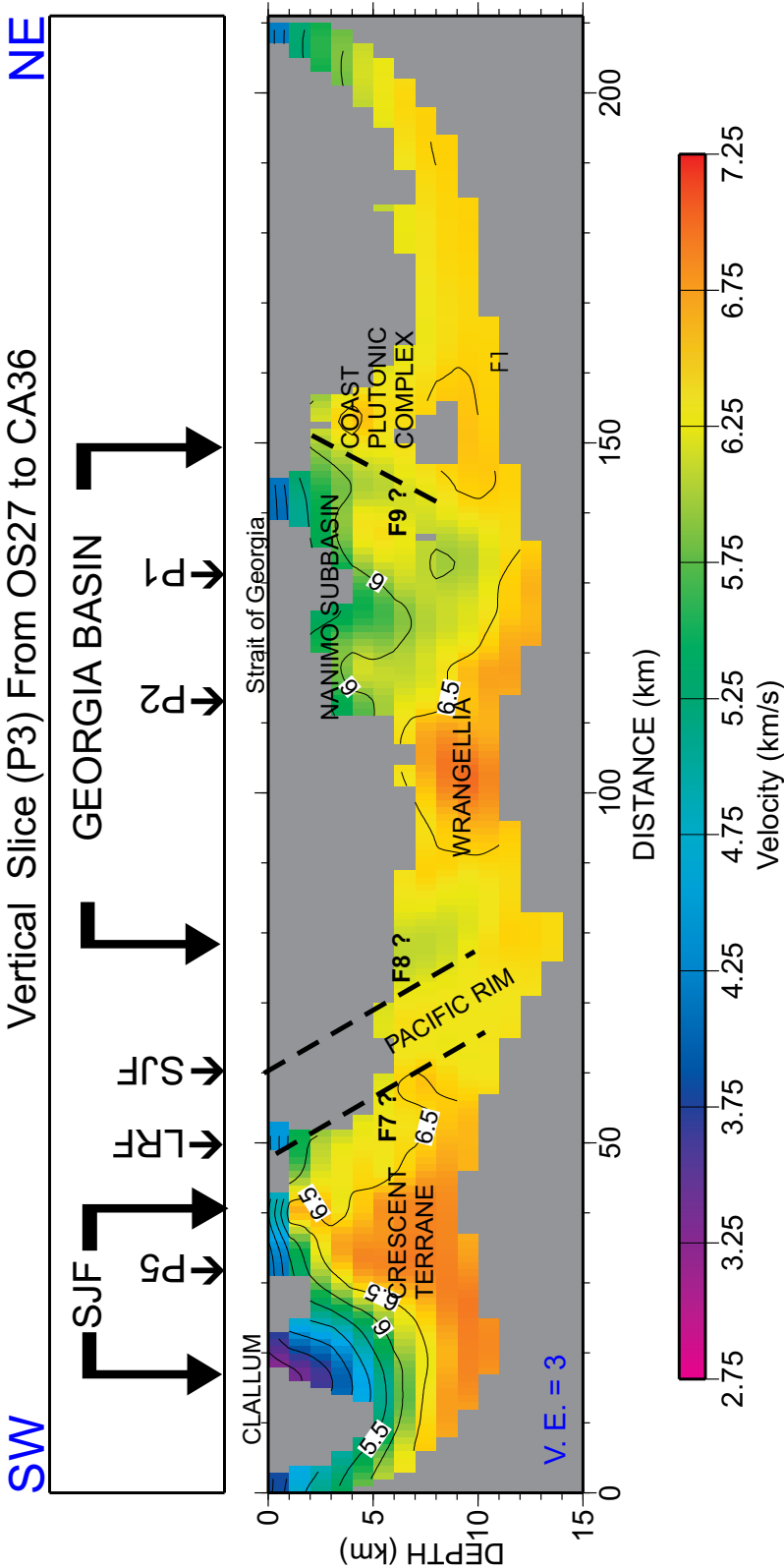


Figure 4.10 NE-SW vertical velocity section P3 from Olympic Peninsula to mainland British Columbia. Well located earthquakes are shown as red stars.

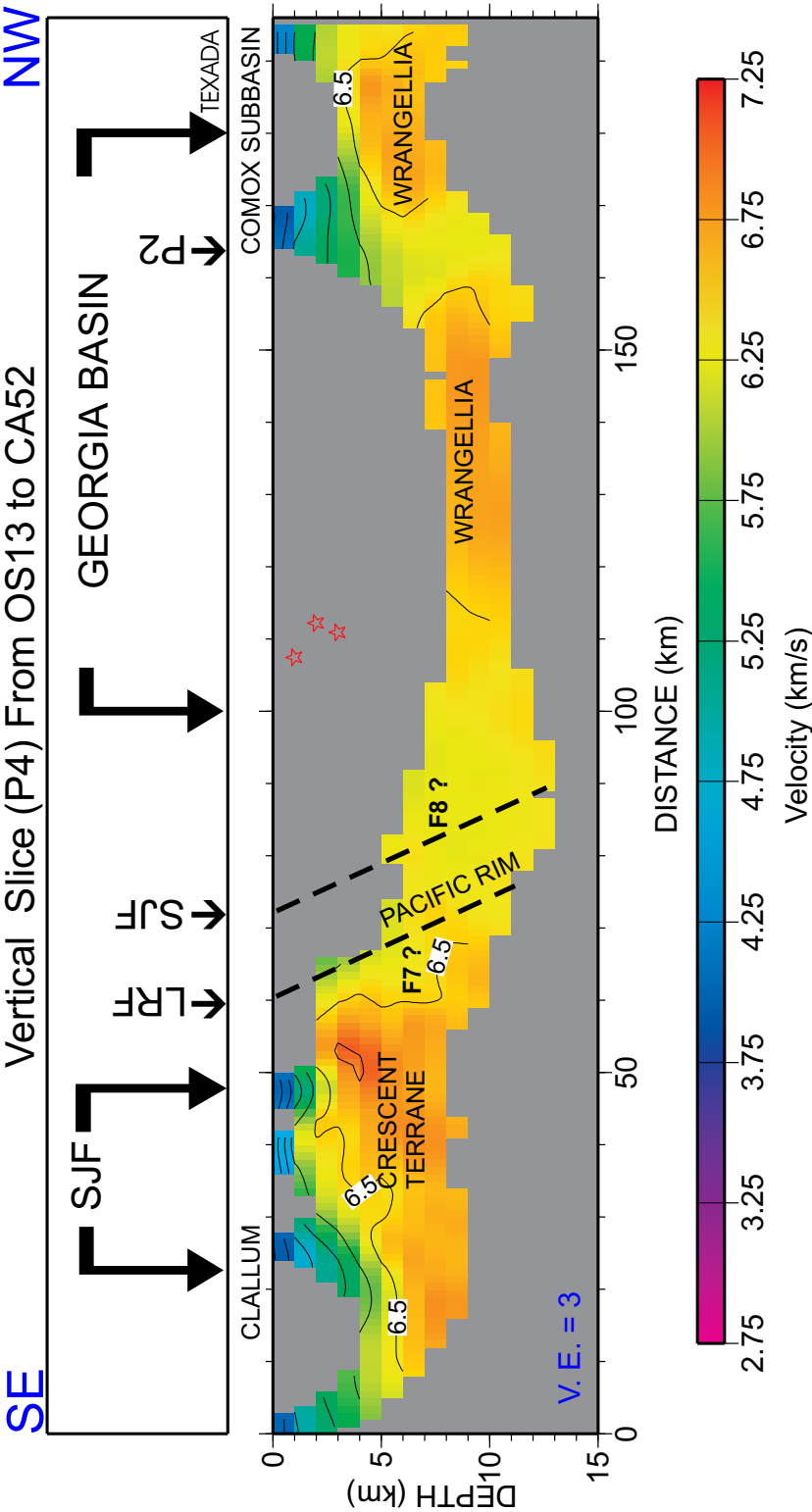


Figure 4.11 NW-SE vertical velocity section P4 from Olympic Peninsula to Texada Island. Well located earthquakes are shown as red stars.

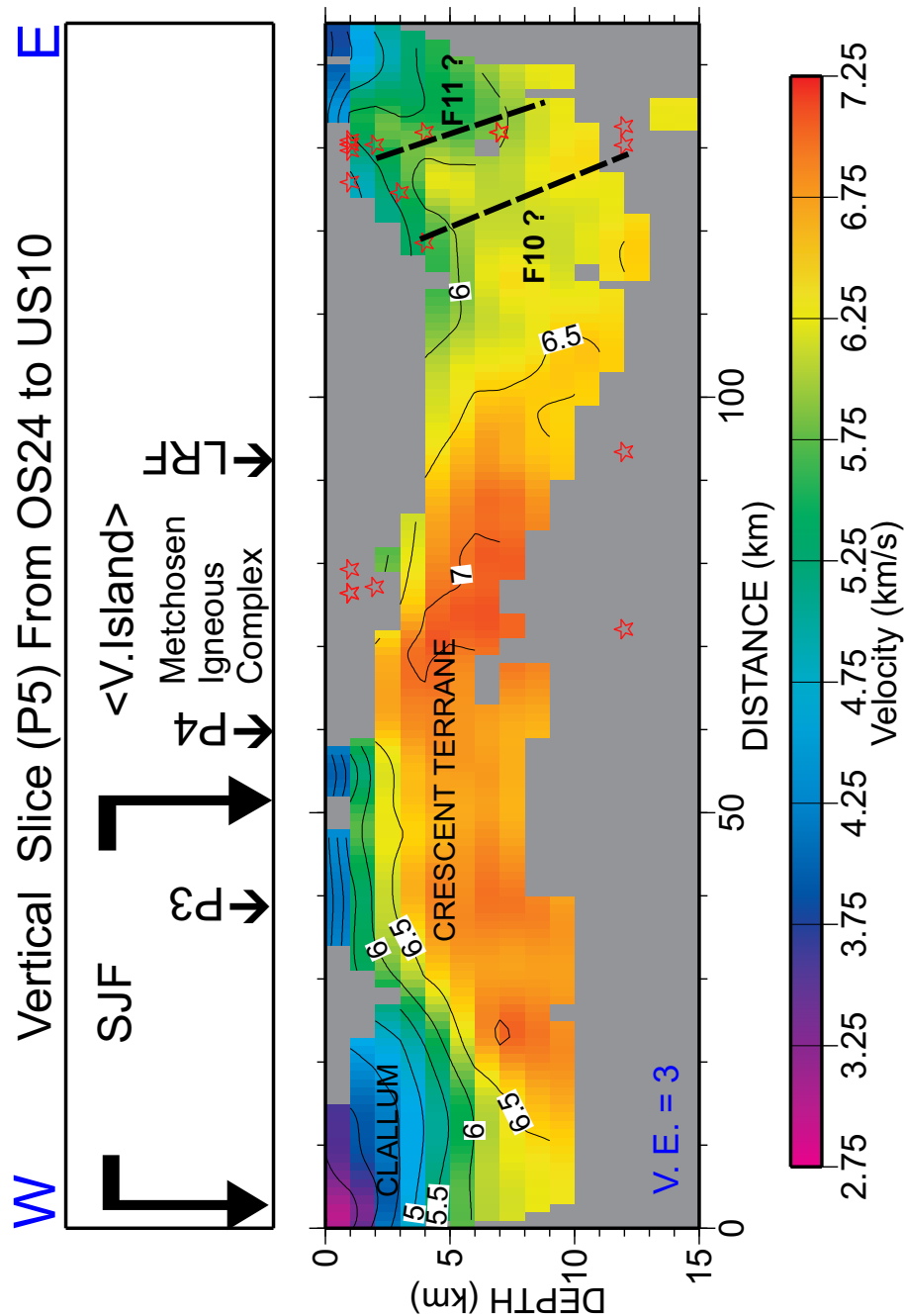


Figure 4.12 W-E vertical velocity section P5 from the tip of Olympic Peninsula to south of San Juan Islands. Well located earthquakes are shown as red stars.

4.6 Interpretation of Isovelocity Surfaces

Isovelocity surface maps provide detailed information about the structural pattern of velocity interfaces. They enable mapping the structural outline of sedimentary basins, and facilitate fault correlation. Two isovelocity surface maps for velocities of 5.5 and 6.0 km/s (Figs. 4.13 and 4.14) are analysed in this section to bring out the major upper crustal features in the study area. The results are correlated with a gravity anomaly map (Fig. 4.15) to ensure validity of mapped sedimentary and structural features. The sedimentary basinal features are interpreted in relation to the 5.5 km/s isovelocity map. The seismogenic zones and the relation to structural features are discussed from the 6.0 km/s isovelocity map.

4.6.1 Interpretation of 5.5 km/s Isovelocity Surface

The isovelocity surface map at 5.5 km/s (Fig. 4.13) well delineates the sedimentary basin features in the Straits of Georgia and Juan de Fuca. Zelt *et al.* (2001) and Brocher *et al.* (2001) mapped the sedimentary basinal features in the Strait of Georgia and Puget Sound, respectively, from separate tomographic studies. The tomographic results of Brocher *et al.* (2001) identified four large, west- to north-west trending sedimentary basins (Tacoma, Seattle, Everett and Port Townsend), separated by regions of higher velocity ridges that are coincident with fault-bounded uplifts of Eocene Crescent Formation and pre-Tertiary basement (Fig. 1.3). In the 5.5 km/s isovelocity map from the present tomographic study, a portion of the Seattle basin and Port Townsend basin (PTB) are mapped. The Southern Whidbey Island fault (SWIF) demarcates the northeastern boundary of the Port Townsend basin. To the southwest of the PTB basin, a low is observed and is informally referred as the Sequim basin (SQB) by van Wagoner *et al.* (2001). This feature is observed as a small low on the gravity anomaly map (Fig. 4.15).

The San Juan Islands are the result of thrust faults within sedimentary, volcanic

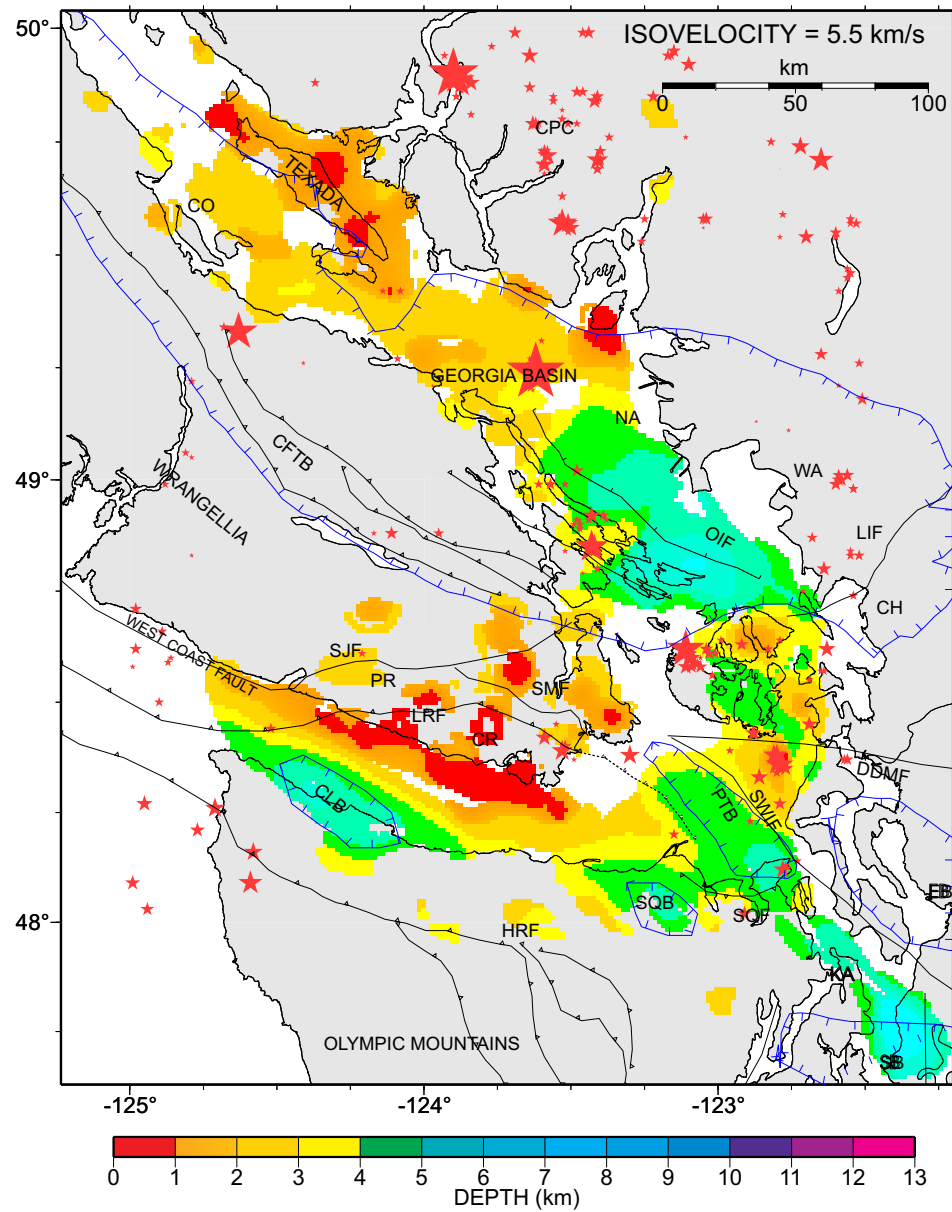


Figure 4.13 Isovelocity surface map at 5.5 km/s. Well located earthquakes between 0–12 km shown as red stars. Abbreviations as in Fig. 1.3.

and metamorphic rocks. North of DDMF, the subsurface beneath the San Juan Islands exhibits a high-low-high structure in the N-S direction. The highs in the isovelocity map possibly represent upthrust blocks. The location of the Lummi Island fault forms the southern boundary of the Georgia basin in the Strait of Georgia. A thick sedimentary column exists between 48.7°N and 49.25°N in the Nanaimo subbasin. The northern edge of this subbasin is a location of marked earthquake activity (Fig. 4.13). The east-west trending high observed at this location correlates with observed seismicity. The northwestern part of the Georgia basin is considerably shallower than that to the southeast. The Comox subbasin with a maximum sediment thickness of approximately 3–4 km is mapped on the northwestern edge of the Georgia basin. The Clallum basin in the Strait of Juan de Fuca, with a WNW-ESE trend, is identified in the isovelocity surface and correlates well with the low on the gravity anomaly map (Fig. 4.15).

4.6.2 Interpretation of 6.0 km/s Isovelocity Surface

Four main clusters of seismicity (*A*, *B*, *C*, *D*) (Fig. 4.14) are observed in the central and western Strait of Georgia. The clusters *A*, *B* and *D* appear to be associated with basement highs. At cluster *B*, on the northern edge of the deepest basinal low, the activity peaks where the NW-SE trend of the CFTB is intersected by E-W trending highs. This effect is observed strongly at the E-W trend of the Devils Mountain fault (cluster *A*). In southwestern Georgia basin, the observed seismic activity is limited to the west of the Outer Island fault (cluster *B*). The earthquake activity at the pronounced E-W structural feature in the Nanaimo subbasin at 49.25°N (cluster *D*) is the limit of the major NW-SE earthquake trend observed in the western margin of the Strait of Georgia.

The shallow depth of the Crescent Terrane correlates with the mapping of basalt and gabbro at locations in southern Vancouver Island (Massey 1986). The associated

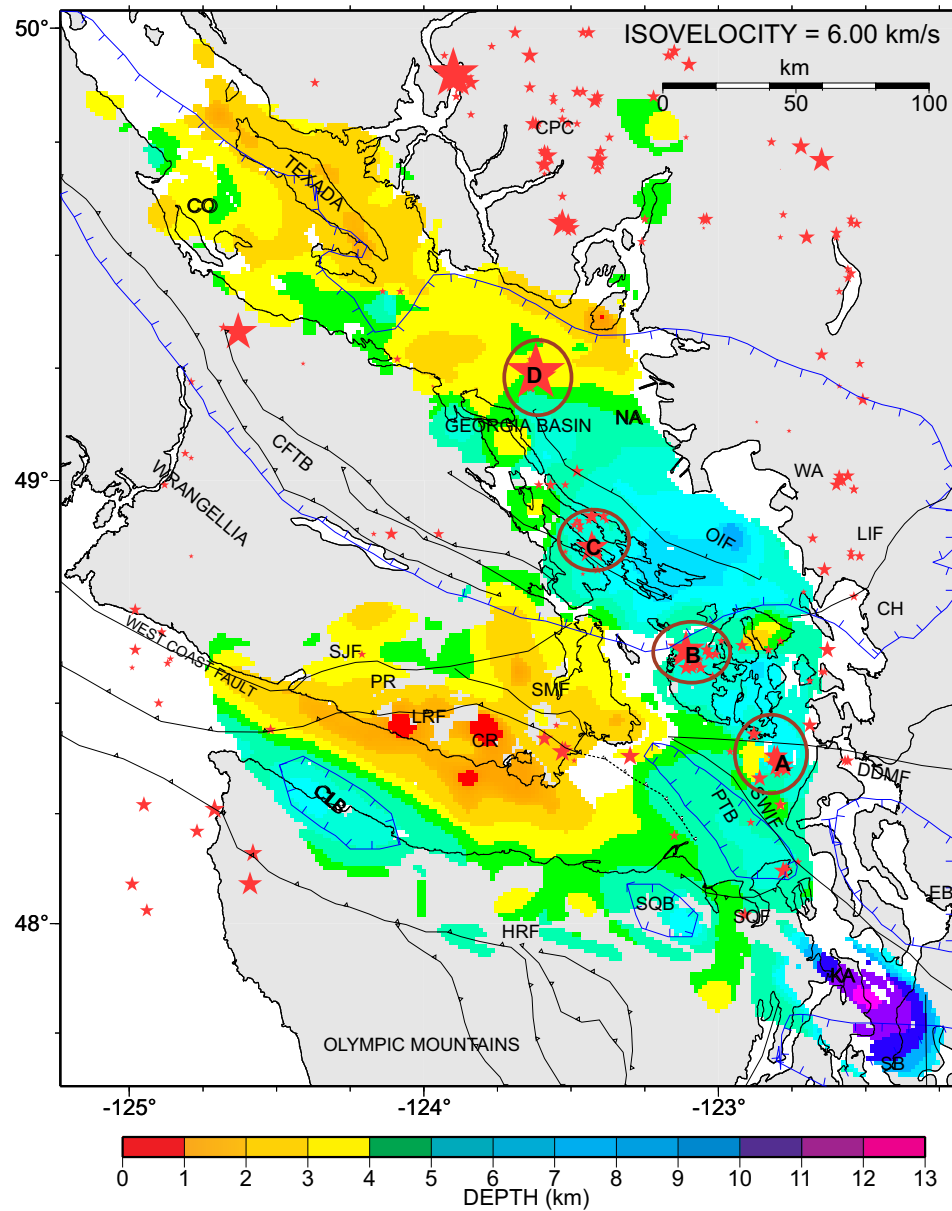


Figure 4.14 Isovelocity surface map at 6.0 km/s. Well located earthquakes between 0–12 km shown as red stars. A, B, C, and D represent the four clusters of earthquakes discussed in text. Abbreviations as in Fig. 1.3.

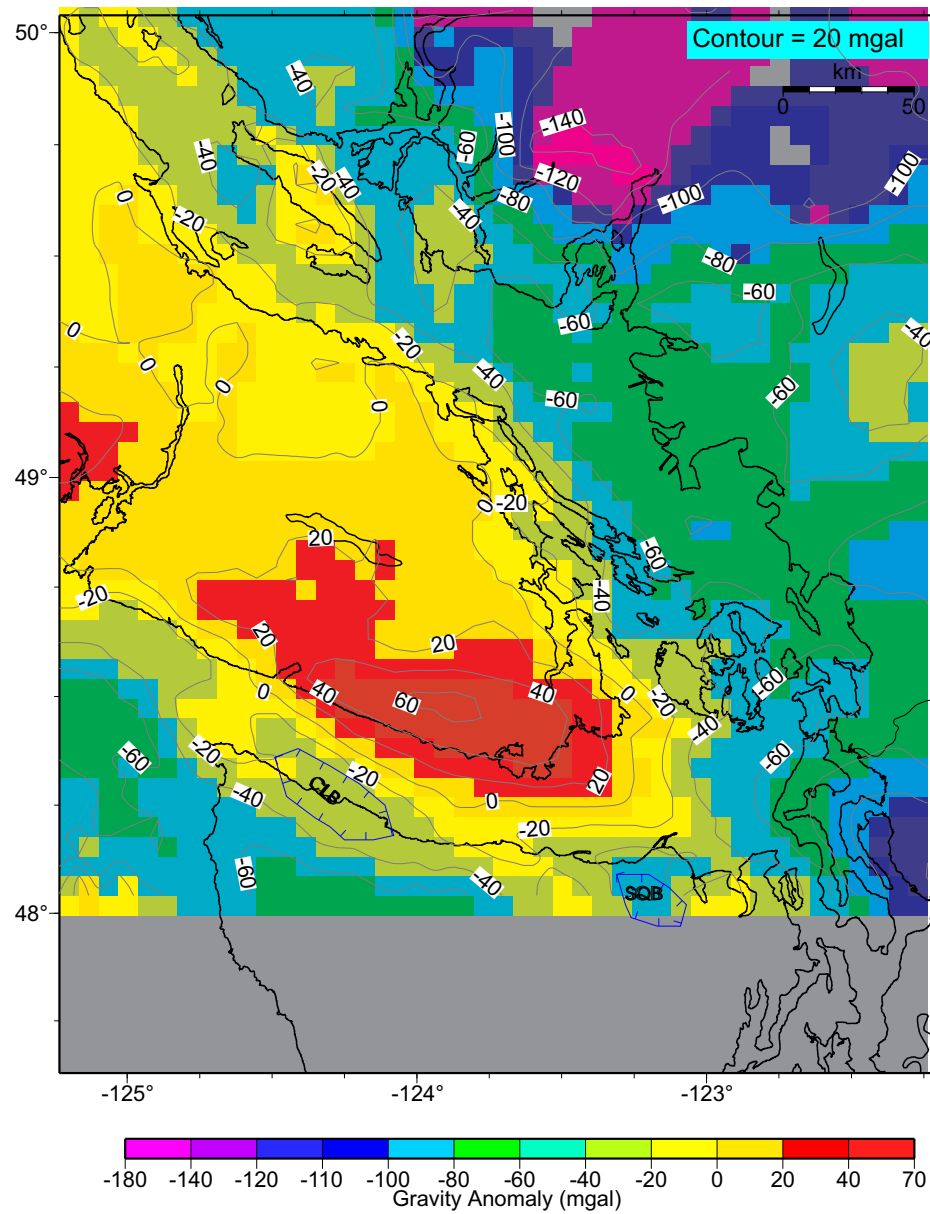


Figure 4.15 Gravity anomaly map (Bouguer anomaly on land and free air anomaly over ocean).

gravity high correlates well with the shallow depth of the Crescent Terrane. The thickness of the Crescent Terrane exceeds 12 km, which is the maximum depth sampled in the present tomographic model. To the northeast of the Survey Mountain fault the shallow depth to the 6.0 km/s contour coincides with the shallow mapped depth of the the Island and West Coast intrusive rocks. In southern Vancouver Island, the southeastern portions of the Leech River fault and Survey Mountain fault correlate with earthquake activity and appear to be active.

4.7 Summary

The velocity model provides excellent constraints on the upper crustal velocity structure down to 12 km depth. The salient features of the interpretation are summarized as follows. A WNW-ESE trending oval shaped Clallam basin is mapped in the Strait of Juan de Fuca with maximum sediment thicknesses of approximately 5 to 6 km. The fault-bounded Sequim and Port Townsend basins are mapped in the eastern Strait of Juan de Fuca. In the Nanaimo subbasin (southwestern part of Georgia basin), sediments reach 8 km in thickness, while in the Comox subbasin (northwestern part of Georgia basin) the maximum sediment thickness is 4 km. The shape and depth of the basins is illuminated clearly in the 5.5 km/s isovelocity map and correlates well with the prominent negative gravity anomaly features. A strong NW-SE trending velocity discontinuity is mapped on the western flank of the Strait of Georgia, and is associated with the Cowichan Fold and Thrust Belt and the Outer Islands fault. The subsurface structural disposition of the volcanic Crescent Terrane (Metchosin igneous complex) is well delineated beneath southern Vancouver Island. For this terrane, high velocities of 6.5 km/s and greater are found within 1 km of the surface; at one location the 7 km/s velocity contour is observed at 3 km depth where it correlates with a positive gravity anomaly and the outcrop of a small area

of gabbro structurally below the basalts. Thus velocities > 7.0 km/s may delineate gabbro components of the Crescent Terrane.

Earthquake activity observed at the southern tip of Leech River fault in the eastern Strait of Juan de Fuca suggests that the fault may be active at this location. Beneath the Strait of Georgia, the earthquake locations show a prominent NW-SE trend, which corresponds to sharp lateral velocity contrasts. In addition, high earthquake activity is associated with the intersection of several E-W trending highs with the NW-SE trend. Earthquakes at depths of 3–4 km in Strait of Georgia are found to coincide with boundaries of strong velocity contrast.

Chapter 5

Interpretation of Deep Crustal Structure

5.1 Introduction

The seismic velocity model of the Cascadia Subduction Zone along the northwestern margin of Washington and southwestern margin of British Columbia is the focus of interpretation in this chapter. The velocity model obtained from the joint tomographic inversion of earthquake and controlled source data, discussed in Chapter 3, is analysed to map features in the continental crust, subducting Juan de Fuca (JdF) crust, and the uppermost continental and oceanic upper mantle. The velocity model is presented and interpreted using vertical slices oriented parallel and perpendicular to the margin. Possible crustal faults are interpreted from the vertical sections by correlating velocity contrasts with prior knowledge of mapped fault boundaries on the surface. The relocated earthquake locations are posted on the vertical sections and are correlated with velocity contrasts and faults extrapolated from mapped surface locations. The depth and dip of the subducting plate is measured at locations with well defined deep velocity structure. The results of a consolidated interpretation combining the salient features from the SHIPS velocity model (SV) and the earthquake tomography velocity model (EV) are presented.

5.2 Previous Studies

McMechan and Spence (1983) constructed a two-dimensional upper crustal P wave velocity structure along a northwest-southeast refraction line (Vancouver Island Seismic Project 80) by iterative forward modelling of travel-times and amplitudes.

Their model constrained the upper crustal features, with a gradually increasing velocity of ~ 5.3 km/s at the surface to ~ 6.6 km/s at 2 km depth to ~ 6.75 km/s at 15.5 km depth. At 15.5 km depth they observed a sharp increase in velocity to ~ 7.0 km/s. Spence *et al.* (1985) interpreted the northeast-southwest trending refraction line from the above survey, and constructed a 2-D velocity structure from west of the continental slope to the mainland in the east. They mapped a sliver of material with mantle-type velocities (7.7 km/s) at the 20–25 km depth range beneath western Vancouver Island and the inner continental shelf. Lithoprobe seismic reflection data on Vancouver Island were interpreted by Clowes *et al.* (1987) to determine the large scale structures of the accreted terranes exposed on Vancouver Island and the geometry and structural characteristics of the subducting Juan de Fuca plate. They mapped three reflective bands and correlated the top reflective unit *C* to the Olympic subduction complex. They proposed that the high velocity middle reflective unit *D* of ~ 7.7 km/s velocity was either a detached slab of oceanic lithosphere or an imbricated package of mafic rocks derived by continuous accretion from the top of the subducting plate. The lower reflective layer *E* was interpreted as accreted marine sedimentary rocks.

Hyndman (1988) proposed that reflectivity arises from fluid-filled porosity created by dehydration reactions associated with a change in metamorphic grade at an approximately isothermal level within the crust. Calvert and Clowes (1990) proposed that the reflectivity is due to intensely sheared sediments that trap the fluid rising from the subducting plate. Beneath southern Vancouver Island the proposed location of the layer is placed at 5–10 km above the Wadati-Benioff zone (Calvert 1996). Calvert (1996) concluded from analysis of reflection profiles that the maximum thickness of Crescent Terrane nowhere exceeds 6–8 km and that beneath southern Vancouver Island the reflections represent a former subduction decollement where one or two mafic units were underplated beneath the overlying continent.

Several 3-D seismic tomography studies conducted in the Puget Lowland and adjoining areas have delineated the structures in the upper and lower crust. Symons and Crosson (1997) presented results from a larger tomographic model of Puget Sound and adjoining areas down to 60 km depth. They mapped a zone of intermediate velocity (7.5 to 8.0 km/s) between the subducted slab and the continental crust beneath the central Puget lowland. Crosson *et al.* (2000) interpreted the high velocity region beneath the Puget Sound region as mafic Crescent/Siletz volcanic rocks with a *P* wave velocity exceeding 7 km/s at a depth of 20 km. Beneath the Crescent/Siletz Terrane, they observed a velocity reversal which they interpreted as lenses of underlying low velocity subducted accretionary prism rocks which are continuous with Olympic Core Rocks found farther to the west. The *P* wave velocity contrast associated with this reversal was typically about 0.5 km/s at a depth of around 30 km. Trehu *et al.* (2001) interpreted the depth to Moho at a depth of 34 km beneath the western Strait of Juan de Fuca with a dip of 7° to the east.

Zhao *et al.* (2001) constructed a velocity model by inverting 28,230 *P* wave arrival times from 2666 earthquakes that occurred in and around Vancouver Island from 1970 to 1990 with a horizontal grid spacing of 30 km and vertical grid spacing of 12–19 km. They identified an extensive low velocity zone above the subducted slab at 45 km depth and interpreted this feature as a possible indicator of partially hydrated mantle, most likely serpentinite.

The direction of the Cascadia margin changes from north-south to northwest-southeast between latitudes 47°N and 49°N, referred to in further discussions as the ‘region of margin direction change’. Rogers (1983) suggested that this could lead to the arching of the plate in this region. This concept was later confirmed by the studies of Crosson and Owens (1987). From tomographic studies, Stanley *et al.* (1999) identified the axis of the arch to be oriented in the direction of current subduction and asymmetrically deformed due to the effects of a northern buttress under the southern Vancouver Island and the North Cascades region of Washington. Brandon

and Calderwood (1990) related the uplift of the Cenozoic marine sedimentary rocks in the Olympic Peninsula to the arch in the JdF plate. Stanley *et al.* (1999) observed higher velocities occurring within the lower crust. They proposed that the anomalous lower crust consists of voluminous mafic and ultramafic cumulates which formed in the large rift system that generated the Crescent Formation. Using data from the 1998 SHIPS experiment, Creager *et al.* (2000) mapped a strong reflector at approximately 30 km depth beneath the Olympic mountains, dipping at 13° to the east, steepening in dip and reaching a depth of about 60 km under Puget Sound. They interpreted this strong reflector as the Moho of the subducting slab. In addition they interpreted a weaker reflector mapped 7 km above the strong reflector as the interplate thrust boundary.

The seismicity observed in the study area from 1984–2000 is shown in Fig. 5.1. Crosson and Owens (1987) interpreted two different zones of seismicity in the Puget Sound region: (i) the shallower seismicity of less than 35 km depth in the North America plate and (ii) Wadati-Benioff seismicity in the subducting JdF plate from 40–70 km depth. Rogers (1994) classified the earthquakes occurring in southwestern British Columbia into three groups: (i) the earthquakes in the upper crust of the overlying continental North America plate, (ii) earthquakes within the subducting JdF plate, and (iii) earthquakes occurring at the interface of these two plates. The seismicity in the subducting JdF crust and mantle is shown in Fig. 5.3. The depth to the top of the subducting JdF plate from prior studies is also shown as contours (Hyndman *et al.* 1990; Crosson and Owens 1987; Cassidy and Ellis 1993).

The maximum age of the subducting JdF plate at the deformation front is 9 MA and such a young lithosphere is thin, flexible and extremely buoyant due to the high ratio of less dense crust to more dense mantle (Rogers 1988; Kirby *et al.* 1996; Peacock 1996). Young lithosphere may have negative buoyancy and subducts into the asthenosphere only after the basaltic rocks in the oceanic crust undergo a phase change to high density eclogite at about 50 km depth. The phase change marks the

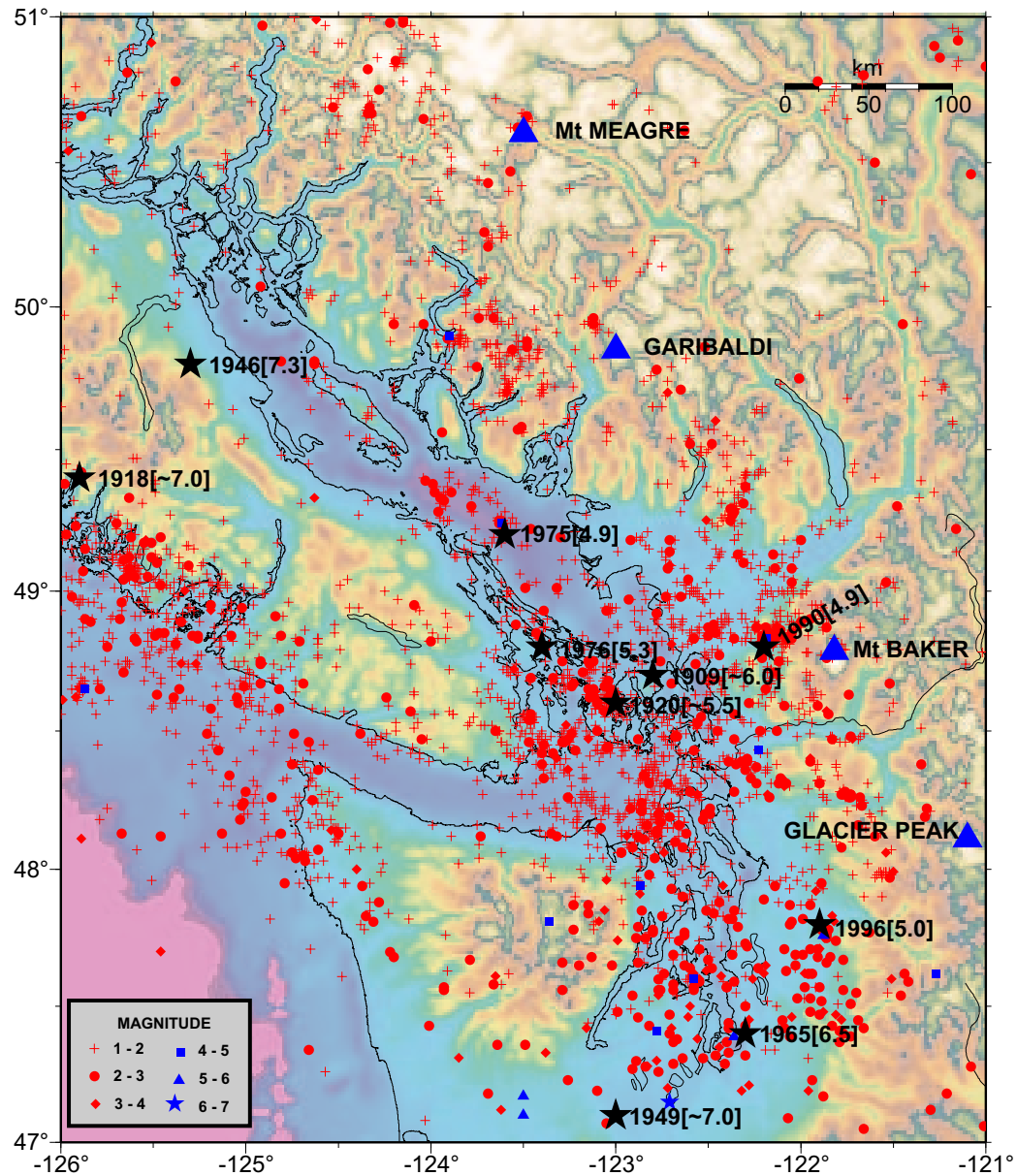


Figure 5.1 Earthquake data (crustal and slab seismicity) of southwestern British Columbia and northwestern Washington from 1984–2000. Seismicity data from Geological Survey of Canada (GSC) database. The black stars denote the locations of great earthquakes.

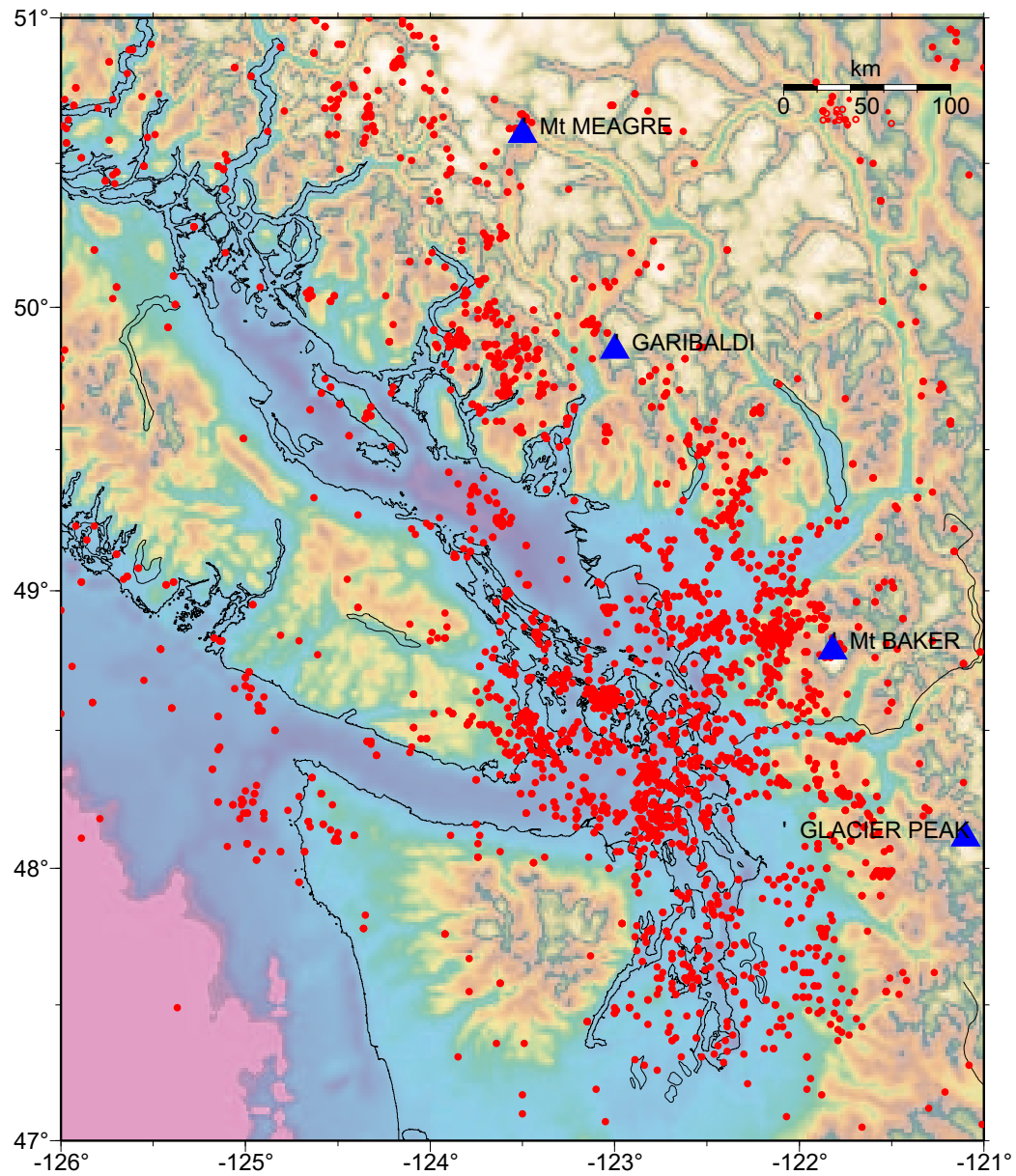


Figure 5.2 Crustal earthquakes in southwestern British Columbia and northwestern Washington from 1984–2000.

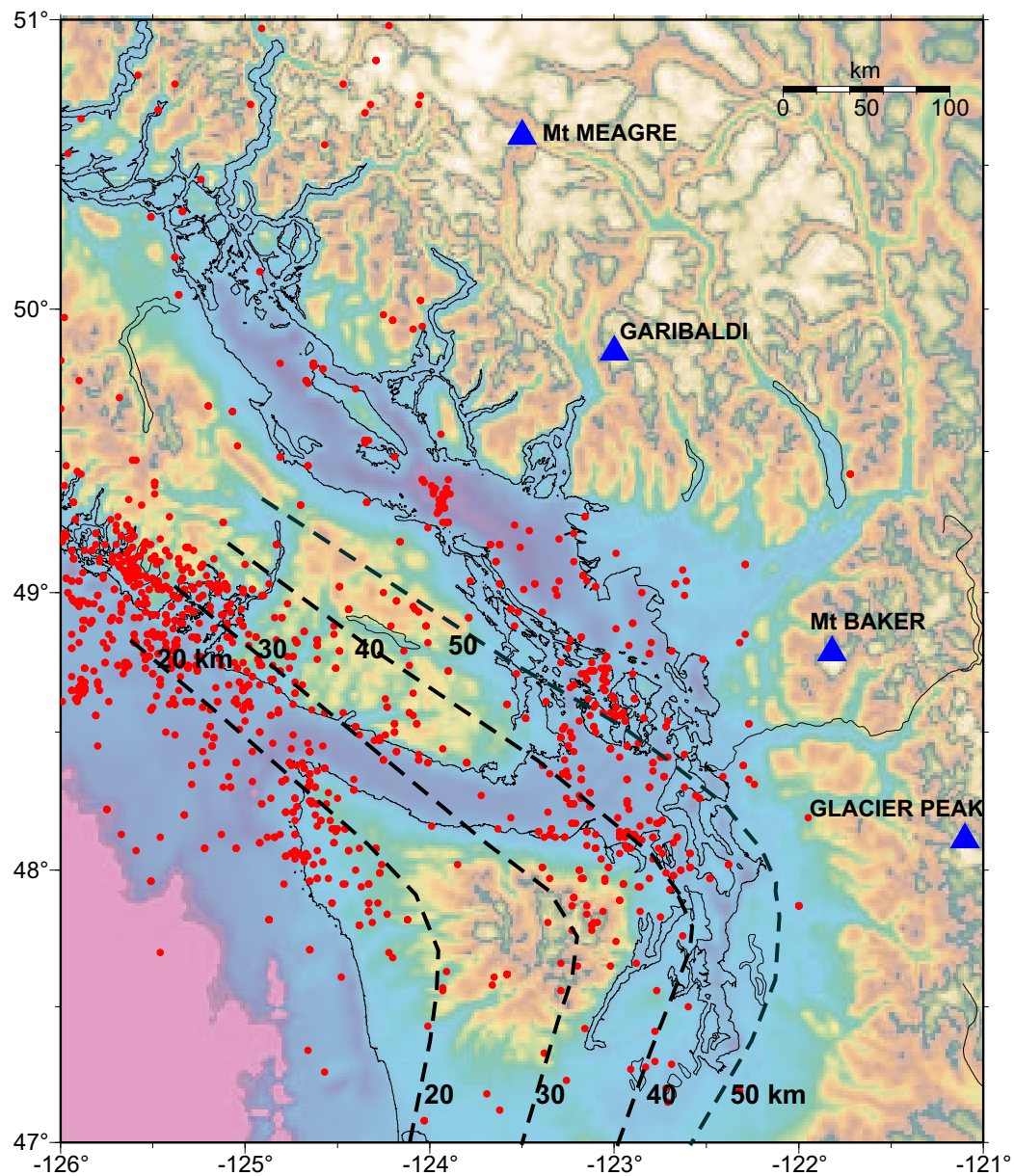


Figure 5.3 Wadati-Benioff earthquakes in southwestern British Columbia and northwestern Washington from 1984–2000. Depth to the top of the subducting JdF plate are represented as contours. Depth data from Hyndman and Wang (1990), Crosson and Owens (1987) and Cassidy *et al.* (1993).

transition of the slab from buoyant to non-buoyant, and appears to produce a bend in the young lithosphere. The slab bending associated with such a phase change and the slab pull may result in Wadati-Benioff earthquakes. The fluids released from metamorphic dehydration of the slab are expected to migrate upwards into the upper crust and may activate pre-existing faults under a stress regime, resulting in crustal seismicity. The metamorphic reaction associated with the phase change from basalt to eclogite increases the density of the oceanic crust by 12% to 15%. The associated decrease in volume creates large internal slab stresses, resulting in extensional stress in the crust and compressional stress in the underlying mantle (Kirby and Wang 2000). In warm and young subducting slabs such as the JdF slab, the depth at which such metamorphic changes occur is less than 100 km (Kirby *et al.* 1996).

With the above concepts providing the background, the new 3-D velocity model is interpreted to further the knowledge of the subsurface disposition of the continental crust and subducting JdF crust and mantle, and to derive pointers to origin and location of earthquakes.

5.3 Margin Parallel and Perpendicular Lines

In this section, vertical velocity sections generated along Vancouver Island margin parallel and perpendicular lines are interpreted for identification of the major features. The location maps of the lines parallel and perpendicular to the orientation of southern Vancouver Island are shown in Figs. 5.4 and 5.5, respectively. The margin parallel lines are 340 km in length. The margin perpendicular lines are 155 km in length and are oriented N62°E, approximately in the direction of plate convergence. In the velocity sections, only cells sampled by rays are shown. The interpreted sections of all the margin parallel and perpendicular lines are provided on the CD-ROM which accompanies this thesis (Appendix IV). Here, a few key lines are presented for

discussion of the mapped subsurface features and their geological significance. Margin parallel lines presented in this chapter for discussion are S1, S2, S3, S4, S5 and S7 (Figs. 5.6 to 5.11). Margin perpendicular lines presented for discussion are D4, D5, D7, D10, D12, D13 and D15 (Figs. 5.12 to 5.18).

The 3-D velocity model derived from tomographic inversion is a smooth representation of the true subsurface velocity structure. The subsurface is represented as blocks of constant velocity. In the present study the block size is $(3 \times 3 \times 3)$ km. The continuous representation of the actual subsurface structure is mathematically mapped by the discrete representation of a physical property, i.e. velocity. In addition, the smoothness constraints imposed for solving the ill-conditioned tomography problem yield a smooth structure with no discontinuities. These two aspects must be taken into consideration in interpretation. The interpretation is carried out here by analysing the velocity structure, the bounds of the minimum and maximum velocity in the structure, and prior knowledge of a given structure/lithology where available.

The range of seismic P wave velocities estimated in Wrangellia rocks, Pacific Rim Terrane, Crescent/Siletz Terrane rocks and sedimentary basins are as described in Chapter 4. P wave velocities in the mafic/ultramafic rocks mapped in the forearc beneath southern Vancouver Island and in the Puget Sound region at a depth of approximately 25 km are in the range of 7.0–7.5 km/s (Symons and Crosson 1997; Stanley *et al.* 1999). Velocities of Core rocks of the Olympic Mountains range from 5.6 to 6.5 km/s (e.g. Clowes *et al.* 1987, Crosson *et al.* 2000). Brocher *et al.* (2001) described the P velocity values for rocks of the Olympic Core complex to be in the range of 5.5–6.0 km/s with an accuracy of 0.2–0.3 km/s.

Brocher and Christensen (2001a) measured P and S velocity of twenty-nine mafic rocks (mainly basalts taken from the Crescent Formation) and eleven greywackes from the accretionary wedge of the Olympic core complex outcropping in the Olympic Peninsula and Puget Lowland. The measured P wave velocity for Olympic mafic rocks at room temperature and pressure of 600 MPa range from 5.59–6.94 km/s.

The measured P wave velocity for Olympic greywackes at room temperature and pressure of 600 MPa range from 5.03–6.24 km/s. The mean P wave velocities for the two different rock suits, at almost all confining pressures, differ by at least 1 km/s (Brocher and Christensen 2001a)

Continental mantle velocity is in the range of 7.4–7.8 km/s and oceanic upper mantle velocity is close to 8.0 km/s (McMechan and Spence 1983; Miller *et al.* 1997; Stanley *et al.* 1999). In the subducting Juan de Fuca plate the main velocity contrast is expected at the Moho of the oceanic mantle (8.0–8.2 km/s) with the subduction thrust at the top of the oceanic crust (6.75–7.0 km/s), normally about 7 km above. In the smooth inversion model, the JdF Moho is taken at an intermediate velocity of 7.5 km/s and the thrust is approximately 7 km higher assuming average oceanic crustal thickness (Fowler 1990). The location of the relocated earthquakes indicate that the uncertainty in locating the top and bottom of the JdF slab may be with in ± 2 km.

5.3.1 Interpretation of Line S1

The major geological features observed in cross section S1 are the high velocity Crescent Terrane and the low velocity Olympic Core Rocks (Figs. 5.4 and 5.6). At the 80–140 km model distance, the high velocity zone mapped above the JdF plate correlates with the structure and disposition of Crescent Terrane as outlined in Fig. 5.4 from previous studies. From the observation of the velocity contrasts and the trend of the earthquakes at this location, the Crescent Terrane is interpreted to lie structurally above the JdF plate. This feature is also mapped well in lines S2, S3 and S4, discussed in later sections.

The velocity contrast between the Olympic Core rocks with the Crescent Terrane stands out with clarity. The top of the JdF plate (> 6.5 km/s) is mapped clearly beneath the Core rocks (< 6.5 km/s) due to the significant velocity contrast. The

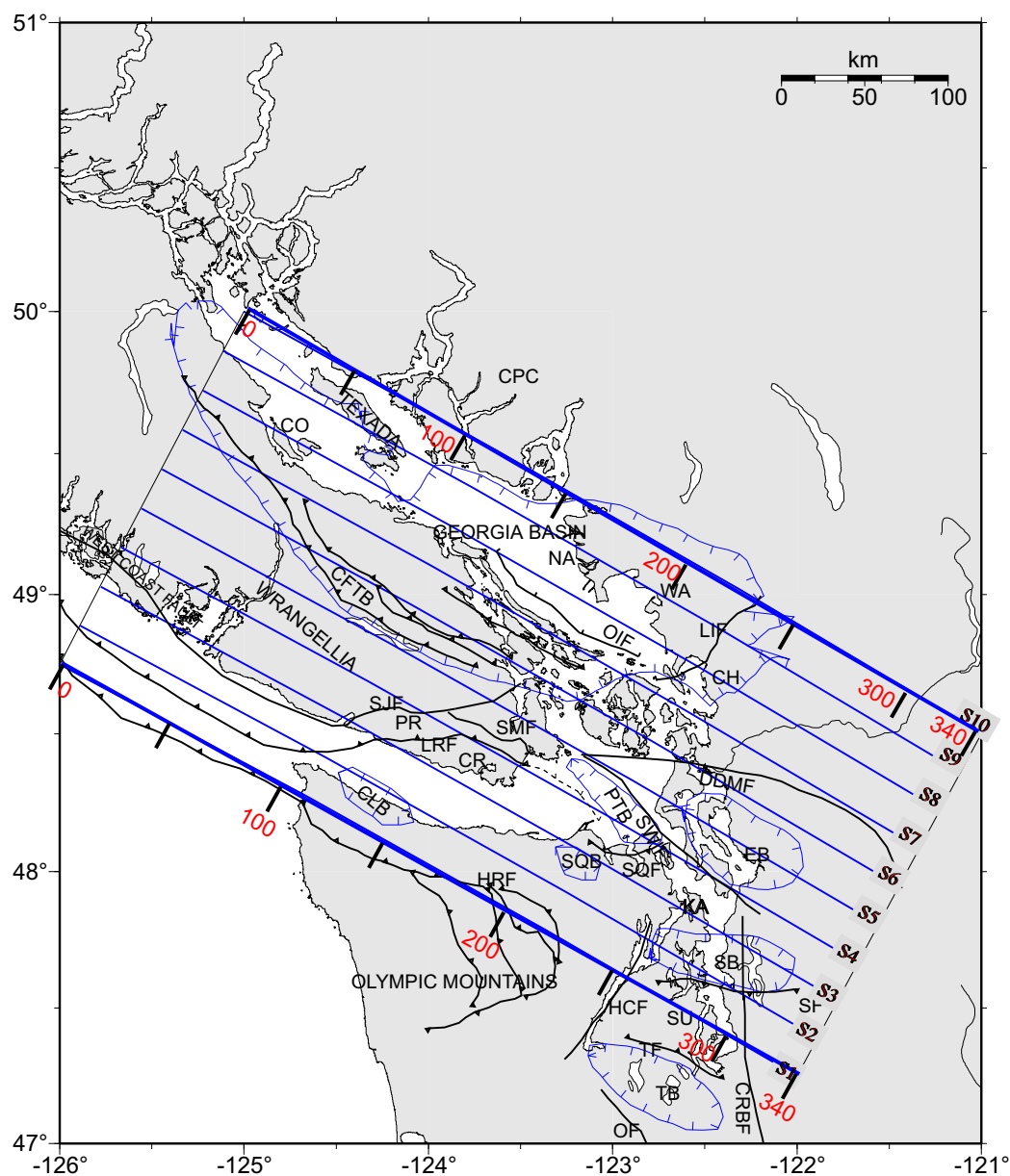


Figure 5.4 Location map of margin parallel lines used in the study. Abbreviations as in Fig. 1.3.

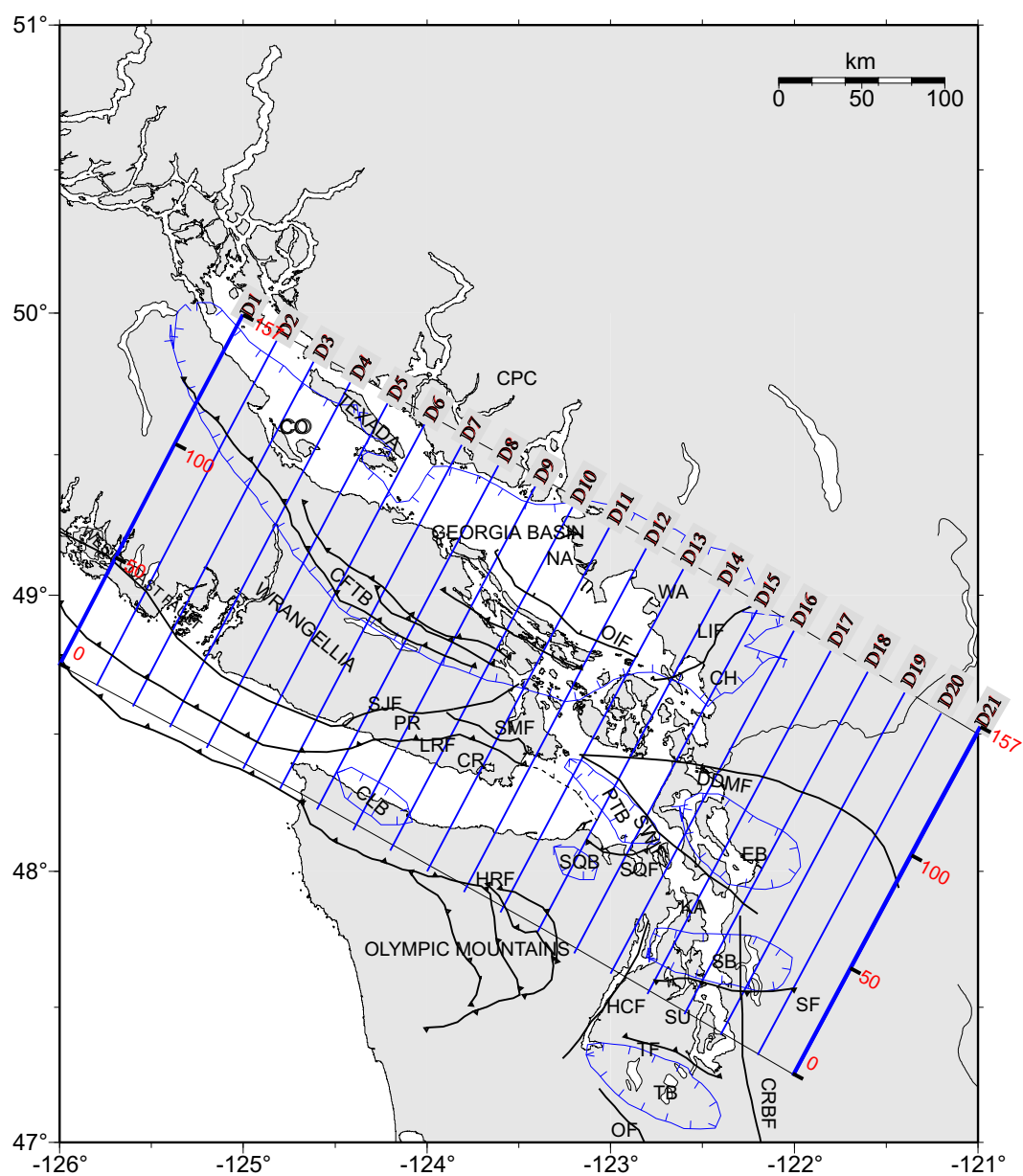


Figure 5.5 Location map of margin perpendicular lines used in the study. Abbreviations as in Fig. 1.3.

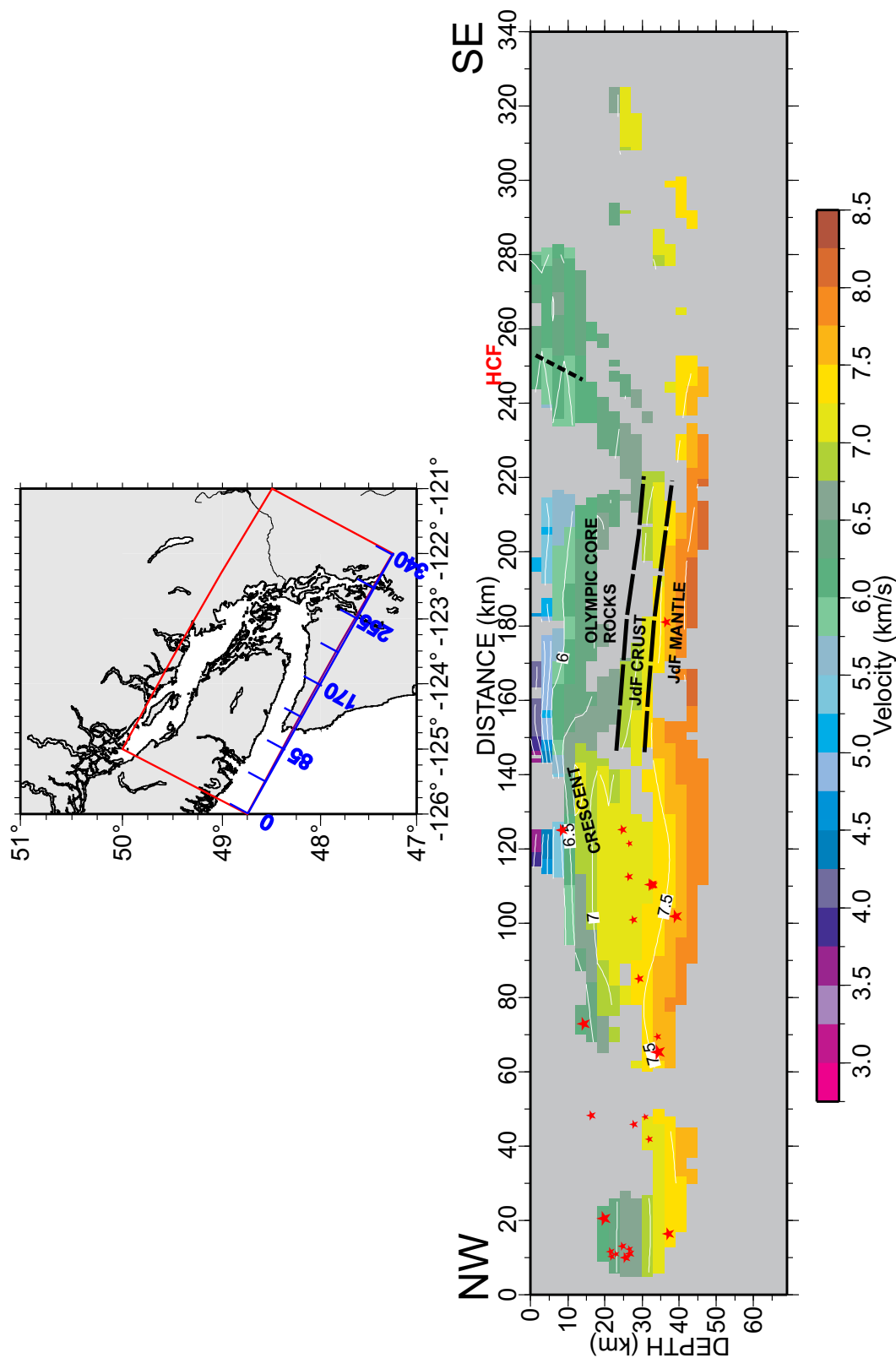


Figure 5.6 Vertical velocity slice along line S1. Abbreviations as in Fig. 1.3.

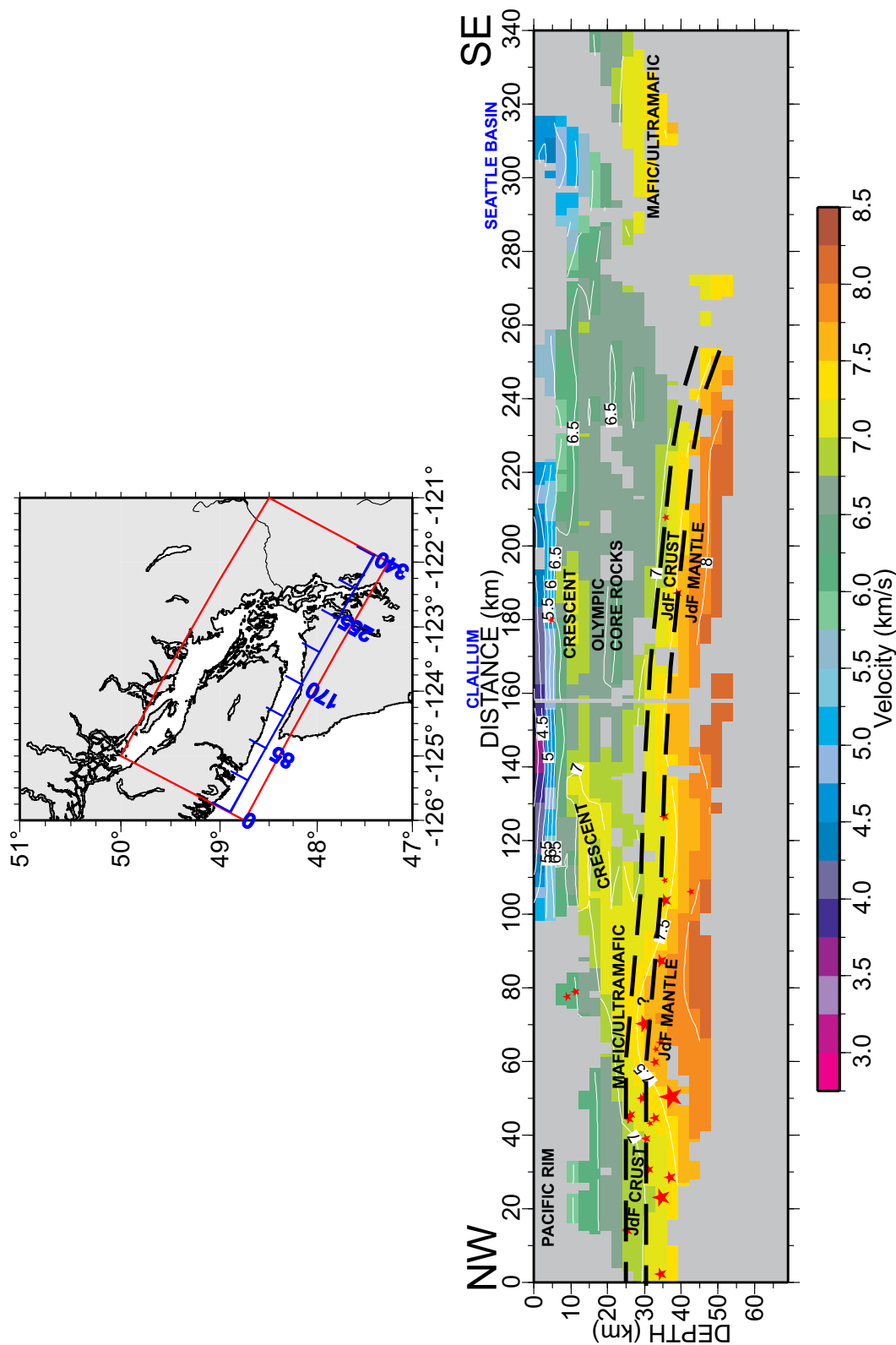


Figure 5.7 Vertical velocity slice along line S2. Abbreviations as in Fig. 1.3.

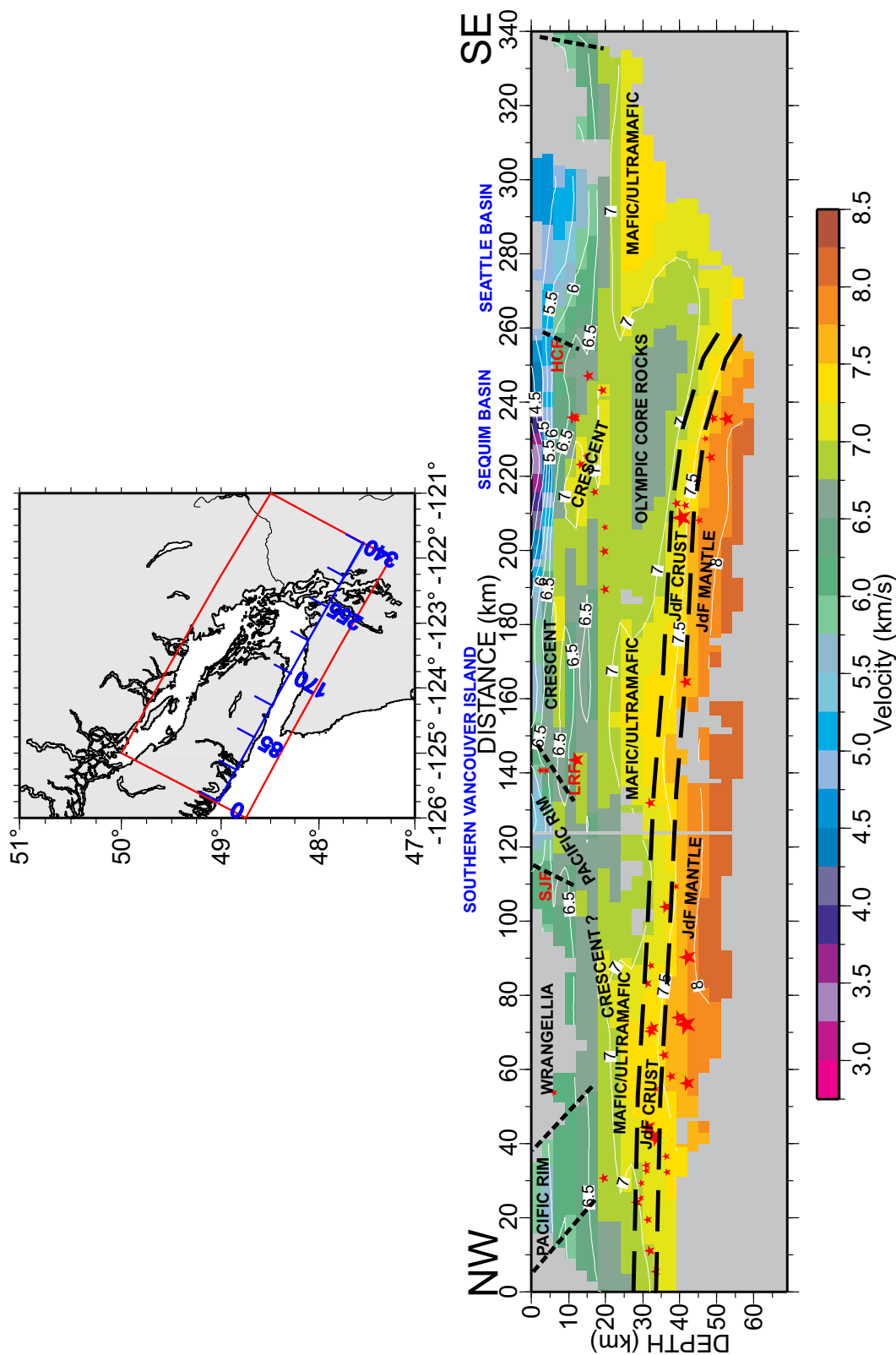


Figure 5.8 Vertical velocity slice along line S3. Abbreviations as in Fig. 1.3.

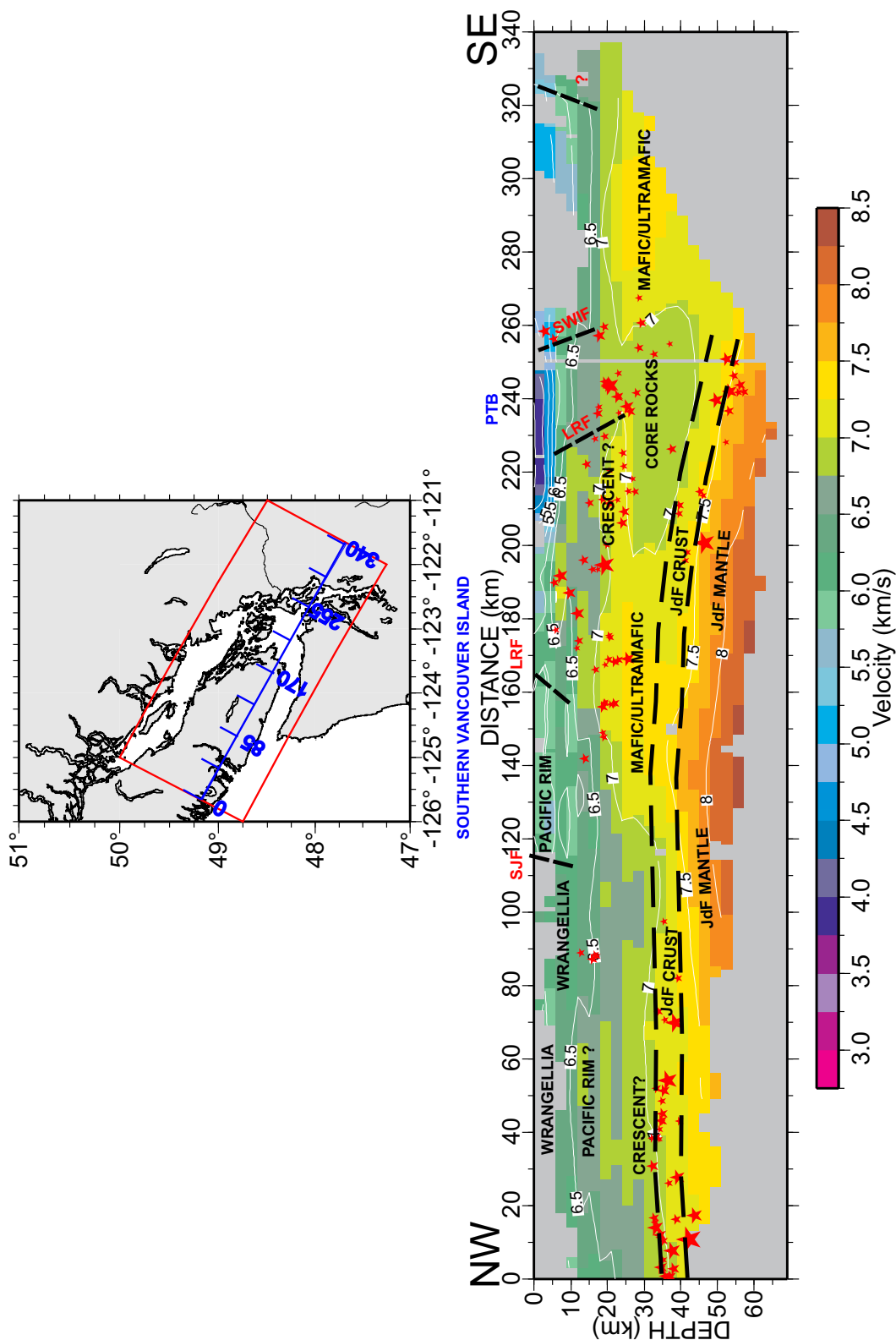


Figure 5.9 Vertical velocity slice along line S4. Abbreviations as in Fig. 1.3.

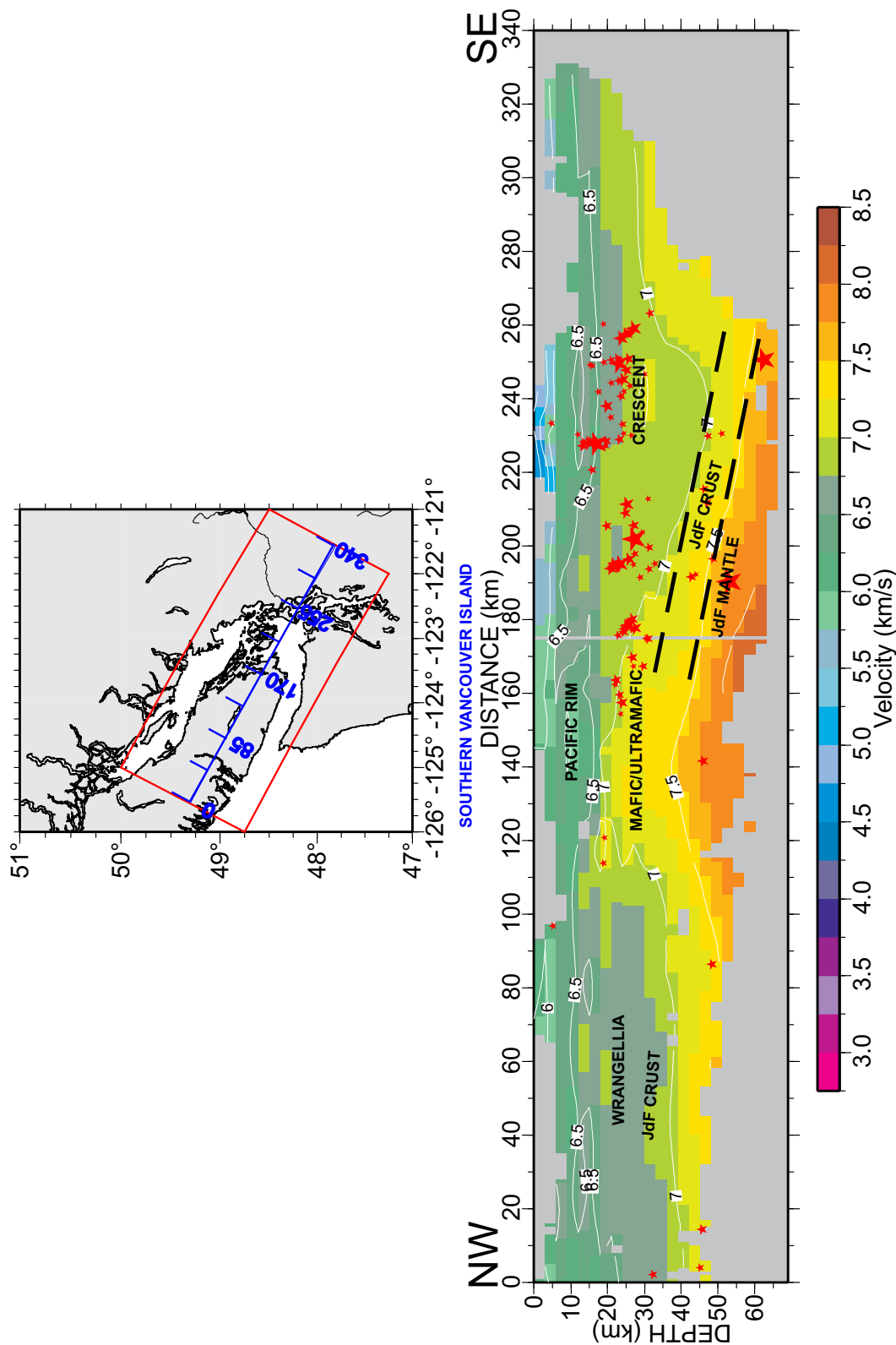


Figure 5.10 Vertical velocity slice along line S5.

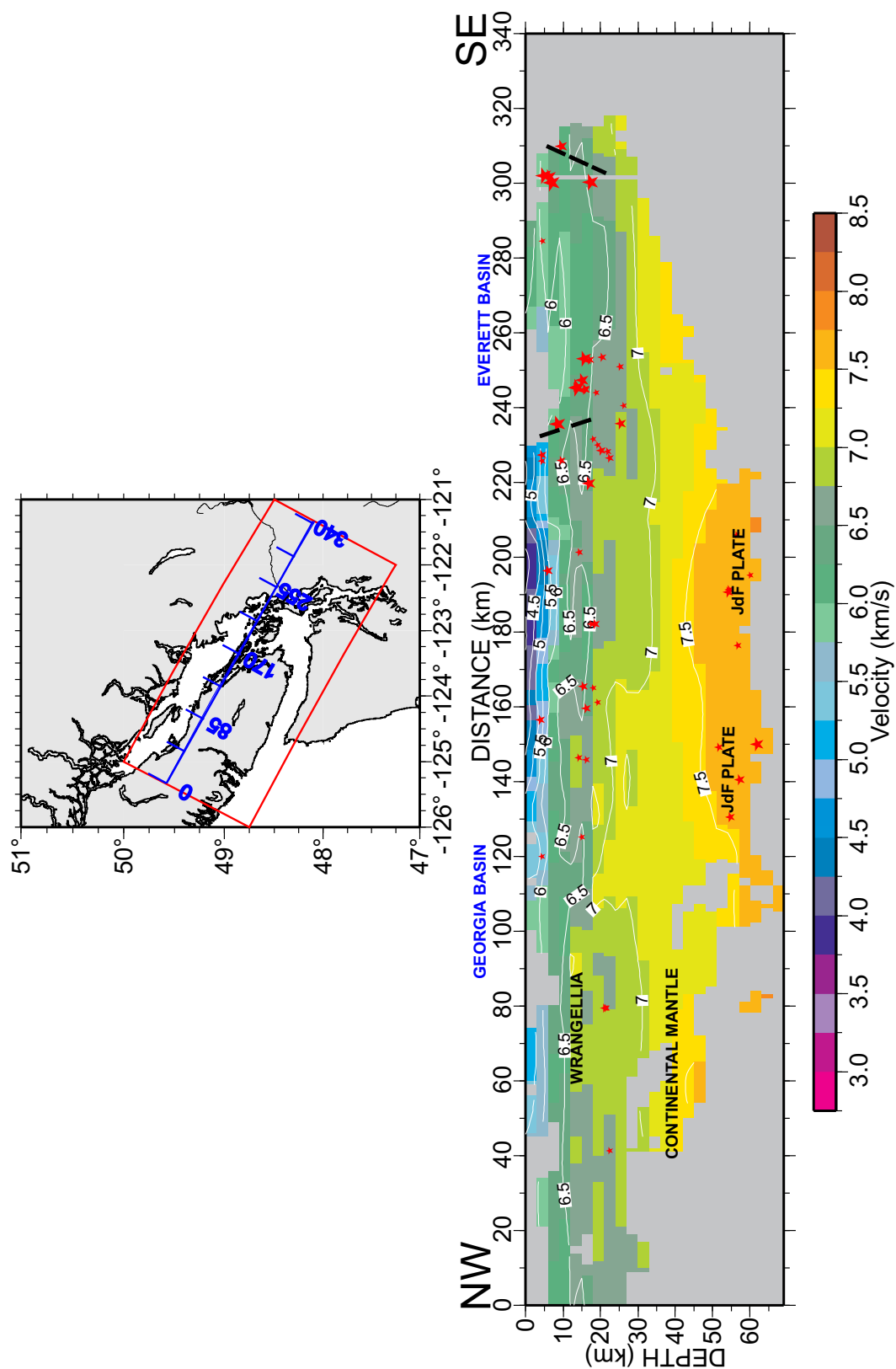


Figure 5.11 Vertical velocity slice along line S7.

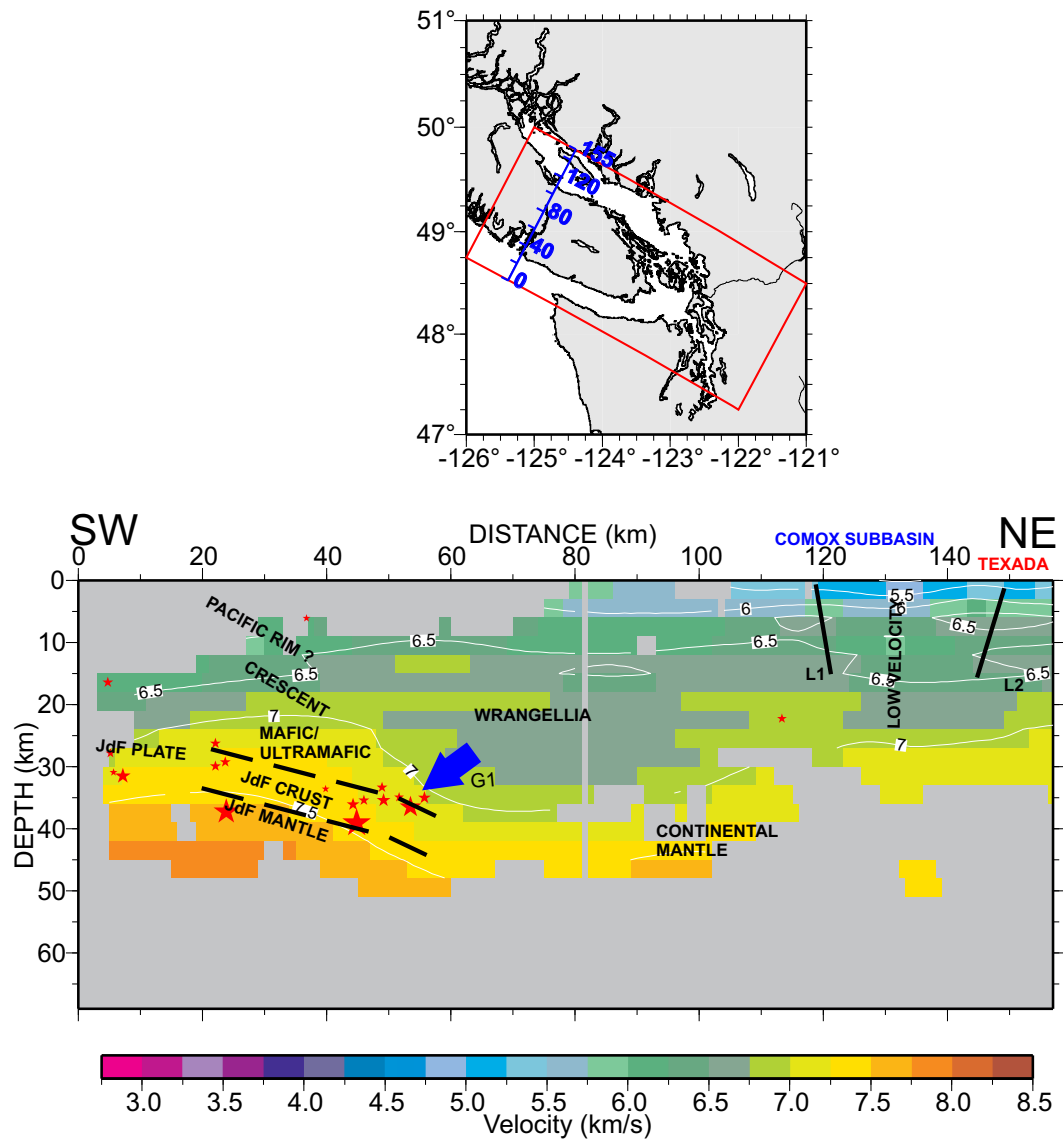


Figure 5.12 Vertical velocity slice along line D4. Description of G1, L1 and L2 given in text.

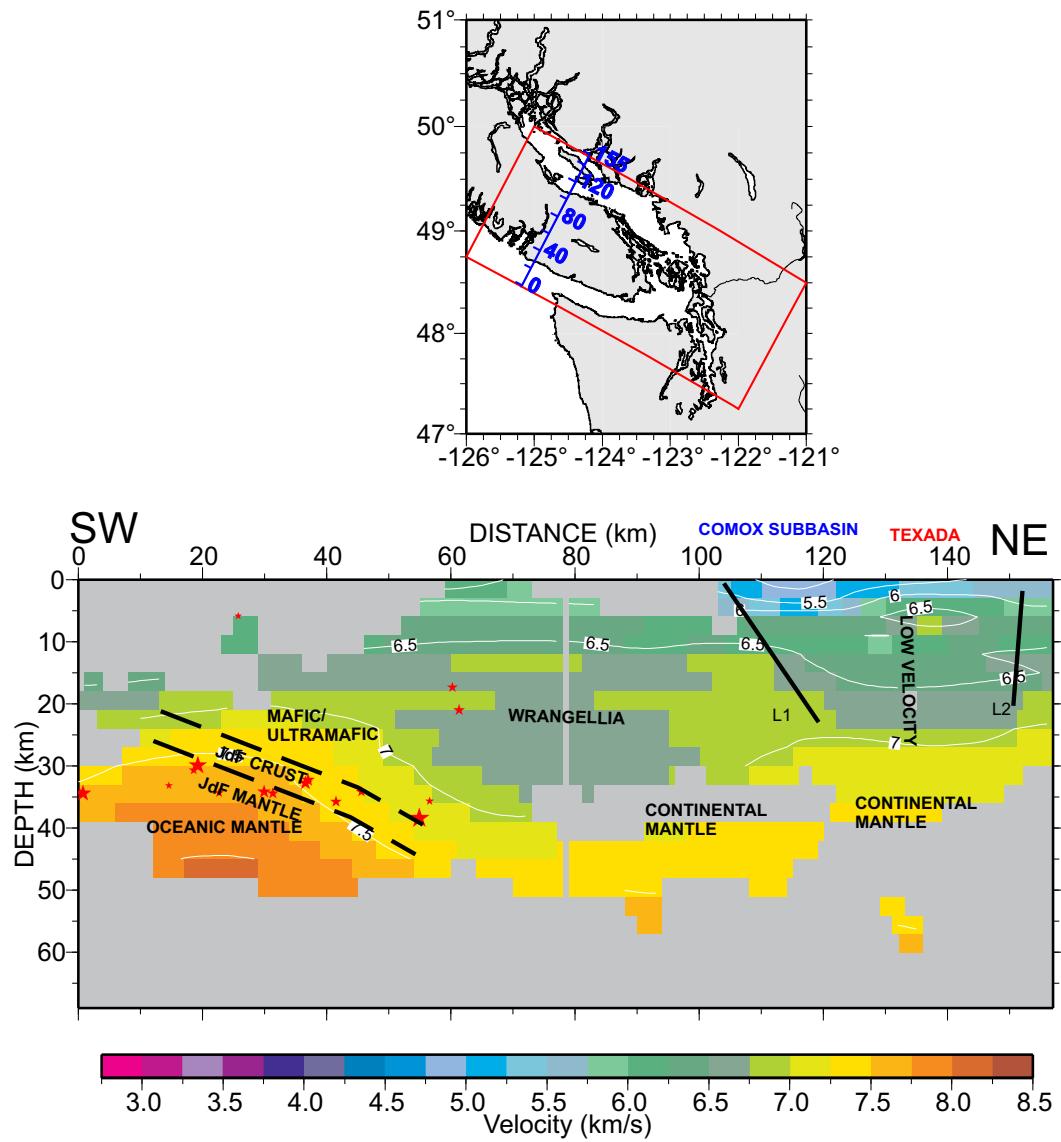


Figure 5.13 Vertical velocity slice along line D5. Description of L1 and L2 given in text.

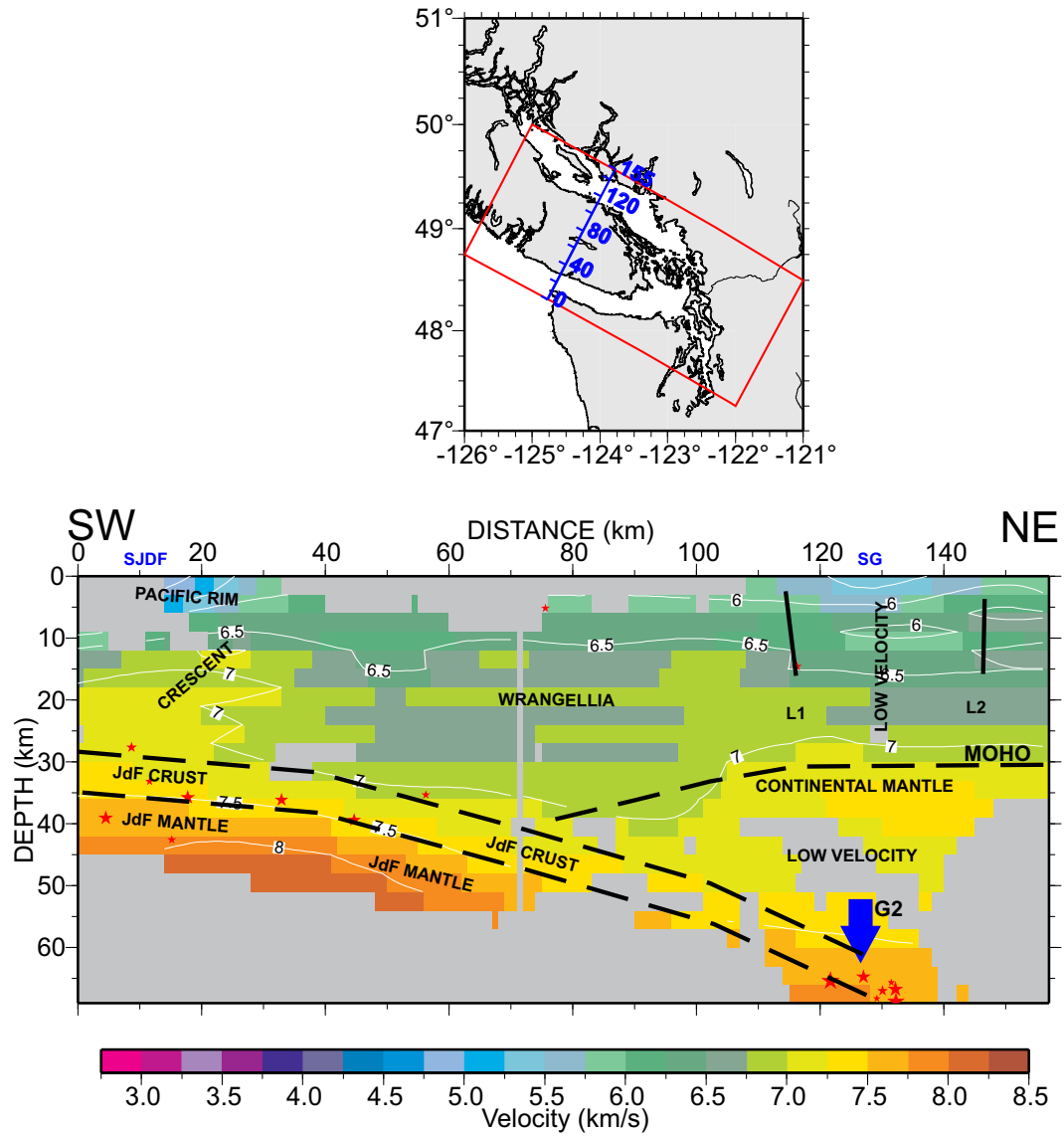


Figure 5.14 Vertical velocity slice along line D7. SJDF-Strait of Juan de Fuca; SG-Strait of Georgia. G2 - cluster of slab earthquakes. Description of L1 and L2 given in text.

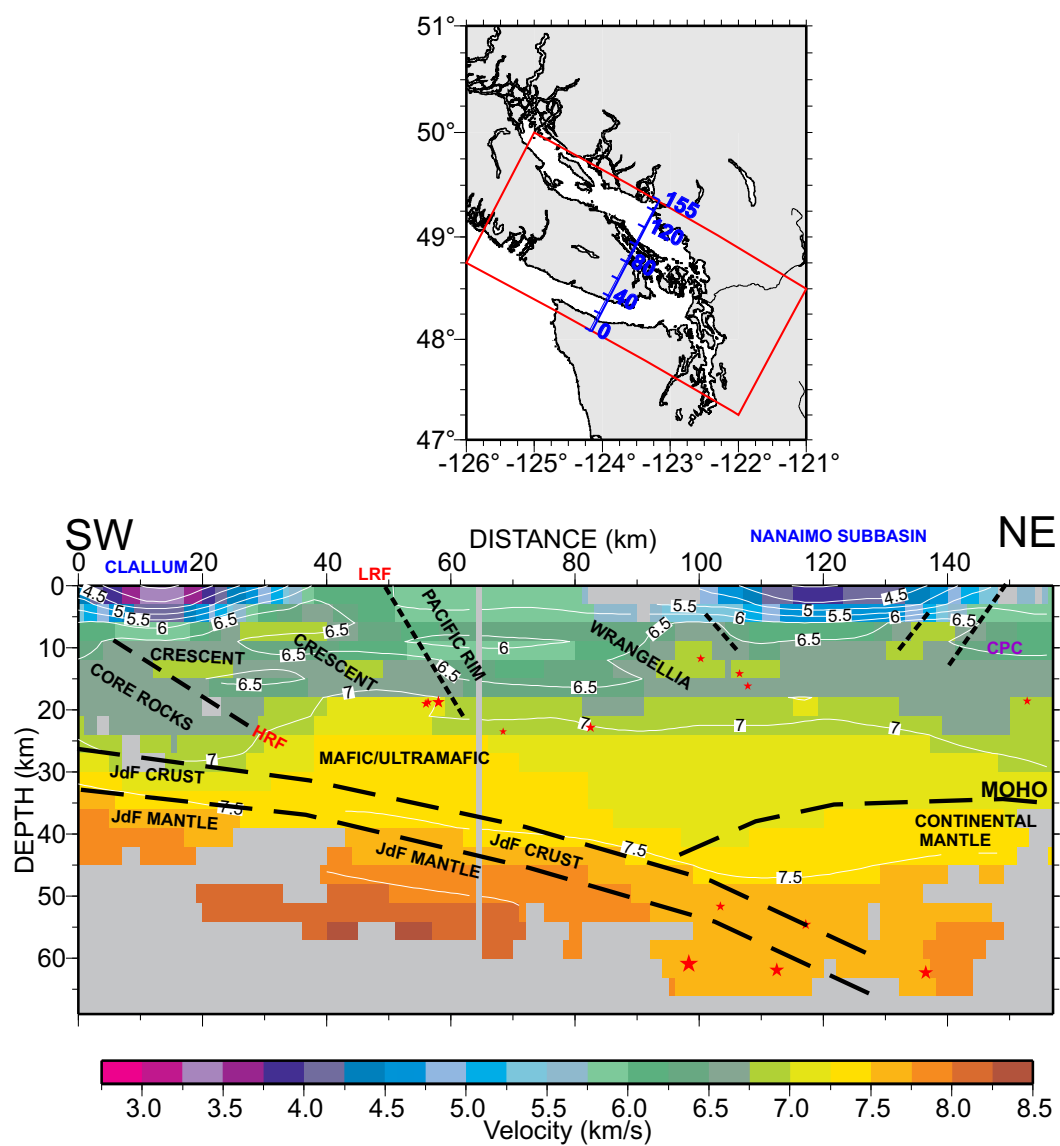


Figure 5.15 Vertical velocity slice along line D10. Abbreviations as in Fig. 1.3.

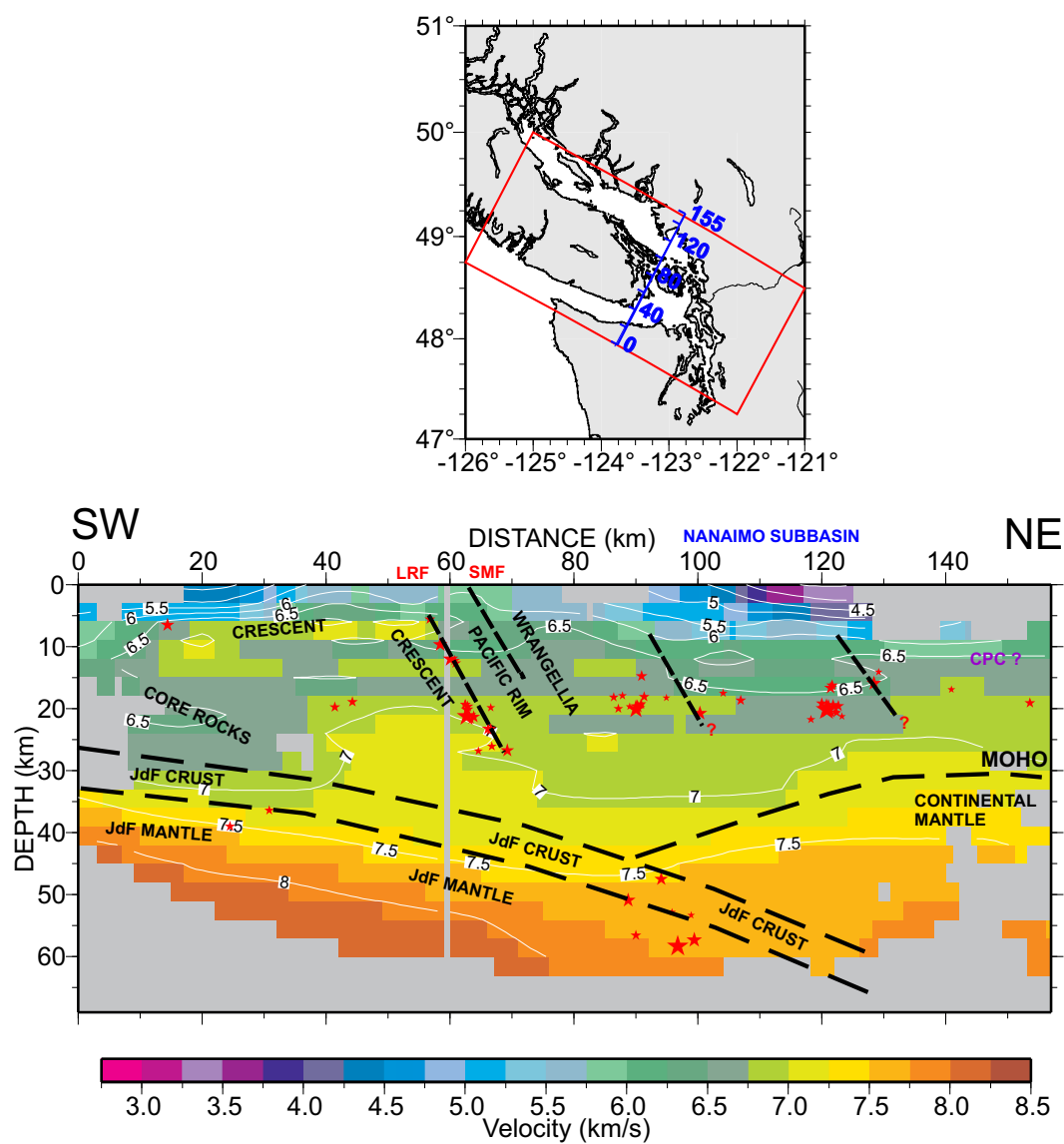


Figure 5.16 Vertical velocity slice along line D12. Abbreviations as in Fig. 1.3.

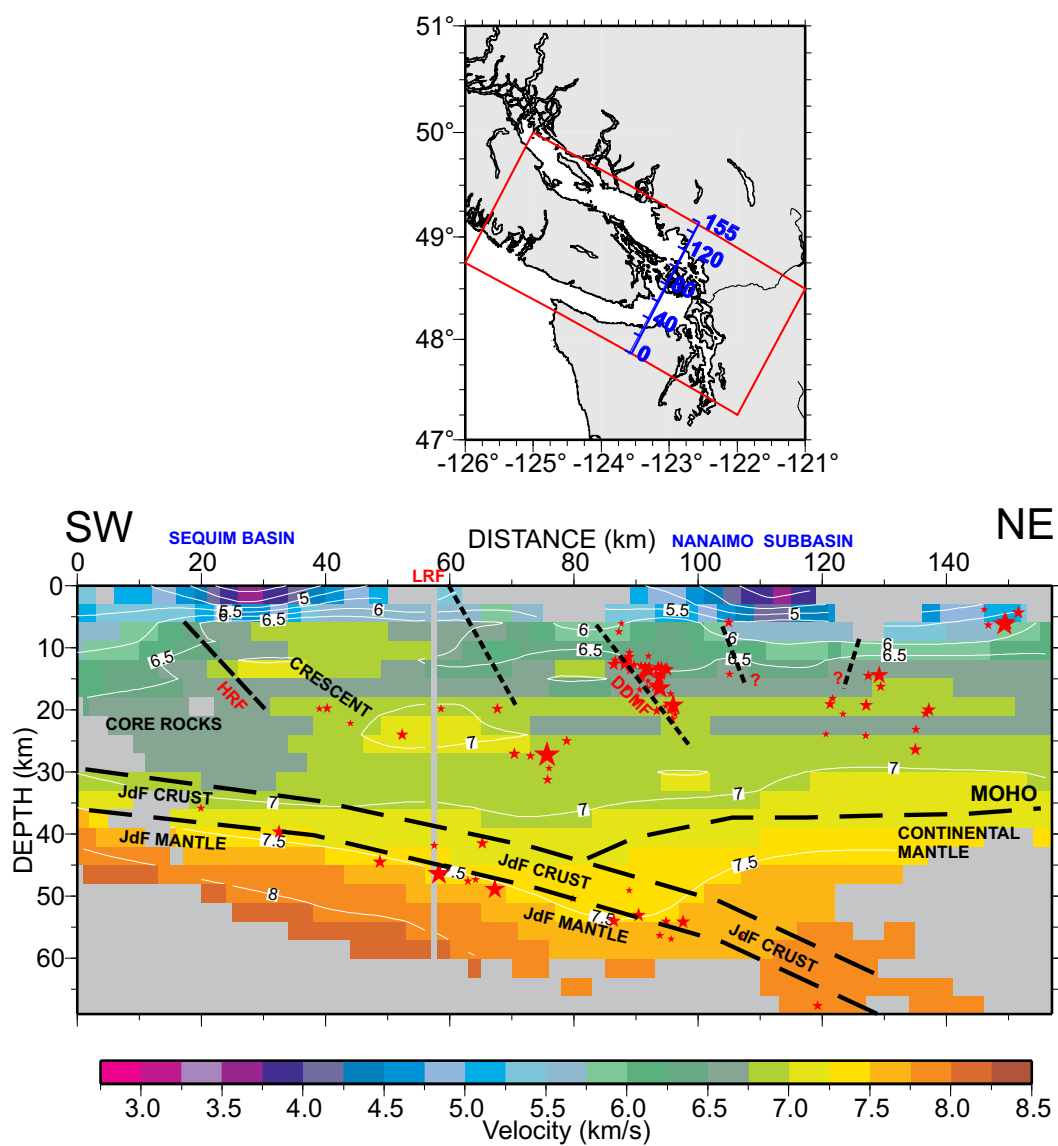


Figure 5.17 Vertical velocity slice along line D13. Abbreviations as in Fig. 1.3.

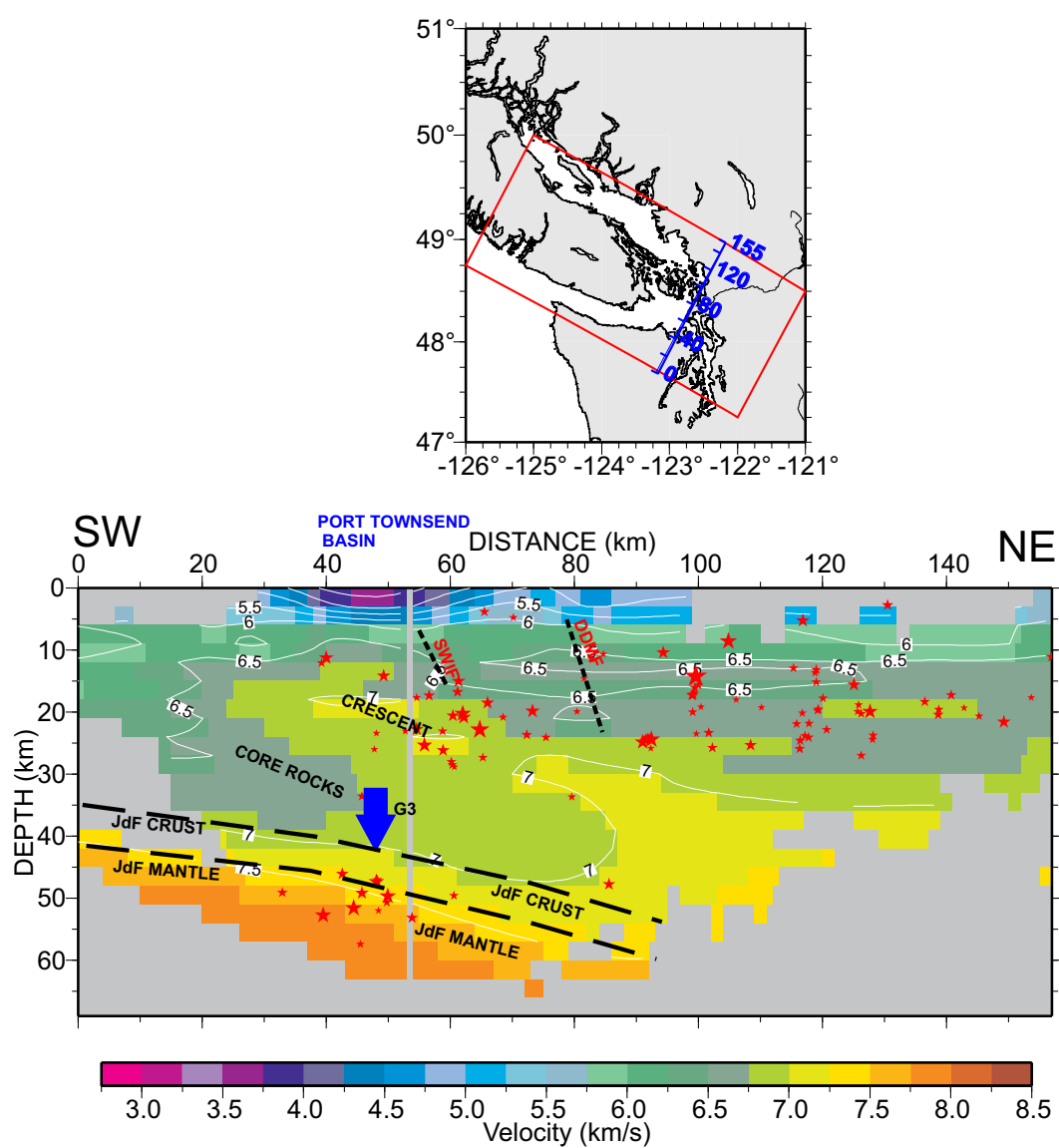


Figure 5.18 Vertical velocity slice along line D15. Abbreviations as in Fig. 1.3. Description of G3 given in text.

small velocity contrast at the 250 km model distance coincides with the location of the Hood Canal fault.

5.3.2 Interpretation of Line S2

Significant earthquake activity is observed in the subducting plate at 0–100 km model distance on profile S2 (Fig 5.7). This is thought to be related to the stress regime created by the subduction of the JdF plate beneath the Crescent Terrane. The Crescent Terrane is observed to be continuous from the sediment basement down to the top of the plate at 80–140 km model distance. At the base of Crescent Terrane at the 70 km model distance, a high velocity zone of 7.25–7.5 km/s is mapped which is considered as the equivalent of the higher velocity material mapped beneath the 320 km model distance (Puget Sound) at a depth of 25 km. These features are interpreted in a manner similar to that discussed by Stanley *et al.* (1999), as the anomalous lower crust composed of mafic and ultramafic cumulates which formed in the large rift system that generated the Crescent Formation.

5.3.3 Interpretation of Line S3

In line S3, three high velocity structures above the JdF crust, with mafic to ultramafic velocities of 7.25–7.5 km/s, are mapped distinctly at locations 40–80 km, 140–160 km and 280–300 km (Fig. 5.8). These locations lie at a depth of 25 km beneath Barkley Sound, southern Vancouver Island and Puget Sound. The high velocity unit mapped beneath southern Vancouver Island shows structural continuity with the high velocity Crescent Terrane, which extends to its mapped location at the surface. The high velocity may be associated with mafic gabbros of the Crescent Terrane or with an ultramafic mantle base to this terrane. In the upper crust, a series of earthquake locations lie at 190–250 km model distance, which are closely associated with the Crescent Terrane imaged at 220 km distance. The high velocity units are

possibly related to Crescent Terrane, as these units underlie the locales of Crescent Terrane at all the three places. At 210–260 km model distance, the Olympic Core rocks are clearly mapped beneath the Crescent Terrane. The dip of the plate changes rapidly here and a few well located earthquakes are mapped in the uppermost part of the slab.

In the upper crust, the contact between Wrangellia, Pacific Rim and the Crescent terranes are identified with clear velocity contrasts at the San Juan fault and the Leech River fault (Figs. 5.4 and 5.8). The Sequim basin, filled with low velocity sediments, is mapped at the 225 km model distance on the profile. The thickness of the low velocity sediments in the Seattle basin at the 300 km model distance is approximately 10 km. The structural elements mapped beneath the Seattle basin are in good agreement with the results of Stanley *et al.* (1999).

5.3.4 Interpretation of Line S4

The earthquake activity in the JdF plate at the 0–80 km model distance on profile S4 (Fig 5.9) is prominent. The high velocity unit beneath southern Vancouver Island is prominent in the velocity section and is continuous with the Crescent Terrane. Shallow earthquake activity is observed beneath southern Vancouver Island, extending from near the surface to the top of the underlying high velocity unit. Close to the 220 km model distance on the profile, the Leech River fault is mapped and is seen as an extension in the eastern Strait of Juan de Fuca. The upper subducting plate is well mapped by earthquakes at 245 km model distance between 50–60 km depth. The high velocity unit mapped at the 280–300 km model distance shows structural continuity with the upper Crescent Terrane unit. A gentle arch in the plate is mapped along this profile and is prominent at 140 km model distance.

5.3.5 Interpretation of Line S5

In line S5, the Wrangellia units are mapped at 0–100 km model distance and show very little large-scale velocity variation, except for a few streaks of high velocity in the upper crust (Fig 5.10). The average velocity of Wrangellia rocks observed is in the range of 6.5–6.75 km/s. The earthquake activity in the upper crust between 180–260 km model distance follows definite spatial patterns and may be related to subsurface faults. The high velocity unit is mapped above the subducting plate, beneath southern Vancouver Island, and intermediate-depth crustal earthquakes are observed at 160–210 km model distance close to these units. The arch in the plate is prominent centered at 140–150 km distance.

5.3.6 Interpretation of Line S7

The lower Wrangellia units are mapped with a velocity of 6.75–7.0 km/s at the 60–160 km model distance on profile S7 (Fig 5.11). This velocity is higher than those mapped on profile S5. This may be explained by the fact that these two profiles fall on either side of the Cowichan Fold and Thrust Belt and may represent lithologically different suites of rocks. The velocity interval of 7.25–7.5 km/s, mapped at 60–260 km model distance, is at a depth of ~ 36 km and is interpreted to be representative of the transition zone from continental crust to mantle. The low velocity sediments to depths of 3–6 km in the Georgia basin at 40–230 km distance are mapped with significant clarity. The earthquakes observed from the 120–190 km model distance are at depths of 55–65 km and indicate the slab position. These depths are in close agreement with the relocated hypocentral depths for the earthquakes beneath the Gulf Islands reported by Cassidy and Waldhauser (2001).

5.3.7 Interpretation of Line D4

Profile D4 (Fig. 5.12) is situated along the main Lithoprobe Corridor discussed in detail by Hyndman (1995). The velocities map a mafic/ultramafic unit above the subducting plate that lies structurally beneath the Crescent Terrane. At 50 km model distance, a number of earthquake locations at a depth of 35–40 km (G1) map the upper subducting plate. The dip of the plate is observed to change after this model distance. Over 50–100 km model distance, the upper crustal velocities for Wrangellia rocks are uniform, except for a streak of high velocity observed at 20 km depth. At 100–120 km model distance, lower Wrangellia rocks have a higher velocity than to the west of the CFTB, indicative of a lithological/structural boundary. The velocity at 100 km distance at a depth of 40–45 km is interpreted to indicate the transition to continental Moho (the underpinnings of Wrangellia). At 120–150 km distance, a low velocity structure extends down to 20 km beneath the Strait of Georgia. The low velocity feature (between L1 and L2) is observed clearly beneath the Strait of Georgia in all the margin perpendicular profiles that cut through the strait.

5.3.8 Interpretation of Line D5

In line D5, a set of well defined earthquakes is observed between 30–40 km depth at 0–40 km model distance (Fig. 5.13), indicative of the subducting plate. The thickness of the mapped ultramafic unit is relatively smaller than that in profile D4. Streaks of mid-crustal high velocity material are mapped over the 50–100 km model distance, at a depth of 10–20 km. The upper crustal structure beneath the Comox subbasin and Texada Island is mapped clearly over 100–150 km model distance. The broad low velocity zone (between L1 and L2) beneath them in the Strait of Georgia extends down to a depth of ~ 20 –25 km.

5.3.9 Interpretation of Line D7

Line D7 is a key velocity section that brings out clearly some of the major aspects of subduction (Fig. 5.14). The Crescent Terrane is mapped over 0–30 km model distance; this terrane extends down to the mafic/ultramafic unit structurally above the subducting plate. A set of well defined earthquakes between depths of 27–36 km over 10–55 km model distance defines the location of the subducting plate. The dip of the plate is observed to increase beyond 40 km model distance on the profile. Wrangellia rocks show a suite of alternating high and low bands at 50–95 km model distance. At 130 km, beneath the Strait of Georgia there is a cluster of earthquakes at 65 km depth (G2). These earthquakes appear to occur within the subducting slab and are likely due to internal stresses caused by the basalt to eclogite phase change reactions. The low velocity zone observed above this region may be explained by the upward migration of fluids released by the phase change reactions. The low velocity feature (between L1 and L2) is observed clearly beneath the Strait of Georgia.

5.3.10 Interpretation of Line D10

The mafic unit lying structurally above the plate, at 40–70 km model distance, is mapped with clarity in line D10 (Fig. 5.15). This mafic unit is again observed to be continuous with the high velocity Crescent Terrane above. The northeastern limit of Crescent Terrane is clearly depicted by the Leech River fault which is observed to be a continuous velocity boundary down to 20 km depth. Beneath the Clallum basin, the Crescent Terrane forms the basement which in turn is underlain by the Olympic Core Rocks. The subducting plate is well defined at the southwest end of the profile at 22 km depth. The plate is observed to exhibit a change in dip at 80 km model distance (close to the Gulf Islands). The Nanaimo subbasin structure is mapped above the more steeply dipping portion of the subducting plate. Towards the end of the profile the transition zone to continental Moho is mapped at a depth of 35 km.

5.3.11 Interpretation of Line D12

Profile D12 (Fig. 5.16) shows a distinct line of earthquakes extending along the projected dip of the Leech River fault at 60 km model distance. This plane of earthquakes is strongest on this profile but is also observed on adjacent lines. At 45–55 km depth and the 90 km model distance, a scattered cluster of slab related earthquakes are mapped, perhaps associated with a steepening slab dip. The thick sediment column in the Nanaimo subbasin is mapped at the 130 km model distance. Continental mantle is mapped at a depth of 35 km at the northeast end of the profile, with velocities reaching 7.5 km/s at 40 km depth.

5.3.12 Interpretation of Line D13

On line D13, the subducting JdF crust is observed clearly extending from a depth of 30 km at 10 km model distance to 55 km at 90 km distance (Fig. 5.17). At the SW end of the profile, low velocities of the Olympic Core rocks are clearly identified above the JdF crust. The Hurricane Ridge fault that separates the Olympic Core rocks from the overlying Crescent Terrane is mapped from 20–30 km model distance. Velocities within the Crescent Terrane at 40–60 km model distance (6.5–6.75 km/s) are higher than those of the Core rocks (6.25–6.5 km/s). The subducting JdF crust and mantle are well defined along this profile by a plane of earthquakes aligned along the 7.5 km/s contour. In the upper crust, the Clallum and the Georgia basins are mapped with clarity with sediment thicknesses of approximately 6 and 8 km, respectively. The Devils Mountain fault, starting beneath the southern tip of Vancouver Island, is possibly associated with the cluster of earthquakes located at a depth of 10–20 km at 90 km model distance.

5.3.13 Interpretation of Line D15

Line D15 shows the underthrusting of accretionary rocks beneath Crescent Terrane between 30–50 km model distance (Fig. 5.18). At this location, the Crescent Terrane swings to the south, bounded to the east by the Southern Whidbey Island fault. High earthquake activity is observed in the upper crust along the full profile northeast of 50 km model distance. At 50 km model distance (southern tip of Vancouver Island), a group of slab related earthquakes are mapped at a depth of 45–50 km centered on the 7.5 km/s contour (G3). In the uppermost crust, the outline of the Port Townsend basin is mapped with a sediment thickness of less than 5 km at 50 km model distance.

5.4 Interpretation of Regional Geology

In this section the geological features mapped and interpreted from the SHIPS tomography velocity model in Chapter 4 (SV) and the earthquake tomography velocity model (EV) in this chapter are consolidated to form a comprehensive interpretation.

5.4.1 Sedimentary Basins

Four main Cretaceous to Recent sedimentary basins and a number of subbasins are mapped by the velocity model. The lateral extent of the Georgia basin is mapped at most locations in the 5.5 km/s isovelocity map constructed from the SV model (Fig. 4.13). A thick sedimentary column of approximately 6–8 km exists between $48.7^{\circ}N$ and $49.25^{\circ}N$ in the Nanaimo subbasin (Figs. 4.10 and 4.13). The northwestern part of the Georgia basin is observed to be considerably shallower than that to the southeast (Fig. 4.13). The Comox subbasin with a maximum sediment thickness of approximately 3–4 km is mapped on the northwestern edge of the Georgia basin (Fig. 4.13). These values are in agreement with the results reported by Zelt *et al.* (2001). The Clallum basin in the Strait of Juan de Fuca, with a WNW-ESE trend,

is identified in the isovelocity surface and correlates well with the corresponding low on the gravity anomaly map (Fig. 4.15). The maximum sediment thickness observed in Clallum basin is approximately 5–6 km (Figs. 4.10 and 4.13). In the SV model, the Port Townsend basin is mapped in the eastern Strait of Juan de Fuca with a maximum sediment thickness of approximately 4–5 km (Fig. 4.13). Brocher *et al.* (2001) observed low velocities in Port Townsend basin down to a depth of 7 km. However, they presented an explanation that favors a thinner sediment column. West of the Sequim fault, the Sequim basin is mapped clearly with a maximum sediment thickness of approximately 4 km.

All the above mentioned basinal structures are clearly identified in the 5.5 km/s isovelocity surface of the EV model (Fig. 5.19). In addition, the Whatcom and Chucknaut subbasins exposed on the mainland side of the southeastern Strait of Georgia are partly mapped. A portion of the Seattle basin is also mapped in the EV model with a sediment thickness of approximately 10 km (Fig. 5.19). The 6.0 km/s isovelocity surface of the EV model (Fig. 5.20) maps the seismic basement beneath the Whatcom and Chucknaut subbasins.

5.4.2 Coast Plutonic Complex

Northwest of the Strait of Georgia, Wrangellia rocks are interpreted to be in contact with the Coast Plutonic Complex. This contact is interpreted from the relatively lower velocities (less than 6.5 km/s) observed on the eastern margin of the Strait of Georgia compared to those on the western margin (greater than 6.5 km/s) at the same depth levels (Fig. 4.10).

5.4.3 Wrangellia

Wrangellia rocks are mapped extensively beneath southern Vancouver Island in the SV model (Figs. 4.8–4.11,). The strong variation in depth of Wrangellia rocks

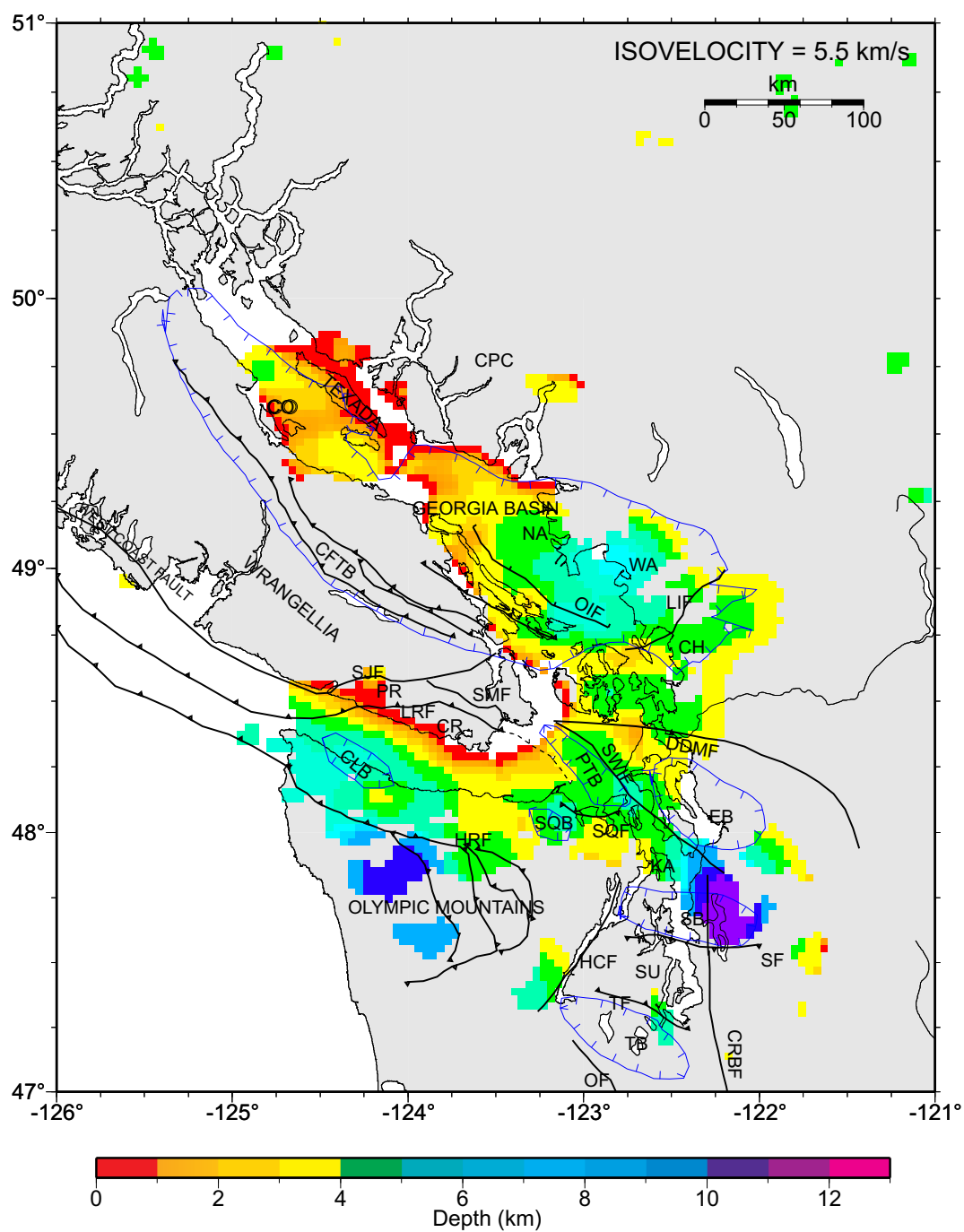


Figure 5.19 Isovelocity surface at 5.5 km/s. Abbreviations as in Fig. 1.3.

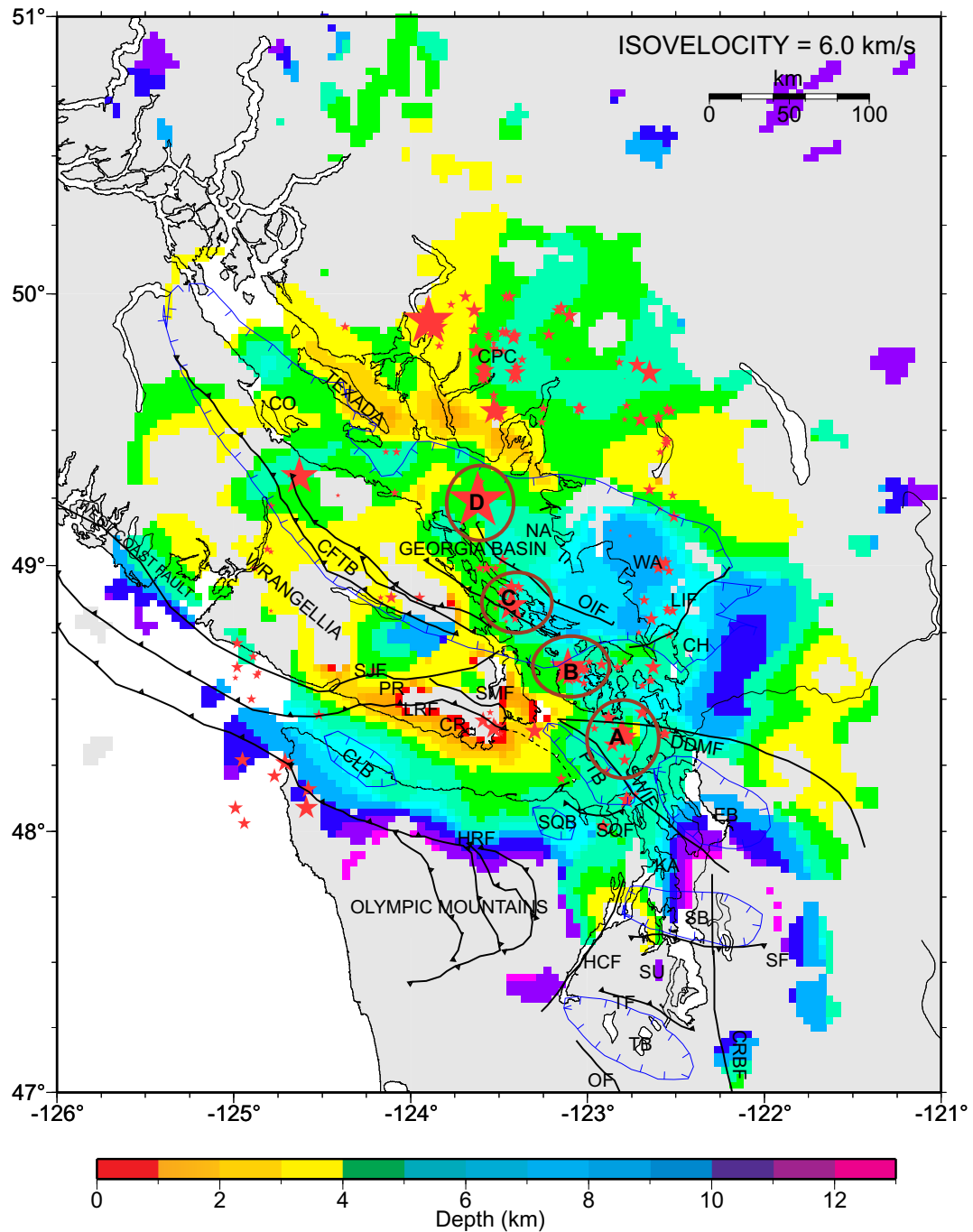


Figure 5.20 Isovelocity surface at 6.0 km/s. Abbreviations as in Fig. 1.3. A, B, C, and D represent the four clusters of earthquakes discussed in text.

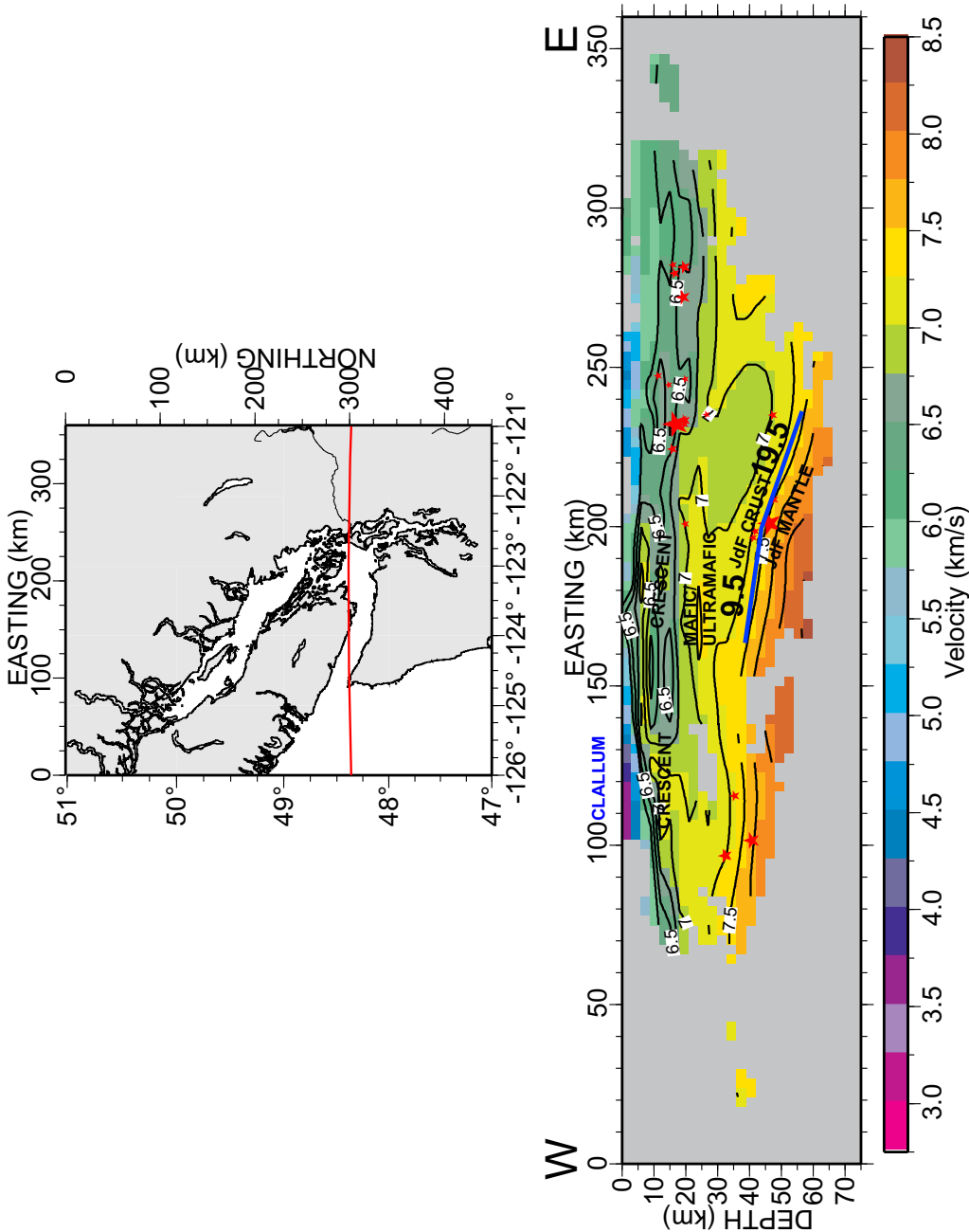


Figure 5.21 Vertical velocity slice along line EW1. Abbreviations as in Fig. 1.3.

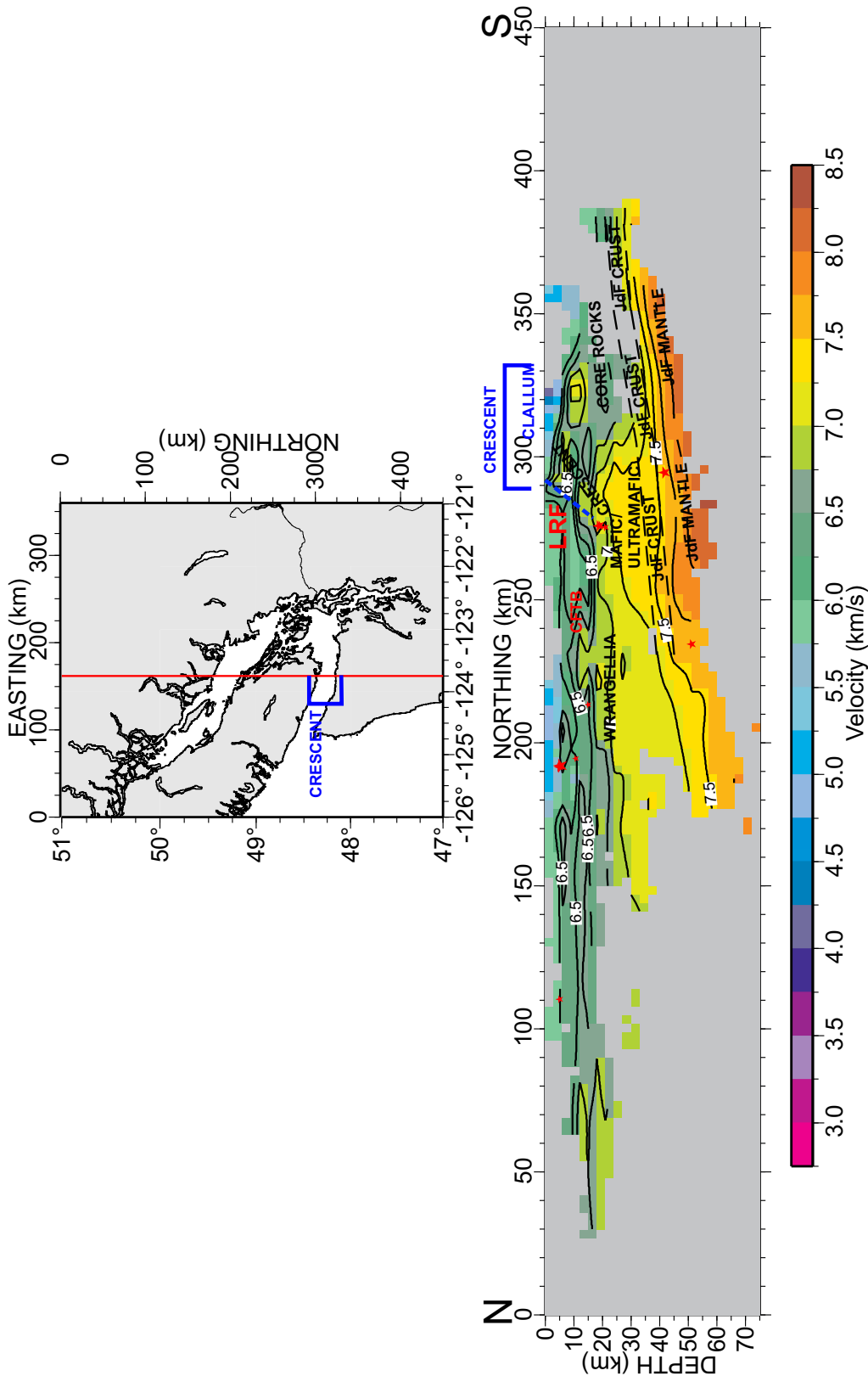


Figure 5.22 Vertical velocity slice along line NS1. Abbreviations as in Fig. 1.3.

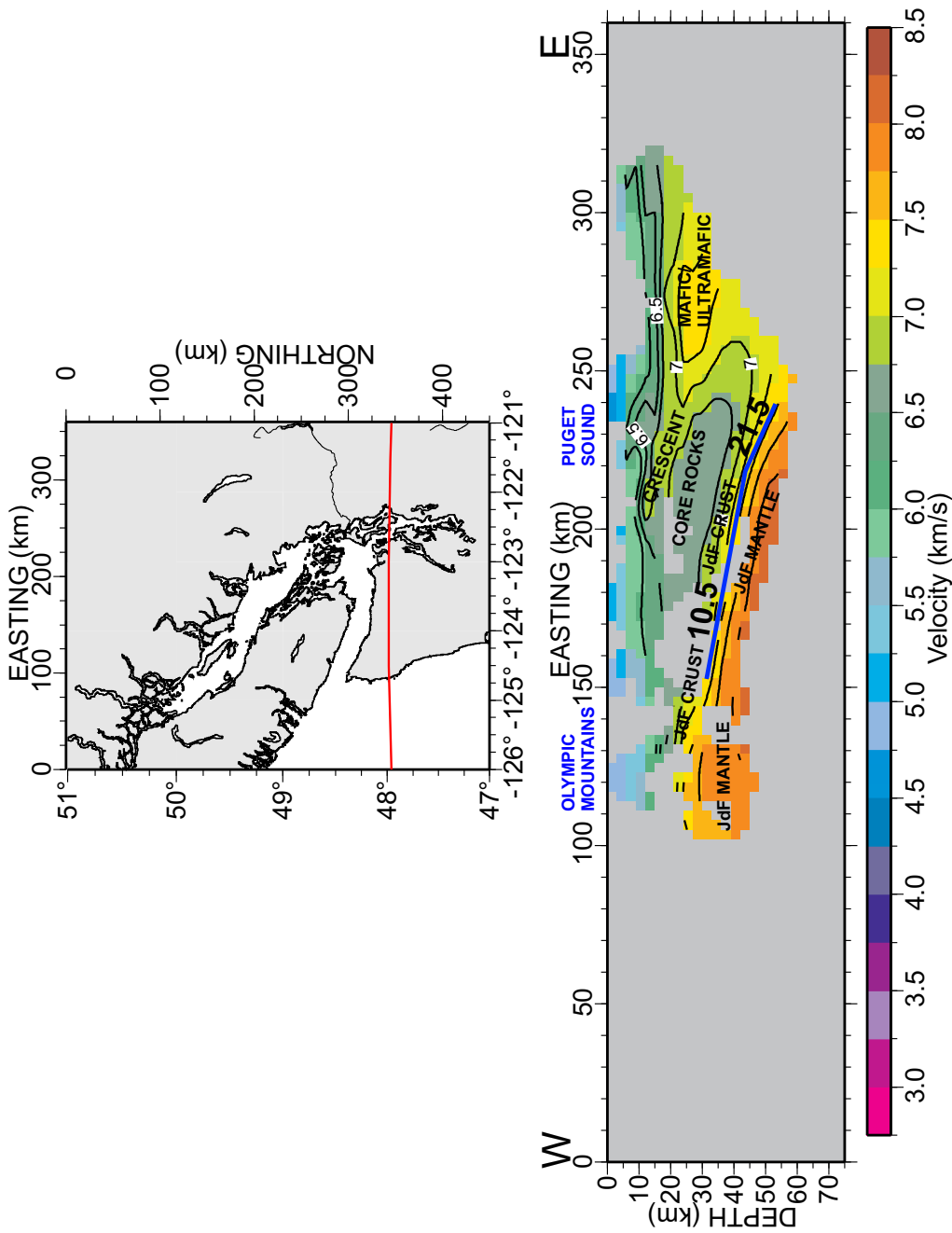


Figure 5.23 Vertical velocity slice along line EW2. Abbreviations as in Fig. 1.3.

along the Strait of Georgia is mapped in profiles P1 and P2 (Figs. 4.8 and 4.9). They are mapped at shallow depths beneath the northwestern Strait of Georgia and at deeper levels in the southeastern part. The Wrangellia basement beneath the eastern margin of the Strait of Georgia is smoother than that beneath the western margin. East-west trending highs are mapped which dissect the northwest-southeast trend of the basement structure.

In the EV model, in line S5 (Fig 5.10), the Wrangellia units are mapped at 0–100 km model distance and show very little macro velocity variation, except for a few streaks of high velocity in the upper crust. The lower Wrangellia units are mapped with a velocity of 6.75–7.0 km/s between the 60–160 km model distance on profile S7 (Fig 5.11). This velocity is higher than those mapped on profile S5. This may be explained by the fact that these two profiles fall on either side of the Cowichan Fold and Thrust Belt and may represent a lithological/structural boundary. The high velocity lower crust of Wrangellia may also possibly be due to the presence of mafic rocks.

In line D4 (Fig. 5.12), at 50–100 km model distance, the observed upper crustal velocities for Wrangellia rocks are uniform, except for a streak of high velocity observed at 20 km depth. Between 100–120 km model distance on this profile, lower Wrangellia rocks to the east of CFTB have a higher velocity than those to the west, probably indicative of a lithological structural boundary.

5.4.4 Pacific Rim Terrane

In southern Vancouver Island, the contact of high velocity Crescent Terrane with the relatively low velocity Pacific Rim Terrane is identified on the horizontal velocity slice at 3 km depth (Fig. 4.2). The low velocity Pacific Rim Terrane at this depth is clearly mapped between the Survey Mountain fault and the Leech River fault (Fig. 4.2). In vertical profile section P3 (Fig. 4.10), Pacific Rim Terrane is mapped at depth

with a clear velocity contrast. Due to limited ray coverage, Pacific Rim Terrane is mapped only at few locations in the SV model. In the EV model, Pacific Rim Terrane is clearly mapped in the margin parallel profile S3 (Fig. 5.8) between the San Juan and Leech River faults.

5.4.5 Crescent Terrane

Profile P5 in the SV model (Fig. 4.12) outlines the structure of Crescent Terrane down to 10 km depth. This profile passes through the Metchosin Igneous Complex and the observed higher velocities of 7.0 km/s correlate well with presence of gabbroic rocks. In the profile section NS1 (Fig. 5.22) generated from the EV model, Crescent Terrane (velocities up to 7.0 km/s) is observed to extend beneath the tip of southern Vancouver Island. The Crescent Terrane is mapped down to a depth of 25 km and is observed to be in continuity with the high velocity mafic/ultramafic unit mapped beneath. The Leech River fault which defines the northern termination of Crescent Terrane is mapped with a dip of 33° , outlined by a clear velocity contrast. The width of the Crescent Terrane at the surface is mapped over a distance of 40 km along this profile. In the east-west profile EW2 (Fig. 5.23), Crescent Terrane is mapped with an eastward dip beneath Puget Sound.

5.4.6 Olympic Core Rocks

The Olympic Core rocks are extensively mapped in the EV velocity model. In profile section NS1 (Fig. 5.22) the Core rocks (velocities less than 6.5 km/s) extend beneath the Crescent Terrane as far north as 300 km model distance. This location is interpreted as the northern limit of the Core rocks. In the east-west profile EW2 (Fig. 5.23), the underthrusting of Core rocks beneath the Crescent Terrane is observed at the 220 km model distance (beneath Puget Sound). This is associated with a velocity reversal of approximately 0.5 km/s and is in agreement with the velocity reversal

discussed by Crosson *et al.* (2000).

5.4.7 Mafic/Ultramafic Units

In profile S3 (Fig. 5.24), mafic/ultramafic units with high velocities in the range of 7.25–7.5 km/s at depths of approximately 25 km are identified beneath Barkley Sound (M1, 40–80 km model distance), southern Vancouver Island (M2, 140–160 km model distance) and Puget Sound (M3, 280–300 km model distance). Unit M1 beneath Barkley Sound is in agreement with the velocity model of Spence *et al.* (1985) who interpreted a high velocity sliver of material beneath western Vancouver Island and the eastern continental shelf. Unit M2 beneath southern Vancouver Island is in agreement with the velocity model of Graindorge *et al.* (2001), based on travel-time inversion of a strong wide-angle reflector at ~ 25 km depth. Unit M3 beneath Puget Sound is in agreement with the velocity model of Stanley *et al.* (1999). The high velocity unit mapped beneath southern Vancouver Island shows structural continuity with the high velocity Crescent Terrane mapped close to surface. The high velocity may be associated with mafic gabbros of the Crescent Terrane. In the upper crust, a series of earthquake locations are located over the distance range 190–250 km, and these are closely associated with the Crescent Terrane mapped at 220 km model distance. The high velocity units are possibly related to Crescent Terrane, as these units underlie the locations of Crescent Terrane at all the three places. In previous studies of reflection data from southern Vancouver Island, a 6 km thick sequence of layered reflections (The ‘E’ layer) above the subducting JdF crust were interpreted as imbricated sediments (Clowes *et al.* 1987 Figs./ 4–6). From the EV model, it appears that these reflections are more likely due to layering within the mafic/ultramafic units as no velocity reversal is observed at this depth level. The upward migrating fluids from slab dehydration below can be trapped in the layering and may possibly be responsible for the observed reflectivity.

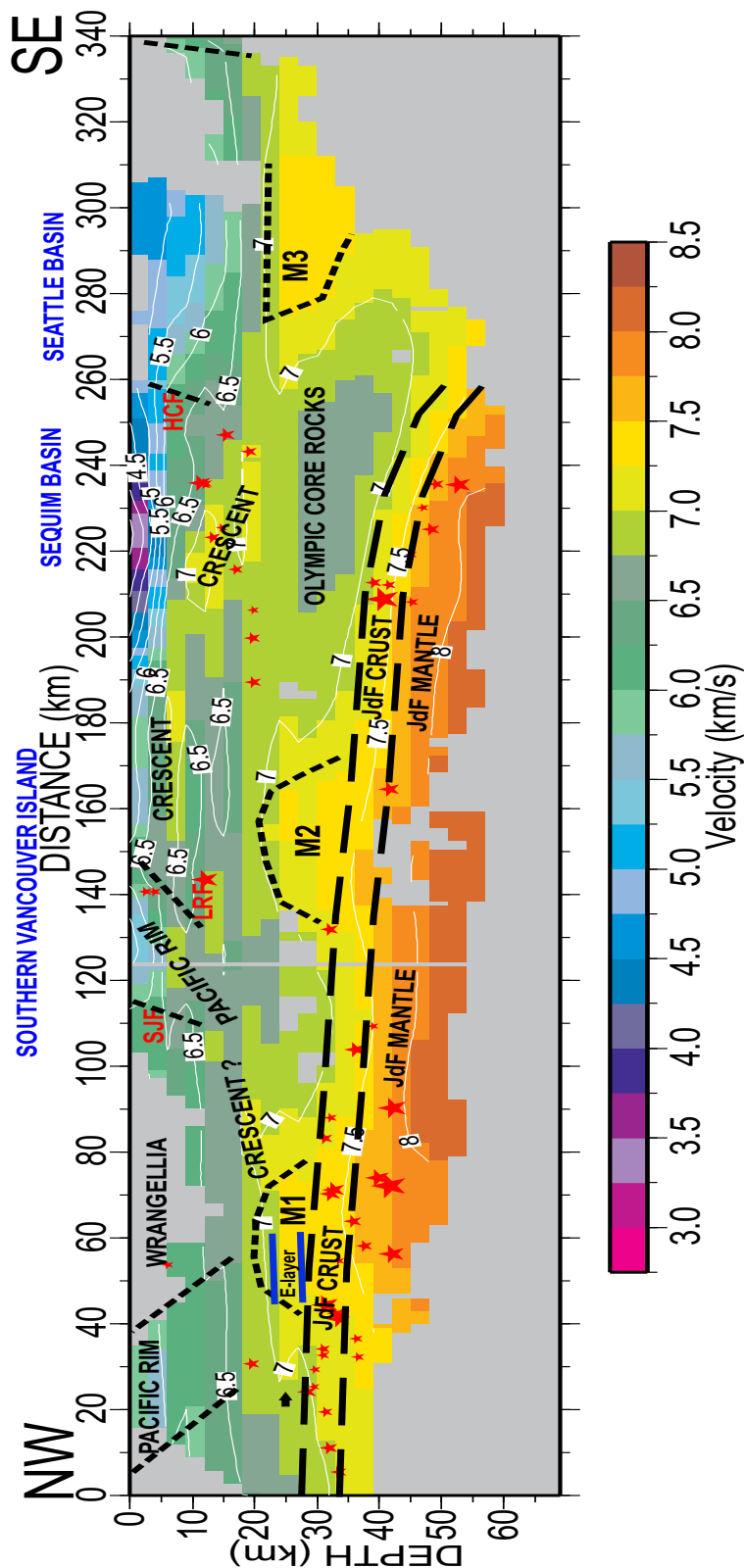


Figure 5.24 Vertical velocity slice along line S3. M1, M2, and M3 - mafic/ultramafic units. Abbreviations as in Fig. 1.3.

5.4.8 Continental Forearc Mantle

McMechan and Spence (1983) modelled continental Moho at 37 km depth for a continental upper mantle velocity of 7.5 km/s. Spence *et al.* (1985) mapped continental Moho at 37 km beneath western Vancouver Island. Miller *et al.* (1997) mapped continental Moho at a depth of ~ 42 km in Northwest Cascades Thrust System (close to Lummi Island Fault). They determined an upper mantle velocity of 7.6–7.8 km/s. In the present study, the continental mantle is not well resolved apparently because the underlying mantle rocks have unusually low velocities < 7.8 km, possibly serpentinized by fluids rising from the downgoing slab. In line D4 (Fig. 5.12), the velocity at 100 km model distance at a depth of 35–40 km is interpreted to indicate the transition from continental crust to mantle (the underpinnings of Wrangellia). In margin perpendicular lines D7, D10, D12, D13 and D15 (Figs. 5.14–5.18), the Moho is mapped at a depth of approximately 35 km in the eastern Strait of Georgia and the adjacent mainland area assuming 7.5 km/s as boundary.

5.4.9 Oceanic Crust and Mantle

The underthrusting JdF crust is mapped beneath much of the study area, although the smooth velocity model does not allow the exact mapping of the top of the crust. The main velocity contrast is expected at the Moho of the oceanic plate, where oceanic crustal velocities (6.75–7.0 km/s) contrast sharply with oceanic mantle velocity (8.0–8.2 km/s). Only a small velocity contrast is expected across the subduction thrust at the top of the oceanic crust, since the material above the subducting crust is either deep sediment (velocity ~ 6.5 km/s) or mafic/ultramafic units (~ 7.0 – 7.25 km/s). In the smooth inversion model, the JdF Moho is taken at an intermediate velocity of 7.5 km/s and the thrust is approximately 7 km higher assuming average oceanic crustal thickness. Depth to the top of JdF plate mapped from the tomographic velocity model is shown as red contours in Fig. 5.25.

In line EW1 (Fig. 5.23), the dip of the JdF plate is computed in a small section with well-defined velocity structure, between 150–230 km model distance. The dip changes from 9.5° to 19.5° at the tip of southern Vancouver Island (200 km model distance) and a few earthquakes are located at this model distance. The dip computed in east-west profile EW2 (Fig. 5.23), 50 km south of EW1, changes from 10.5° to 21.5° at the 220 km model distance (beneath Puget Sound).

The change in dip of the plate as it enters the regime of Strait of Georgia suggests that the transformation of the basalt/gabbro to eclogite at this location may result in an increase in density of the subducting crust with an associated reduction in volume. This may be reflected as a down-drop in the topography forming a basin in the fore-arc region (Rogers 2000b). The broad velocity low observed in the upper crust in the region of Strait of Georgia may then be explained by the probable upward migration of the expelled fluids from the phase change reactions in the subducting crust. Fluid expulsion is heterogeneous, and much fluid reaches the surface (Hyndman and Peacock *et al.* 2001). The margin perpendicular line D7 (Fig. 5.26) shows a clear example of this behavior. At 130 km model distance, a velocity reversal is observed directly above a cluster of earthquakes (G1) at 65 km depth. The lowering of velocity observed in the forearc mantle may be indicative of serpentine and other hydrous minerals (Hyndman and Peacock *et al.* 2001).

5.4.10 Seismicity Correlation With Structure

Profile D12 (Fig. 5.16) shows a distinct line of earthquakes extending along the projected dip of the Leech River fault at the 60 km model distance. This plane of earthquakes is strongest on this profile but has events on adjacent lines. On line D13 (Fig. 5.17) the Devils Mountain fault, starting beneath the southern tip of Vancouver Island, is possibly associated with the cluster of earthquakes located at a depth of 10–20 km at 90 km model distance.

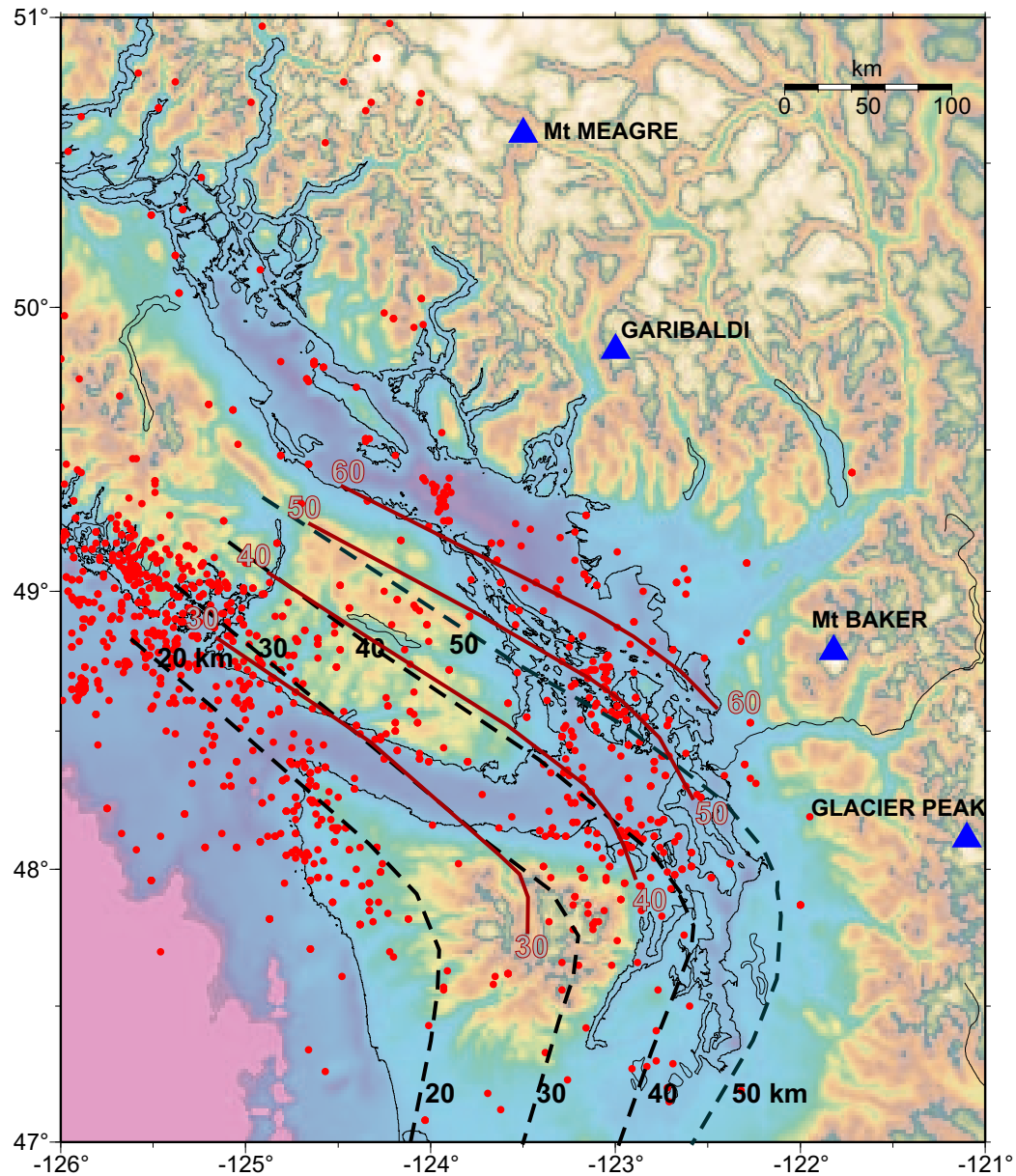


Figure 5.25 Depth to the top of the JdF crust mapped from the tomographic velocity model is shown by the red contour lines. Depth values from previous are represented by black, dashed contour lines. Depth data from Hyndman and Wang (1990), Crosson and Owens (1987) and Cassidy *et al.* (1993). Wadati-Benioff earthquakes in southwestern British Columbia and northwestern Washington from 1984–2000 are shown by red dots.

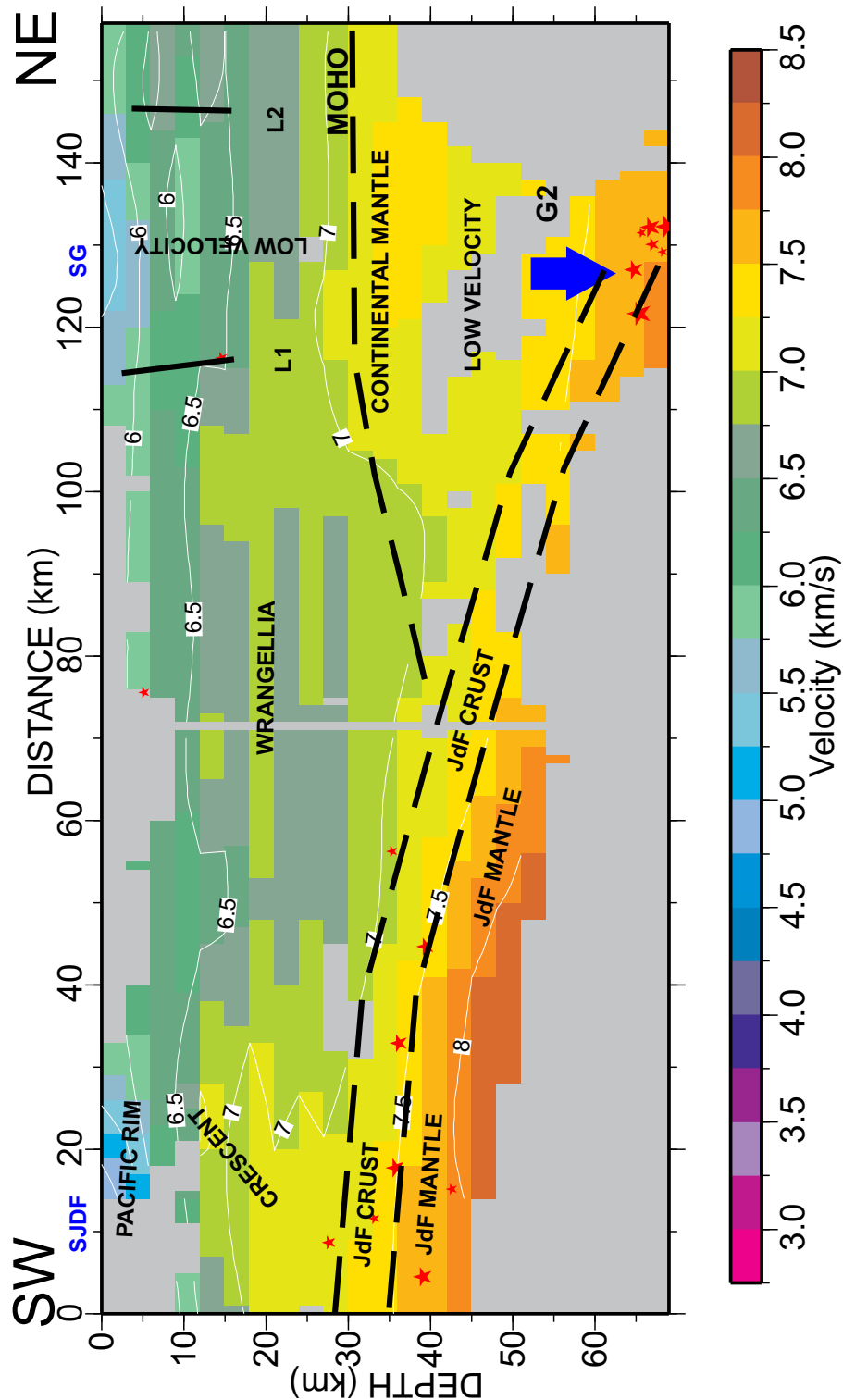


Figure 5.26 Vertical velocity slice along line D7. SJDF-Strait of Juan de Fuca; SG-Strait of Georgia. G1 - cluster of Wadati-Benioff earthquakes.

In the 6.0 km/s isovelocity surface of the SV model (Fig. 4.14), four main clusters of seismicity (*A*, *B*, *C*, *D*) are observed in the central and western Strait of Georgia. The 6.0 km/s isovelocity surface of the EV model (Fig. 5.20) shows the relocated hypocentral locations down to a depth of 15 km. The clusters *A*, *B* and *D* appear to be associated with basement highs. Cluster *C* lies on the northern edge of the deepest basinal low. The activity peaks at cluster *C* where the NW-SE trend of the CFTB is intersected by E-W trending highs. This effect is observed strongly at the E-W trend of the Devils Mountain fault and the Lummi Island fault. The earthquake activity at the sharp E-W structural feature in the Nanaimo subbasin at 49.25° N is the limit of the major NW-SE earthquake trend observed in the western margin of the Strait of Georgia. A few relocated earthquakes are observed in the vicinity of Leech River fault at the southern tip of Vancouver Island indicating a possible activation of the fault (Fig. 5.20). Wadati-Benioff earthquakes are concentrated near the interpreted depth of the oceanic Moho, i.e. about 7.5 km/s. Thus the data cannot resolve conclusively whether they occur in the lowermost crust or uppermost mantle.

5.5 Summary

The interpretation of the velocity slices of the SV and EV models leads to the following major conclusions regarding upper crustal and slab features in the study area. The high velocity Crescent Terrane and the mafic/ultramafic units are observed in proximity at three different locations (Profile S3) and are interpreted to be related. At the southern tip of Vancouver Island the Leech River fault and Devils Mountain fault correlate with seismicity in the subsurface. The slab seismicity beneath the Strait of Georgia is observed to correlate with a low velocity zone in the mantle wedge at depths of about 40–55 km. The Juan de Fuca crust and upper mantle are mapped with clarity beneath southern Vancouver Island, the Olympic Peninsula,

the Strait of Georgia, and Puget Sound. The tomographic velocity model provides valuable constraints for further studies to invert reflection events for locating the top and base of the subducting slab, and for hypocentral parameter estimation and relocation.

Chapter 6

Discussion and Conclusions

The major focus of this thesis was the application of non-linear seismic tomography to controlled source and earthquake data of southwestern British Columbia and northwestern Washington, and the interpretation of the results in terms of regional subsurface geological features to further understanding of the tectonic processes in action. The tomographic inversion of controlled source seismic data from the 1998 SHIPS experiment yielded a velocity model for the upper crust with a cell size of 1 km. The checkerboard test conducted on the velocity model indicated a lateral resolution in the scale of 20 km and above. The ray coverage well constrained the subsurface beneath Strait of Georgia, Southern Vancouver Island and Strait of Juan de Fuca down to 10 km depth.

The interpretation of the controlled source velocity model was aimed at identifying the thicknesses of sediments in localised basins and at mapping seismogenic zones relative to geological structures, which were some of the original objectives for the SHIPS experiment. Basins in Georgia Strait stand out clearly in profile sections P1 and P2 (Figs. 4.8 and 4.9). Sedimentary thicknesses of approximately 8 km and 4 km were mapped in Nanaimo and Comox subbasins, respectively. The Clallum basin overlies Crescent Terrane in the Strait of Juan de Fuca with a sediment thickness of approximately 5 km (Fig. 4.10). At several locations, the contact of Wrangellia with Coast Plutonic Complex is mapped close to the eastern margin of the Strait of Georgia (Fig. 4.10). The subsurface disposition of the Crescent Terrane is well mapped beneath southern Vancouver Island. The depth extent of Crescent Terrane beneath Southern Vancouver Island exceeds 10 km (Fig. 4.12). In the southeastern part of the Strait of Georgia a strong correlation is observed between the shallow

seismicity and the structural features mapped in the velocity model. At this location, the major northeast-southwest structural trend is dissected by east-west trends (Fig. 4.14). The structural trends associated with the Leech River Fault at the southern tip of Vancouver Island correlate with observed seismicity and indicate that the fault may be active in this region (Fig. 4.14).

The tomographic algorithm developed for earthquake tomography was successfully tested on synthetic data. The synthetic model tests recovered the known hypocentral parameters and the velocity structure within reasonable accuracy. The application of a joint inversion algorithm on earthquake data and SHIPS data resulted in a velocity model with a cell size of 3 km, depicting shallow and deeper crustal features in the continental crust and the subducting oceanic crust and mantle. One important aspect of this inversion was that the upper crustal features were constrained by the SHIPS data. This in turn imposed better control on the recovery of deeper features. The lateral resolution indicated by checkerboard tests was about 30 km and above.

The Crescent Terrane is well mapped in the earthquake velocity model and continuity below 10 km depth is identified. The Leech River fault which defines the northern termination of Crescent Terrane is mapped with a dip of 33° and extends down to 20 km depth (Fig. 5.22). Close to the Clallum basin, the width of Crescent Terrane at the surface level is mapped over a distance of 40 km. The Olympic Core rocks extend north, beneath the Crescent Terrane. Beneath southern Vancouver Island, the mafic/ultramafic units together with the Crescent Terrane are identified as the northern limit of Olympic Core rocks. The Crescent Terrane and the mafic/ultramafic units are observed in close proximity at three different places, close to Barkley sound, beneath southern Vancouver Island and central Puget Sound. The mafic/ultramafic units are thus interpreted to be related to the formation of Crescent Terrane (Fig. 5.8). At the southern tip of Vancouver Island, the Leech River fault and Devils Mountain fault correlate with seismicity in the subsurface and are interpreted to be active (Figs. 5.16 and 5.16). Additional confirmation from focal mechanism studies

and study of deformation in Holocene sediments will lead to a better understanding of their role in crustal earthquake mechanism in this region.

The subducting Juan de Fuca plate is well mapped beneath southern Vancouver Island, the Strait of Juan de Fuca, Strait of Georgia, Olympic Peninsula, and Puget Sound. The change in dip of the JdF plate beneath the Strait of Georgia (Fig. 5.8) suggests that the transformation of the basalt/gabbro to eclogite in the subducting JdF crust at this location may be responsible for an increase in the density of the oceanic crust with associated shrinkage in volume and vertical contraction. The broad velocity low observed in the upper crust in the region of the Strait of Georgia can then be explained by the upward migration of the expelled fluids from the phase change reactions in the subducting crust.

The tomographic velocity model provides valuable constraints for further studies to invert reflection events for locating the top and base of the subducting slab, and for hypocentral parameter estimation and relocation.

6.1 Suggestions for Further Work

With the use of a greater subset of data from the 1998 SHIPS experiment, the shallower structure can be mapped with a larger spatial coverage. The 1998 SHIPS data recorded at the permanent recording stations can also be incorporated into the inversion which will enhance the knowledge of subsurface velocity at these locations. There is a wealth of controlled source refraction data recorded in earlier experiments which can be added to the inversion data set and fill the spatial gaps in the velocity model.

The use of earthquake data from northwestern Washington will offer a continuous spatial coverage and extend the velocity model more to the south. This aspect is to be taken as a priority to understand the seismicity that peaks at the junction of

the Strait of Juan de Fuca, Strait of Georgia and Puget Sound. The continuity of Crescent Terrane in the subsurface beneath Puget Sound would help to delimit the terrane boundary to the east.

Gravity modelling and inversion studies of the mafic/ultramafic units and the Crescent Terrane observed beneath Barkley Sound, Southern Vancouver Island and Puget Sound would offer additional control of their structure, velocity and density. It becomes immensely important to focus a study on the relationship between Crescent Terrane and the mafic/ultramafic units observed in southwestern British Columbia and northwestern Washington since this is expected to lead to additional clues in understanding the structure and seismicity of the subducting plate. Another intriguing aspect to be studied is the relationship between the low velocity zone observed beneath the Strait of Georgia and its relation to phase change mechanisms in the subducting JdF crust.

References

- Aki, K., Overview, *Seismic Tomography: Theory and practice*, Edited by H.M. Iyer and K. Hirahara, Chapman and Hall, London, 1993.
- Aki, K., and Lee, W. H. K., Determination of three dimensional velocity anomalies under a seismic array using first *P* arrival time from local earthquake, 1. A homogeneous initial model, *J. Geophys. Res.*, **81**, 4381-4399, 1976.
- Aki, K., Christoffersson, A., and Husebye, E. S., Three-dimensional seismic-velocity anomalies in the crust and upper-mantle under the U.S.G.S. California seismic array (abstract), *Eos, Trans. Am. Geophys. Union*, **56**, 1145, 1974.
- Backus G., and Gilbert, F., Numerical applications of a formalism for geophysical inverse problems, *Geophys. J. R. Astron. Soc.*, **13**, 247-276, 1967.
- Brandon, M. T., and Calderwood, A., R., High-pressure metamorphism and uplift of the Olympic subduction complex, *Geology*, **18**, 1252-1255, 1990.
- Brandon, M. T., and Calderwood, A., R., Late Cenozoic Exhumation of the Cascadia accretionary wedge in the Olympic Mountains, Northwest Washington State, *Geological Society of America Bulletin*, **110**, 985-1009, 1998.
- Brocher, T. M., Parsons, T., Blakely, R. A., Christensen, N. I., Fisher, M. A., Wells, R. E., and the SHIPS Working Group, Upper crustal structure in Puget Lowland, Washington: Results from 1998 Seismic Hazards Investigation in Puget Sound, *J. Geophys. Res.*, **106**, 13541-13564, 2001.
- Brocher, T. M., Christensen, N. I., Density and velocity relationships for digital sonic and density logs from coastal Washington and laboratory measurements

-
- of Olympic peninsula mafic rocks and greywackes, *Open File Report* 01-264, U.S.Geological Survey, 2001a.
- Brocher, T. M., Parsons, T., Creager, K. C., Crosson, R. S., Symons, N. P., Spence, G. D., Zelt, B. C., Hammer, P. T. C., Hyndman, R. D., Mosher, D. C., Trehu, A. M., Miller, K. C., ten Brink, R. S., Fisher, M. A., Pratt, T. L., Alvarez, M. G., Beaudoin, B. C., Loudon, K. E., and Weaver, C. S., Wide-angle seismic recordings from the 1998 Seismic Hazards Investigation Of Puget Sound (SHIPS), Western Washington and British Colombia, *Open File Report* 99-3314, U.S. Geological Survey, 1998.
- Calvert, A. J. Seismic reflection constraints on imbrication and underplating of the northern Cascadia convergent margin. *Canadian Journal of Earth Sciences*, **33**, 1294-1307, 1996.
- Calvert, A. J., Clowes, R. M., Deep, high amplitude reflections from a shear zone above the subducting Juan de Fuca plate, *Geology*, **18**, 1091-1094, 1990.
- Cassidy, J. F., and Ellis, R. M., *S* Wave velocity structure of the northern Cascadia subduction zone, *J. Geophys. Res.*, **98**, 4407-4421, 1993.
- Cassidy, J. F., and Waldhauser, F., Precise relocations of slab seismicity in the northern Cascadia Subduction Zone. *Abstract*, Seismological Society of America, 2001.
- Christensen, N. I., and Mooney, W. D., Seismic velocity structure and composition of the continental crust: A global view, *J. Geophys. Res.*, **100**, 9761-9788, 1995.
- Clayton, R. W., and Comer, R. P., A tomographic analysis of mantle heterogeneities from body wave travel time (abstract), *Eos, Trans. Am. Geophys. Union*, **64**, 776, 1983.

- Clowes, R.M., Brandon, M. T., Green, A. G., Yorath, C. J., Sutherland Brown, A., Kanasewich, E. R., and Spencer, C., LITHOPROBE - southern Vancouver Island: Cenozoic subduction complex imaged by deep seismic reflections, *Canadian Journal of Earth Sciences*, **24**, 31-51, 1987.
- Clowes, R. M., Baird, D. J., and Dehler, S. A., Crustal structure of the Cascadia subduction zone, south western British Colombia, from Potential field and seismic studies, *Canadian Journal of Earth Sciences*, **34** 317-335, 1997.
- Constable, S. C., Parker, R. L., and Constable, C. G., Occam's inversion: a practical algorithm for generating smooth models from electromagnetic sounding data, *Geophysics*, **52**, 289-300, 1987.
- Creager, K. C., Preston, L. A., Crosson, R. L., and Trehu, A., and the SHIPS working group, 3-D reflection image of the subducting Juan de Fuca Plate, *Intraslab Earthquakes Workshop Abstracts*, September 18-21, 2000, Victoria, BC, Canada, p 85-88, 2000.
- Crosson, R. S., Crustal structure modeling of earthquake data, 1, Simultaneous least-squares estimation of hypocenter and velocity parameters, *J. Geophys. Res.*, **81**, 3036-3046, 1976.
- Crosson, R. S., and Owens, T. J., Slab geometry of the Cascadia subduction zone beneath Washington from earthquake hypocenters and teleseismic converted waves, *Geophys. Res. Letters*, **14**, 14824-14827, 1987.
- Crosson, R. S., Symons, N.P., Creager, K. C., Preston, L. A., Van Wagoner, T., Brocher, T. M., Fisher, M., and the SHIPS working Group 3-D structure of Cascadia Forearc region from SHIPS active experiment and earthquake observations:

- tomographic inversion provides a high-resolution view into the core of the Cascadia Forearc complex, *Intraslab Earthquakes Workshop Abstracts*, September 18-21, 2000, Victoria, BC, Canada, p 89, 2000.
- Davis, E. E., and Hyndman, R. D., Accretion and deformation of sediments along the northern Cascadia subduction zone, *Geological Society of America Bulletin*, **101**, 1465-1480, 1989.
- Dehler, S. A and Clowes, R. M., Integrated geophysical modelling of terranes and other structural features along the western Canadian margin, *Canadian Journal of Earth Sciences*, **29**, 1492-1508, 1992.
- England, T. D. J., and Bustin, R. M., Architecture of the Georgia Basin, southwestern British Columbia, *Bulletin of Canadian Petroleum Geology*, **46**, 288-320, 1998.
- Fowler, C. M. R., *The Solid Earth: An Introduction to Global Geophysics*, Cambridge University Press, New York, 1990.
- Graindorge, D., Spence, G., Hyndman, R. D., Collot, J. Y., Charvis, P., and Trehu, A., Crustal structure beneath Juan de Fuca Strait and southern Vancouver Island from seismic and gravity analyses, (In Preparation), 2001.
- Green, A. G., Clowes, R. M., and Ellis, R. M., Crustal studies across Vancouver Island and adjacent offshore margin; in *Studies of Laterally Heterogeneous Structures Using Seismic Refraction and Reflection Data*, ed. A. G. Green; Geological Survey of Canada, Paper 89-13, 3-25, 1990.
- Geiger, L., Probability method for the determination of earthquake epicenters from the arrival time only, *Bull. St. Louis Univ.*, **8**, 60-71, 1912.
- Hammer, P. T. C., Dorman, L. M., Hildebrand, J. A., and Cornuelle, B. D., Jasper sea mount structure: Sea-floor seismic refraction tomography, *J. Geophys. Res.*, **99** 6731-6752, 1994.

-
- Hearn, T. M., and Ni, J. F., Pn velocities beneath continental collision Zones: The Turkish -Iranian Plateau, *Geophys. J. Int.*, **117**, 273-283, 1994.
- Hole, J. A., Nonlinear high-resolution three-dimensional seismic traveltime tomography, *J. Geophys. Res.*, **97**, 6553-6562, 1989.
- Hole, J. A. and Zelt, B. C., Three-dimensional finite difference reflection travel times, *J. Geophys. Res.*, **121**, 427-434, 1995.
- Humphreys, E. D., and Clayton, R. W., Adaptation of back-projection tomography to seismic travel-time problems, *J. Geophys. Res.*, **93**, 1073-1085, 1988.
- Humphreys, E. D., and Clayton, R. W., Tomographic image of the southern California mantle, *J. Geophys. Res.*, **95**, 19725-19746, 1990.
- Hyndman, R. D., Dipping Reflectors, electrically conductive zones and free water beneath a subduction zone. *J. Geophys. Res.*, **93**, 13391-13405, 1988.
- Hyndman, R. D., Giant earthquakes along the west coast of North America, *Scientific American*, **273**, 68-75, 1995a.
- Hyndman, R. D., The Lithoprobe corridor across the Vancouver Island continental margin: the structural and tectonic consequences of subduction, *Canadian Journal of Earth Sciences*, **32**, 1777-1802, 1995b.
- Hyndman, R. D., and Hamilton, T. S. Queen Charlotte area Cenozoic tectonics and volcanism and their association with relative plate motions along the north eastern Pacific Margin, *J. Geophys. Res.*, **98**, 14257-14277, 1993.
- Hyndman, R. D., Peacock, S. M., Serpentinisation of the Forearc Mantle, (In Preparation), 2001.

-
- Hyndman, R. D., and Wang, K., Thermal constraints on the zone of major thrust earthquake failure: The Cascadia subduction zone, *J. of Geophys. Res.*, **98**, 2039-2060, 1993.
- Hyndman, R. D., Riddihough, R. P., and Herzer, R., The Nootka fault zone - a new plate boundary off western Canada, *Geophysical Journal of Royal Astronomical Society*, **58**, 667-683, 1979.
- Hyndman, R.D., Yorath, C.J., Clowes, R.M., and Davis, E.E., The northern Cascadia Subduction Zone at Vancouver Island: Seismic structure and tectonic history, *Canadian Journal of Earth Sciences*, **27**, 313-329, 1990.
- Irving, E., Whence British Columbia, *Nature*, **314**, 673-674, 1985.
- Jackson, D. D., The use of a priori data to resolve non-uniqueness in linear inversion. *Geophys. J. R. Astron. Soc.*, **57**, 137-157, 1979.
- Johnson, S.Y., Evidence for a margin truncating transcurrent fault (pre-late Eocene) in western Washington, *Geology*, **12**, 538-541, 1984.
- Kirby, S. H., Engdahl, E. R., and Denlinger, R., Intermediate-depth intraslab earthquakes and arc volcanism as physical expressions of crustal and uppermost mantle metamorphism in subducting slabs, *Subduction: Top to bottom, Geophysical Monograph 96*, Bebout, G., D., Scholl, S. Kirby, J. Platt, eds., pp. 195-214, American Geophysical Union, Washington, D.C., 1996.
- Kirby, S., and Wang, K., Introduction to a global systems approach to Cascadia slab processes, *Intraslab Earthquakes Workshop Abstracts*, September 18-21, 2000, Victoria, BC, Canada, p 9, 2000.
- Lees, J. M., and Crosson, R. S., Tomographic inversion for three dimensional velocity structure at Mount St. Helens using earthquake data, *J. Geophys. Res.*, **94**, 5716-5728, 1989.

-
- Massey, J. E., The Metchosin Igneous Complex, southern Vancouver Island; Ophiolite stratigraphy developed in an emergent setting, *Geology*, **14** , 602-605, 1986.
- McMechan, G. A., and Spence, G., D., P-wave velocity structure of the Earth's crust beneath Vancouver Island, *Canadian Journal of Earth Sciences*, **20**, 742-752, 1983.
- Menke, W., *Geophysical Data analysis: Discrete Inverse theory*, Academic Press, San Diego, California, 1989.
- Miller, K. C., Keller, G. R., Gridley, J. M., Luetgert, J., Mooney, W., and Thybo, H., Crustal structure along the west flank of the Cascades, western Washington, *J. Geophys. Res.*, **102**, 17857-17873, 1997.
- Monger, J. W. H., Price, R. A., and Tempelman-Kluit, D. J., tectonic accretion and the origin of the two major metamorphic and plutonic belts in the Canadian Cordillera, *Geology*, **10**, 70-75, 1982.
- Mulder, T. L., *Small earthquakes in southwestern British Columbia (1975-1991)*, M.Sc., Thesis, University of Victoria, Victoria, BC, Canada, 117p, 1995.
- Muller, J. E., Evolution of the Pacific Margin, Vancouver Island, and adjacent regions, *Canadian Journal of Earth Sciences*, **14**, 2062-2085, 1977.
- Muller, J. E., Chemistry and Origin of Eocene Metchosin Volcanics, Vancouver Island, British Columbia, *Canadian Journal of Earth Sciences*, **17**, 199-209, 1980.
- Nolet, G., *Seismic Tomography*, Reidel, Dordrecht, 1987.
- Paige, C. C. and Saunders, M. A., 1982, LSQR: An algorithm for sparse linear equations and sparse least squares, *Assoc. Comput. Mach. Trans. Math. Software* , **8**, 43-71, 1982.

-
- Parker, R. L., Unpublished Manuscript on methods of inverse theory.
- Parsons, T. J., McCarthy, J., Kohler, W. M., Ammon, C. J., Benz, H. M., Hole, J. A., and Criley, E. E., Crustal structure of the Colorado Plateau, Arizona: application of new long-offset seismic data analysis techniques, *J. Geophys. Res.*, **101**, 11173-11194, 1996.
- Peacock, S. M., Thermal and petrological structure of subduction zones in *Subduction: Top to Bottom*, edited by G. Bebout, D. W. Scholl, S.H. Kirby, and J.P. Platt, American Geophysical Union, Washington, D.C., 119-133, 1996.
- Riddihough, R. P., Gravity and structure of an active margin - British Columbia and Washington, *Canadian Journal of Earth Sciences*, **16**, 350-363, 1979.
- Riddihough, R. P., One hundred years of plate tectonics in Western Canada, *Geoscience Canada*, **9**, 28-34, 1982.
- Riddihough, R. P., Recent movements of the Juan de Fuca plate system, *Journal of Geophysical Research*, **89**, 6980-6994, 1984.
- Riddihough, R. P., and Hyndman, R. D., Modern plate tectonic regime of the continental margin of western Canada, *In Geology of the Cordilleran Orogen in Canada*, Edited by , H. Gabrielse and C.J. Yorath, Geological Survey of Canada, Geology of Canada, **4**, 435-455, 1991.
- Rogers, G. C., *Seismotectonics of British Columbia*, Ph.D. dissertation, University of British Columbia, Vancouver, BC, Canada, 247p, 1983.
- Rogers, G. C., An assessment of the megathrust earthquake potential of the Cascadia subduction zone, *Canadian Journal of Earth Science*, **25**, 844-852, 1988.
- Rogers, G. C., Earthquakes in the Vancouver area, in J.W.H. Monger,(ed) *Geology*

-
- and Geological Hazards of the Vancouver Region, Southwestern British Columbia*, Geological Survey of Canada, Bulletin, 481, p. 221-229, 1994.
- Rogers, G. C., Phase changes, fluids and the co-location of the deep and shallow seismicity beneath Puget sound and southern Strait of Georgia, *Intraslab Earthquakes Workshop Abstracts*, September 18-21, 2000, Victoria, BC, Canada, p 105, 2000.
- Rogers, G. C., The role of phase change in the development of forearc basins, in *Intraslab Earthquakes Workshop Abstracts*, September 18-21, 2000, Victoria, BC, Canada, p 107, 2000.
- Shaw, P. R., Orcutt, J. A., Waveform inversion of seismic refraction data and applications to young Pacific crust, *Geophys. J. R. Astr. Soc.*, **82**, 375-414, 1985.
- Spence, G. D., Clowes, R. M., Ellis, R. M., Seismic structure across the active subduction zone of Western Canada, *J. Geophys. Res.*, **90**, 6754-6772, 1985.
- Spence, G. D., Hyndman, R. D., Davis, E. E., and Yorath, C. J., Seismic structure of the northern Cascadia accretionary prism: evidence from new multichannel seismic reflection data, *In Continental lithosphere: deep seismic reflections. Edited by R.Meissner, L. Brown, H.Durbaum, W.Franke, K.Fuchs, and F. Seifert, American Geophysical Union, Geodynamics Series*, **22**, 257-263, 1991
- Spence, G.D., and McLean, N.A., Crustal seismic velocity and density structure of the Intermontane and Coastal belts, southwestern Cordillera, *Can. J. Earth Sciences*, **35**, 1365-1379,1998.
- Stanley, D., Villaseñor, A., and Benz, H., Subduction zone and crustal dynamics of western Washington: A tectonic model for earthquake hazards evaluation, *Open File Report 99-311*, U.S. Geological Survey, Denver, Colarado, 1999.

- Symons, N. P., and Crosson, R. S., Seismic velocity structure of the Puget Sound Region from nonlinear tomography, *Gephys. Res. Lett.*, **24**, 2593-2596, 1997.
- Tarantola, A., and Valette, B., Inverse problems = quest for information, *J. Geophys. Res.*, **50**, 159-170, 1982
- Thurber, C. H., Earthquake locations and three dimensional crustal structure in the Coyote Lake area, central California, *J. Geophys. Res.*, **88**, 8226-8236, 1983
- Thurber, C. H., Analysis methods for kinematic data from local earthquakes, *Reviews of Geophysics*, **24**, 793-805, 1986.
- Tikhonov, A. N., and Arsenin, V. Y., Solutions of ill-posed problems, John Wiley, 258 pp., 1977.
- Toomey, D. R., Solomon, S. C., and Purdy, G. M., Tomographic imaging of the shallow crustal structure of the East Pacific Rise at 9° 30'N, *J. Geophys. Res.*, **99**, 24135-24157, 1994.
- Trehu, A. M., Brocher, T. M., Creager, K. C., Fisher, M. A., Preston, L., and Spence, G. D., Geometry of the subducting Juan de Fuca Plate: New constraints from SHIPS98, (In Preparation), 2001.
- Vidale, J. E., Finite-difference calculation of traveltimes in three dimensions, *Geophysics*, **55**, 521-526, 1990.
- Wang, K., Mulder, T., Rogers, G. C., and Hyndman, R. D., Case for low coupling stress on the Cascadia subduction fault, *J. Geophys. Res.*, **100**, 12907-12918, 1995.
- van Wagoner, M. T., Crosson, R. S., Creager, K. C., Medema, G., Preston, L., and the SHIPS Working Group, Crustal structure and relocated earthquakes in the

Puget Lowland, Washington from high resolution seismic tomography, (Paper Submitted to JGR).

Wiggins, R. A., The geneal linear inverse problem: Implication of surface waves and free oscillations for Earth structure, *Reviews of Geophysics*, **10**, 251-285, 1972.

Williams, R. A., Stephenson, W. J., Odum, J. K., and Worley, D. M., Site response related shallow P- and S- wave velocity measurements in Seattle, and on the Crescent Formation Near Olympia Washington, AGU Abstracts, 2000.

Zelt, B.C., Ellis, R. M., Clowes, R. M., Kanasewich, E. R., Asudeh, I., Luetgert, J. H., Hajnal, Z., Ikami, A., Spence, G. D., and Hyndman, R. D., Crust and upper mantle velocity structure of the Intermontane belt, south Canadian Cordillera, *Canadian Journal of Earth Sciences*, **29**, 1530-1548, 1992.

Zelt, B.C., Ellis, R. M., Zelt, C. A., Hyndman, R. D., Lowe, C., Spence, G. D., and Fisher, M. A., Three dimensional crustal velocity structure beneath the Strait of Georgia, British Columbia. *Geophys. J. Int.* , **144**, 695-712, 2001.

Zelt, C. A., and Barton, P. J., 3-D Seismic refraction tomography: A comparison of two methods applied to data from the Faroe basin, *J. Geophys. Res.*, **103**, 7187-7210, 1998.

Zhao, D., *A Tomographic Study of Seismic Velocity Structure in the Japan Islands*. Ph.D Thesis, Tohoku University, 1990.

Zhao, D., Wang, K., Rogers, G. C., and Peacock, S. M., Tomographic image of low *P* velocity anomalies above slab in northern Cascadia subduction Zone, *Earth Planets Space*, **53**, 285-293, 2001.

Appendix A

Pseudo Code for Controlled Source Tomography

Set Parameters

1. Maximum number of iterations for inversion.
2. Starting λ (tradeoff parameter) value and reduction factor.
3. Number of λ values to be tested per iteration.

START OUTER LOOP

- (a) FD : finite difference travel-time computation.
- (b) RAY : ray tracing to compute \mathbf{L} (path length) matrix.

START INNER LOOP

- i. Calculate tradeoff parameter λ for the current iteration.
- ii. INVERSE (3-D) : Invert for the slowness perturbations.
- iii. UPDATE : Update slowness parameters with the computed perturbations.
- iv. ARCHIVE : Archive current model.
- v. FD : Compute RMS travel-time misfit and normalised χ^2 .
- vi. STOP : Check if normalised $\chi^2 \approx 1$ and stop the iterations.

END INNER LOOP

- (c) Analyse χ^2 vs λ values.
- (d) Select the best model from the models archived in the above iteration by picking the model with the smallest χ^2 .

(e) Archive the Best Model

END OUTER LOOP

Appendix B

Pseudo Code for Checkerboard Tests

Set Parameters

1. Compute the input checkerboard anomaly for the specified grid size.
2. Add the computed input checkerboard anomaly to the final velocity model (FVM) arrived at from inversion.
3. Compute synthetic travel-times for the actual source-receiver geometry in the above velocity model.
4. Add Gaussian noise to the computed travel-times according to the observed uncertainties in the data.
5. Set this synthetic travel-times as input to the inversion.
6. Set FVM as the starting model.
7. Set tradeoff parameter λ (set equal to λ value of final iteration in the actual data inversion).
8. FD : Finite difference travel-time computation.
9. RAY : ray tracing to compute \mathbf{L} (path length) matrix.

START LOOP

- (a) Compute tradeoff parameter λ .
- (b) Inverse(3-D) : Invert for the slowness perturbations.
- (c) Update : Update slowness parameters with the computed perturbations.

- (d) Archive : Archive current model.
- (e) FD : Forward computation to compute RMS misfit and normalised χ^2 .
- (f) STOP : Check if $\chi^2 \approx 1$ and stop the iterations.
- (g) Archive the velocity model.
- (h) Compute tradeoff parameter λ and do the next iteration if necessary.

END LOOP

10. Compute the recovered anomaly pattern.
11. Compute the semblance between input and recovered anomaly pattern.

Appendix C

Pseudo Code for Earthquake Tomography

Set Parameters

1. Maximum number of iterations for inversion.
2. Starting λ (tradeoff parameter) value and reduction factor.

START LOOP

- (a) FD : finite difference travel-time computation.
- (b) RAY : ray tracing to compute \mathbf{L} (path length) matrix.
- (c) Calculate tradeoff parameter λ for the current iteration.
- (d) INVERSE (3-D) : Invert for the slowness and hypocentral parameter perturbations.
- (e) UPDATE : Update slowness and hypocenter parameters with the computed perturbations.
- (f) FD : Compute RMS travel-time misfit and normalised χ^2 .
- (g) STOP : Check if normalised $\chi^2 \approx 1$ and stop the iterations.
- (h) ARCHIVE : archive the model and do the next iteration.

END LOOP

Appendix D

CD-ROM Contents

The CD-ROM supplement contains the velocity models constructed from the inversion of SHIPS data and the joint inversion of earthquake and SHIPS data. The figures constructed from the velocity models are provided for reference. The figures are in the postscript (ps) format or the encapsulated postscript (eps) format and can be viewed using the ghostview program or printed on any postscript printer. Animation clips are provided in the AVI format and can be viewed using the Windows Media Player or Real Player.

SHIPS Tomography Velocity Model (SVM)

- The velocity model constructed from the inversion of SHIPS data is provided as an ascii file ‘cdromvel.sh’ under the directory \ships\velocity-model.
- The description of data format of the file and a sample fortran code to read the file are provided in the file ‘cdromsh.f’ under the above directory.

Figures Constructed From SVM

- The horizontal slice plots are provided under the directory \ships\plots\horizontal.
- The five profile plots discussed in Chapter 4 and the location map are provided under the directory \ships\plots\profile.
- The isovelocity surfaces for the 5.5 and 6.0 km/s velocity are provided under the directory \ships\plots\iso.

Earthquake Tomography Velocity Model (EVM)

- The velocity model constructed from the inversion of SHIPS data is provided as an ascii file ‘cdromvel.eq’ under the directory \eq+ships\velocity-model.
- The description of data format of the file and a sample fortran code to read the file are provided in the file ‘cdromeq.f’ under the above directory.

Figures Constructed From EVM

- The horizontal slice plots are provided under the directory \eq+ships\plots\horizontal.
- The profile plots discussed in Chapter 5 and the location maps are provided under the directory \eq+ships\plots\profile.
- The isovelocity surfaces are provided under the directory \eq+ships\plots\iso.
- Animation clips generated with the horizontal and vertical slices are provided under the directory \eq+ships\plots\movie.

Vita

Surname: Ramachandran
Given Names: Kumar
Place of Birth: Madurai, Tamil Nadu, India

Educational Institutions Attended:

University of Victoria, BC, Canada	1999–2001
Indian School of Mines Dhanbad, Dhanbad, Bihar, India	1982–1985, 1989–1990
Madurai Kamaraj University, Madurai, Tamilnadu, India	1977–1980

Diplomas & Degrees Awarded:

Master of Technology, Indian School of Mines	1990
Master of Science Technology, Indian School of Mines	1985
Bachelor of Science, Madurai Kamaraj University	1980

Publications:

Ramachandran, K., Dosso, S., Zelt, C., Spence, G. D., and Hyndman, R. D., Upper Crustal Velocity Structure of Southwestern British Columbia From 3D Nonlinear First Arrival Traveltime Tomography, Abstract, AGU-2000.

Ramachandran, K., Dosso, S., Zelt, C., Spence, G. D., and Hyndman, R. D., 3D Velocity Structure from Tomographic Inversion of SHIPS Data from Southwestern British Columbia, Abstract, SSA-2001.

Ramachandran, K., Spence, G. D., Dosso, S., Hyndman, R. D., Brocher, T. M., and Fisher, M. M., 3-D Velocity Structure of Southwestern British Columbia and Northern Washington, Abstract, AGU-2001.

Partial Copyright License

I hereby grant the right to lend my thesis to users of the University of Victoria Library, and to make single copies only for such users or in response to a request from the Library of any other university, or similar institution, on its behalf or for one of its users. I further agree that permission for extensive copying of this thesis for scholarly purposes may be granted by me or a member of the University designated by me. It is understood that copying or publication of this thesis for financial gain shall not be allowed without my written permission.

Title of thesis:

Velocity Structure of S.W. British Columbia, and N.W. Washington, From 3-D
Non-linear Seismic Tomography

Author:

Kumar Ramachandran

November 24, 2001